Measurement of the Cross Section of W Bosons Produced in pp Collisions at $\sqrt{s} = 7$ TeV With the ATLAS Detector

A dissertation presented
by

Srivas Prasad

to
The Department of Physics
in partial fulfillment of the requirements
for the degree of
Doctor of Philosophy
in the subject of

Physics

Harvard University
Cambridge, Massachusetts
May 2011

Thesis advisor Author

João Pedro Barreiro Guimarães da Costa **Srivas Prasad**

Measurement of the Cross Section of W Bosons Produced in pp Collisions at $\sqrt{s} = 7$ TeV With the ATLAS Detector

Abstract

This dissertation presents a measurement of the inclusive W boson cross section in the muon decay channel, using 7 TeV proton-proton collisions at the Large Hadron Collider. The measurement probes Standard Model QCD predictions at a new regime, at high-Q^2 and low-x in the parton distribution functions. It is also fruitful in understanding the ATLAS detector response to the production of leptons and neutrinos, which are present in many other physics signals.

The dataset used corresponds to an integrated luminosity of 33 pb^{-1}, collected by the ATLAS detector during 2010. Lepton quality, kinematic, and isolation requirements, as well as missing energy and transverse mass criteria are adopted to extract the $W \to \mu\nu$ signal. The major backgrounds come from $W \to \tau\nu$, $Z \to \mu\mu$ where a muon is lost, and from QCD, particularly from heavy-flavor quark decays. Cross sections and kinematic distributions are compared with Standard Model expectations using next-to-leading-order QCD calculations and several PDF sets.

Contents

Citations to Previous Work

Several parts of this dissertation have appeared in ATLAS publications and internal documentation previously. Chapter 6 on t_0 refitting has appeared with some additional details as an ATLAS internal communication:

> "In-situ t0 calibration for MDT segments", A. Belloni et al
> ATL-COM-MUON-2009-006 [26]

The discussion there on MDT timing is reworked with minor changes from:

> "Beam Splash Studies with MDT Chambers: Timing and Flux", A. Belloni et al
> ATL-COM-MUON-2010-006 [27]

The $W \to \mu\nu$ analysis with 310 nb^{-1} of data presented in Chapter 7 has been published:

> "Measurement of the $W \to \ell\nu$ and $Z/\gamma^* \to \ell\ell$ production cross sections in proton-proton collisions at $\sqrt{s} = 7$ TeV with the ATLAS detector",
> ATLAS Collaboration
> JHEP12(2010)060 [19]

The discussion draws heavily upon the above publication. It also utilizes and abridges the extensive supporting documentation for this result. Details specific to $W \to \mu\nu$ (and $Z \to \mu\mu$) analysis have appeared in an ATLAS internal note:

> "$W \to \mu\nu$ and $Z \to \mu\mu$ cross sections measurements in proton-proton collisions at $\sqrt{s} = 7$ TeV with the ATLAS Detector", ATL-PHYS-INT-2011-019 [65]/ATL-COM-PHYS-2010-685 [64]

The material about muon quality definition for early data in Section 7.3 is found in expanded form as an internal note:

> "Muon Definition for High-p_{T} Physics: Algorithmic Fakes", A. Belloni et al
> ATL-COM-MUON-2010-009 [28]

The cross section analysis strategy and theoretical systematic uncertainties that are explicated in the above documents are based on the analysis in

> “Total inclusive W and Z boson cross section measurements, cross section ratios and combinations in the electron and muon decay channels at 7 TeV based on 300 nb^{-1}”, M. Schott et al
> ATL-COM-PHYS-2010-703 [93]

The cross section analysis in Chapter 8 is an ATLAS preliminary (conference) result:

> “A measurement of the total W and Z/γ^*cross sections in the e and μ decay channels and of their ratios in pp collisions at $\sqrt{s} = 7$ TeV with the ATLAS detector”, ATLAS Collaboration
> ATLAS-CONF-2011-041 [41]

The discussion in that chapter is a condensation of the supporting documentation:

> “$W \to \ell\nu$ and $Z \to \ell\ell$ cross sections measurements in proton-proton collisions at $\sqrt{s} = 7$ TeV with the ATLAS Detector”, ATLAS Collaboration
> ATL-COM-PHYS-2011-178 [42]

Acknowledgments

It is a pleasure to slip into the first person singular, if only for a moment. I am very thankful to several people without whom this work would have been impossible. Foremost I must thank my advisor, João Guimarães da Costa, who has played such a vital role in my education as a physicist, taking away considerable dross and doing his utmost to cultivate and polish what was left. Each of our innumerable meetings led to a new idea, a way forward, or at least an interesting experience. You *were* mostly right! George Brandenburg, Melissa Franklin, John Huth, and Masahiro Morii, in whom there were always wise minds to pick when faced with seemingly unanswerable problems, and sources of ideas and perspective whenever things seemed not to be working. I acknowledge here my wise postdocs, Alberto Belloni and Kevin Black and Corrinne Mills, who've probably taught me more than I could hope to remember. The excellent Verena Martinez Outschoorn, always helpful and clever. She egged me on through my first ski lesson without giggling. Orange! Fellow graduate students; we have studied, struggled, learned and laughed together, and formed that healthy bond whose essential glue is caffeine and late nights before note deadlines. Lashkar Kashif, Ben Smith, Michael Kagan, and all, it's been fun! I thank too the innumerable ATLAS collaborators both at CERN and in the United States. It does not do to achieve here a miniature of the author list, but I thank particularly Maarten Boonekamp, Kevin Einsweiler and Domizia Orestano for taking an interest and lighting the way. My committee members Masahiro Morii and Howard Georgi, for their incisive comments, and for taking the time to peruse this.

I appreciate and cherish above all my family, my parents and my sister, for being an unshakeable support. This is for you.

Chapter 1

Introduction

This dissertation describes a measurement of the inclusive cross section times branching fraction of W bosons decaying to $\mu\nu$, measured with the ATLAS detector using protons colliding at the Large Hadron Collider with $\sqrt{s} = 7$ TeV.

The W boson is a vital ingredient of modern physics. It is the carrier of the charged weak current, and so governs a wide range of interactions, from heavy quark decay and neutron beta decay to neutrino interactions as a whole. Experimentally, its discovery together with the Z boson at the S$p\bar{p}$S was important confirmation of the Standard Model description of particle physics. Precise measurements of its mass, for example at the Tevatron, have provided constraints on the Higgs, which radiatively imposes a logarithmic correction upon the W. At the LHC too, detailed investigation of electroweak vertices involving the W is expected to constrain models of new physics.

The W boson cross section has been computed to next-to-next-to leading order in perturbative QCD theory. Its measurement is therefore a stringent probe of those expectations, and is also helpful in constraining parton distribution functions. Understanding of the W is also useful in measuring the top, in searches for $W^{'}$ models, and generally as a background to analysis in the standard model and beyond. Further, W bosons decaying to muons and neutrinos are a vital tool in studying the detector with collision data. The process is a copious source of high-momentum, isolated muons, which are a key detector signature. W and Z boson events are therefore valuable in understanding muon efficiencies and resolutions. Further, the neutrino provides a missing energy signature, so studying it helps understand this experimentally complex quantity.

The dissertation is organized as follows. Chapter 2 provides an overview of the physics relevant to the $W \rightarrow \mu\nu$ measurement, commencing with a whirlwind tour through the Standard Model. We pay emphasis to electroweak theory and its vector gauge bosons, as also to quantum chromodynamics, which is at the heart of hadron collider physics. We then introduce the parton distribution functions, and describe the separation of a hadronic collision into its initial state, hard scattering, showering and hadronization phases. W boson production and decay modes at the LHC are explained. We then sketch the status of theoretical cross section calculations, and summarize previous experimental results.

Our focus shifts thereafter to experimental concerns. Chapter 3 gives a quick overview of the Large Hadron Collider (LHC), which produces the collisions analyzed in this document. After listing the characteristics of the machine, we provide brief argumentation explaining key technology and design choices for the machine. The LHC makes use of the CERN acceleration complex to boost protons from rest to up to 7 TeV; we explain the steps involved. A digest is given of the detectors at the LHC and their physics programs.

In Chapter 4, we describe the ATLAS detector in some detail. We survey its technologies for tracking and calorimetry, and overview relevant aspects of software reconstruction. These include track finding in the silicon and transition radiation trackers, primary vertex finding and missing energy computation. Experimental aspects of the $W \to \mu\nu$ analysis are heavily impacted by the muon spectrometer (MS). The MS triggers on hard muons, its measurement is crucial to muon reconstruction, and it in addition supplies the bulk of the missing energy imputed to the event. Given the importance of the muon to our analysis, we dedicate Chapter 5 to explaining the muon spectrometer. The precision tracking technologies, and in particular the drift tube (MDT) chambers are described in detail, as are the triggering technologies used in the central and forward regions of the detector. We also explain muon software reconstruction and the different types of muons, reconstructed using different strategies and combinations of detector technologies. Our analysis uses "combined" muons, formed by merging muon tracks from the spectrometer and the inner detector; hence, particular attention is given to reconstruction in the MS, and to track matching and combination.

Cosmic rays were used extensively in 2008-09 to commission and calibrate the then newly-assembled ATLAS detector, to ensure readiness for collision data. Muon reconstruction in the cosmic ray environment is the theme of Chapter 6. Reconstructing cosmic rays presents technical challenges in terms of hit timing, since they are mis-timed relative to the machine clock. We describe a technique that was developed to fit for muon timing offsets in-situ during reconstruction, and discuss its performance and some uses.

With basic ingredients in place, the $W \to \mu\nu$ cross section analysis itself moves to center-stage. We present two different analyses. The first, in Chapter 7, discusses the first $W \to \mu\nu$ publication by ATLAS, with early 2010 data. Instead, Chapter 8 discusses the inclusive cross section measurement performed using the hundred-times larger dataset acquired by ATLAS in 2010. In each case, we discuss the muon, missing energy and event selection, as well as the backgrounds, the acceptances/efficiencies, the calculation methodology and systematic uncertainties, and the results obtained. The focus in Chapter 7 is on challenges in understanding W events and the ATLAS detector at the start of data-taking. Muon matching and combination between the ID and MS re-appears, as quality criteria are defined that were used in this first dataset to reject poor-quality fake muons from loose track-matching. We discuss a variety of estimation strategies for various backgrounds, including the cosmic ray background, which is non-negligible at low instantaneous luminosity. The timing offset fitter discussed in Chapter 6 is reawakened to test candidate events under cosmic ray hypotheses. Techniques to measure muon performance with single-muons, appropriate for low statistics, are used in the early analysis.

Chapter 8's analysis by contrast is a high-precision analysis. The enhanced statistics permit the use of finely-binned analysis, and the result emerges from a sum over bins in muon pseudorapidity and charge. More powerful techniques to measure performance in data, together with improved understanding of the luminosity allow this result to test next-to-next-to-leading-order predictions.

We have just discussed in brief what we are about to discuss in detail; after the detailed discussion will come concluding remarks in Chapter 9, where will be discussed again in brief aspects of what will by then have been discussed in detail. Let us begin.

Chapter 2

Theoretical Overview

We provide an overview of physics relevant to this measurement. We begin by describing the Standard Model (Section 2.1), which forms the framework underlying our work. We describe in particular the Electroweak Force (Section 2.2), for which the W is a carrier particle, and the Strong Force (Section 2.3), which describes quarks and gluons and holds the proton together. This last point leads us to a discussion of proton structure and Parton Distribution Functions (PDF), and of proton-proton collisions as seen at the LHC (Section 2.4). We end by describing the production and decay of the W boson (Section 2.5), and give the current theoretical understanding of its cross section, which we then compare to existing results (Section 2.6).

2.1 The Standard Model

Our understanding of nature invokes fundamental particles and the forces they interact via. Particles are classified in terms of their spin as fermions, which have halfinteger spins, and bosons, whose spins take integral values. Four fundamental forces have been observed: gravity, electromagnetism (EM), strong force, and weak force. Gravitation and electromagnetism (EM) are the two familiar classical forces, gravity being understood in Newtonian or General Relativistic terms, while electromagnetism is governed by Maxwell's Equations. EM is given a quantum field theoretical description, Quantum Electrodynamics (QED), relying crucially upon the notion of local gauge invariance. In QED, charged particles like electrons and positrons interact through the exchange of photons, the photon being the gauge boson for the EM force.

Gauge theoretic analogues of QED are found to describe two additional forces, the weak and strong interactions. The strong force describes the constituents of particles like protons and neutrons, while the weak force is needed to understand neutrinos and phenomena such as radioactive decay. These forces are also mediated by gauge bosons: the W and the Z for the weak force, and eight gluons for the strong force. Fermionic particles are further classifiable based on their charge under the strong force - while leptons lack color and interact only under the electromagnetic or weak forces, quarks are colored (have strong charges) and experience the strong force [57, 105, 106] in addition.

This understanding of the fundamental particles and forces (gravity excepted) is encapsulated in the Standard Model (SM) [59, 90, 104]. The SM combines Quantum Chromodynamics (QCD), the theory of the strong force, with electroweak (EW) theory, which accounts together for the weak force and electromagnetism. A comprehensive explication of the Standard Model would dramatically lengthen this document while partaking only dubiously of the essence of research; we direct the interested reader to various excellent treatments [62, 67, 89], and discuss some salient features in upcoming sections. The overall particle content of the Standard Model is shown in Figure 2.1. Both quarks and leptons are seen to exist in three generations with increasing mass [63].

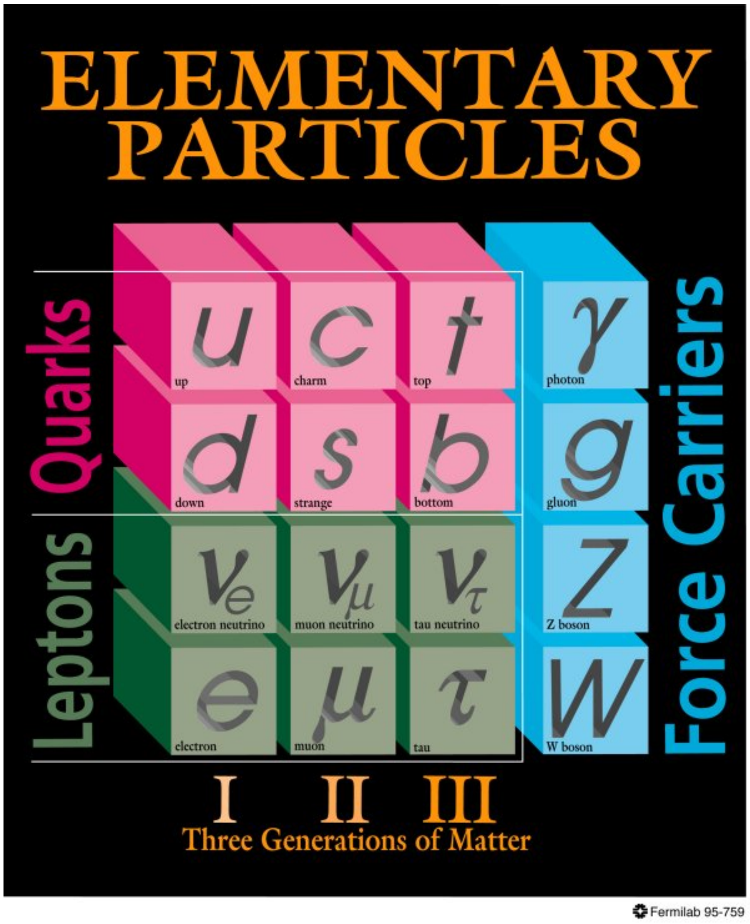

Figure 2.1: Particle Content of the Standard Model [51].

2.2 Electroweak Theory

Electroweak theory is a combination of the electromagnetic and weak forces. Quantum Electrodynamics (QED) describes electromagnetic interactions in terms of an exchange of photons between charged particles [100, 94, 52, 53, 48]. The strength of the interaction is governed by the fine structure constant, $\alpha = e^2/\hbar c \approx 1/137$, setting a typical time scale for electromagnetic decays at $\sim 10^{-16}$ s. For example, the neutral pion decays to two photons with a lifetime of 8.4×10^{-17} s.

The weak force by contrast affects all fermions, charged or not. In the SM, it emerges from the exchange of the massive W and Z bosons, accounting for its small range and low rate at low energies. Typical weak decay lifetimes range from $\sim 10^{-13}$ s (for example, the τ lifetime is 2.9×10^{-13} s) to upward of several minutes, as for the neutron. The force is interesting for a number of reasons; for example, it allows for interactions between quarks of different flavors, permitting quarks to change from one to another. It also uniquely violates symmetries, like charge conjugation (C) and parity (P) as well as their combination CP[1]. In addition, it is the only force (in addition, presumably, to gravity) that neutrinos interact under. A first description of the weak force is Fermi's contact theory, directly coupling four fermions. For example, muon decay is handled through a vertex with a muon and its neutrino, together with an electron and its anti-neutrino. This is shown in Figure 2.2 as the interaction of muon and electron weak currents. The discovery of parity violation in the process entailed a change in the theory from using vector to a vector - axial-vector ($V - A$) formalism.

---

[1] The strong force also allows for CP violation, but this has not been experimentally observed

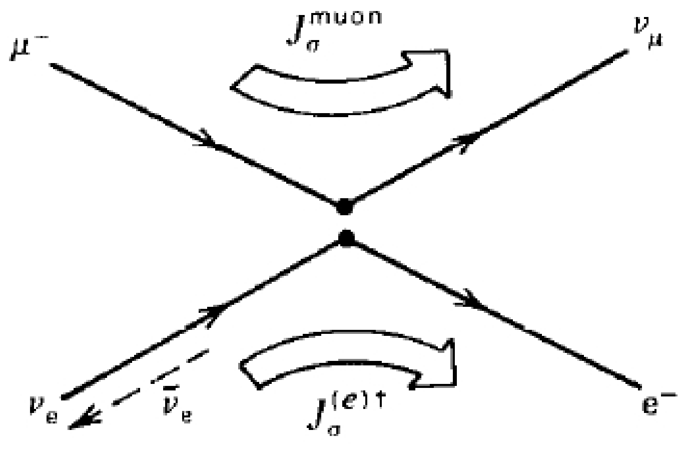

Figure 2.2: Muon decay in Fermi theory [67].

Electroweak theory is a unification of this weak force with the QED description of electromagnetism. This is achieved under the symmetry group SU(2) × U(1), which provides for four massless gauge bosons. These are a triplet W^+, W^- and W^0 for SU(2) and a singlet B^0 for the U(1). Mass is achieved for the weak bosons using the Higgs mechanism [49, 70, 66], yielding the familiar massive W and Z bosons together with a massless photon. The Z and γ are related to the W^0 and B^0 through the Weinberg Angle (θ_W):

$$\begin{pmatrix} \gamma \\ Z^0 \end{pmatrix} = \begin{pmatrix} \cos\theta_\mathrm{W} & \sin\theta_\mathrm{W} \\ -\sin\theta_W & \cos\theta_W \end{pmatrix} \begin{pmatrix} B^0 \\ W^0 \end{pmatrix} \tag{2.1}$$

The Weinberg Angle also relates the masses of the W and Z bosons,

$$\cos\theta_W = \frac{m_W}{m_Z} \tag{2.2}$$

The important vertices for W and Z interactions with fermions are shown in Figures 2.3 and 2.4. We see that the electroweak interaction allows for quark flavor-change. First, the W couples up and down type quarks, for example $u \to d$ or

$t \to b$. In addition, quarks can mix across generations via the Cabibbo Kobayashi Maskawa (CKM) matrix [35, 73]. That is, interactions of the form $u \to s$ or $b \to u$ are permitted. The Z boson participates in vertices that allow for flavor-changing neutral currents, however these cancel out at tree-level [58].

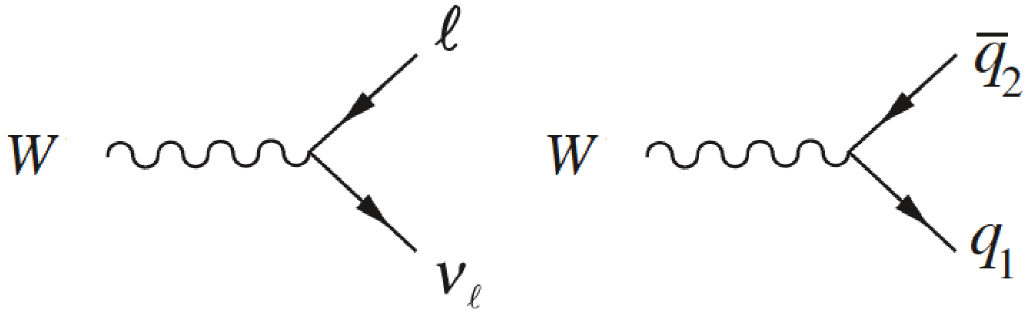

(a) (b)

Figure 2.3: Interactions of the W to lepton-neutrino, and to quark pairs [83].

2.3 Chromodynamics

Quantum Chromodynamics (QCD) is the gauge theory in the Standard Model for the interaction of quarks and gluons. The theory has an SU(3) structure, where quarks can carry one of three color charges, and interact by exchanging one of eight bi-colored gluons. The basic vertex in QCD is then one where two quarks interact via gluon emission, with strength α_s which is the strong coupling constant. Because gluons themselves carry the color charge however, they self-interact. Therefore, the theory has two additional vertices, coupling three and four gluons with strength α_s

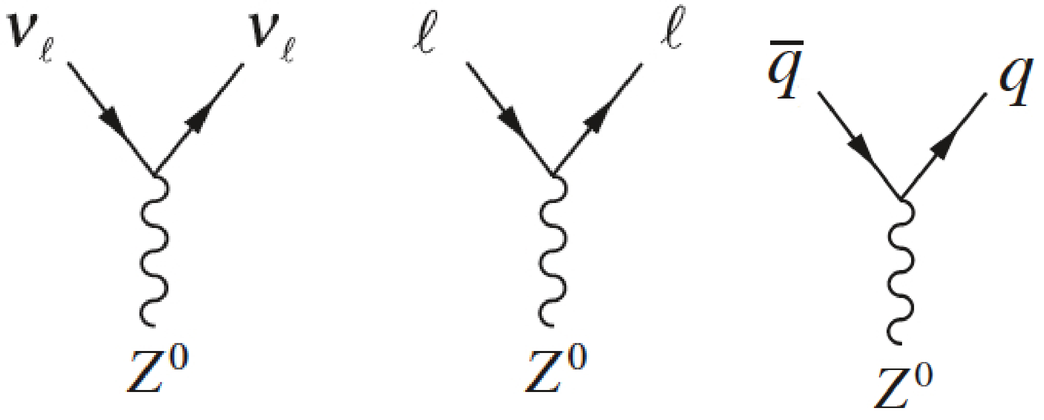

(a) (b)

Figure 2.4: Interactions of the Z to neutrinos, lepton pairs and quarks [83].

and α_s^2. The basic Feynman diagrams of QCD are summarized in Figure 2.5.

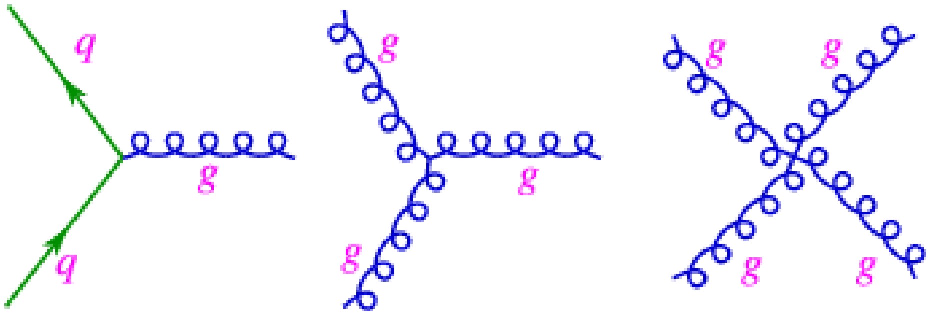

Figure 2.5: Feynman Diagrams in QCD.

One important consequence of the fact that gluons carry color-charge is that QCD field strength renormalization via vacuum polarization diagrams also involves gluon loops. Unlike quark-loops, which screen the color charge as for charge in QED, gluon loops anti-screen, which is to say that they cause the force between two quarks to *rise* with distance. The net effect of the quark and gluon loops is given by the coupling strength running:

$$\alpha_s\left(\left|q^2\right|\right) = \frac{\alpha_s\left(\mu_R^2\right)}{\left(1+\frac{\alpha_s\left(\mu_R^2\right)}{12\pi}\right)(11n-2f)\ln(|q^2|/\mu_R^2)} \tag{2.3}$$

Here, n is the number of colors and f is the number of flavors. Note that the coupling constant at scale q^2 is expressed in terms of a renormalization scale, μ_R. Exact calculations do not have a dependence on this unphysical scale. Looking at the denominator in Equation 2.3, we see that for the Standard Model, with six flavors and three colors, $11n - 2f > 0$, so the net force between two quarks rises with distance (decreases with increasing $|q^2|$). In other words, quarks are confined, experiencing strong non-perturbative forces at low energy. At the same time, they are relatively free when close together at high energies. This behavior, known as *asymptotic freedom*, has some important consequences for us: first, at high energies, we can treat QCD perturbatively. That is, we can think of the hard process in a high energy collider as involving quarks and gluons, not protons. At the same, asymptotic freedom explains why we have confined quarks in protons and not free partons, and the structure of the proton in terms of PDFs is complicated. Similarly, the quark and gluon decay products of the hard process are never seen in isolation, since any colored decay products can pair-produce from the vacuum to create color-neutral states. This is qualitatively the origin of jets. We elaborate on these matters in Section 2.4.

2.4 Hadron Collider Physics

Quarks and gluons are not observed freely, and are confined in colorless combinations, as described in Section 2.3. Thus, while we have shown interaction vertices involving quarks and leptons in the preceding sections, in a hadron collider like the LHC, we must in fact understand the physics starting from protons, which are more complicated entities composed of the fundamental quarks and gluons. The simplest quark-based description of the proton is as three quarks. Two colliding protons then represent a very complicated process. The difficulty is meliorated by asymptotic freedom, which allows for a *factorization* of the collision into perturbative and non-perturbative parts. The separate treatment of physics at different momentum scales enables us to treat collisions as a combination of a “hard” scatter and “soft” physics. Since the QCD coupling declines with the interaction scale, the hard scatter involves effectively free quarks and gluons. The “soft” components of the physics include the structure of the proton, as well as soft radiation and the dressing of final state quarks into hadrons. We schematically explain factorization, proton structure using the so-called Parton Distribution Functions (PDF), as well as parton showering, initial and final state radiation, and hadronization.

2.4.1 Parton Distribution Functions

Protons are not point-particles; their sub-structure is seen by sufficiently hard probes, with large momentum transfer Q between probe and proton. They are seen to contain three *valence* quarks, two up and one down. These quarks sum to yield the overall charge of the proton. The quarks interact in QCD through the exchange of gluons. Moreover, the gluons self-interact to produce more gluons, and the gluons can pair-produce quark pairs and so forth. This is represented in Figure 2.6. Hence, the structure of the proton must include a description of gluons, and of this *sea* of additional quarks all contained in it.

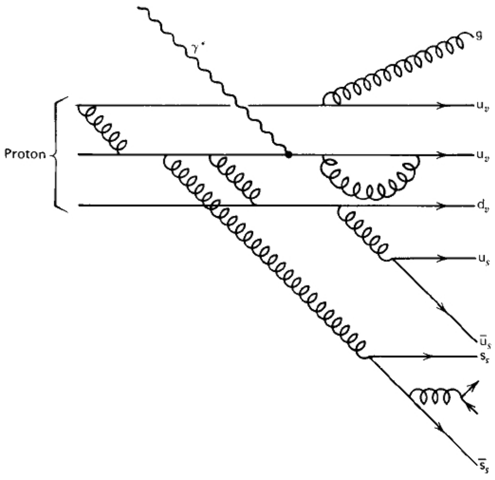

Figure 2.6: Proton, showing valence quarks, gluons and sea quarks [67].

This is achieved using the PDF, which describes probabilistically how the proton's momentum is distributed among its various constituent partons. If parton i carries a fraction x of the proton's total momentum:

$$p_i = x p_{\text{proton}} \tag{2.4}$$

PDFs indicate the probability of a parton carrying a given fraction x of the proton's momentum. At scales lower than the proton mass, this momentum is distributed primarily among the three valence quarks. For $Q \gtrsim 1$ GeV, the gluon and sea-quark momentum fractions also start to be significant. Roughly, valence quarks typically carry the bulk of the proton momentum, while the PDFs for other partons peak at low x. By construction, PDFs depend logarithmically on the momentum scale Q^2 to include gluon emission. Essentially, the emission of hard or large-angle gluons can be treated perturbatively - and indeed it seems conceptually appropriate to treat their interactions as part of the hard event. Such gluon radiation is not included in the parton distribution function, and is treated as part of the hard collision. However, as we go to low energy and α_S becomes large, the theory becomes non-perturbative, and there is a large increase in the emission of ever softer, collinear gluons. Such logarithmically diverging soft and collinear gluon emission terms are treated as part of the PDFs, [36], introducing a scale dependence. Hence, as a function of x and Q^2, $f_i(x, Q^2)$ gives the probability density for parton type-i to have momentum fraction x, at scale Q^2. An example is shown in Figure 2.7 for two different scales. We can observe the presence of sea and the gluon contributions principally at low x.

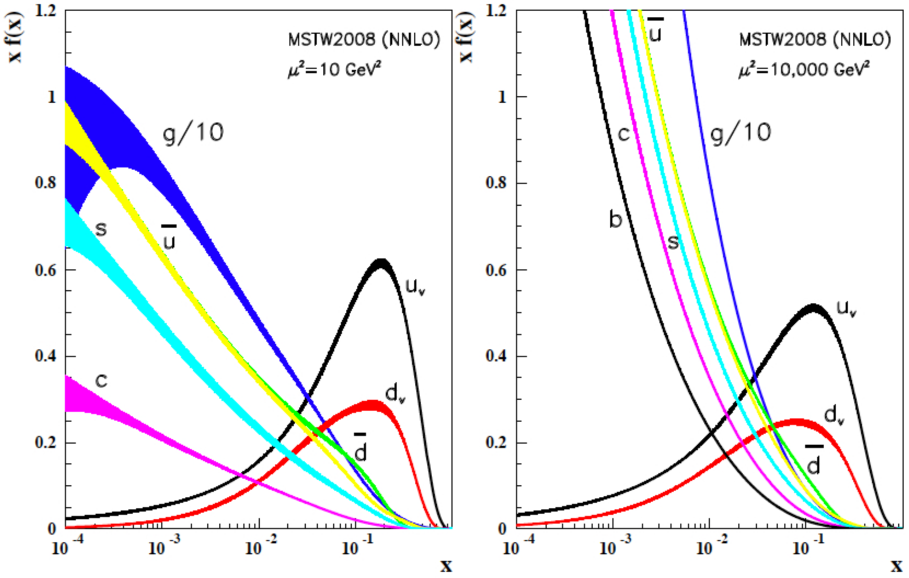

Figure 2.7: Parton distribution functions from the MSTW group. μ is the factorization scale (see text), set to Q [87].

The PDFs for the different partons integrate out to yield the proton's quantum numbers. For example, since the total u (d) quark content of the proton is 2 (1), we have:

$$\int_0^1 dx[u_{\text{valence}}(x) + u_{\text{sea}}(x) - \bar{u}_{\text{sea}}(x)] = 2 \tag{2.5}$$

$$\int_0^1 dx[d_{\text{valence}}(x) + d_{\text{sea}}(x) - \bar{d}_{\text{sea}}(x)] = 1 \tag{2.6}$$

Similarly, since the proton should have no net strangeness,

$$\int_0^1 dx[s_{\text{sea}}(x) - \bar{s}_{\text{sea}}(x)] = 0 \tag{2.7}$$

PDFs are not calculated from first principles, since they involve non-perturbative physics. The scale dependence is analytically tractable, using the Altarelli-Parisi or DGLAP equations [17, 45, 61]. However, the x structure is taken mostly from data. Fits are performed to experimental data from many sources, including fixed target experiments, deep inelastic scattering (DIS) particularly from HERA, and Tevatron results. These experiments are complementary, probing differing regimes in x, Q^2, and parton flavor, as seen in Figure 2.8. For example, the fixed target data are at low momentum transfer Q^2, while the Tevatron data are at large Q^2. Several groups, including CTEQ [86] and MSTW [82] periodically provide updated PDFs. Observe that the low-x, large Q^2 regime is not well probed currently, so PDFs are an important source of uncertainty on theoretical cross section predictions at the LHC.

2.4.2 Factorization

The factorization theorem [46] allows for hadronic interactions to be split into two parts: the interaction between partons, and the distribution of partons inside the hadron. The interaction between partons depends on the process involved, and is calculated in the perturbative regime of QCD using the appropriate Feynman rules.

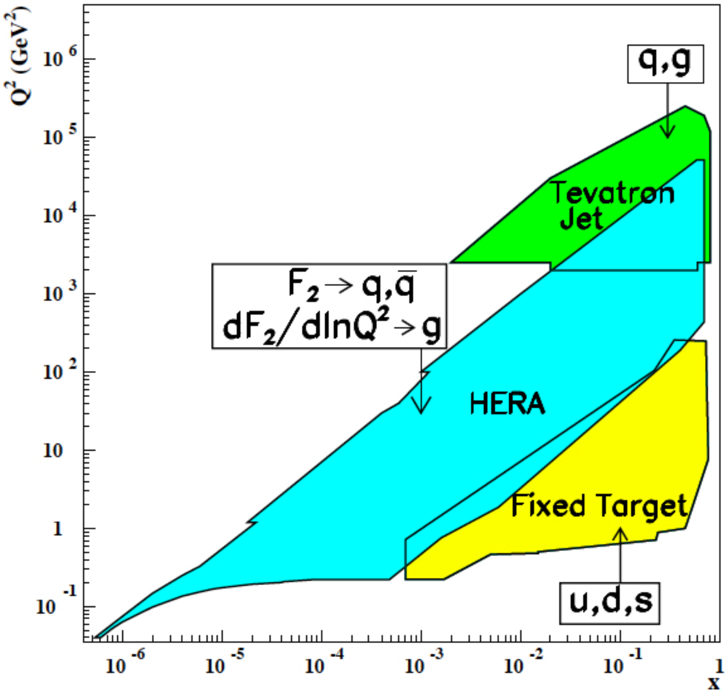

Figure 2.8: PDF constraints in x and Q^2 from different types of experiments [87].

By contrast, the distribution of partons inside the proton is process-independent, and described using PDFs as was discussed in Section 2.4.1. The scheme is represented in Figure 2.9. The overall interaction is separated into a hard scatter (shown as yellow bubble), together with several aspects of the soft physics: incoming hadrons, soft radiation, hadronization of final state partons and interactions between other partons in the colliding protons.

The total cross section for a process producing final state X, involving two hadrons, is formed by summing over the cross sections for the partons contained in the two hadrons. Mathematically, for the interaction of hadrons A, B with PDFs $f_a(x, Q^2)$

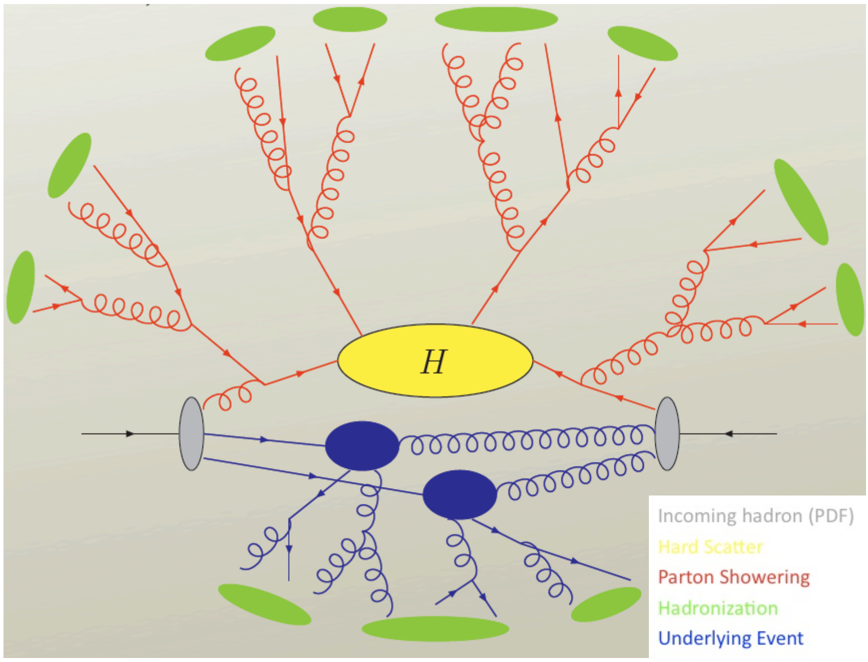

Figure 2.9: Schematic representation of factorization [98].

and $f_b(x, Q^2)$, we have:

$$\sigma_{\mathrm{AB}\rightarrow\mathrm{X}} = \sum_{a,b} \int dx_a dx_b f_a(x_a, Q^2) f_b(x_b, Q^2) \hat{\sigma}_{\mathrm{ab}\rightarrow\mathrm{X}}(x_a, x_b) \tag{2.8}$$

Here $\hat{\sigma}$ is the cross section formula using the partons a and b in the two hadrons. Such cross sections are calculated in perturbative theory as a series expansion in powers of α_s. The Q^2 dependence of the PDFs reflects the inclusion of gluon emissions into the PDFs, as described earlier. This so-called factorization scale $\mu_{\mathrm{F}} = Q$ is the scale connecting the perturbative (hard) and non-perturbative (soft) regimes. The three leading terms in the perturbative expansion in powers of α_s are labeled LO (leading order), NLO (next-to-leading-order) and NNLO (next-to-next-to-leading order). The termination of the calculation at some fixed order introduces an uncertainty from the higher order terms; in addition, it also introduces an uncertainty emerging from the choice of the factorization scale μ_{F}, which gets smaller with increasing order in perturbation.

After the hard interaction, there are colored quarks and gluons, which shower gluons and undergo hadronization to produce colorless final states involving baryons and mesons. and mesons. The hadronization process is non-perturbative and hence complicated, and various phenomenological techniques are used by different Monte Carlo programs[2] to model it. In `Pythia` [96], for example, color field lines are modeled as color strings whose tension / energy increases with distance.

2.5 *W* Production and Decay at the LHC

We elaborate on the physics of W bosons, describing their production at the LHC, and decay mechanism. We then mention the status of the theoretical calculation of the W cross section and its uncertainties, and compare these predictions to experimental results from collider experiments.

The W is measured to have a mass $m_{\mathrm{W}} = [80.420 \pm 0.031]$ GeV (Figure 2.10(a)), from a combination of LEP and Tevatron results. It decays almost immediately, in $\sim 0.3 \times 10^{-24}$ s, with a width measuring $\Gamma_{\mathrm{W}} = [2.046 \pm 0.049]$ GeV (Figure 2.10(b)). Hence, the W is not observed directly, and must be reconstructed from its decay products.

Since the LHC is a hadronic machine, the W is produced primarily through $q\bar{q}$

---

[2] These software programs are used for a variety of purposes in our analysis to compare results to expectations: to obtain theoretical predictions for cross sections, to simulate particle decays and kinematics for different processes, and to model the expected behavior of events in the ATLAS detector. See Sections 7.1 and 8.1 for details on the programs used.

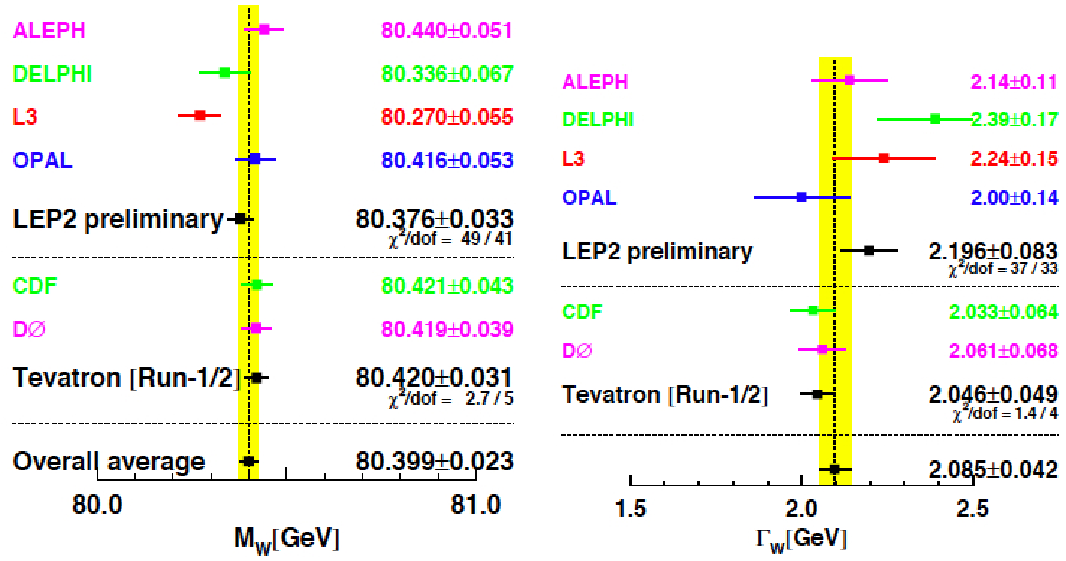

(a) Mass (b) Width

Figure 2.10: Measured mass and widths of the W boson. [87].

annihilation. The quark composition of W production is shown in Figure 2.11. The dominant production modes are via $u\bar{d}$ and $\bar{u}d$ for the W^+ and W^- respectively. Any $\bar{q}$ or non-u or d quark must be pulled from the proton sea with sufficient energy to make a W. Also, across-family production is suppressed by the smallness of the off-diagonal elements of the CKM matrix (compare, for example, $u\bar{s}$ and $\bar{u}s$ production to $c\bar{s}$ and $\bar{c}s$ production in Figure 2.11.) Note that, while at a $p\bar{p}$ machine like the Tevatron the W^+ and W^- cross sections are equal, this is not the case at the LHC, where W^+ production is greater because of the larger u quark component of the proton.

The W decays either to lepton-neutrino or to quark anti-quark pairs. The total hadronic branching fraction is approximately two-thirds, $(67.60 \pm 0.27)\%$ [87], and is

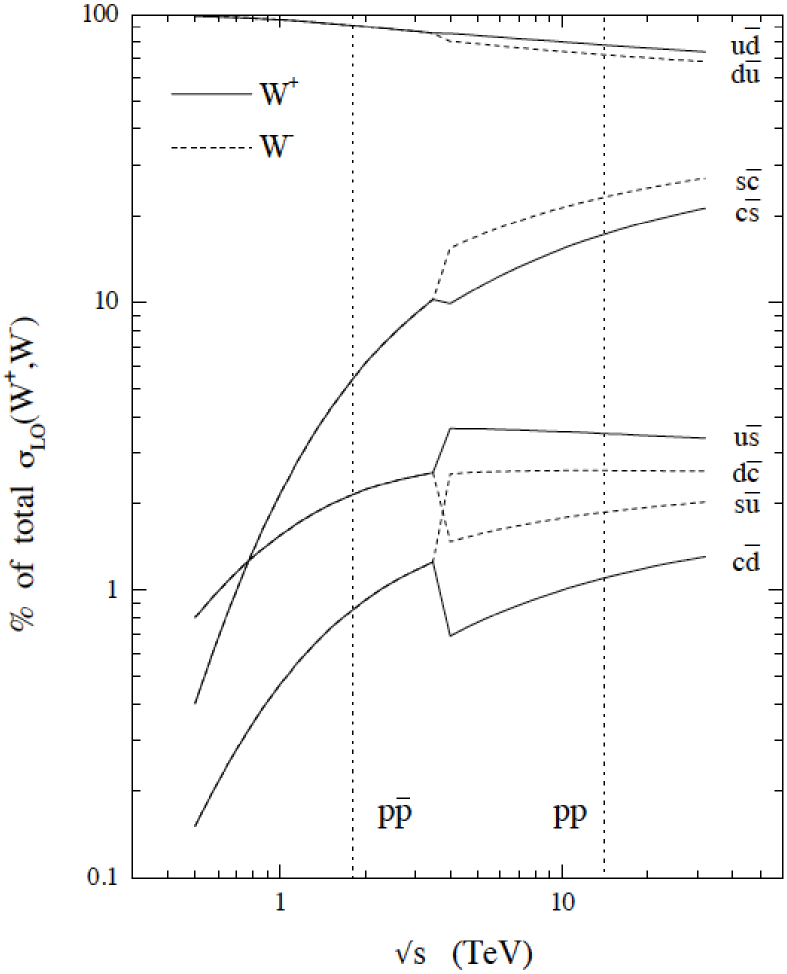

Figure 2.11: Quark flavor composition of W production in $p\bar{p}$ and pp collisions [82].

dominated by CKM diagonal $u\bar{d}$ and $c\bar{s}$ decays (the top quark is too heavy). These diquark decays lead to a dijet final state that is extremely hard to separate from the vastly larger QCD background. In practice therefore the leptonic decays are analyzed instead. These leptonic decays, to $\ell\nu_\ell$ have almost equal branching fractions in the e, μ and τ channels. Specifically, the $\mu\nu_\mu$ branching fraction has been measured at $(10.57 \pm 0.15)\%$. Of the three leptons, the electron and muon decay channels are most typically used in analyses: the electron is stable, while the muon is long-lived by detector-physics time-scales. They can be observed directly. By contrast, the τ itself decays rapidly, to either hadrons or to a lepton (e or μ) and neutrinos. The hadronic decay of a τ looks in the detector like a narrow jet, and its reconstruction is complex. By contrast, W decays to leptonic τ look similar to W leptonic decays directly in the muon or electron channels. They can be "accounted" for as either part of the signal or as background (the latter approach is chosen here.)

In this analysis, the muon decays of the W are studied. The muon is observed directly, while the neutrino, which passes through the detector, is instead inferred as missing energy using the imbalance of measured energy. The missing energy is determined only in the transverse plane, since the momentum in the event along the beam-axis is unknown. That is, the kinematics of the W can be reconstructed only in the transverse plane. The ATLAS detector and event reconstruction are described later, in Chapters 4 and 5.

2.6 W Cross Section: Theory and Measurements

W boson cross section predictions are available at up to NNLO in α_s, using programs like FEWZ [18, 56] and ZWPROD [68]. The predictions are shown in Table 2.1 separately for the W, W^+ and W^-. Four different NNLO PDF sets are utilized: ABKM09 [14, 13], MSTW08 [81], HERA [4, 3] and JR09 [72]. With the MSTW08 PDF set and FEWZ in particular, the central values for W, W^+ and W^- $\sigma \times \mathrm{BR}$ are 10.46 nb, 6.16 nb and 4.30 nb respectively. The uncertainties quoted in the table correspond to the PDF uncertainties only, at 68 % CL. Additional uncertainty on the prediction comes from uncertainty on α_s, higher order contributions and the choice of factorization and renormalization scales[3]. The total uncertainty on the predicted W cross section times muon branching fraction is 5%.

	MSTW08	ABKM09	HERA	JR09
W^+	6.16 ± 0.11	6.42 ± 0.09	6.42 ± 0.16	5.92 ± 0.12
W^-	4.30 ± 0.08	4.29 ± 0.07	4.42 ± 0.10	4.03 ± 0.08
W	10.46 ± 0.18	10.71 ± 0.15	10.84 ± 0.26	9.94 ± 0.19
Z/γ^*	0.964 ± 0.018	0.987 ± 0.015	0.994 ± 0.029	0.909 ± 0.018

Table 2.1: Cross sections times leptonic branching ratios in nb, for W^+, W^-, W and Z/γ^* production, using FEWZ, for different PDF sets at NNLO in QCD.

The W boson production cross section has been previously measured at a variety of energies by various collider detectors. The discovery and first measurements were performed by the UA1 [12] and UA2 [15] collaborations at $\sqrt{s} = 450$ GeV at the S$p\bar{p}$S. At the Tevatron ($p\bar{p}$), measurements were carried out by both CDF [6, 7] and D∅ [5] in Run I (1.8 TeV) and Run II (1.96 TeV). RHIC (pp) has produced a result from PHENIX [9] at 500 GeV. These results are shown in Figure 2.12, where they are compared to predictions using ZWPROD/FEWZ and MSTW08. The predictions are shown for both proton-proton and proton-antiproton colliders. These existing results are in agreement with expectations. This dissertation describes W cross section measurements at 7 TeV, carried out using the ATLAS detector.

---

[3] In addition to fixed-order calculations, it is also possible to sum the dominant contributions at each order in the perturbation. This "resummation" technique provides an alternate calculation that is better in certain regimes. This technique is employed for gluon emission by the ResBos [23, 74] program in addition to NLO calculation.

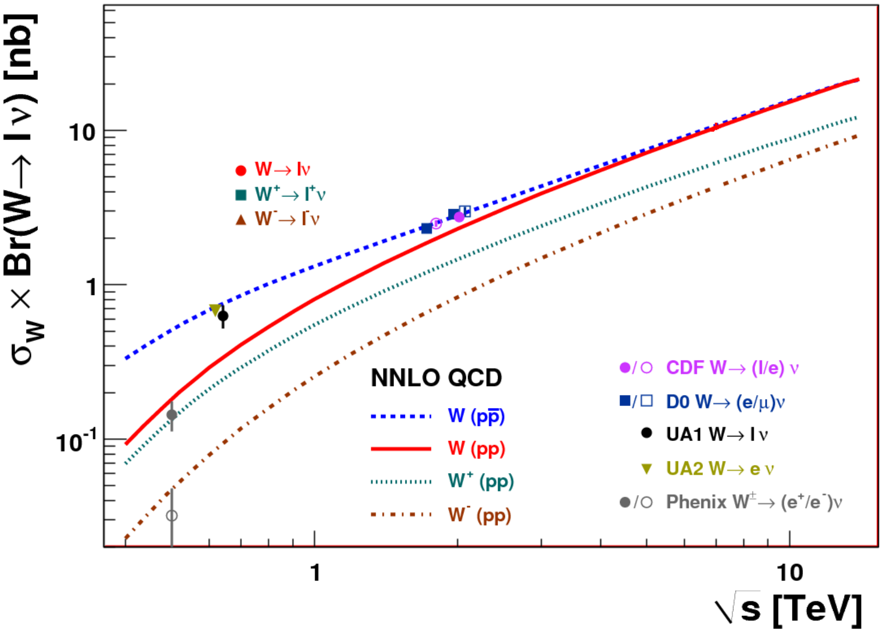

Figure 2.12: W cross section measurements from UA1, UA2, CDF, DØ and PHENIX, compared to NNLO theoretical predictions. (The plot is taken from the 2010 ATLAS result) [19, 99].

Chapter 3

The Large Hadron Collider

The Large Hadron Collider (LHC) at CERN, in Geneva is a circular collider, intended to accelerate proton beams to a design centre-of-mass energy $E_{\mathrm{CM}} = 14$ TeV, with a luminosity of 10^{34} cm^{-2}s^{-1}. This is a significant improvement in machine capability over the Tevatron (a factor of seven in energy and twenty-five in luminosity) and affords exciting scope for the discovery of new physics at the TeV scale, where beyond-the-Standard-Model phenomena are expected to arise for a variety of theoretical reasons. The machine also has a heavy-ion mode of operation, wherein lead ions with energy 2.76 TeV per nucleon collide with peak luminosity 10^{27} cm^{-2}s^{-1}. To extract the TeV-scale physics of the LHC, the collider is furnished with four detectors, ALICE, ATLAS, CMS and LHCb. This chapter provides a brief but self-contained overview of the LHC's design, acceleration scheme and performance. It moves on to describe the physics reach of the machine, the installed detectors and their physics programs. The interested reader is directed to various sources [50, 103, 78] for additional details about these topics.

The structure of the LHC is represented in Figure 3.1. It is a circular collider of 27 km circumference, with two counter-circulating beams. The chief segmentation is into eight sectors, each containing a straight section and an arc. Collisions occur at four of eight junctions between the sectors, specifically at Points 1, 2, 5, and 8, where detectors serving different physics programs are installed. Dipole, quadrupole and higher-order magnets provide bending and focusing. Beams are accelerated, and energy-loss compensated, by electric fields in RF cavities, located in the straight section at Point-4. The cavities operate at 400 MHz, providing an accelerating gradient of 5 MV/m.

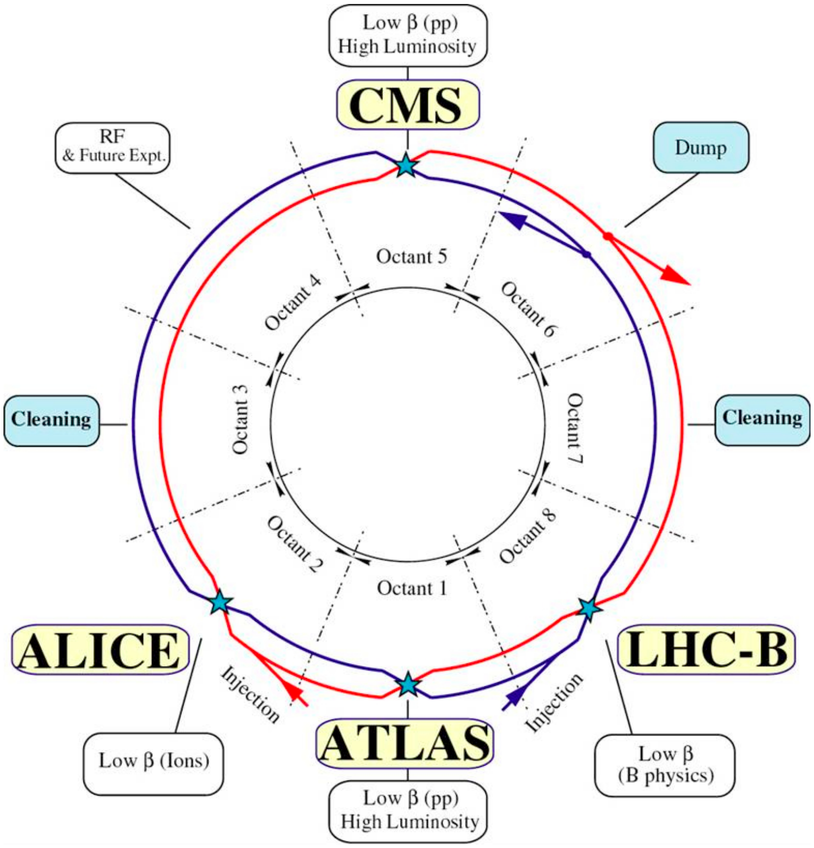

Figure 3.1: Schematic of the Large Hadron Collider.

3.1 Design Considerations

Some salient features of the LHC include proton-proton collision and the use of superconducting technology. They are discussed and placed in context, emerging from the high energy and luminosity needs the collider must furnish, as also from historical context.

One fundamental design decision at the LHC is the use of protons instead of protons and antiprotons. To provide high luminosity, the LHC must have high particle flux in the beams $\sim 10^{14}$/beam/s. Such large quantities of antiprotons are not currently possible to produce rapidly, so that a $p\bar{p}$ collider would have unmanageably long beam refill time. Additionally, at the design energy of 14 TeV, most collisions emerge from the gluonic component of the proton, so the valence antiquark enhancement applicable at lower energies is less significant. These factors led naturally to the adoption of *proton-proton* technology for the LHC, in contrast to the Tevatron or the S$p\bar{p}$S. Since counter-circulating protons need opposite fields to achieve the same bending, the LHC must utilize *two rings*, instead of circulating both beams in the same pipe, as is done at the Tevatron. In practice this is achieved with a so-called "twin-bore" design, where the two pipes and magnets are housed in a common cryostat, which saves costs and space.

To achieve the bending required while retaining use of the 27 km LEP tunnel, the LHC needs magnets providing 8.3 T of field, which can only be achieved in superconducting magnets. In addition, resistive power losses become unmanageable with regular non-superconducting electromagnets. The LHC uses superfluid helium, at a temperature of 1.9 K to cool the magnet system because of its excellent heat-transfer properties and low viscosity permitting good solid-liquid interface.

The machine luminosity is increased using both high bunch intensity and large bunch count. Per design, there are 10^{11} protons per bunch, the number being limited from above by the need to limit nonlinear beam-beam interactions between the protons in the bunches. There are 2808 bunches in each beam, implying a small bunch spacing of 25 ns. Near the interaction regions, the two proton beams share a common beam pipe. This creates parasitic interaction points ($\sim$ 34 per interaction region at design operating parameters) between bunches away from the nominal interaction point. To minimize this effect, a crossing angle is imposed to increase the distance between the beams away from the IP. At the LHC, a crossing-angle is needed when there are more than 156 bunches. The crossing-angle is 285 μrad, the size being governed by the 10σ size of the beam screen (The beam screen is used to shield the cryogenic system from beam-related heat sources, including synchrotron radiation and image currents.)

3.2 Acceleration Scheme

Figure 3.2 shows the proton acceleration procedure at the Large Hadron Collider. The LHC uses a succession of injections from older lower energy machines to successively accelerate protons from rest to the design beam energy of 7 TeV. The current beam energy for pp operation in 2009-2012 is half of the design value, at 3.5 TeV. The process begins at LINAC2 (LINear ACcelerator2) which accelerates protons from hydrogen to 50 MeV. These protons are fed to the Proton Synchrotron Booster (PSB), which accelerates them to an energy of 1.4 GeV, and feeds them in turn to the Proton

Synchrotron (PS) which circulates them at 25 GeV. The Super Proton Synchrotron (SPS) increases this energy to 450 GeV after which they are injected separately into both (clockwise and anti-clockwise) rings of the LHC, which boosts the energy up to the operating value.

Injection from the SPS to the LHC to fill the bunches takes on average twenty minutes, while the ramp to high energy typically takes another twenty-five. The beam half-life at the LHC is on the order of ten hours, governed by beam-losses from Coulomb scattering.

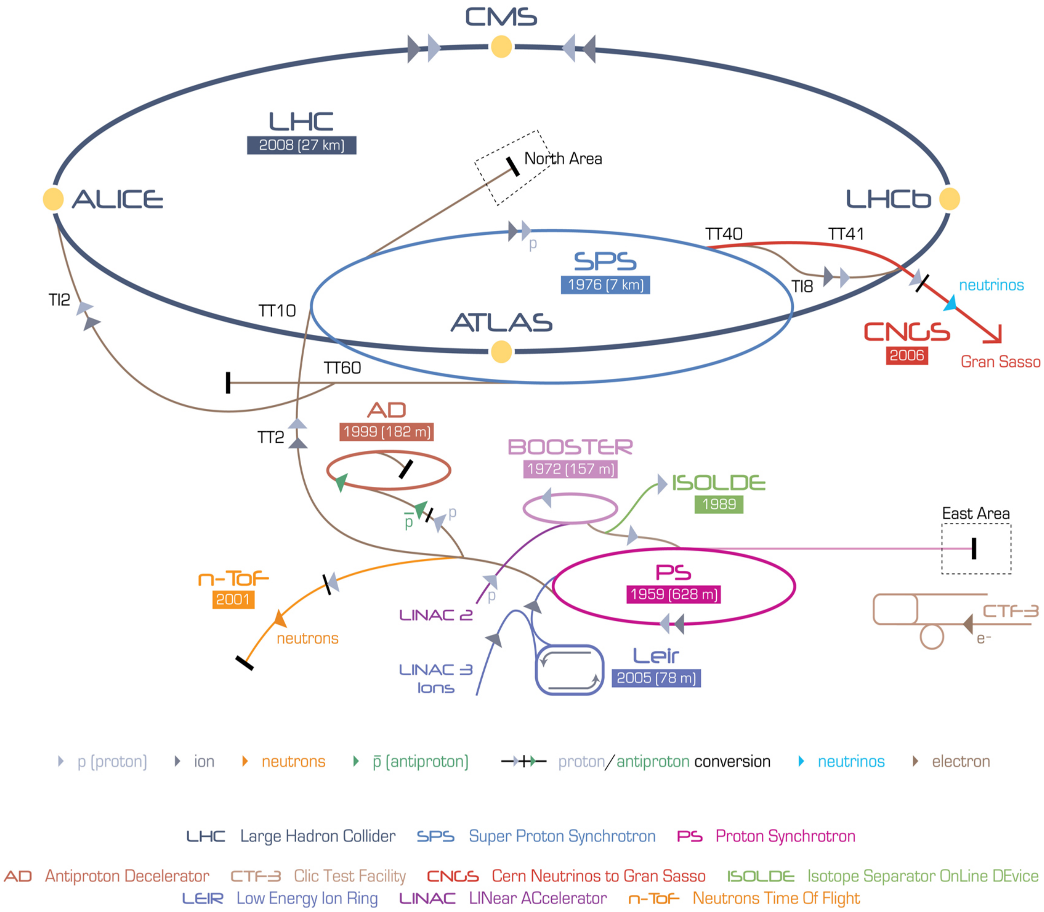

Figure 3.2: Proton acceleration complex at the Large Hadron Collider.

3.3 Installed Detectors

To take advantage of the high energy and luminosity at the LHC, there are four main detectors installed at the complex: ALICE, ATLAS, CMS and LHCb:

- ALICE ("A Large Ion Collider Experiment") focuses on understanding the lead-ion collisions produced at the LHC. A noteworthy goal is the characterization of the properties of the quark-gluon plasma, a high temperature/density state with deconfined quarks and gluons, under investigation at RHIC and theorized to have existed in the early universe. ATLAS and CMS also have heavy-ion programs, but are not designed specifically around this objective; ALICE has the largest Time Projection Chamber ever designed as its central tracking detector, to manage the large track multiplicities found in central ion-ion collisions.

- ATLAS ("A Toroidal LHC ApparatuS") and CMS ("Compact Muon Solenoid"): these are the two flagship general-purpose detectors with comprehensive physics programs aiming at completing the Standard Model with the Higgs Particle, finding or excluding physics models beyond the Standard Model such as Supersymmetry or Technicolor, understanding the properties of Dark Matter, and seeking evidence for extra dimensions. The work summarized in this document is conducted at ATLAS, whose structure is dealt with in depth in Chapter 4.

- LHCb, standing for LHC beauty, is a b-Physics detector, probing CP violation in the B meson system among other things, to better understand matter-antimatter asymmetry in the universe. The luminosity at LHCb is lowered by defocusing the beam, to reduce the number of interactions per bunch-crossing.

This is needed for optimal understanding of meson vertices.

Chapter 4

The ATLAS Detector

ATLAS, or *A* *T*oroidal *L*HC *A*pparatu*S*, is a general-purpose detector to study the properties of high-energy collisions produced at the Large Hadron Collider. A representation of the ATLAS detector is provided in Figure 4.1. The detector has a hermetic design covering nearly the full angular acceptance. Different detector systems are layered around the interaction point (IP) to measure particle and jet momenta and energies. An Inner Detector (Section 4.3) immediately surrounding the beam pipe measures tracks and vertices using a combination of silicon and straw tube technologies. These measurements depend on track curvature in a solenoidal magnetic field. Surrounding the Inner Detector, a sampling calorimeter consisting of electromagnetic and hadronic components is utilized to contain and measure energy depositions from electrons, photons and hadrons. The imbalance of energy measurements in the calorimeter is used to measure the missing energy in the transverse plane, helping to infer the energy carried away by non-interacting particles. The calorimeter also provides triggering capability for electrons, photons, jets and missing energy. In

Section 4.4 the calorimeter is described in greater detail.

Muons, unlike electrons or hadrons, pass through the ATLAS calorimeter with limited (3 − 4 GeV) energy loss. Hence, their momentum is measured outside the calorimeter as well using a dedicated Muon Spectrometer embedded in an air-core toroidal magnet system. The muon system uses principally drift tubes for precision measurements. In addition it incorporates two technologies for triggering on muons. Since the muon is significant in the $W \rightarrow \mu\nu$ final state - in addition to the μ itself, the missing energy in the event is provided principally by the muon - an understanding of muons is crucial to this analysis. The muon spectrometer, aspects of muon reconstruction and some details about tracking and calibration are therefore dealt with in depth separately in Chapter 5.

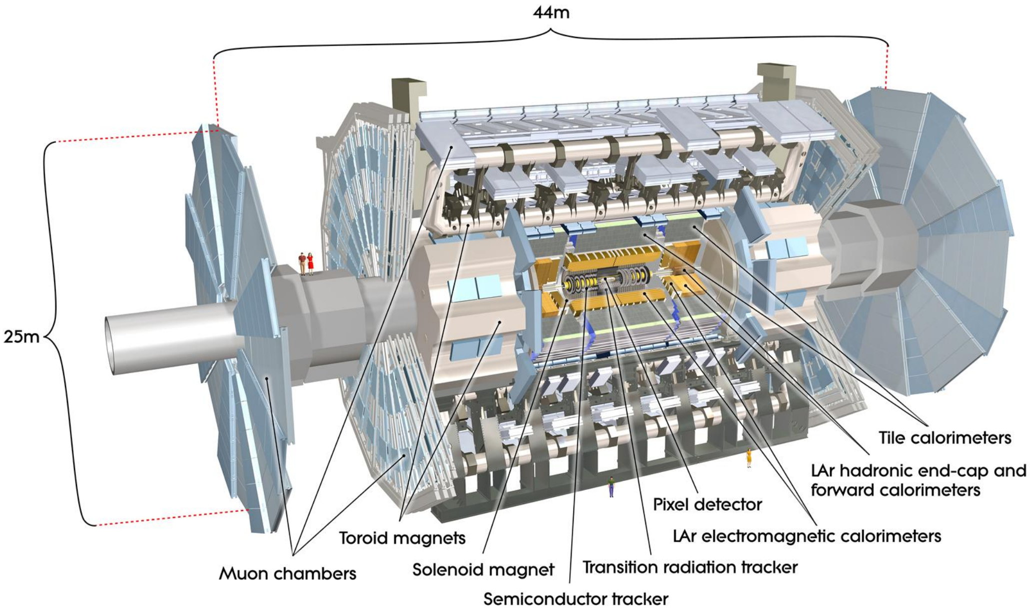

Figure 4.1: Schematic of the ATLAS detector, showing the inner detector, calorimeter, muon and magnet systems.

4.1 Coordinate System

We describe the ATLAS global coordinate system here to establish basic variables used throughout the remainder of this document. The origin of the coordinate system is at the center of the detector, at the nominal interaction point. The beam pipe defines the z-axis, and the plane orthogonal to it passing through the origin is the transverse $x - y$ plane. The y-axis picks out the vertical, while the horizontal x-axis points inward toward the center of the LHC ring. Quantities like p_{T} and $E_{\mathrm{T}}^{\mathrm{miss}}$ refer to this plane. Track impact parameters resolve into their longitudinal (z_0) and transverse (d_0) components.

A spherical coordinate system is also set up, with polar angle θ measured relative to the beam axis, and azimuthal angle ϕ measured about it in the transverse plane. The defining equations for these are:

$$\begin{aligned} R &= \sqrt{x^2+y^2+z^2} && (4.1) \\ \cos\theta &= z/R \\ \tan\phi &= y/x \\ & && (4.2) \end{aligned}$$

The θ coordinate ranges from 0 to π, while ϕ lives in $(-\pi, \pi]$. Observe that the top and bottom halves of the detector have positive and negative ϕ respectively. The rapidity (also y, not to be confused with the Cartesian coordinate) is defined as:

$$y = \frac{1}{2} \ln \frac{E + p_{\mathrm{z}}}{E - p_{\mathrm{z}}} \tag{4.3}$$

This is a useful physical quantity, Δy being invariant under boosts in z. In the massless (ultrarelativistic) limit, the rapidity is well approximated by the pseudorapidity, η, which is defined as

$$\eta = -\ln \tan \theta/2 \tag{4.4}$$

The angular separation ΔR is $\sqrt{\Delta\eta^2 + \Delta\phi^2}$. The positive and negative z halves of the detector are, respectively, the "A" and "C" sides. Note that the A side has $\eta > 0$.

4.2 Magnet System

The ATLAS magnet system is a hybrid of a solenoidal and three toroidal field elements. The toroid has a diameter of 22 m and is 26 m long, setting the overall scale of the detector. A schematic of the magnets is shown in Figure 4.2. The field for the Inner Detector is provided by a superconducting solenoid surrounding it, providing a field of 2 T. Three air-core superconducting toroidal systems provide bending for muons in the barrel and two endcaps. The large toroidal field system furnishes muons with large bending and a long lever arm, giving ATLAS superb standalone muon momentum resolution for high-momentum tracks. Tracks bend in ϕ in the ID and in η in the MS.

4.3 Inner Detector

The Inner Detector (ID) immediately surrounds the beam-pipe. It must measure track trajectories in terms of their curvature in the solenoidal 2 T field, providing momentum information for charged particles. The tracking also needs to provide primary

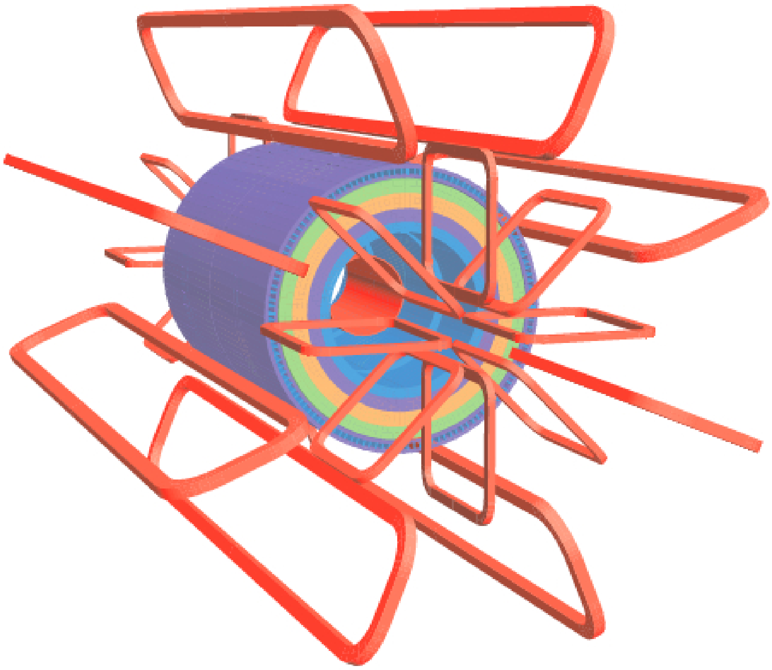

Figure 4.2: Schematic of the ATLAS Magnet System. The toroidal system consists of eight air-core toroidal coils for the barrel, with coils for the two endcaps interleaved. The solenoidal magnet coils are contained inside the calorimeter.

vertex information, to pick out the hard event from the multiple collisions in each bunch, and secondary vertexing capability to reconstruct the decays of heavy-flavor quarks and jets, τ-leptons, as well as long-lived neutral particles (like K_S or Λ_0). The ID needs to function in a challenging high-radiation environment, and handle the high track ($\sim 1,000$ charged particles produced per bunch-crossing) and vertex (~ 23 pileup interactions per bunch) multiplicities produced every 25 ns while reducing contamination from preceding bunches. It must provide momentum resolution for sub-GeV tracks for vertexing, while retaining performance into the few hundred GeV regime for high momentum electron and muon reconstruction. To handle this demanding requirement set, ATLAS has chosen a three-component tracking system, composed of a central silicon Pixel Detector, surrounded immediately by a Silicon

Strip Tracker (SCT) and a Transition Radiation Tracker (TRT). A schematic of the ID is shown in Figure 4.3. The ATLAS inner detector weighs 4.5 tonnes, and has a significant material budget (Figure 4.4) by historical standards; this material must be accounted for in the inner detector reconstruction and extrapolation.

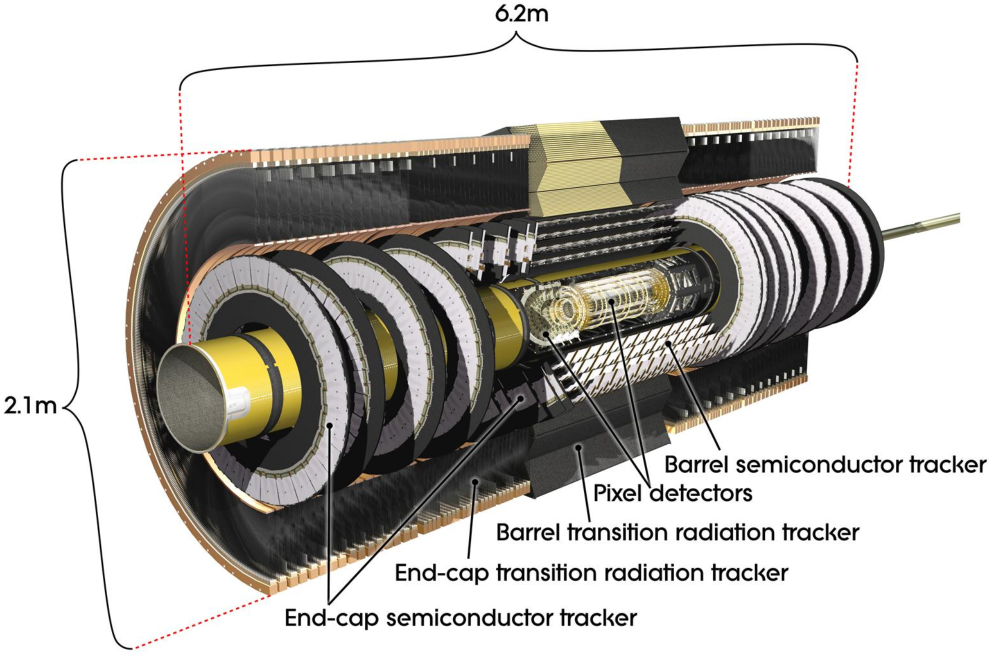

Figure 4.3: Schematic of the ATLAS Inner Detector, showing the Pixel, SCT and TRT detectors.

4.3.1 Pixel Detector

The pixel detector [1] immediately surrounds the beam-pipe, between 5 cm and 12 cm in z, and extends to $z = 0.65$ m. It provides high resolution space point measurements close to the interaction region out to $|\eta| = 2.5$. The pixel detector consists of identical rectangular "modules" measuring approximately 6 cm by 2 cm, each containing pixels of size 50 μm (along the azimuth) and 400 μm (along the beam). The

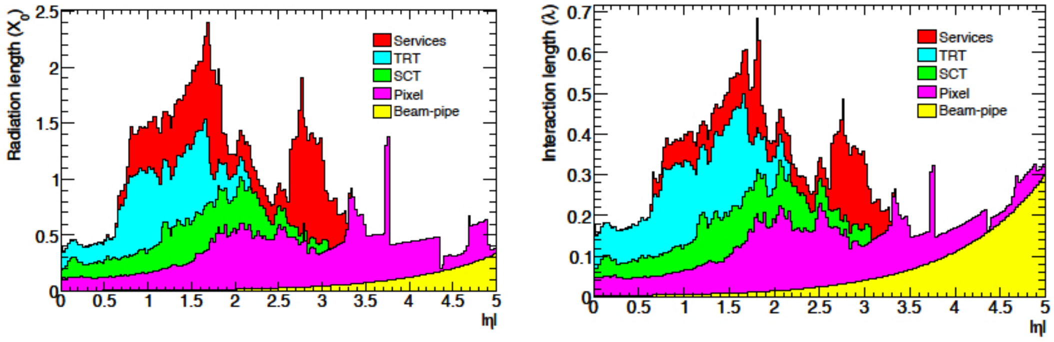

(a) X_0

(b) λ

Figure 4.4: Material in the inner detector: radiation lengths (a) and interaction lengths contained (b). The distributions are averaged over ϕ

signal in each readout pixel channel, after amplification, shapping and comparison against a threshold, provides a binary output along with time-over-threshold information. There are $\sim 46,000$ pixel channels in each module, and $\sim 1,700$ modules, giving a total of more than 80 million channels for the pixel. The pixels are arranged in beam-centered cylindrical layers in the barrel, and in transverse disks in the two endcaps. By design, each particle from the IP crosses three pixel layers, each of which provides a 10 μm measurement in $r - \phi$ and a 115 μm measurement in the third direction (z in the barrel, r in the endcap). The pixels are crucial to the detector's vertex reconstruction performance, for the reconstruction of primary vertices in the presence of multiple interactions at high luminosity, and for finding secondary vertices in b-tagged jets.

4.3.2 SCT

The intermediate tracking region of the ID, between the Pixels and the TRT, contain SCT layers. The SCT extends the high-resolution tracking capability of ATLAS, balancing costs with performance by using silicon strip technology with high resolution in one direction. The SCT provides four three-dimensional space point measurements for each track out to $|\eta| = 2.5$. It uses thin double-sided silicon strips, with four double layers in the barrel and nine disks in each of the two endcaps. A 40 mrad stereo-angle within each double layer provides fine-grained information along the non-precision direction. The measurements have 16 μm resolution along $r - \phi$ and 580 μm along the third direction. The SCT has 6.2 million readout channels, and covers 61 m^2 of area, the radial extent being from 30 cm to 52 cm. It is the backbone of the momentum reconstruction performance.

4.3.3 TRT

The Transition Radiation Tracker (TRT) is a combined tracking and particle identification system, providing momentum measurements with a large number of drift-tube measurements, as well as electron-pion separation using transition radiation measurements. It consists of straw tubes in a polypropylene radiator. The drift tubes, 4 mm in diameter, are made of polyimide layered with aluminium, and contain a gas mixture of xenon (70%), carbon dioxide (27%) and oxygen (3%). Each tube has an anode wire made of gold-plated tungsten, of 31 μm thickness. Particles traveling through the tubes ionize the gas, producing electrons which propagate toward the anode wire, avalanching near it and producing a signal that is converted to a position measurement using a radius-time (RT) function. The gas gain is about 25,000 for the chosen mixture. The maximum signal collection time is 48 ns while the nominal resolution per tube is 130 μm.[1]

The straw tubes are axial in the barrel with length 1.4 m, split at the center and read out separately at both edges. In the endcaps, they are arranged radially in wheels, with a tube length of 37 cm. This configuration yields position information along the ϕ direction - the information provided along the non-bending direction (z in the barrel, r in the endcap) is of poor resolution, so in practice inner detector tracks obtain these coordinates from the silicon measurements. There are a total of $\sim 350,000$ readout channels in the TRT. A track usually crosses ~ 36 TRT tubes, providing multiple independent measurements. The TRT operates at room temperature, and the per-tube noise occupancy is about 2% at design luminosity. This problem is limited by the pattern recognition, and the use of silicon-based track-seeding in the reconstruction. The TRT provides a large number of high-lever-arm measurements per track, significantly improving momentum resolution for hard tracks. For reasons of cost, the TRT extends outward only to $\eta = 2$, so inner tracking between $2 \leq |\eta| \leq 2.5$ relies only on the silicon.

The particle identification capability of the TRT arises from the physics of transition radiation: ultrarelativistic particles emit X-ray photons when crossing a boundary between materials with different dielectric constants [31]. The probability of radiation depends on the particle's relativistic γ, so particles with different masses at a given momentum produce different numbers of radiation photons. For example,

---

[1] For comparison, the maximal drift time in the MDT is ~ 750 ns. The hit resolution is radius dependent, but a typical resolution of 80 μm is obtained.

electrons ($m = 511$ keV) produce significant transition radiation at a momentum of 500 MeV, while pions ($m_{\pi^\pm} = 139.6$ MeV) produce comparable radiation only for momenta in the 100 GeV regime. In addition to the tracking threshold that corresponds to regular hits in the gas, the TRT has a high threshold specifically for transition radiation emitted by electrons. Seven to ten high threshold transition hits are usually found for electrons with energies above 2 GeV.

4.3.4 Inner Detector Reconstruction

Reconstruction of charged particle tracks [43] begins with information from the silicon; this benefits from the high resolution and low noise occupancy of the pixels and SCT. The silicon raw data are converted to three-dimensional space points. Space points from the pixel detector and from the first SCT layer then seed the tracking. The tracking uses a Kalman-filter based approach to propagate [91] seed tracks outwards, while incorporating an optimized material description [92]. It removes outliers based on the degradation caused to the track χ^2. Tracks so formed may share space points, necessitating resolution of ambiguities in hit assignment. For this, a quality/scoring system evaluates each track for the likelihood of its emergence from a real particle, clusters being assigned iteratively to the highest scoring tracks followed by refitting. Quality cuts help reject fake tracks from random combinatorics. Such cuts include requirements on the number of shared clusters and on missing hits ("holes") on track.

Next, the reconstruction extends tracks with sufficiently high score to the TRT. First, it converts TRT raw data to calibrated drift circles, and associates them to nearby silicon-only tracks. It then performs a fit on the extended track the full silicon and TRT information. After comparing extended tracks to the silicon-only tracks above, it retains them if they are superior. If instead the extension is deemed to be bad, the TRT hits are labeled as outliers, and not included in the fit.[2].

The method described here is the so-called "inside-out" tracking procedure. It has a low efficiency for tracks from long-lived decays and photon conversions, which do not leave hits in the inner silicon. A complementary "back-tracking" procedure is therefore used in the reconstruction after the inside-out tracking, which starts with unused TRT hits, and tracks them back to the SCT, and in addition utilizes TRT only tracks. Other tracking procedures are also used to identify photon conversion, address electron bremsstrahlung and handle alignment and calibration issues. With reconstructed tracks, vertex-finding and beam-spot finding are conducted, as discussed below.

4.3.5 Beam Spot Determination Using Primary Vertices

The distribution of reconstructed primary vertices is used to determine the beam spot. The beam-spot is described by a 3-dimensional Gaussian distributions parameterized by centroid positions and widths in x, y, and z, as well as tilt angles in the $x - z$ and $y - z$ planes, and correlation parameter ρ_{xy} describing possible rotations of a non-circular beam spot in the transverse plane. These are found using an unbinned maximum-likelihood fit to the distribution of reconstructed primary vertices fit without a beam spot constraint [16].

Figures 4.5(a)-4.5(f) show the x, y, and z positions and widths of the beam spot

---

[2] Such silicon-only tracks contributed to problems with identifying muons in early data; see Chapter 7.3 for details.

as a function of run number for early 2010 data. The beam spot position in x and y is stable over many runs. The z position moves by a few mm, so that loose requirements on muon z are called for. The beam spot width in z is ~ 30 mm, while the width in x and y is a function of the beam squeezing.

4.3.6 Primary Vertex

Primary vertex reconstruction uses an "adaptive fitting" approach. The procedure is to select tracks with silicon hits which pass criteria on the impact parameter, and two or more selected tracks are used to find a seed vertex. The beam spot is used as a constraint in the fit, to remove vertices incompatible with the beam spot. The procedure is iterative, so that tracks far from the vertex seed are removed and used to form possible seeds, until vertex candidates are all found. After vertex reconstruction, the vertex with the highest Σp_{T}^2 of the included tracks is considered the primary vertex of the collision. More complete discussion and descriptions of vertexing can be found in [16, 39]

Primary vertex distributions are shown in Figure 4.6 for events with a muon with $p_{\mathrm{T}} > 6$ GeV, in early ATLAS 2010 data[3]. Observe that the beam is squeezed in the transverse plane even in early running, with x and y widths of $30-40$ μm. The width in z is instead $\mathcal{O}(3$ cm$)$. We note that typical track multiplicities in vertices are high, with an average of 56 for these events. With these properties, vertex criteria imposed in our analysis are not stringent, as will be discussed later in Chapter 8.

---

[3] Specifically, runs `152777-153599` acquired in April 2010.

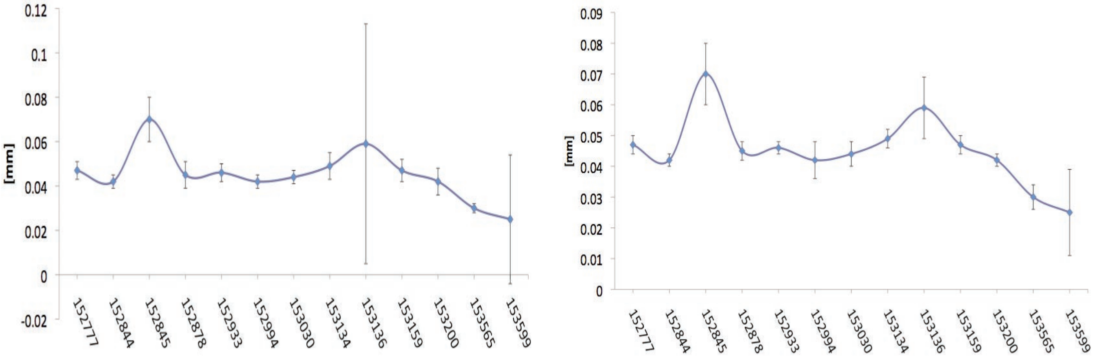

(a) Beam Spot X-position (b) Beam Spot X-width

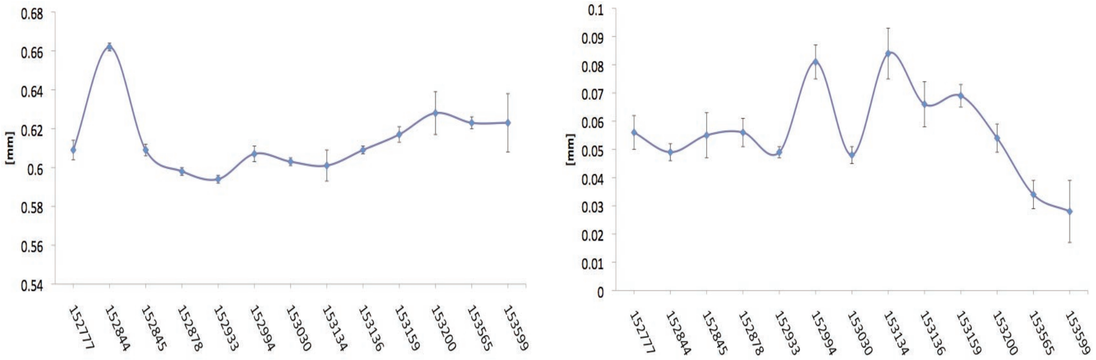

(c) Beam Spot Y-position (d) Beam Spot Y-width

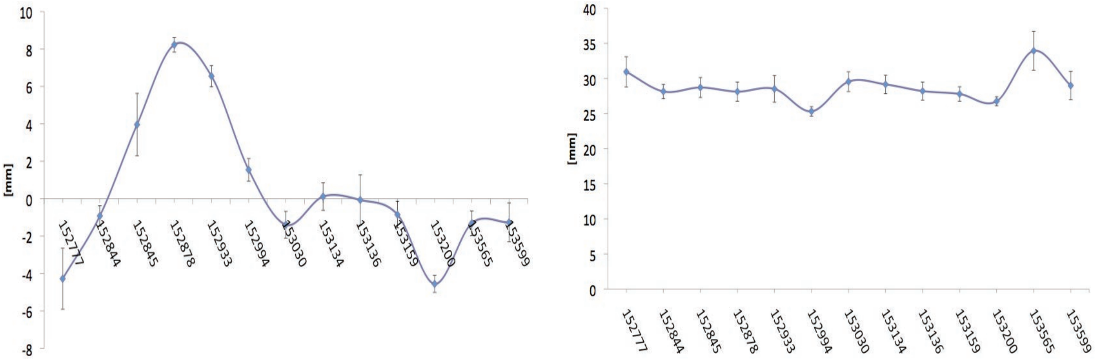

(e) Beam Spot Z-position (f) Beam Spot Z-width

Figure 4.5: Beam spot positions and widths as a function for run number, for early 7 TeV runs.

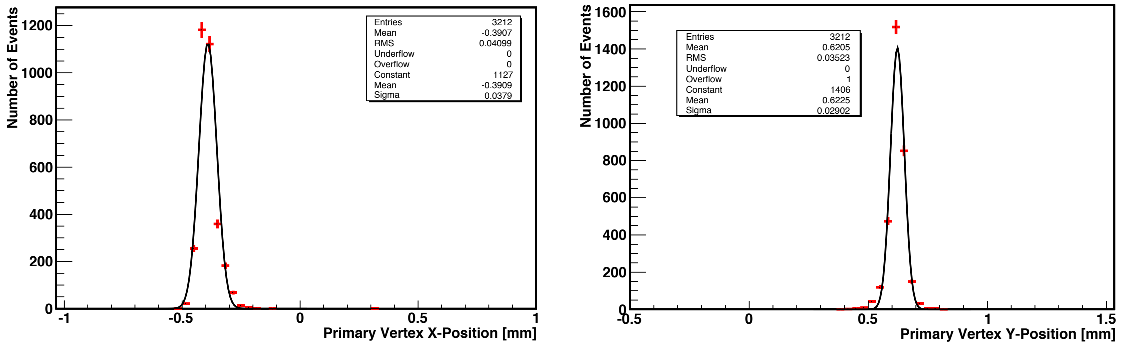

(a) Primary Vertex X-position

(b) Primary Vertex Y-position

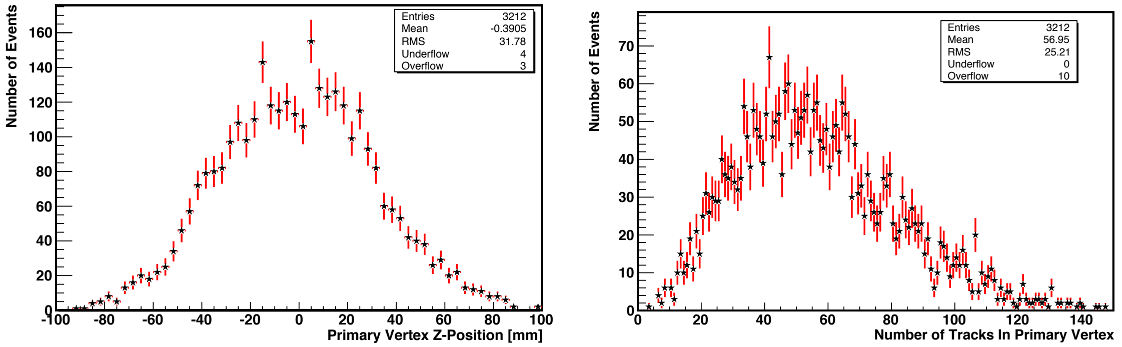

(c) Primary Vertex Z-position

(d) Primary Vertex Track-Multiplicity

Figure 4.6: Primary vertex positions and track multiplicity for early 2010 data. A combined muon with $p_{\mathrm{T}} > 6$ GeV is required for each event.

4.4 Calorimeter

Calorimetry in ATLAS measures the energy deposited by electrons, photons, and taus, as well as jets to distinguish them from leptons and photons. In addition, it helps measure the missing transverse energy from the detected imbalance in the transverse measurement, for which purpose good hermeticity is especially important.[4] To handle these needs, the calorimeter consists of electromagnetic (EM) and hadronic components. The configuration of the ATLAS calorimeter system is shown in Figure 4.7. The electromagnetic calorimeter relies on Iron/Liquid Argon (LAr) technology, and provides high resolution electron/photon measurements. The hadronic calorimeter serves to contain and measure hadronic jet energy. It utilizes iron/scintillator technology in the barrel (the Tile Calorimeter) and copper/LAr in the endcap. To maximize the rapidity range of energy measurements, the calorimeter contains a Forward component, which uses tungsten/LAr technology.

The calorimeter granularity in pseudorapidity and azimuth is schematically depicted in Figure 4.8. The calorimeter system extends out to $|\eta| = 4.9$ to ensure reconstruction of jet and missing energy kinematics over the maximum rapidity range. The overlap region with the inner tracking ($|\eta| < 2.5$) has fine granularity to satisfy performance requirements for photon and electron reconstruction. The calorimeter's material must contain showers to reduce punch-through and provide good energy resolution. The material budget is graphically depicted in Figure 4.9 - 4.10. The electromagnetic calorimeter has a radiation thickness of 22 X_0 in the barrel and 24 X_0 in the endcap. The hadronic calorimeter has an active interaction length of

---

[4] For additional details on $E_{\mathrm{T}}^{\mathrm{miss}}$, see Section 7.2.2.

9.7 λ (10 λ) in the barrel (endcap) with another 1.3 λ of support material, to provide good jet energy resolution. This material is also sufficient to reduce punch-through into the muon system to under the level of decay-in-flight muons.

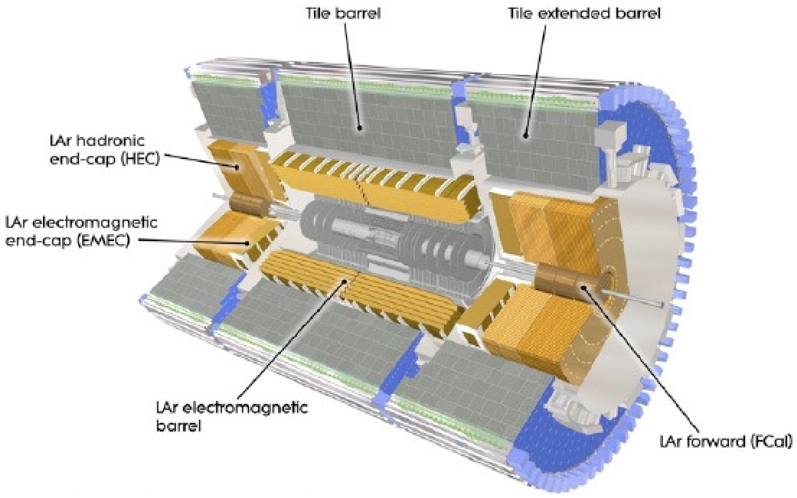

Figure 4.7: Components of the ATLAS calorimetric system.

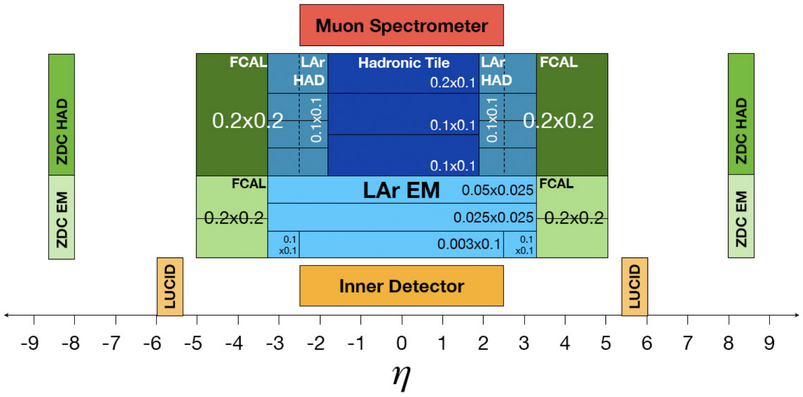

Figure 4.8: Segmentation of the ATLAS calorimetry in $\eta - \phi$.

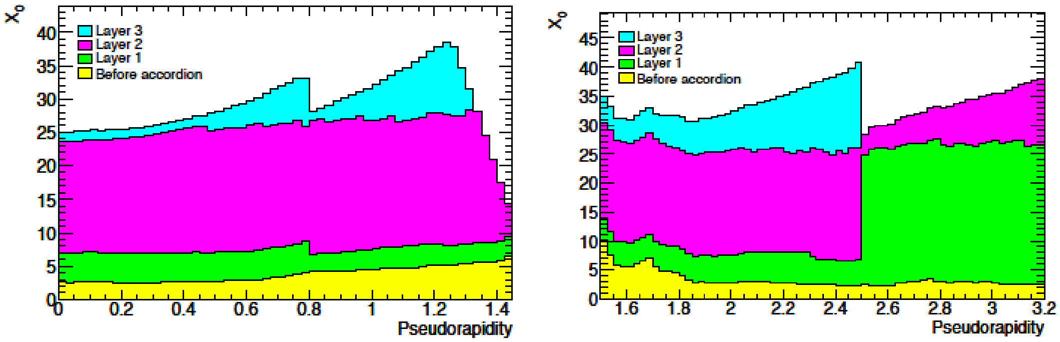

(a) X_0 Barrel (b) X_0 Endcap

Figure 4.9: Material in the calorimeter showing the number of radiation lengths in the electromagnetic barrel (a) and endcap (b) as a function of pseudorapidity.

4.4.1 Electromagnetic Calorimeter

The ATLAS Electromagnetic Calorimeter (ECAL) uses Liquid Argon as active substance; advantages of this choice include radiation hardness, ease of calibration compared to crystals, and flexibility in granularity. Photons and electrons create showers in the lead plates (predominantly through pair-production and bremsstrahlung), which ionize the liquid argon proportionally to the particle energy. The signal is read out via kapton electrodes. The ECAL has an "accordion geometry" (see Figure 4.11). Instead of orienting absorbers orthogonal to the particle trajectory as in a typical projective geometry, the accordion structure has particles traverse absorber at 45˙ angle, permitting full azimuthal coverage without gaps. The ECAL extends out to $|\eta| = 3.2$, with a barrel section extending till $|\eta| = 1.475$ and two endcap sections beginning at $|\eta| = 1.375$. The barrel is separated physically into two halves. In the endcap, the ECAL consists of two wheels, the outer wheel extending from $1.375 < |\eta| < 2.5$ and the inner from $2.5 < |\eta| < 3.2$ The electromagnetic calorimeter contains a total of

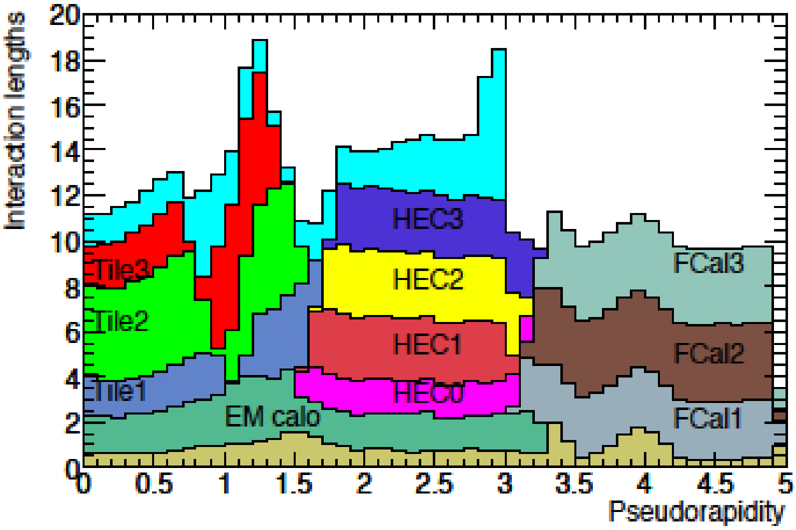

Figure 4.10: Material in the calorimeter showing the number of interaction lengths contained as a function of pseudorapidity.

$\sim$ 170,000 readout channels.

Longitudinally, the EM calorimeter has three layers. The first layer has a depth of 4.3 X_0. This layer has extremely fine granularity in η to separate prompt photons from neutral pion decays. The bulk of the electromagnetic shower is contained in the second layer, which has a depth of 16 X_0. The third layer serves to extend the measurement to high energy photons and electrons. In the endcap region $2.5 < |\eta| < 3.2$, which lacks inner tracking, and is therefore not used for precise e/γ measurements, the ECAL has a coarser segmentation into two layers. One important feature of the ATLAS detector is the significant material contained upstream of the calorimetry in the inner detector and especially the solenoidal magnet. In part this problem is reduced in scope by utilizing a common cryostat for the solenoid and the calorimeter in the barrel region. Nevertheless, the upstream material results in more than 40% of photons converting before reaching the calorimeter. To deal with this problem, a presampler installed in front of the EM calorimeter inside the cryostat helps correct for upstream energy loss. The presampler extends out to $|\eta| < 1.8$, and consists of a LAr layer 1.1 cm (0.5 cm) thick in the barrel (endcap).

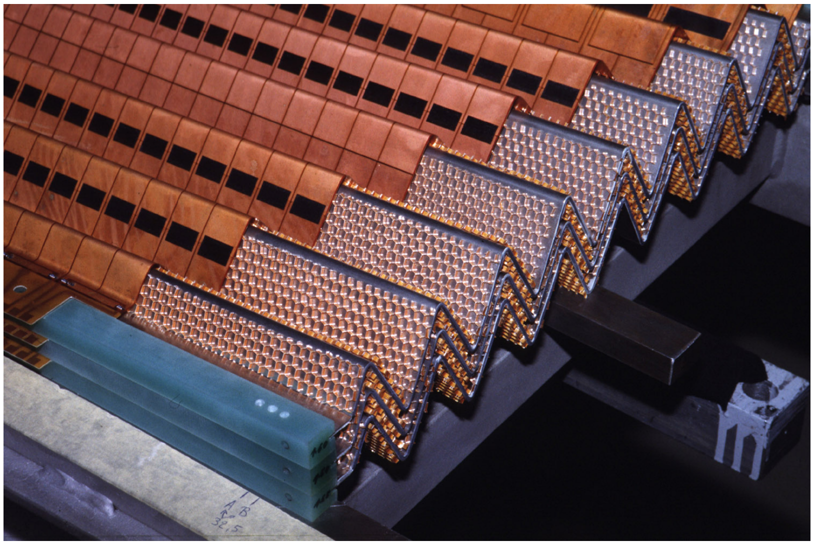

Figure 4.11: The Accordion geometry of the Liquid Argon Calorimeter. This design extends the azimuthal coverage and reduces cracks.

4.4.2 Hadronic Calorimeter

The hadronic calorimeter uses a combination of tile scintillator technology in the barrel and LAr technology in the endcap.[5] The motivation for this difference in technologies is the need to maintain performance and radiation hardness in the high occupancy forward region.

In the central region, the Tile Calorimeter (TileCal) is directly outside the ECAL. The detector uses scintillator tiles as active material, where charged particles in show-

---

[5] ATLAS does *not* use compensating calorimetry. The difference between hadronic and electromagnetic response must be corrected for in the reconstruction.

ers produce ultraviolet light, converted to lower frequency by scintillator dies. The scintillators connect to wavelength-shifting fibers at their edges, which guide the light to photomultipliers. The tile calorimeter is further divided into a barrel ($|\eta| < 1.0$) and two extended barrels ($0.8 < |\eta| < 1.7$), the segmentation serving to allow space for detector services. Its inner radius is 2.28 m, while the outer radius is 4.25 m. The hadronic endcap calorimeter instead is a liquid argon based sampling calorimeter using parallel copper plates. It extends over $1.5 < |\eta| < 3.2$.

4.4.3 Forward Calorimeter

The forward calorimeter (FCal) extends over $3.1 < |\eta| < 4.9$. In this region, particle fluxes are very high. To cope with this, the technology used is a metal matrix with holes containing electrodes. The electrodes feature a high-voltage rod and tube arrangement, with the gaps between the rods and tubes filled by LAr. The FCal has a three-part longitudinal segmentation: the first performs electromagnetic measurements using a copper absorber while the other two measure hadronic activity using tungsten as absorber. The FCal is valuable information for missing transverse energy determination and forward jets, though it is not typically used for precision measurements. The thickness for the FCal is about 10 interaction lengths.

Chapter 5

Muons in ATLAS

This chapter describes the Muon Spectrometer (MS) and its components for triggering and precision measurements with particular emphasis laid upon the "MDT" technology. A description is given of muon reconstruction for different types of muons."Combined" muons, used in this analysis, are briefly described: pattern recognition, straight-line segment finding in drift chambers, curved track fitting in the MS and combined track formation from inner detector and MS tracks.

The Muon Spectrometer (Figure 5.1 is the outermost layer of the ATLAS detector. It measures the tracks of charged particles (mostly muons) that exit the calorimetry. It also provides triggering capability for high momentum muons, which are typically a signal of non-QCD physics. Our trigger for this analysis is based upon muons satisfying various trigger momentum thresholds.

The MS measures track curvature in a *toroidal* magnetic field as discussed in Section 4.2. As a consequence, and in contrast to the ID, the curvature gives the r-component of the muon momentum. For hard muons from the IP, this is essentially

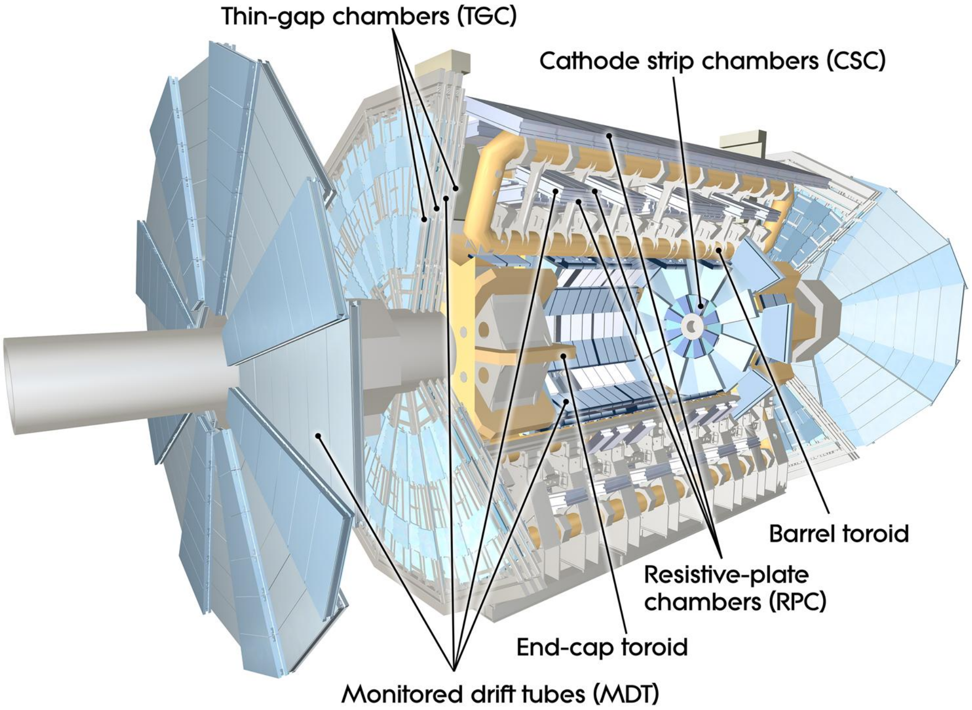

Figure 5.1: Diagrammatic view of the Muon Spectrometer showing its components.

the muon momentum itself. This momentum measurement is independent of that in the ID. Because of the large lever arm, high magnetic field, and low-material air-core technology, the MS offers excellent standalone muon momentum measurement, particularly for very-high momentum muons, for which the inner detector measurement is inadequate. As a benchmark figure, the MS is designed to provide 10% momentum resolution for 1 TeV muons. A TeV track has a sagitta of 0.5 mm and it therefore requires measurement with 50 μm precision. Good standalone reconstruction and charge identification is possible over a broad range of momenta, 4 GeV $< p <$ 3 TeV.

The configuration of the MS is shown in Figure 5.2, separately in the precision and non-bending planes. The MS has a built-in eightfold symmetry because of the toroidal system, and segments into sixteen ϕ sectors. The sectors alternate between large and small, with an overlap region in between them. The overlap maximizes azimuthal coverage, and in addition helps provide alignment between the sectors using tracks passing through the overlap region. There are multiple layers of detector in each sector, providing precision measurements and trigger. In the barrel ($|\eta| < 1.05$), there are three cylindrical layers of chambers at approximately R = 5 m, R = 7.5 m and R = 10 m. These are called the inner (I), middle (M) and outer (O) layers respectively. The layers are all instrumented with drift tubes (MDT, or Monitored Drift Tube chambers) for precise measurements in the bending coordinate (η). In addition, the outer and both sides of the middle layer contain Resistive Plate Chambers (RPC) for triggering capability. The endcap ($1.05 < |\eta| < 2.7$) instead has inner, middle and outer layers at $z = 7.4$ m, $z = 14$ m and $z = 21.5$ m respectively. The first two layers are installed as movable wheels, while the outermost layer is stationary and installed on supporting structures of the ATLAS cavern. The endcap toroid system is located between the inner and middle layers. Precision measurements are provided in each layer by MDT technology. However, in the far forward ($|\eta| > 2.0$) region in the inner wheel, the high rate necessitates the use of Cathode Strip (CSC) technology. Triggering capability in the endcap uses three layers of Thin Gap Chambers (TGC) located on the second layer of endcap detectors. The triggering capability of the muon system extends out to $|\eta| = 2.4$. A fourth TGC layer is part of the small wheel layer, but only affords readout measurements, and does not participate in the trigger. To maximize the acceptance of the detector, there are a number of special MDT chambers installed at the detector feet, on and around the endcap toroids, and in the transition region between the barrel and the endcap. The total number of MDT chambers is 1150, which together cover a total area of $5,500$ m^2. There are over a million readout channels in the Muon Spectrometer, corresponding to $354,000$ MDT channels, $318,000$ and $373,000$ from the TGC and RPC respectively, and $31,000$ from the CSC.

5.1 MDT

The Monitored Drift Tube (MDT) chamber is the workhorse of the Muon Spectrometer, providing the bulk of the standalone momentum precision. MDTs cover the full $|\eta|$ range of $(0, 2.7)$ with the exception of acceptance gaps, and the forward CSC region in the inner layer.

5.1.1 Drift Chamber Structure

A schematic of an MDT chamber is shown in Figure 5.3. Each chamber contains multiple parallel gas-filled tubes, typically grouped into two multilayers. Each multilayer has three layers of tubes, except in the innermost barrel and endcap detector layers, where the higher particle flux makes an additional tube layer per multilayer useful for pattern recognition. That is, chambers have six or eight tube layers. The number of tubes in each layer varies depending on chamber location and configuration; values between $30 - 72$ are typical. The smallest chambers have tubes ~ 1 m long, while the longest tubes in the outer endcap layer can be more than ~ 6 m long. The drift tubes point along the ϕ direction; in the barrel they group into rectangular chambers in each of the three detector layers discussed above. In the endcap

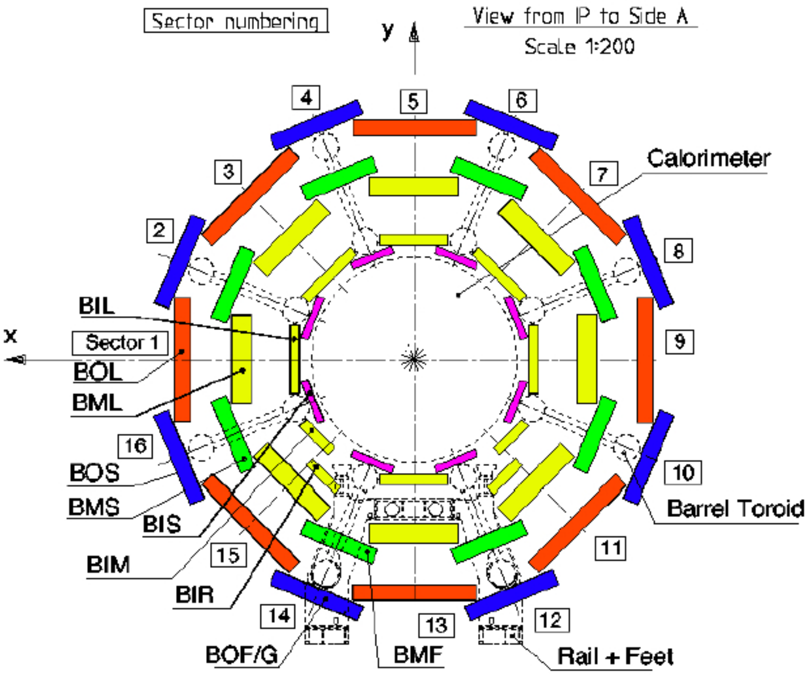

(a) Transverse Section

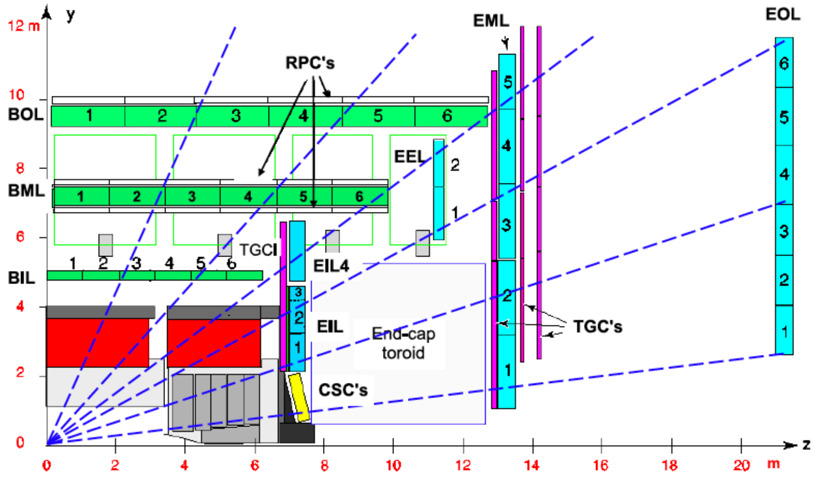

(b) Longitudinal Section

Figure 5.2: The configuration of the Muon Spectrometer, in the $x-y$ (a) and $y-z$ (b) planes. In the upper figure, note the eightfold symmetry provided by the toroid coils (dotted), dividing the detector azimuthally into sixteen ϕ sectors.

instead, the chambers are trapezoidally shaped, filling out ϕ sectors in each z layer. Chambers have optical alignment monitoring systems to monitor their locations and deformations. They also have magnetic field and temperature sensors to monitor local conditions. Alignment is the dominant effect upon muon resolution for high momentum ($p_{\mathrm{T}} > 200$ GeV) muons together with the intrinsic tube resolution.

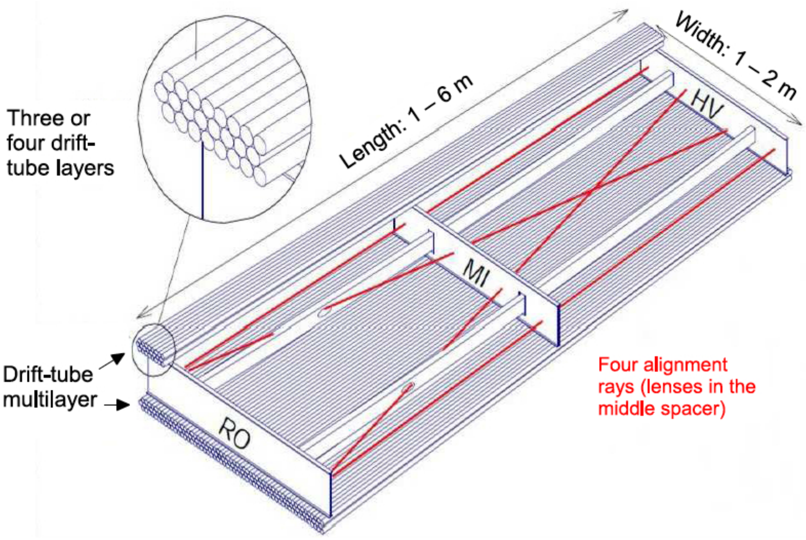

Figure 5.3: Schematic of an MDT chamber, showing the multilayers of drift tubes and alignment rays.

5.1.2 Drift Tube Design and Operation

Each MDT is an aluminium tube of diameter 30 mm, containing a drift gas and a central anode wire. The gas chosen for the MDT system is a mixture of argon (93%) and carbon dioxide (7%). The gas mixture is nonlinear, but has excellent aging properties. The gas pressure in the tubes is 3 bar. The anode wire is made of a tungsten-rhenium alloy, plated with gold. The wire has 50 μm thickness, and it is kept at a voltage of 3080 V, generating a radial electric field. A diagram of an MDT tube is shown in Figure 5.4.

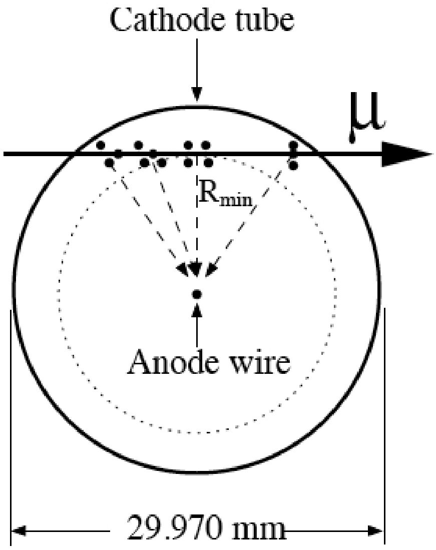

Figure 5.4: Schematic representation of MDT, showing the cathode tube and anode wire, and the ionization produced by a propagating muon.

When a muon passes through the drift tube, it ionizes the gas. The produced electrons (ions) drift toward the anode wire (cathode tube). Near the high field of the wire, an avalanche is produced, leading to a signal in the wire in the form of a voltage drop. These are read out by the on-chamber electronics. An ASD (Amplifier Shaper Discriminator) card feeds signal pulses (defined as crossing a threshold, typically 5σ, over the noise) to a Time to Digital Converter (TDC) which encodes the signal time and the charge integrated under the leading edge of the pulse. The charge helps suppress noise, and facilitates time-slewing corrections. The signal *time* maps to the *distance* of the muon from the drift wire: the first electrons produced along the muon track to arrive at the wire travel perpendicular to the muon track. The time taken for the leading electrons to arrive at the wire therefore corresponds to the distance from the wire at which the muon traveled.

Calibrated "RT" (drift velocity) functions are used to reinterpret the time signal as a drift-circle. We examine the calibration of pulse timing offsets and gas RT functions in greater detail in Chapter 6. Single-hit resolutions are a function of the hit radius, in the $\mathcal{O}(80\ \mu\text{m})$ regime, while for a chamber resolutions of $\mathcal{O}(35\ \mu\text{m})$ are obtained.

Note that the coordinate along the drift tube is not well-resolved by the drift tube system. In this "second-coordinate", i.e. ϕ direction, the measurement relies instead upon the trigger chambers. This direction is not as critical as the precision/bending direction, and millimetric precision suffices to match tracks to the inner detector. Tube drift-circles are used to fit straight-line segments and curved tracks for muons. We expand upon muon reconstruction in Section 5.6.

5.2 CSC

The MDTs can operate at a maximum occupancy of 150 Hz/cm^2, which is too low for the flux expected close to the beam-pipe in the forward region. For this reason, the innermost layer of the endcap uses Cathode Strip Chambers (CSC) in the $|\eta|$ region $2 - 2.7$. These have a rate capability of 1 kHz/cm^2, which is sufficient for operation at the nominal luminosity of 10^{34} cm^{-2}s^{-1}. Other features of the CSC technology include excellent resolution in the bending direction, a second coordinate measurement, and fast timing resolution of 7 ns corresponding to peak electron drift-times of under 40 ns.

The CSCs inhabit the endcap small wheel, 7 m from the interaction point. There are sixteen chambers in each endcap, alternating small and large chambers as for the MDTs. The two chamber types are organized as two discs of eight chambers each, as shown in Figure 5.5(a). The chambers have a tilt relative to the vertical, since their resolution is best for normal incidence. The CSCs are designed as multiwire proportional chambers with radial anode wires and separate cathode strips measuring η and ϕ (the wires are not read out). The CSC utilizes a symmetric cell, wherein the spacing between the wires is the same as that between the wire and the strip layer, at 2.54 mm (0.1 inch). A chamber consists of four layers, each providing measurements in η and ϕ, so that a track acquires four precision and four non-precision measurements in the CSC.

The gas is a mixture of argon (80%) and carbon dioxide (20%). When a muon passes through, it ionizes the gas, producing electrons which avalanche near the anode wire (operating at 1900 V). The electrons (and positive ions) induce a positive charge distribution on the cathode strips, orthogonal to the wire direction, as shown in Figure 5.5(b). Typically three to five strips around the peaking strip contain the charge induction. This signal is collected on multiple electrodes, and the information from adjacent cathode strips is combined to determine the track position. The spacing between precision readout strips is 5.08 mm, yielding a chamber resolution is 40 μm in η (60 μm per plane). The strips in ϕ are coarser, with 15.7 mm spacing, leading to a 5 mm resolution in ϕ.

5.3 RPC

The muon trigger in the barrel ($|\eta| < 1.05$) uses Resistive Plate Chambers. There are three sets of RPC chambers per ϕ sector, configured as shown in Figure 5.6(a). There are RPC chambers on both sides of each middle MDT chamber, (numbered RPC1 and RPC2 from inside out) and in addition one more layer, RPC3, attached to the outer MDT layer. The third RPC layer is below (above) the MDT in the small (large) sectors. Each RPC chamber contains two adjacent units embedded in a light paper honeycomb matrix. A unit comprises two gas volumes (layers), each of which

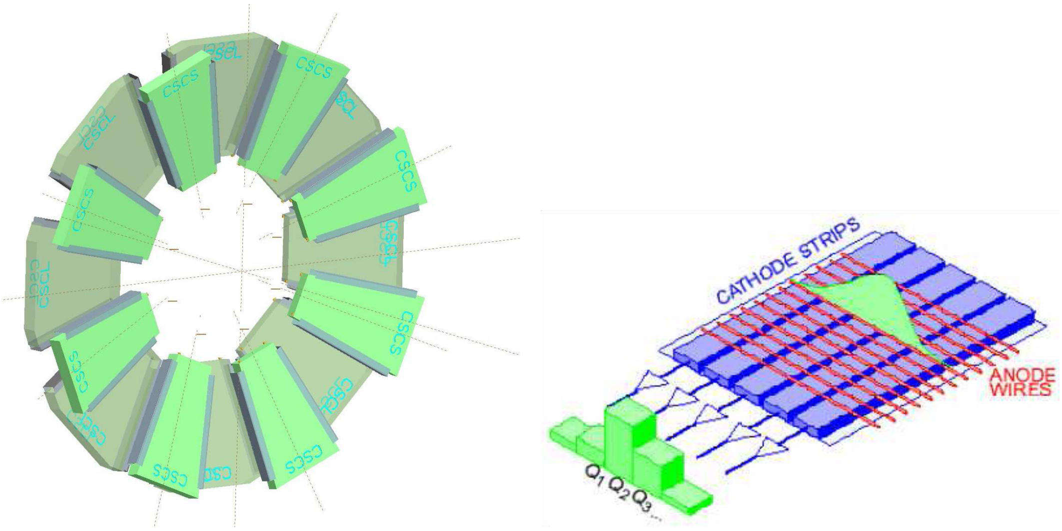

(a) CSC Wheel

(b) Charge collection

Figure 5.5: Schematic of the CSC layout in an endcap (a), showing the small and large chambers. To the right(b), induced charges on CSC strips from a track. The Gaussian distribution on adjacent strips enables position determination by interpolation.

furnishes a measurement in both η and ϕ. Thus, in an RPC chamber, a track typically yields two measurements in each coordinate. The structure is shown in Figure 5.6(b). The entire system then typically achieves six measurements in each direction for a muon track. The multiple measurements aid efficient triggering for both low and high momentum tracks. Because of detector structures like the feet and toroid coils, the acceptance of the RPC is reduced. This is mitigated to an extent using special RPC chambers near the feet which are not attached to any MDT chamber given the space constraints. Nonetheless, the acceptance averaged over the barrel is $\sim 80\%$ for low-p_{T} triggers, and only $\sim 70\%$ for high-p_{T} triggers.

Each gas-volume in an RPC chamber is a gaseous parallel-plate detector (see Figure 5.7). The plates are made of phenolic-melamine plastic, kept separated by

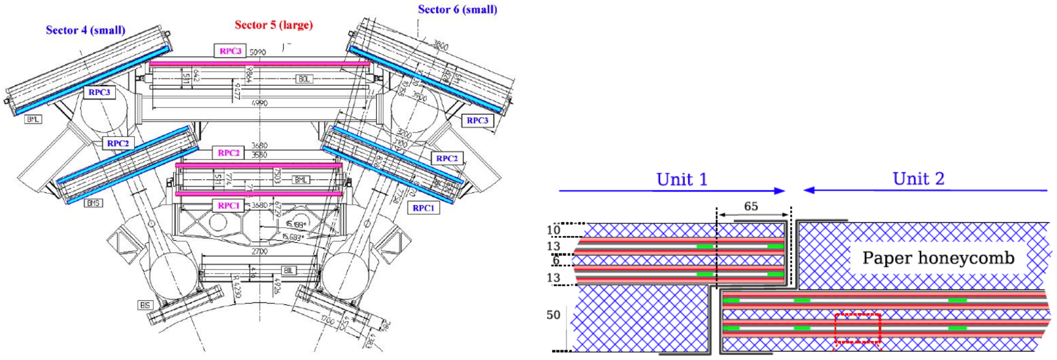

(a) RPC detector layout

(b) RPC chamber structure

Figure 5.6: The layout of RPC chambers is shown in the barrel (a). There are three RPC stations per sector. The structure of each chamber (b) includes two units, each containing two parallel plates containing a gas volume. These gaseous parallel plates are the fundamental measuring unit of the RPC.

2 mm using insulating spacers. The field between the plates is 9.8 kV. The gas mixture is $C_2H_2F_4$ (94.7%) / isobutane (5%) / SF_6, chosen for its low voltage, non-flammability and low cost. Charged particles traversing the gas produce electrons which induce an avalanche, generating a signal. Metallic strips capacitively coupled to the plates are mounted on them, permitting readout. There are separate strips for η and ϕ measurement. The strip pitch is $25 - 35$ mm, giving the technology 10 mm position resolution in both directions. The signal width in the RPC is 5 ns (FWHM), with intrinsic jitter of only 1.5 ns, facilitating excellent bunch-crossing identification.

5.4 TGC

Triggering in the endcap is challenging: because of physical constraints, the trigger chambers are outside the toroids, the field is highly inhomogenous in the transition

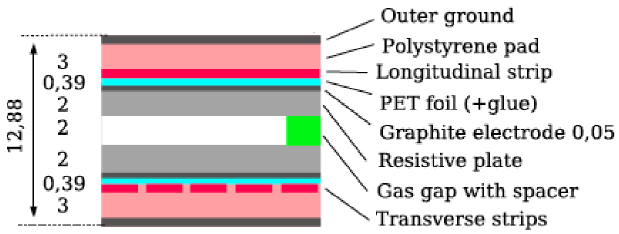

Figure 5.7: Section of an RPC gas volume, showing the parallel plates containing the gas mixture, and the longitudinal and transverse readout strips.

regions, and there is more radiation. There is also an intrinsic "physics" challenge: at higher pseudorapidity, a given transverse momentum corresponds to higher momentum. For all these reasons, we need better granularity and rate capability in the endcap trigger than in the barrel. The challenge is met using Thin Gap Chambers. These chambers cover the pseudorapidity range $(1.05, 2.7)$, with triggering capability for $1.05 < |\eta| < 2.4$.

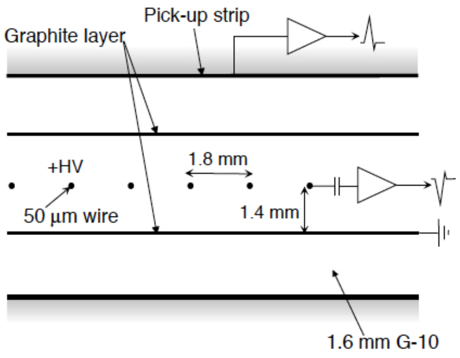

Figure 5.8: Schematic view of TGC, showing the wires and strips.

The sub-detector comprises four parallel wheels in z, TGC wheels 1-3 next to the middle layer of the endcap MDT chambers, and TGC4 on the small wheel or on the supports of the endcap toroid (the trigger uses only TGC1-3). Within a wheel, there are twelve sectors in ϕ, each containing multiple radial chambers. The TGCs use multiwire proportional chamber technology, with anode wires and cathode strips, as shown in Figure 5.8. The wires are along the azimuth and measure the precision coordinate η. The strips are radial and measure ϕ. The strip/wire separation of 1.4 mm is smaller than the 1.8 mm space between adjacent anode wires (hence the name “thin” gap). The gas mixture chosen uses carbon dioxide (55%) and n-pentane (45%), and the wires are at 2.9 kV. Charged particles produce ionization which drifts in the electric field of the wire. Both wires and strips provide measurements.[1] Each TGC layer contains multiple layers of wire/strip elements in a honeycomb structure: the innermost layer (TGC1) in the middle station is a triplet, while the other layers TGC2-4 are doublets (see Figure 5.9). The doublets have two wire and strip layers, while the triplets have two strip and three wire layers, providing an additional precision measurement. The spatial resolution of the TGC is $3-7$ mm in ϕ and $2-6$ mm in η. The timing resolution is excellent, 4 ns compared to the 25 ns bunch window.

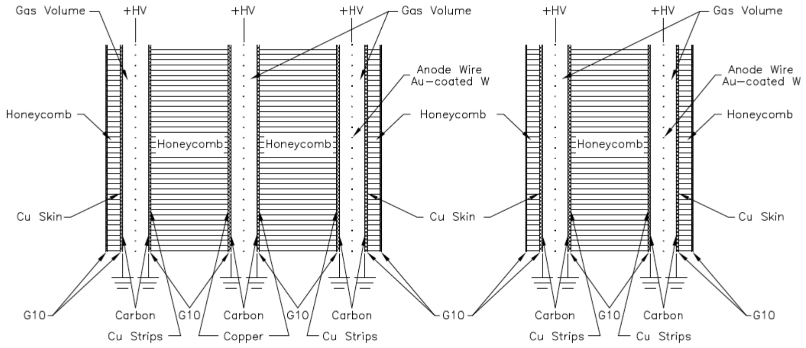

Figure 5.9: Cross section of triplet and doublet TGC modules. TGC1 (the innermost TGC big wheel) is structured as a triplet, while the other layers are doublets.

---

[1] The wire-ganging is in groups of 6-31 as a function of η to provide the needed momentum resolution.

5.5 Muon Trigger Logic

The triggering technologies, RPC and TGC, provide the muon Level-1 trigger. In each case, the trigger uses fast coincidences between up to three layers along the muon trajectory. The coincidences are formed using deviations of a track from the straight, infinite-momentum line. These deviations correspond to momentum (since softer tracks bend more in the detector), and hence provide momentum thresholds. A sketch of the procedure appears in Figure 5.10. Starting from a reference trigger layer (the "pivot plane"), the slope of a line from the interaction point to a hit on this layer is formed. The trigger compares this slope to the deviation of the track segment between two trigger chambers.

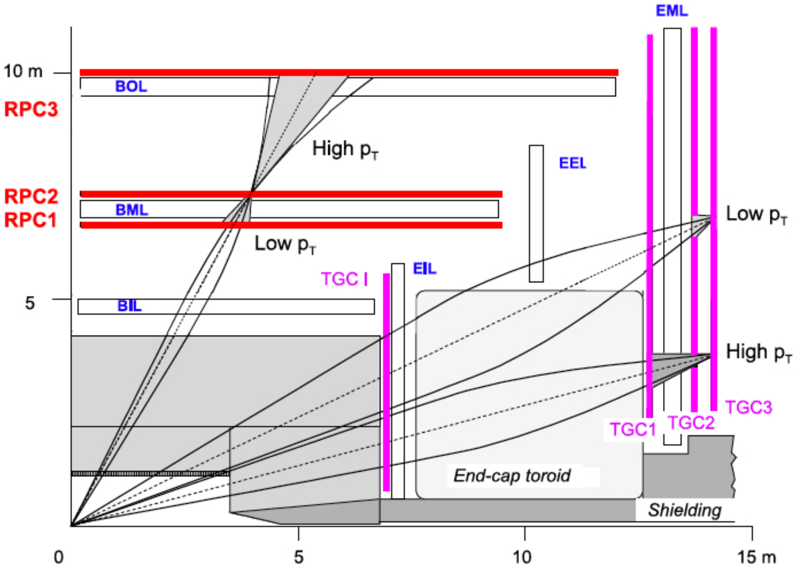

Figure 5.10: Muon L1 trigger logic.

In the RPC, the two inner layers provide a low-p_T trigger, in the $6 - 9$ GeV regime. The middle RPC layer is the pivot plane in the barrel region. Given a hit in this plane, the logic looks for hits in RPC1, in a threshold-dependent road, and in the same bunch crossing. The logic searches for a three-out-of-four coincidence in both η and ϕ to issue a low-p_{T} trigger. The long lever arm between the middle and outer stations enables high-p_{T} triggering in the $9 - 35$ GeV range. For the high-p_{T} thresholds, the logic starts with a low-p_{T} trigger, then looks for a hit in the third RPC station (RPC3) in the same time window.

The procedure in the TGC is analogous, with the outermost TGC wheel (TGC3) used as pivot plane. Hits from TGC3 are extrapolated to the interaction point in the infinite momentum approximation. In roads centered at this extrapolation, hits in η and ϕ are sought in TGC2 for the low-p_{T} trigger. A three-out-of-four coincidence in both coordinates is the triggering criterion. For the high-p_{T} case, the triplet wheel (TGC1) is also examined, for two-out-of-three (one-out-of-two) coincidence in the wires (strips).

The muon high-level trigger (HLT) is software-based, and runs on commercial PC farms. Note that throughout the muon Level-1 trigger, only RPC and TGC information is used; the drift tubes which provide the bulk of the momentum resolution are not utilized because of long readout times and fiber lengths. By contrast, the high-level trigger uses information from the entire muon system, and even from the inner detector and calorimeter. The HLT encompasses two levels, the Level-2 (L2) and the Event Filter (EF). The L2 trigger algorithms access data in regions-of-Interest (RoI) defined by the L1 candidate. MS standalone momentum and track parameters of the muon candidate are found by fast fitting algorithms and look-up-tables (LUT) which use the MDT drift times. Additionally, the muon L2 trigger uses inner detector tracks to combine with the muon candidate reconstructed with data from the MS. This refines track parameter resolution and aids rejection of low momentum muon tracks.

The EF muon trigger uses data from the entire detector, not just the RoI. The trigger software is closely based on the full offline software reconstruction discussed in Section 5.6. Specifically, the `MuID` suite of algorithms runs online in the EF, and available trigger chains include the `MuID Combined`, `MuID Standalone` and `MuGirl` algorithms.[2]

5.6 Muon Offline Reconstruction

The entire ATLAS detector provides useful information for reconstructing and identifying muons. Muons leave tracks in the inner detector, which are reconstructed as described in Section 4.3.4. Prompt muons are expected to arise from the primary vertex (Section 4.3.6). In addition, muons leave characteristic energy deposits in the calorimeter, on the order of $3-4$ GeV. Both the ID and the calorimeter are useful in understanding the isolation of the muon, to separate prompt muons from those that are produced in the decay of heavy-flavor quarks. Finally, the MS provides by design a muon momentum measurement independent of the one from the ID.

The ability to track in both the ID and MS is especially important, and leads to excellent muon resolution over a wide momentum range, from $p_{\mathrm{T}} = 4$ GeV to 1 TeV. The Inner Detector is very powerful at very low momentum ($p_{\mathrm{T}} < 30$ GeV), because the solenoidal field is strong, and (unlike in the MS) fluctuations in energy loss have

---

[2] The chain-names for the three include the tags “EF”, “EF_MSonly” and “EF_MG” respectively.

minimal impact. For very high momentum ($p_{\mathrm{T}} > 100$ GeV) by contrast, the large lever arm of the spectrometer is crucial, and the performance is limited by factors like MS alignment and single-tube resolution. In the intermediate-p_{T} region - which is relevant to the $W \to \mu\nu$ analysis, both the ID and the MS contribute comparably to the muon measurement.

The multiple detector technologies permit a variety of muon reconstruction algorithms using different parts of the detector: MS only, ID with calorimeter tagging, ID with MS tagging, and combined muons. A brief description is given below of the reconstruction methods for each case. At the outset, we note that muon algorithms in ATLAS are grouped into two competing suites, `MuID` and `STACO` [88], which are substantially equivalent in performance and reconstruction philosophy. Differences will be highlighted where pertinent. Useful overviews of muon reconstruction are provided in [85, 76, 77, 79, 101, 97].

5.6.1 Standalone Muons

Muon reconstruction in the spectrometer, yielding so-called “spectrometer-only” tracks, utilizes only information provided by the spectrometer technologies (MDT, CSC, TGC and RPC). In ATLAS this is done by two algorithms `MOORE` [8] and `MUONBOY`. Muon track parameters are then expressed at the interaction point using extrapolation, by the `MUONBOY` or `MuID SA` (from `MOORE`) algorithms. The extrapolation takes into account both energy loss and multiple scattering in the detector material. For energy loss, the reconstruction utilizes either a parameterization (`MUONBOY`) [80] or actual measurements (`MuID SA`) of calorimeter energy losses, together with parameterization of energy loss in inert material.

Standalone muon reconstruction proceeds in three broad stages: pattern/crude segment finding, segment reconstruction, and track fitting and extrapolation to the origin.

Pattern recognition: before starting segment building using hits, it is necessary to identify chambers and roads likely to contain muon activity. This is used to minimize processing time, since segment finding is CPU intensive.

`MOORE` uses a Hough Transform [47, 97] technique for this purpose. Conceptually, this involves expressing a line in normal form:

$$r = x\cos(\theta) + y\sin(\theta) \tag{5.1}$$

Here θ is the slope angle, while r is its perpendicular distance from the origin. Given a point (x_0, y_0), the lines passing through it form a two-parameter family in r and θ:

$$r(\theta) = x_0\cos(\theta) + y_0\sin(\theta) \tag{5.2}$$

This is a sinusoidal curve in the $r - \theta$ plane. Each point gives a different curve, and *curve intersections correspond to collinear points.* The method then reduces the problem of finding a line from a collection of points to that of finding the intersection of curves. This latter problem is readily solved with a histogramming approach: for each point a histogram is filled by scanning over parameter values, and any line candidates are seen as peaks in the histogram. Hits are associated to patterns based on distance. The transform runs in both the bending and non-bending planes, yielding η and ϕ patterns. These are combined to form full three dimensional patterns by associating hits. Segment finding then proceeds inside the roads defined by these patterns, at the chamber-level.

`MUONBOY` has a different strategy for identifying regions with muon activity. It uses the trigger chamber hits to define Regions of Activity (ROA) in $\eta - \phi$ directly. The regions have size $\sim 0.4 \times 0.4$. Reconstruction is performed in all chambers intersecting these regions.

Segment fitting: starting from the patterns, segments are found in each chamber. The process starts with MDT drift circles. `MOORE` takes pairs of hits, and forms all four possible tangent lines to the drift circles (Figure 5.11). It uses these lines if they are near a pattern, and picks up nearby hits. Then, a χ^2 based fit finds best-fit lines to the drift circles, with hits removed if they degrade its quality. To these segment candidates, trigger ϕ and η hits are associated. If there are multiple segment candidates in a chamber using similar hit collections, a quality/scoring procedure runs to rank them. Criteria used include the number of hits, holes and χ^2 of the fit.

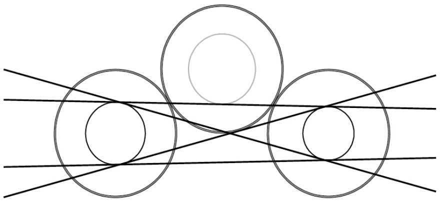

Figure 5.11: Possible segment tangent lines passing through two drift circles [101].

`MUONBOY` performs a similar reconstruction, but has a different procedure for segment quality/scoring, defining three segment categories. "Strict segments" require at least one ϕ hit (and hence are not made in the inner barrel or outer endcap stations). A looser segment search, undertaken after strict segments have been found, then runs with looser χ^2 requirements and no ϕ hit requirement. Finally, in a third pass, unused hits are used to form segments in single multilayers.

Track Finding and Extrapolation: in `MOORE`, the tracking starts by finding candidate tracks; segments are combined if they are compatible in location and direction. Once the candidates are found, they are fitted to find their parameters, and ambiguities are removed. The fitting uses a global χ^2 minimization approach. Once these candidates are fitted, a repeat of the tracking step starts from segments in the outer muon layer and works inwards. This second iteration takes material effects into account, and also picks up extra hits not associated to any segments. These tracks are then ranked in quality using criteria like number of hits, holes and χ^2, and higher ranking tracks incorporate shared hits. These tracks are then extrapolated (using `MuID SA`) to the origin/interaction point through the calorimeter, taking into account scattering in the material and energy loss.

For the `MUONBOY` algorithm instead, "strict" muon segments (middle-outer in the barrel, inner-middle in the endcap) give an approximate momentum estimate. The algorithm then extrapolates these segments to the first common layer using the magnetic field. This extrapolation is a momentum scan, with multiple trials using momentum values near the approximate estimate above. Given a match to some loose segment in an extrapolation, it is included in the candidate and the whole is fitted and the process is iterated. For retention, a candidate must have at least two segments. Once the candidate tracks have been formed using the segments, a global fit runs using the hits directly instead of the track segments. Backtracking to the interaction region is performed using a parameterization for energy loss, and scattering centers for multiple scattering.

The momentum resolution expected for standalone muons appears in Figure 5.12. The standalone resolution is poor at the feet of the detector, in the barrel-endcap transition region, and in the η region $[1.3, 1.6]$ because of magnetic field transition/toroid coil material. The gaps at $\eta = 0$ emerge from acceptance holes. A 3% standalone resolution is typical for 100 GeV tracks.

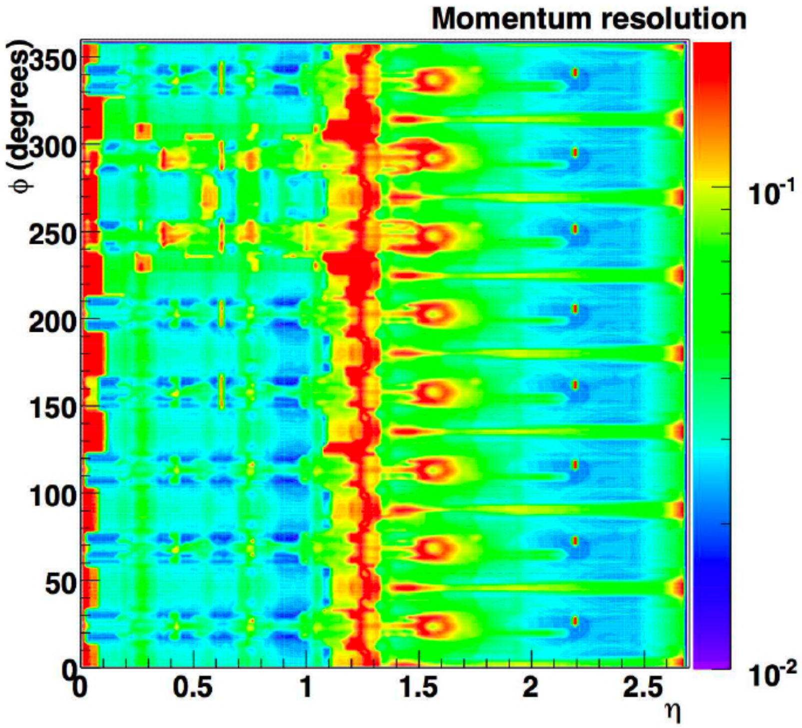

Figure 5.12: Standalone muon resolution for a 100 GeV muon track [38].

5.6.2 Combined Muons

“Combined” muons utilize tracking in both the ID and the MS. They take standalone tracks as above and combine them with Inner Detector tracks, described in Section 4.3.4. The association between standalone and ID tracks is different for the two algorithm suites. `STACO` takes `MUONBOY` and ID tracks and combines them statistically (`STACO` stands for STAtistical COmbination). If the tracks have parameters P_1 and P_2 and covariance matrices C_1 and C_2, the solution (P, C) is:

$$\left(C_1^{-1} + C_2^{-1}\right) \times P = C_1^{-1} \times P_1 + C_2^{-1} \times P_2 \tag{5.3}$$

$$C = \left(C_1^{-1} + C_2^{-1}\right)^{-1} \tag{5.4}$$

This solution yields a matching χ^2, a figure of merit, calculated as:

$$\begin{aligned} \chi^2 &= (P - P_1)^T \times C_1^{-1} \times (P - P_1) + (P - P_2)^T \times C_2^{-1} \times (P - P_2) && (5.5) \\ &= (P_1 - P_2)^T \left(C_1^{-1} + C_2^{-1}\right)^{-1} (P_1 - P_2) && (5.6) \end{aligned}$$

Tracks with satisfactory match-χ^2 are accepted as combined muons, and their kinematics are weighted averages of the ID and MS tracks, as computed above. `MuID Combined` performs a match like `STACO`, taking tracks with good χ^2 as a starting point, but then performs a full refit of the inner detector and spectrometer tracks. The fit parameters of this refit furnish the kinematics of the muon.

We note a few features that follow from the detector η coverage. First, since the trigger capability extends out to $|\eta| = 2.4$, muons more forward than this cannot be triggered. As such, a muon selection for the $W \to \mu\nu$ analysis in particular is naturally restricted to this η window. Observe too that muons in the far forward ($2.5 < |\eta| < 2.7$) region cannot benefit from inner detector information, and that in the forward ($2.0 < |\eta| < 2.4$) region the measurement from the ID does not include the constraints imposed by the TRT.

5.6.3 Tag Muons

ID tracks are deemed "tag" muons by association to segments in individual spectrometer layers. Such tracks are muon-rich given material interactions and attenuation for particle types other than muons. The approach is especially powerful for low p_T muons, which do not form complete tracks in the MS, and for regions in the MS (such as the detector feet or barrel-endcap transition) where we are not guaranteed to find multiple layers hit by a muon going through the detector.

There are multiple approaches to tagging muons. The `STACO` suite uses tagging (`MuTag`) as a complement to combined (`STACO Combined`) and standalone (`MUONBOY`) muon reconstruction, using only segments not already used in a combined or standalone muon track. Such segments, matched to unused ID tracks in ϕ and η, form tag muons. The `MuID` suite instead has two independent tagging approaches, `MuTagIMO` and `MuGirl`. `MuTagIMO` is similar to `MuTag`, but runs on all muon segments, whether or not they are also used in a standalone or combined track.

`MuGirl` instead extrapolates ID tracks inside-out to the spectrometer, and uses a Neural Network based method to identify nearby spectrometer hits and segments. `MuGirl` can also perform a full refit on the ID and MS hits, so that in this case it too outputs combined muons.

5.6.4 Calo-Muons

ID tracks are also tagged to calorimeter depositions consistent with muon propagation to yield "calo-muons". These muon reconstructions are entirely independent of the Muon Spectrometer, and are fruitful in regaining efficiency from regions of the detector lacking MS coverage. They are also significant at low momentum, where the muon may not reach the spectrometer. The kinematics for a calo-muon come from the inner detector.

5.6.5 Analytical Considerations

In the $W \to \mu\nu$ analysis, we focus on combined muons, though other muon types help characterize efficiencies and systematic uncertainties. This approach has a variety of justifications. First, these muons, combining ID and MS track information, have the best resolution muon reconstruction in the ATLAS muon arsenal. In addition, because of the excellent fiducial coverage of the ATLAS detector, combined muons have excellent relative efficiency compared to reconstructed muons as a whole. For example, in the 7 TeV W Monte Carlo sample, 99% of reconstructed muons have combined tracks - the gain from also using tagged muons and standalone muons is only 0.4% and 0.6% respectively. Further, the full combination of ID with spectrometer tracks gives superior fake rejection compared to the use of “tagged” muons, since the latter do not require hits in multiple layers of the spectrometer, utilize bending information in the MS, or combine and match track parameters in the two independent detector technologies. Standalone only muons, meanwhile, are, for muon momenta seen in Standard Model W or Z analyses, less competitive than measurements that also include the ID. In addition, they are less powerful for regions of the Muon Spectrometer that have sub-optimal alignment, low bending in the integrated field, or extra detector material.

Chapter 6

Muon Software Commissioning with Cosmic Rays

As ATLAS detector installation neared completion in early 2008, the experimental focus expanded to issues like subdetector commissioning, tests of triggering and data acquisition, improvement of detector description, software reconstruction and calibration. Cosmic ray data provided an invaluable physics signal for these purposes until the start of collision data-taking, and have been used in a variety of studies. For the muon spectrometer in particular, cosmic ray muons have proved to be invaluable in understanding reconstruction efficiencies and resolutions, detector calibration, data quality and detector alignment[2]. In this chapter, we describe some pertinent features relevant to cosmic ray muon reconstruction, focusing on MDT timing calibration.

We then describe an algorithmic process developed to fit for timing offsets during muon reconstruction. The procedure continued to be used with collision data in 2010, to compensate for imperfect timing calibration values in the software database, and to improve these values. The method is also being developed for use as a cosmic ray filter based on their shifted or wrong-signed timing offsets. For example, in the $W \to \mu\nu$ analysis presented in Chapter 7, candidate W events were tested against cosmic ray hypotheses based on these timing offsets. This is described in Section 7.5.3.

We begin with a quick description of the process of interpreting MDT time signals as hits.

6.1 MDT Time Offsets

As discussed in Section 5.1.2, when a muon passes through a tube in an MDT chamber, it ionizes the gas leading to the production of a signal in the drift wire. The time after muon passage taken to produce a signal in the wire is related to its distance from the wire, as can be seen from Figure 5.4. The precise relation involves subtracting an offset time, t_0, followed by the application of a drift-velocity function, called an “RT function”, to convert offset-subtracted times to hit radii.

By design, when a hit occurs on an MDT tube, its time is recorded by a local clock, and continuously stored into a circular buffer. When a suitably high-momentum muon passing through the detector causes the TGC or RPC to satisfy a trigger threshold, it leads to the issuance of a Level-1 Trigger-Accept by the Central Trigger Processor (CTP). Then, the MDT data for this event need to be retrieved for further online (and offline, if the event passes the full trigger chain) processing. The CTP distributes the accept signal to the MDT chamber electronics to retrieve the data. Note that there are several timing delays inherent in this process: the CTP takes $\sim 2\ \mu$s to process an accept, the signal propagation times from the CTP to the MDT (or from the trigger to the CTP) depend on fiber lengths, etc. Hence, when the MDT receives an L1A signal, it must effectively determine the amount to "look back" into the timing buffers to retrieve the correct signal for the triggered event. For this purpose, timing windows relative to the trigger signal time are programmed into TDC chips, enabling them to look back into the buffer and find the correct hits. The MDT on-chamber electronics finds all MDT hits inside a window[1], the beginning of which is determined by the arrival-time of the trigger signal, as seen in Figure 6.1. If the various timing delays are known, they can be subtracted out, yielding a hit time that represents how long it actually took the muon passing through the tube to generate a signal at the wire. The smallest time measurement for a muon tube is known as the tube t_0. It is the time from the TDC for muons which pass right by the drift wire.

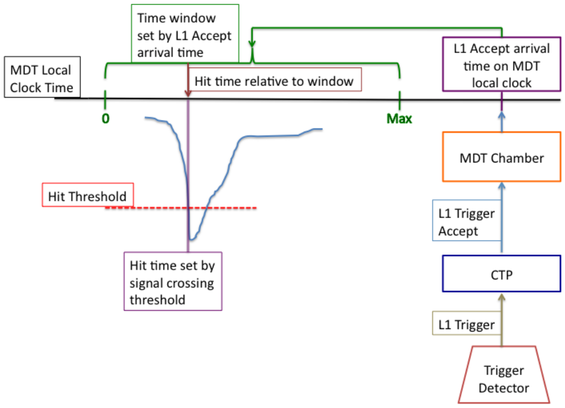

Figure 6.1: Hit and L1 Accept timing on MDT chambers. Figure taken from [27], [69].

A representative drift time spectrum is shown, in Figure 6.2, for cosmic rays trigged upon using the TGC. Each entry is a signal in a tube from some muon, where

---

[1] For early data-taking, the window is broad, ~ 2400 ns. It can be made narrower, to reduce the chances of picking up hits from noise.

many triggers (and hence muons) have been accumulated over. Effectively, it is the spectrum for a drift tube illuminated homogeneously as a function of radius.[2] The shape - which is not smooth or linear - reflects the non-linear drift properties of the Ar/CO_2 gas mixture, and the non-uniformity of the electric field across the tube radius. The maximum drift time (the width of the distribution) is a function of gas and detector conditions, and values of $\sim$ 700 ns are typical. In the plot shown, the t_0 offset is about 850 ns.

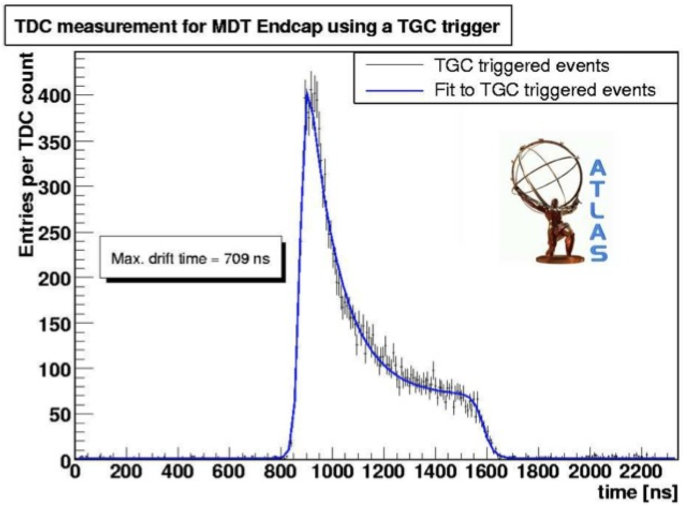

Figure 6.2: Tube time spectrum. The time at which the distribution rises, in this case at $\sim$ 850 ns, is the t_0.

During normal operation with collisions, the timing offsets between a machine collision and a trigger are known. These include the trigger processing time, the cable and fiber lengths from the trigger chambers to the CTP and from the CTP to the drift chambers, the time of flight of the muon from the interaction point to the chamber, signal transmission times along the tube wire, and time offset structure within the

---

[2] In fact, this particular distribution has been summed over many tubes in a chamber; offset differences between the tubes of a chamber also exist.

tubes of a chamber. Hence, software databases and the reconstruction can be tuned to store - on a tube-by-tube basis - timing information consistent with overall delays from the trigger chambers, the trigger processor and the chamber. Indeed, given a sufficiently wide readout window and accumulated statistics, one may *fit* distributions like those in Figure 6.2 to determine the offset empirically. Hit times are converted to radii using a function integrating the drift-velocity of electrons in the gas. The general shape of such radius-time or "RT" functions is understood in simulation using `Magboltz` [30] and `GARFIELD` [102]. Dedicated calibration centers [22] provide t_0s and time-dependent RT functions from data. A scintillator instrumented test chamber using the same gas-lines as ATLAS MDT chambers is used to provide a data-driven RT function (see for example Figure 6.3), which is then corrected at the chamber-level for temperature, magnetic field, pressure etc.

6.2 MDT t_0 Fitting

Timing for cosmic ray data faces a different set of constraints from the beam setup however:

- There is an intrinsic 25 ns timing *jitter* because cosmics do not come in sync with the LHC clock.
- Unlike with beam data, the time of flight is not known. In a collision event, the muon has a well-specified trajectory. It originates at the center of the detector, moves outward, and traverses trigger and precision chambers in a standard order and topology. A cosmic ray muon can have any top-down orientation, so that

flight times are not clear. Indeed, a cosmic muon need not trigger "near" the precision chamber - a muon may trigger RPCs in the barrel while leaving also hits in the endcap for example. If so, timing delays calculated using the RPC trigger may not work for the endcap, and vice versa.

- There are practical difficulties involving the commissioning exercise - changes from run to run in trigger conditions that are not always synchronized to the database, runs with very small statistics and so on. (In fact, the software databases did not contain timing constants for all chambers.)

We note that these are large effects: the 25 ns jitter alone means that a cosmic muon's hit time may be off by $\sim$ 12 ns. This corresponds to a $\sim$ 200 μm impact upon the hit radius used in reconstruction. Times of flight in the ATLAS detector can be much larger, $\sim$ 80 ns straight down or as much as $\sim$ 150 ns horizontally across. This leads to unacceptable loss of resolution in muon tracking performance, which translates directly into loss of power in commissioning exercises. For these reasons, it is fruitful to seek hit calibration for cosmic ray muons through other means. Since the factors above mentioned all correspond - for a given muon/event, in a given chamber - to a constant offset between the nominal and true t_0 value, we may modify the reconstruction code to not form segments and tracks with fixed drift circles (corresponding to the nominal t_0) but instead shrink or expand these hits by varying the t_0 as a fit parameter. Through this *in-situ* calibration we may recover better tracks.

We have implemented code running within `MOORE` that performs such calibration during segment reconstruction, and present results using it with cosmic ray data triggered by the TGC. This code has been incorporated into the `MOORE` suite of reconstruction algorithms for cosmic ray data-taking, and continued to be used with collision data in 2010.

6.3 In-situ Refitting Algorithm

Our work, as presented in [26], modifies the segment fitting procedure that is normally deployed in fitting straight-line segments to hits in single MDT stations (typically single chambers.) It consists in varying the time offset t_0 of all the drift circles in a segment by some amount, and picking that value which results in the best fit between the hits and the straight-line segment through them. We minimize the weighted residuals in quadrature, corresponding to the χ^2:

$$\chi^2 = \sum_i \frac{\left(\left|\frac{az_i - y_i - b}{\sqrt{1+a^2}}\right| - r(t_i - t_0)\right)^2}{\sigma_i^2} \tag{6.1}$$

$$= \sum_i \frac{\left[r(t_i - t_0) - \sqrt{b\cos\theta + z_i\sin\theta - y_i\cos\theta}\right]^2}{\sigma_i^2} \tag{6.2}$$

Here, the fit parameters a, b, and t_0 are, respectively, the slope ($\tan\theta$) and intercept of the segment in the bending plane (perpendicular to the drift tubes) and the time offset by which the drift circles are shrunk or expanded. The coordinate system $y-z$ in Equations 6.1 and 6.2 is centered at the mean position of the hit wires, weighting positions using the corresponding hit errors. The z direction points along the seed segment line, while y is orthogonal to it. Each hit is defined by its coordinates z_i and y_i, and drift time t_i. Note that this t_i already includes the timing information present in the conditions database, as well as corrections from hit calibration, so the t_0 above is in fact an *offset* to the default timing calibrations. Hence, the method continues to work unmodified as the database acquires more fine-grained timing information, at the per-mezzanine-card or even per-tube level. The drift radius r is computed as a function of the drift time $t_{\mathrm{drift}} = t_i - t_0$ via RT relations such as those plotted in Figure 6.3.

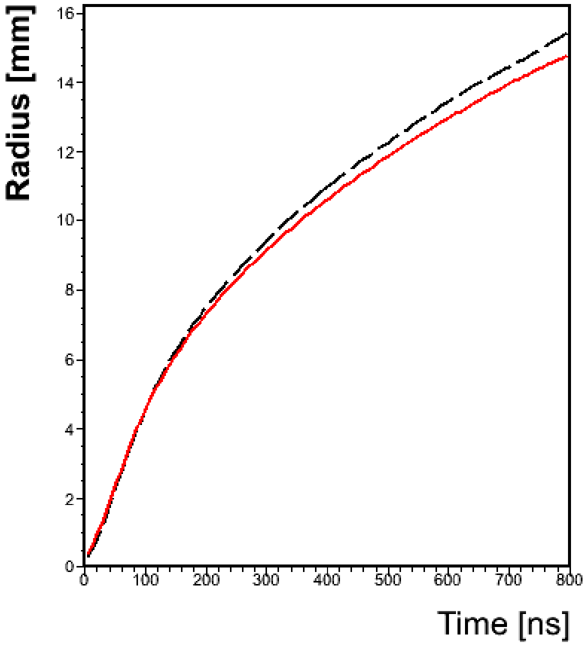

Figure 6.3: Drift circle radius versus drift time. RT functions as a function of detector and gas conditions, obtained from the dedicated calibration centers, are used by default. The solid/red curve is an example, obtained from the University of Michigan calibration center [44], and corresponding to detector conditions during the morning of 28th January 2009. The black/dashed curve is a backup RT function hard-coded into the algorithm, used in the absence of database access to the calibrated functions.

The χ^2 is smoothly blown up to large values in the fit where any hit is assigned a drift time that is either too large (outside the tube) or too small (negative). The function used for this purpose[3] is given below and sketched in Figure 6.4.

$$\begin{aligned} \chi^2_+ &= \left(t - t_{\text{max}}\right)^2 / 100 \text{ ns}, \ t > t_{\text{max}} \\ &= \left(t_{\text{min}} - t\right)^2 / 100 \text{ ns}, \ t < t_{\text{min}} \\ &= 0, \ \text{otherwise} \end{aligned} \tag{6.4}$$

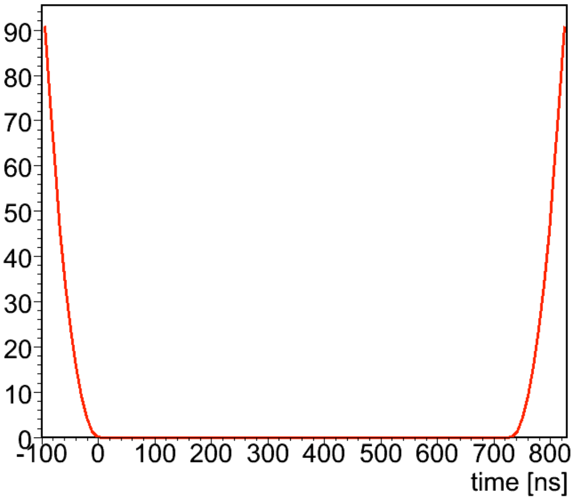

Figure 6.4: Smooth, additive increase to χ^2, used to minimize the possibility of fitted times giving negative drift radii or straying outside the drift tubes

The fitting is performed with `ROOT` / `Minuit` [33, 34, 71], using `MIGRAD` to minimize the χ^2. Step sizes are set to 0.01 for a and b and to 0.1 ns for the t_0. A one dimensional minimization is first performed on just the time shift, holding the segment

---

[3] Exponential functions can also be used for this purpose, such as the following multiplicative scale applied to the hit-line distance where the hit is too large or small.

$$\begin{aligned} \chi^2_\times &= 1 + \left(t - t_{\text{max}}\right)^3 \times e^{t - t_{\text{max}}} \text{ ns}, \ t > t_{\text{max}} \\ &= 1 + \left(t_{\text{min}} - t\right)^3 \times e^{t_{\text{min}} - t} \text{ ns}, \ t < t_{\text{min}} \\ &= 0, \ \text{otherwise} \end{aligned} \tag{6.3}$$

The cubic polynomial in this case serves to make the factor and its derivative continuous.

position and direction fixed, before freely fitting for all parameters. This facilitates a smoother integration into the segment reconstruction, so that fit minima correspond to particular segment tangent hypotheses and not to global minima. The code is in the form of an `ATHENA` tool, and accesses the calibration service for the correct RT relation for the dataset. Initial hit drift times are also taken from the calibration service, so the method preserves the benefits of calibrations, which can account for effects like slewing, B-fields, signal propagation, wire sag etc.

6.4 Performance

The performance of this procedure is studied on cosmic ray data corresponding to almost 18 million events. The toroid magnet is off for these events, which allows us to study the effect of t_0 calibration without the additional complication of muon tracking in a magnetic field. To test the performance of the in-situ refitting procedure, comparisons are presented where the same events are reconstructed with and without enabling the segment-by-segment t_0 refitting procedure. We emphasize that these results correspond to studies conducted in 2008-09, and that muon reconstruction performance has improved considerably since those dark days - this work documents the *improvement* in performance as a result of using in-situ timing calibration, not the best case performance.

6.4.1 Event Displays

It is instructive to begin with some event displays, to obtain a qualitative sense for the changes in reconstruction performance using in-situ fitting. (For the following plots, the hits are blue, in black tubes. Hits in red indicate those with zero radius, which is to say hits passing very close to the MDT wire.) In Figure 6.5, we see a typical example of the change induced by varying hit times. In this case hits without recalibration have times that are systematically too-large, which is corrected for by the fit. We also see that while all these hits have had their times shifted by the same amount, the changes in the radii are far from identical. This is expected from the RT functions in Figure 6.3, which are quite non-linear in time. The effect can be quite dramatic, as shown in Figure 6.6, where even as all the hits are shrunk by 110 ns, the hit on the bottom right shrinks to practically zero. Finally, in Figure 6.7, we can see how even the set of hits used in the segment can change because of such recalibrations. In Figure 6.7(a), before refitting, we see in addition to the regular hits, a hit (marked with (*), in yellow) which is not included in the segment. In the corresponding segment formed after recalibration, we see how this hit is included, while one of the earlier zero radius hits is removed. Clearly, the hit selection as well as the segment direction have met with significant change.

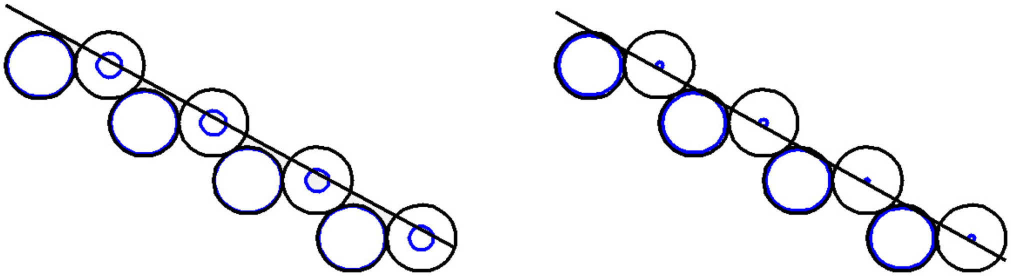

(a) before

(b) after

Figure 6.5: Changed hits and segments after in-situ calibration. Observe how the hits without recalibration have times that are too large, and with better timing we get a better segment through these hits.

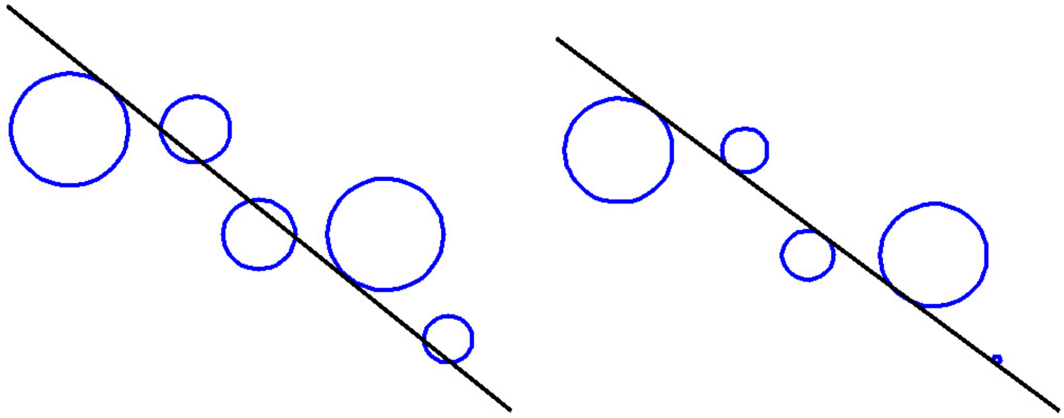

(a) before (b) after

Figure 6.6: The effect upon segments is particularly pronounced for hits with small times, both because of the non-linear RT function and because hits with negative hit times are all set to zero radius

6.4.2 Residuals on Segment and on Track

It is a common, and expected, feature of our displays that the residuals come down as a result of t_0 refitting. We present some plots and numbers to quantify this. The plots use the same configuration, and differ only in their usage of t_0 refitting. The distributions are fitted with two Gaussians with the same mean. The residuals for hits on segment show significant improvement, as seen in Figure 6.8, where the width of the central region of the residual distribution goes from 242 μm to 127 μm. The tail widths also get smaller, with the width of the broad Gaussian going from 1.546 mm to 1.194 mm, a 30% improvement. We see similar improvement in the track residuals (Figure 6.9) when using the refit. The central region improves from a width of 0.83 mm to 0.38 mm and the tail width from 3.56 mm to 1.90 mm. We should remark that these residuals were higher than those for segments, since detector alignment issues are much less significant for segments, which are mostly in a single

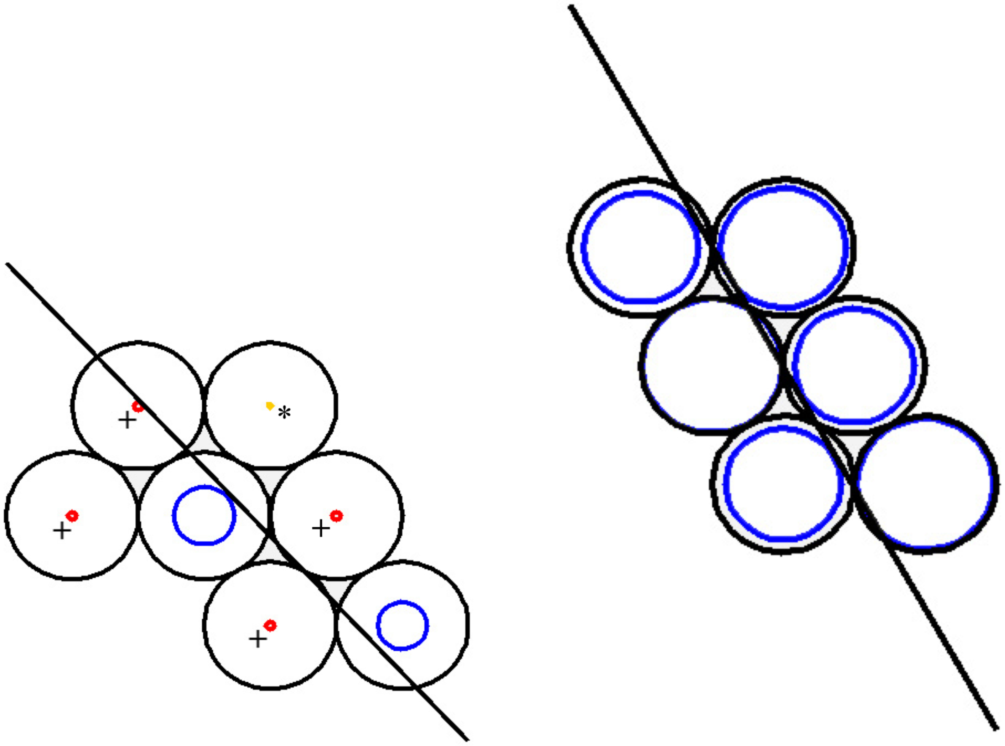

(a) before

(b) after

Figure 6.7: The selection of hits used in a segment can change, as seen above, where the yellow hit (marked *) is not used initially, while one of the zero radius hits (red, marked with a +) is removed by the fitting.

chamber. Finally, to get a sense of the *best-case* performance obtained with early 2009 software, we exhibit in Figure 6.10 a fit to a Gaussian of just the central peak region. In this case, we find a width of 94.6 μm for segments and of 316 μm for tracks. This core resolution is close to design targets for segments.

We have just documented the current performance for segments as a whole. However, our current setup uses in-situ calibration only for segments with at least five hits, to minimize problems with fit instability for segments with small number of hits. Hence, it is informative to consider resolution separately for segments with three or

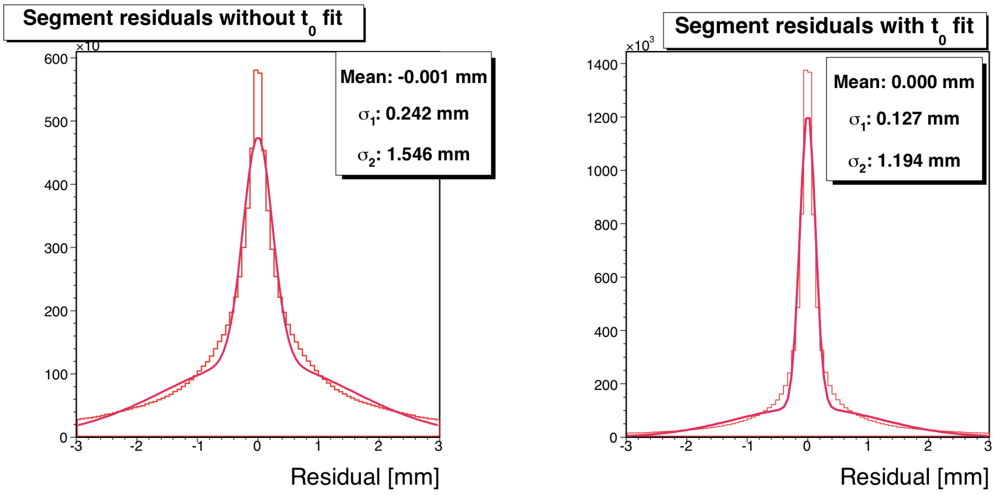

(a) before

(b) after

Figure 6.8: Segment residuals before and after the calibrated fitting.

four hits, and for those with at least five. These plots are shown in Figure 6.11. We observe that for segments with at least five hits, we get a central width of 126 μm, and a tail width of 1006 μm. For segments with three or four hits in contrast, we find central and tail widths of 262 μm and 2156 μm respectively. In addition, the proportion in the peak regions is 60% for segments with five or more hits, and only 24% for those with fewer than five. We observe that the central width in Figure 6.11(a), for segments with fewer than five hits, corresponds to that in Figure 6.8(a), for reconstruction as a whole without in-situ fitting. Similarly, Figure 6.11(b), corresponding to segments with at least five hits, provides the central width already seen in Figure 6.8(b) for reconstruction with in-situ calibration. Observe too that the large tails arrive disproportionately from segments with three or four hits.

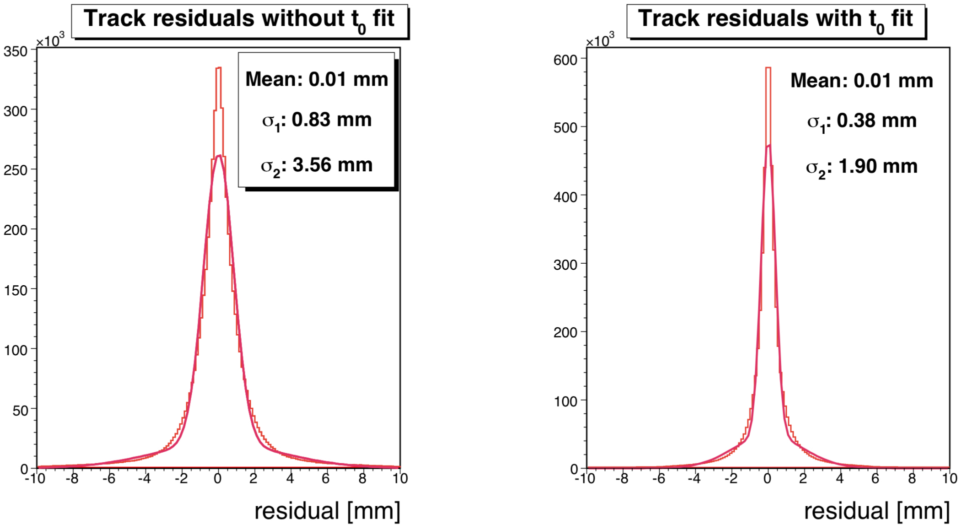

(a) before (b) after

Figure 6.9: Track residuals before and after the calibrated fitting.

6.4.3 Shifts in t_0 for Different Datasets

Since the in-situ fitting changes the hit t_0's, we would like to see that the drift time $(t - t_0)$ spectra are improved by the procedure. Consider, for example, the drift time spectra for hits on segment for TGC triggered cosmic events in Figure 6.12. These segments mostly come from the MDT endcap big wheels, and are as such predominantly triggered by TGC chambers next to them. As we can see from the uncorrected (red) drift time spectrum, the rise time is relatively sharp, reflecting our expectation that while there should be jitter, we should not see large time of flight issues. However, note that there is a large 150 ns systematic offset in this drift time spectrum. The fitting procedure produces the new (blue) spectrum, where this offset is removed, as can be seen from the plot of the difference between the final / corrected and initial / uncorrected t_0 for the hits. Consider next the drift time spectra, this

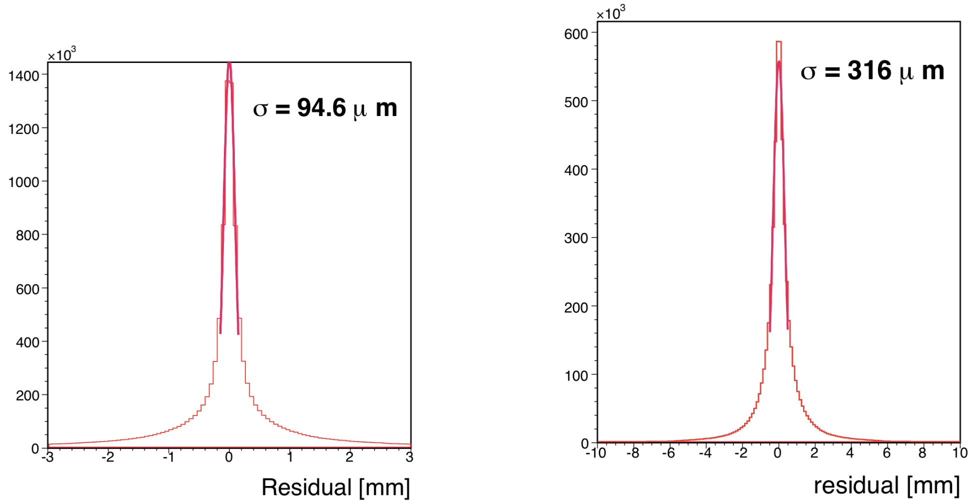

(a) segment (b) track

Figure 6.10: Best-case resolution in the bulk of the distribution, in release 14.5.2, with calibrated fitting. Note that the tails are *not* fitted for in the above, and correspond to 57% and 43% of the distribution for segments and tracks respectively.

time for RPC triggered cosmic events, shown in Figure 6.13. For geometrical reasons, we expect significant time of flight issues with these segments, as segments can be formed even at one end of the barrel while being triggered at an RPC on the other end. We see this in the extremely broad rise for the spectrum. In addition of course we expect jitter and also see a systematic offset. Again, we see the corrected spectra (blue) where these issues are taken care of. Finally, for a Monte Carlo $Z \to \mu\mu$ sample, which is correctly calibrated to begin with, the algorithm seems to preserve the spectrum as it should. The difference between the corrected and uncorrected t_0's for segments is fitted to a Gaussian, and has a width of 3.5 ns.

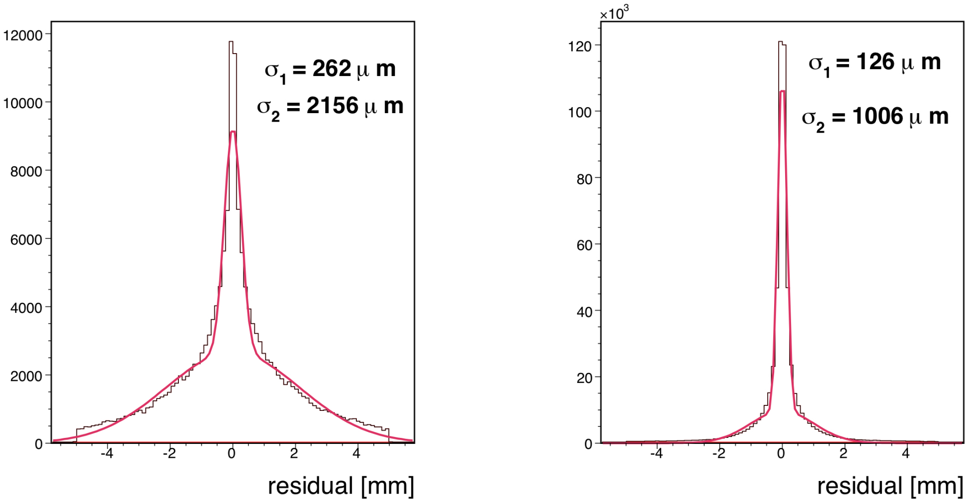

(a) Less than five hits (b) At least five hits

Figure 6.11: Segment residuals, with in-situ calibration running. With at least five hits, the in-situ calibration is turned on, while it is not in the contrary case. Note that with fewer than five hits, the algorithm reverts to that of segment finding without in-situ calibration.

6.4.4 Fitted t_0 by Chamber

It is also useful to compare the corrected t_0's from this procedure to expected distributions. See, for example, the distribution of obtained times for chambers in the A-side endcap middle layer in Figure 6.16. These times are found from the fitted t_0's for all segments going through a particular chamber (see for example Figure 6.15), by taking the peak of the chamber distribution. It is reassuring to see chamber level patterns in cable lengths reproduced. Note however, that the times obtained attempt to account for times of flight and jitter, and so incorporate effects additional to those from the usual trigger latency (cable lengths, for example).

To summarize, the use of an in-situ procedure for segment timing calibration

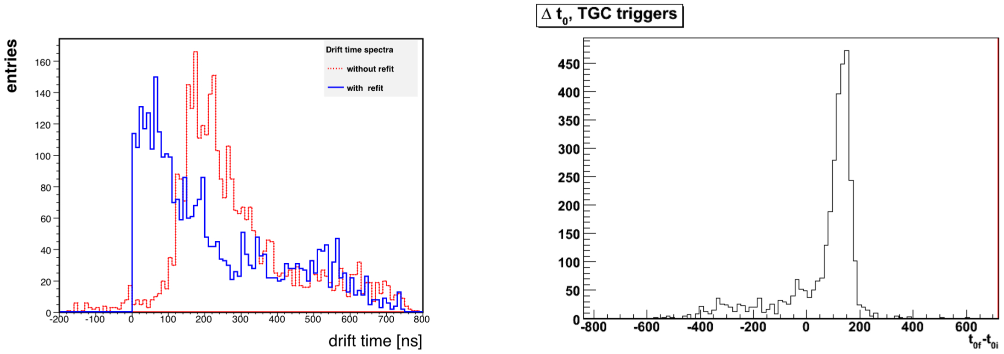

(a) $t - t_0$

(b) $t_{0,f} - t_{0,i}$

Figure 6.12: Drift time spectra for TGC triggered events (left) before (dotted, red) and after (solid, blue) the in-situ fit. On the right, the correction made by the fit to the segment t_0. Notice that the large initial offset in the hit times from miscalibration is corrected.

during reconstruction produces a significant performance boost with cosmic ray muons as measured using track and segment residuals. We see that the drift time spectra after refitting are more in line with expectations for our tubes, and correct both for systematic timing offsets (which shift the spectrum) and for effects like jitter and varying flight times (which make the rise of the spectrum broader). We also see that for a properly calibrated Monte Carlo sample, the timing information is preserved. Because of these properties, the method continued to be used for collision data-taking in 2010, to handle imperfect timing offsets for MDT chambers, and to improve calibrations. Another application, that of flagging cosmic ray muons, is discussed in detail in Section 7.5.3.

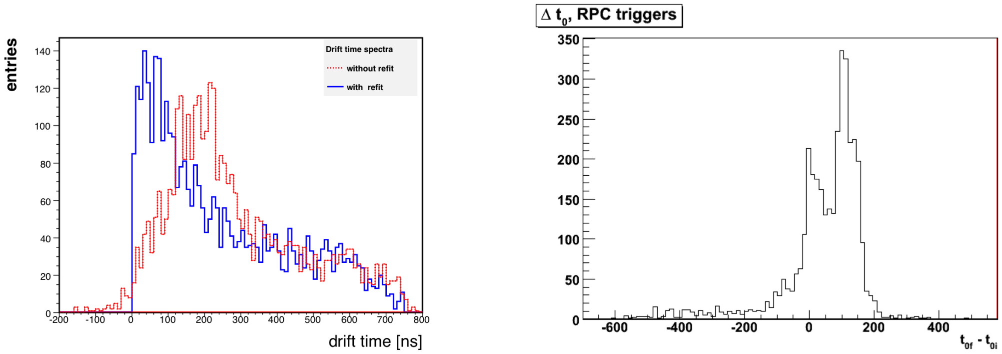

(a) $t - t_0$ (b) $t_{0,f} - t_{0,i}$

Figure 6.13: Spectra for RPC triggered events (left) before (dotted, red) and after (solid, blue) the in-situ fit. On the right, the correction made by the fit to the segment t_0. Observe both the correction of initial offsets and the sharpening of the rise time.

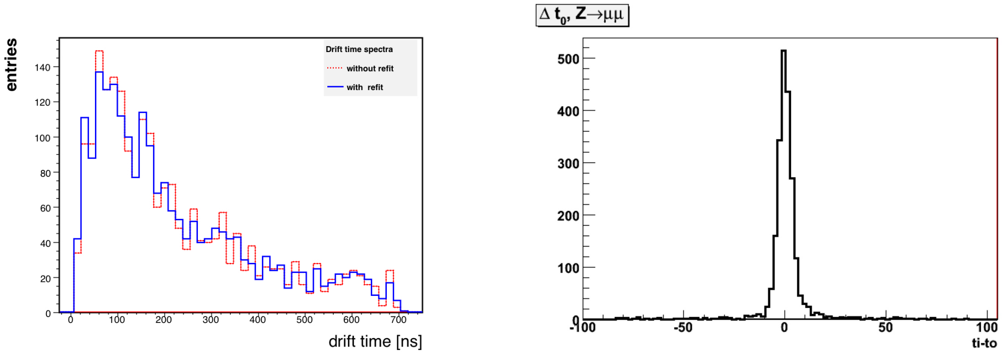

(a) $t - t_0$ (b) $t_{0,f} - t_{0,i}$

Figure 6.14: Correction applied to a Monte Carlo $Z \to \mu\mu$ sample whose initial calibration is good. On the left, we show drift-time spectra before (dotted, red) and after (solid, blue) the in-situ fit. On the right, the correction made by the fit to the segment t_0. The width of this $t_{0,f}$ - $t_{0,i}$ distribution is 3.5 ns.

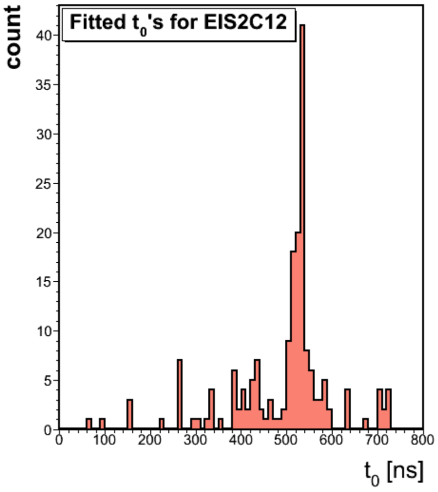

Figure 6.15: Fitted t_0 for segments in EIS2C12.

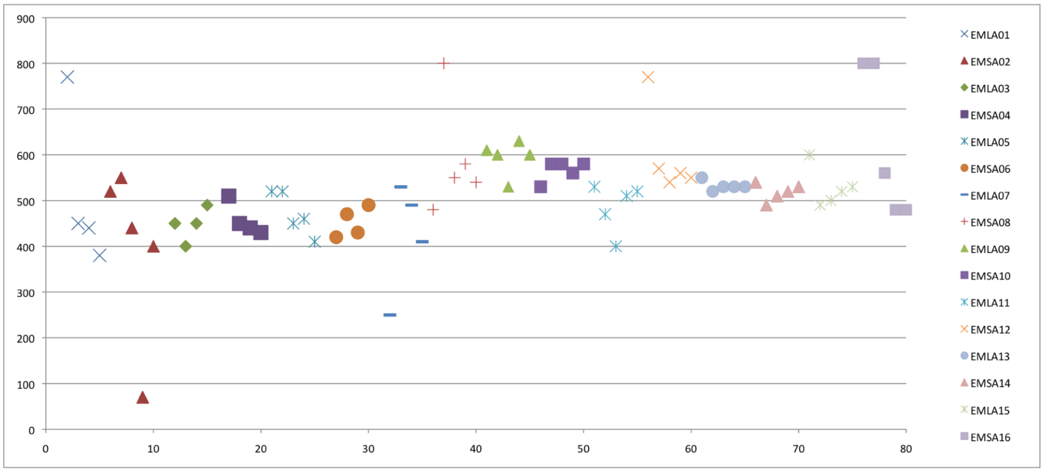

Figure 6.16: t_0 vs chamber for the endcap middle layer, side A. Empty bins occur because the data are plotted only where the chamber has at least a hundred segments, and because some chambers are not functioning (for example, EMS1A01 had high voltage turned off for this run).

Chapter 7

Early $W \to \mu\nu$ Analysis and First Cross Section

This is the first of two chapters on $W \to \mu\nu$ analysis with data acquired with ATLAS over the course of 2010. Here we describe the first W cross section measurement in ATLAS made with 310 nb^{-1} of integrated data. The measurement has been published [19], and was the first such result obtained at 7 TeV. The luminosity used is but a fraction of the full 2010 dataset (33 pb^{-1}), and an improved analysis with the full event sample has been produced in 2011 [41]. We set forth this latter analysis in Chapter 8.

A typical $W \to \mu\nu$ event display is shown in Figure 7.1, showing an isolated high-p_{T} muon track and the inferred $E_{\mathrm{T}}^{\mathrm{miss}}$ which is back-to-back with respect to the muon. This chapter describes the 310 nb^{-1} analysis in some detail, in terms of dataset and samples, event reconstruction and selection, backgrounds, acceptance and its uncertainties, systematic uncertainties from muon and $E_{\mathrm{T}}^{\mathrm{miss}}$ performance, and the final cross section result. The early $W \to \mu\nu$ observation and analysis addressed several issues, such as:

- Common muon, isolation and missing energy criteria.
- Event selection for the W signal.
- Additional useful samples such as preselection and control samples were defined.
- Estimation of electroweak and top backgrounds from simulation, and the estimation of QCD background from data.
- Methodology for acceptance and cross section calculation.

In addition, there were a number of challenges which were specific to early analysis. For example, the small dataset provided only small Z statistics for muon performance, so single muon techniques were used for trigger and reconstruction efficiency studies. The muon itself needed kinematic cleaning criteria to reject backgrounds from decays in flight matched to ID tracks. Particularly at low instantaneous luminosity, the cosmic-ray background needed to be understood. We discuss these matters along the way, paying particular attention to the definition criteria applied to muons, and to the QCD and cosmic ray background estimation.

7.1 Dataset and Simulated Samples

This analysis is based on a sample of collisions collected from April to July 2010. The sample integrated luminosity, after imposing machine and ATLAS detector and quality requirements, is 310 nb^{-1}.

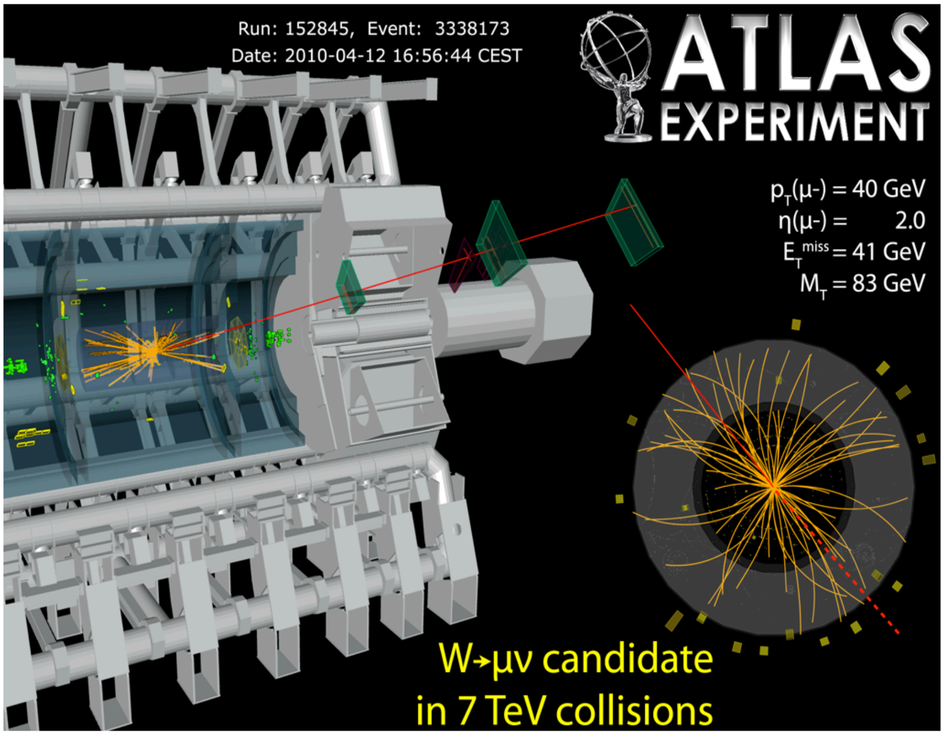

Figure 7.1: $W \to \mu\nu$ candidate event, with an isolated muon passing through the endcap of the MS, and firing the TGC trigger. The missing energy is back-to-back with the muon [24].

Physics process	Generator	$\sigma\cdot$ BR [nb]	
$W \to \ell\nu \quad (\ell = e, \mu)$	`Pythia` [96]	10.46±0.52	NNLO [68, 18]
$W^+ \to \ell^+\nu$		6.16±0.31	NNLO
$W^- \to \ell^-\overline{\nu}$		4.30±0.21	NNLO
$Z/\gamma^* \to \ell\ell \quad (m_{\ell\ell} > 60$ GeV)	`Pythia`	0.99±0.05	NNLO
$W \to \tau\nu$	`Pythia`	10.46±0.52	NNLO
$W \to \tau\nu \to \ell\nu\nu\nu$	`Pythia`	3.68±0.18	NNLO
$Z/\gamma^* \to \tau\tau \quad (m_{\ell\ell} > 60$ GeV)	`Pythia`	0.99±0.05	NNLO
$t\bar{t}$	`MC@NLO` [54], `PowHeg` [55]	0.16±0.01	NLO+NNLL [32, 84, 29]
Dijet (μ channel, $\hat{p}_{\mathrm{T}} > 8$ GeV)	`Pythia`	10.6×10^6	LO[96]

Table 7.1: Signal and background Monte-Carlo samples as well as the generators used in the simulation. For each sample, we give the production cross section, multiplied by the relevant branching ratios (BR), to which the samples were normalized. For the electroweak (W and Z boson production) and for the $t\bar{t}$ production, contributions from higher order QCD corrections are included. The inclusive QCD jet and heavy quark cross sections are at leading order (LO). These samples were generated with requirements on the transverse momentum of the partons involved in the hard-scattering process, $\hat{p}_{\mathrm{T}}$.

The analysis uses simulated ATLAS Monte Carlo samples to calculate acceptances and to model the properties of the signal and backgrounds. Event generation utilizes `Pythia` [96] (with the exception of the $t\bar{t}$ background sample, for which `PowHeg` [55] is used). We interface the generators to `Photos` [60] to simulate the effect of final state QED radiation. We use the MRST LO* [95] parton distribution functions, and `GEANT4` [10] to model the passage of particles through the ATLAS detector. In the $W \to \mu\nu$, $Z \to \mu\mu$, and filtered jet samples, the effect of multiple interactions per bunch crossing ("pileup") is modeled by overlaying simulated minimum bias events over the original hard-scattering event, as discussed in Section 7.2.3.

The cross sections quoted in the table are used to normalize predicted event counts for the various samples. For the dijet samples, the cross section listed is computed using `Pythia`. For the other processes, the cross sections are as follows. The electroweak processes considered, signal and background, include: $W \to \mu\nu$, $Z \to \mu\mu$, $W \to \tau\nu$, and $Z \to \tau\tau$. In the $W \to \tau\nu$ sample, the tau decays only leptonically. The W and Z cross sections are normalized to the NNLO cross sections as provided by the FEWZ program [18] ($\sigma_{W\to\ell\nu} = 10,454$ pb and $\sigma_{Z\to ll}(\sqrt{\hat{s}} > 60 \text{ GeV}) = 989$ pb). The uncertainties on those cross sections arise from the choice of PDF (3%), from factorization and renormalization scale dependence, and the size of the correction from NLO to NNLO (4%). The total is about 5%, which we take as an uncertainty on any event count predictions normalized using these cross sections.

The $t\bar{t}$ cross section, calculated at $m_t = 172.5$ GeV, is 161 pb, taken from Ref. [75]. The uncertainty is 6% plus the PDF uncertainty quoted above.

7.2 Event Reconstruction

In this section, we describe pertinent aspects of the event reconstruction which directly impact the W event selection. We discuss the muon algorithm selection, trigger and isolation criteria used. Particular attention is paid to quality requirements imposed to reject fake muons observed in collision data. Missing energy selection is discussed as well, followed by a note about the treatment of pileup events.

7.2.1 Muon Selection

All our events are required to pass a low momentum, single muon level-1 trigger with a 6 GeV momentum requirement, referred to as `L1_MU6`. At the first (hardware) level of trigger selection, the muon track is reconstructed using hits on two or three layers of the muon trigger chambers within a single geometrical section of the muon detector. The trigger detectors use RPC technology in the central region, and TGC technology in the forward region. No higher-level selection has been applied on the top of the `L1_MU6` during the data taking period, which is to say that muon triggering in the sample is driven exclusively by the RPC and TGC chambers. Since the trigger system extends out only to $|\eta| = 2.4$, this is a natural boundary for the analysis in pseudorapidity.

For an early high-p_{T} muon measurement, it is desirable to balance between conflicting desiderata: on the one hand, the relative paucity of data impel one to use a relatively loose muon definition, to increase the usable sample. However, in the first data one is naturally presented with the need to deal with imperfect calibration and alignment, algorithmic tracking settings that are not tuned on data, and challenges involving the full understanding and mapping of detector material and magnetic fields. In this analysis, we focus on *combined* muons, as discussed in Section 5.6.5. The algorithm chosen is `STACO`, since the software setup used for the analysis lacked muon track corrections for $E_{\mathrm{T}}^{\mathrm{miss}}$ for `MuID`, rendering the decision between these two splendid algorithm suites trivial. Additional muon quality criteria chosen to reject fake muons from matching are described in Section 7.3.

In order to reject muons from hadron decays, we utilize a track-based isolation requirement. Muons from W and Z bosons are expected to be very isolated from other tracks in the event, in contrast to the background which is typically associated with collimated jets of particles. For these analyses we require that the muon track be isolated from other tracks in the inner detector. This proceeds by taking the sum of the track p_{T} in a cone in ΔR around the muon candidate, and making a 'relative isolation' quantity:

$$\text{isolation}_{\mu} = \frac{\Sigma \text{track}_{\mathrm{p_T}}}{\mu_{\mathrm{p_T}}} \tag{7.1}$$

This study uses a cone of size 0.4, and requires this variable to be less than 0.2.

7.2.2 Missing Energy Reconstruction

The transverse missing energy in ATLAS is primarily reconstructed from energy deposits in the calorimeter and reconstructed muon tracks. The E_T^{miss} reconstruction used in the $W \rightarrow \mu\nu$ analysis presented here is based on the following vectorial sum:

$$\vec{E}_T^{miss} = \vec{E}_{T,\ LocHadTopo}^{miss} + \vec{E}_{T,\ muon}^{miss} - \vec{E}_{T,\ energy\ loss}^{miss} \tag{7.2}$$

where $E_{T,\ topo}^{miss}$ (`MET_LocHadTopo`) is the missing transverse energy calculated from topological cluster cells calibrated locally to electromagnetic and hadronic scale depending on the energy deposit classification. The term $E_{T,\ muon}^{miss}$ (`MET_MuonBoy`) is given by the sum of two components: the sum of muon momenta from all isolated combined muons (and muons from gaps in the spectrometer acceptance) and the sum of all non-isolated muons reconstructed as tracks in the muon spectrometer. In this case an isolated muon is defined as one for which the ΔR to the nearest jet is at least 0.3, for jets found by the anti-k_T algorithm with a cone of 0.4. The third term (`MET_RefMuon_Track`, available early on only for `STACO`) is the sum of calorimeter cell energy crossed by isolated muons. This term is subtracted from the sum of the first two to avoid double-counting the energy loss already taken into account by the combined muon momentum and the calorimeter component.

7.2.3 Pileup Event Reweighting

Increasing instantaneous luminosity at the LHC leads to multiple proton-proton interactions occurring in the same bunch crossing, referred to as pileup. Additional interactions can influence the efficiency of event selection through the effect of additional tracks on lepton isolation and $E_{\mathrm{T}}^{\mathrm{miss}}$. To model the effects of additional interactions on our acceptance times efficiency for signal and backgrounds, we use MC samples in which simulated minimum bias interactions have been overlaid on top of the hard-scattering event. We correct the distribution of number of vertices in the simulation by reweighting it to match data. The events are required to pass the W preselection and the zero vertex bin is excluded.

The number of vertices per event is compared between data and the Monte Carlo simulation in Figure 7.2. The average number of vertices per event is significantly higher in simulation (~ 2.6) than in data (~ 1.6). Therefore, we reweight events in the pileup Monte Carlo. For an event with N vertices, we take as the event weight the ratio of the fraction of events with N vertices in data to the fraction with N vertices in simulation. We count vertices with $|z| < 150$ mm and at least three tracks, corresponding to the requirements used to select W events.

The event weights used to correct the simulated data samples, as well as the input fraction of events with each vertex multiplicity, are given in Table 7.2. The unreweighted W acceptance measured in the $W \rightarrow \mu\nu$ sample with pileup is 0.3925, while instead the reweighted acceptance is 0.3922, suggesting the negligible impact of reweighting upon the acceptance[1].

---

[1] This value for the acceptance does not match the number quoted later in this note for W analysis

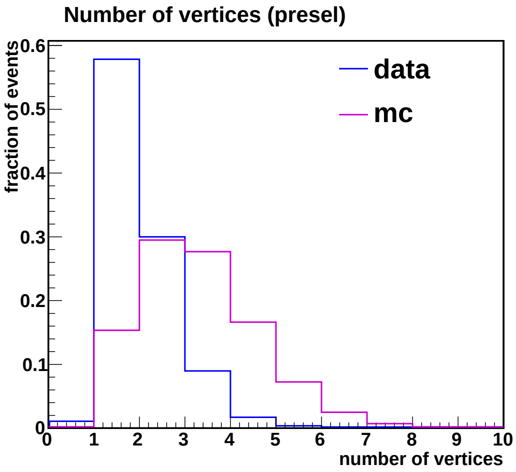

Figure 7.2: Comparison of number of reconstructed vertices in data and simulation (right).

Number of Vertices	Fraction of events in data	in simulation	Event weight
0	-	-	1
1	0.5848	0.1538	3.803
2	0.3032	0.2956	1.026
3	0.0907	0.2773	0.327
4	0.0173	0.1666	0.104
5	0.0037	0.0726	0.051
6	0.0002	0.0250	0.008
7	0.0001	0.0071	0.007
8	0.	0.0017	0.
9	0.	0.0003	0.

Table 7.2: Fraction of events with N vertexes in simulation ($W \to \mu\nu$ pileup Monte Carlo) and data. Last column reports the weights that have been used to correct Monte Carlo in this analysis.

7.3 Muon Selection and Fakes

As discussed in Section 5.6, muon tracks in ATLAS can be formed by combining measurements in the ID and the MS. These provide the best momentum measurement over the range of interest in $W \to \mu\nu$ physics, and the requirement of matching tracks in the ID and MS reduces fake rates, while maintaining high efficiency in the excellent ATLAS tracking and muon systems.

In the formation of these combined tracks, muon candidate tracks in the ID and MS are *matched*, and their parameters statistically averaged, as detailed in Section 5.6.2. This ID/MS matching merits investigation in data for several reasons:

- Alignment issues: the detector alignment and its Monte Carlo description differ, since the position is not known precisely for all detector elements. To make this more vivid, for the case of the MS at the start of collisions data taking, the forward (CSC) region, the barrel-endcap transition, and the small/large sector overlaps of the barrel were not yet at nominal alignment, as were special chambers such as the BIS78s and BEEs. The ID-MS relative alignment had been performed only using the relatively small sample of cosmic tracks going through both. This method had the extra limitation of having been exercised on tracks whose pointing is not typical of muons from collision. Such alignment issues complicate the problem of track matching between MS and ID since the reconstructed trajectory of tracks need not correspond to the true location.

- Fake missing E_{T}: a $W \to \mu\nu$ event selection involves a high-p_{T} muon and missing energy from the neutrino. If ID and MS measurements for the muon

---

because the trigger efficiency and reconstruction correction factors are not included.

disagree sharply, the combined track momentum, which combines them, is likely to be mismeasured as well. This is especially important since the bulk of the missing energy measurement in $W \to \mu\nu$ events comes from the muon track.

- Algorithmic muon fakes: the muon reconstruction algorithm used in the analysis, `STACO`, was in commissioning mode in 2010, imposing very loose matching between inner detector and spectrometer tracks. In such a configuration, algorithmic backgrounds to high-p_{T} muon samples are possible. By this we mean high-p_{T} muons that are in reality artifacts of the reconstruction software. Spurious matches between unrelated candidates in different detector subsystems are clearly a source of fakes. By contrast, `MuID` had tighter reconstruction settings, and in addition uses a combined track refit, and is therefore expected to have fewer bad matches.

Examining the 310 nb^{-1} data using a baseline muon preselection of combined muons with $p_{\mathrm{T}} > 15$ GeV, we observe that for the case of `STACO` tracks without a full track refit, loose matching does in fact yield several muons that have large momentum differences (> 10 GeV) between measurements in the ID and in the MS. Some sample event displays are shown in Figures 7.3, 7.4 and 7.5, where we see that the `STACO` track has “kinks”, suggesting discrepancy between the ID and MS tracks.

Monte Carlo studies indicate that the low momentum MS tracks come from π/K decays-in-flight. These muons are characterized (Figure 7.6) by atypically low Muon Spectrometer momenta (expressed at the primary vertex) below 10 GeV, and a low number (often zero) of TRT hits.

After applying the full muon selection and isolation requirements of the W-

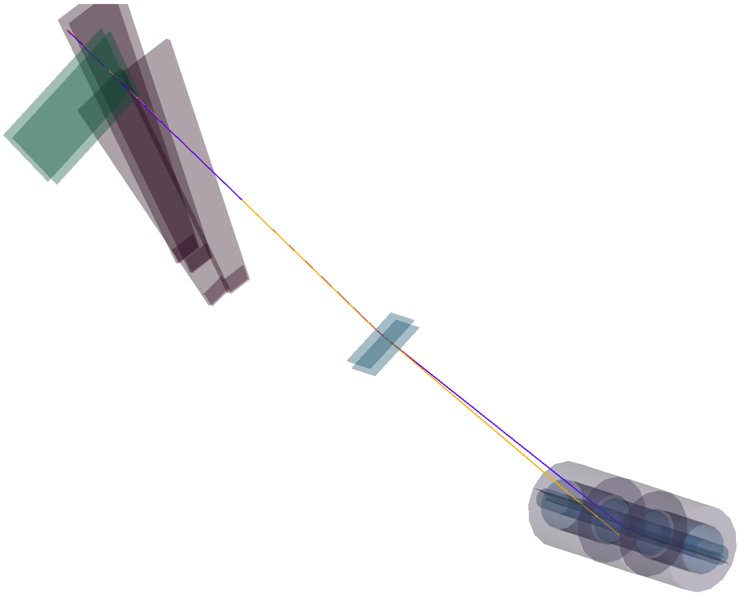

Figure 7.3: Display for Run `152878`, Event `2256547`, showing a `STACO` combined track. Observe the kink, indicative of an incorrect match. `MuID` does not form a combined track for this muon, but the muon spectrometer tracks for the two algorithms are in agreement.

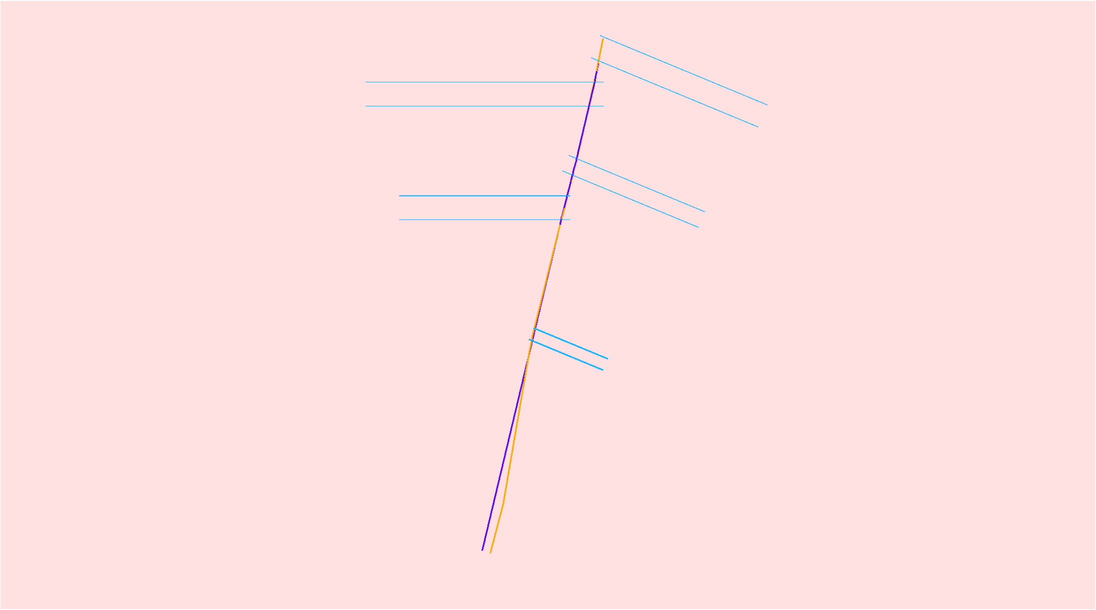

Figure 7.4: Display for Run `152933`, Event `1637230`, showing a `STACO` combined track.

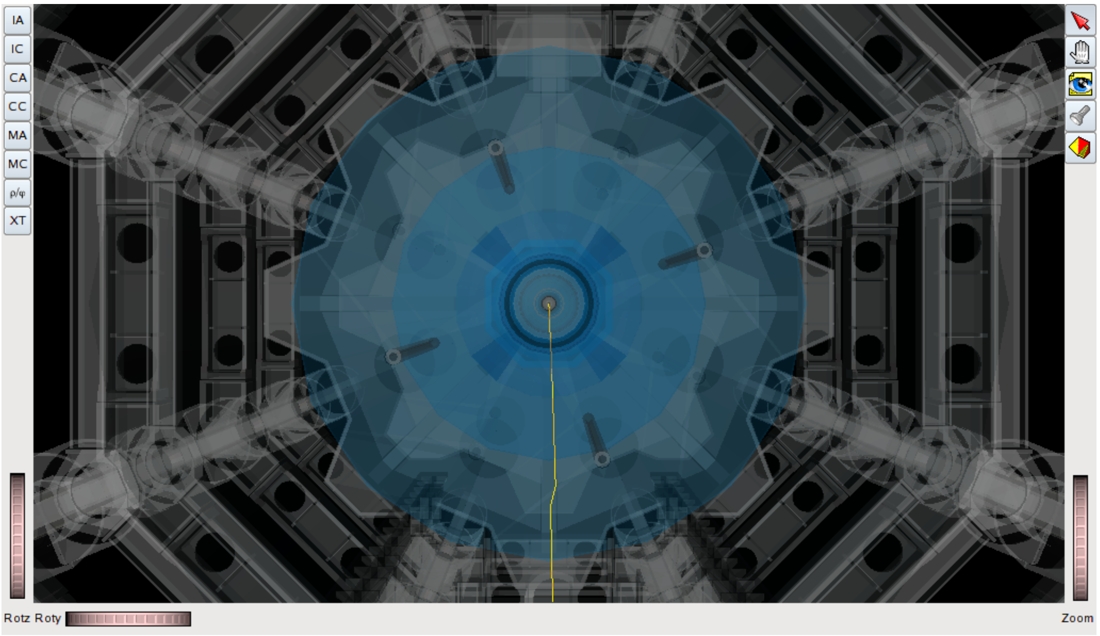

Figure 7.5: Display for Run `153565`, Event `22180828`, showing a `STACO` combined track. Notice the kink, indicative of an incorrect match.

analysis, we can see in Figures 7.6(a)-7.6(c) that tracks with large p_{T} difference, low MS track-p_{T}, or missing TRT hits all have high match-χ^2; the aforementioned infelicities correspond to the same set of tracks. This is a set of fake tracks we would like to remove from our sample. Regarding regional dependence, the labels in Figure 7.6(a)-7.6(c) indicate the region of the detector where the track is found, and we note several problematic tracks in the forward, and transition regions, but, intriguingly, in the MS barrel as well. We show in Figure 7.7 the number of muons (for `STACO`) in the barrel, transition, endcap and forward regions, noting that for a W Monte Carlo sample, we expect the percentage of muons falling into these regions to be 44%, 3%, 34% and 19% respectively. We do note however that problematic muons are seen throughout the detector.

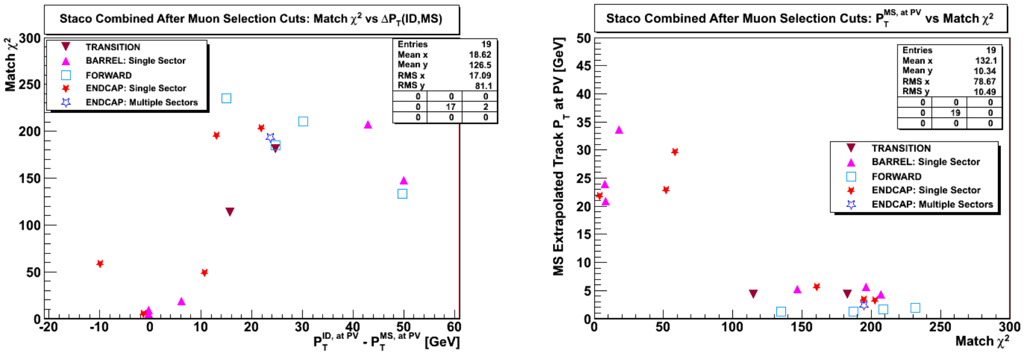

(a) Match χ^2 versus $\Delta p_{\rm T}$ between ID and MS tracks

(b) MS track $p_{\rm T}$ versus Match χ^2

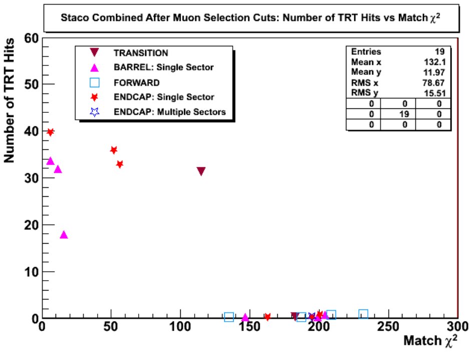

(c) Number of TRT track hits versus Match χ^2

Figure 7.6: Features of fake muons: 7.6(a) Large $\Delta p_{\rm T}$ between ID and MS tracks. 7.6(b) Very low MS standalone track $p_{\rm T}$. 7.6(c) ID track does not have TRT hits. A combined muon with $p_{\rm T} > 10$ GeV is required for each event.

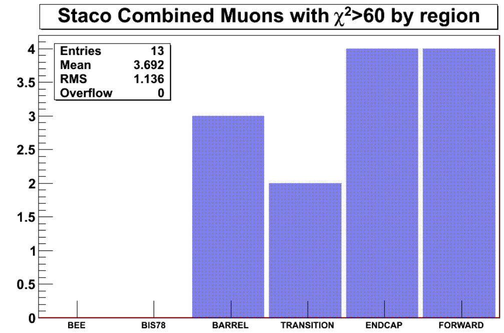

Figure 7.7: Number of poorly-matched `STACO` muons passing event selection requirements for the different detector regions. For comparison, in the W Monte Carlo, 44% of muons pass through the barrel (including BIS78), 34% through the endcap (including BEE), 19% through the forward region and 3% through the transition

7.3.1 Elimination of Poor ID-MS Matches

A multitude of methods of eliminating such muons suggest themselves to us, based upon the previous plots. A requirement on the match-χ^2 itself is certainly a possibility, given the strong correlation between poor matching and the track inadequacies seen. Such a requirement focuses directly on a basic property of the track reconstruction, and is as such easy to conceptualize and motivate. We do find, however, that in data this requirement needs to be quite hard (50-60, with five degrees of freedom), though such a cut is highly efficient in the Monte Carlo (Figure 7.8) This hard requirement risks losing good signal in the early detector environment, with known need for augmentation in alignment and calibration. Another possibility is the requirement of TRT hits on track, which clearly seem to be missing in the ill-matched muons. Indeed, it is the case for every muon in the TRT acceptance without TRT hits that it has poor matching. Such a requirement is well-motivated, though it cannot be applied in the forward region. The per-muon efficiency of a TRT hit requirement is 87.1% in Monte Carlo, where of the remaining 12.9%, 6.7% are in the forward region. (Figure 7.9).

One ideal requirement we identify however as meriting adoption to filter out such muons is on the MS standalone track momentum, which as we have shown is anomalously low. Such a requirement is well-motivated for a high-p_{T} analysis. The expectation that a muon passing a typical 20 GeV requirement (as done in our analysis) fails a 10 GeV requirement in the standalone measurement is negligible, 0.05% in the W Monte Carlo sample (Figure 7.10). An MS p_{T} requirement also serves to reduce a known source of muons with kinks, decays-in-flight, which are not of interest to us in

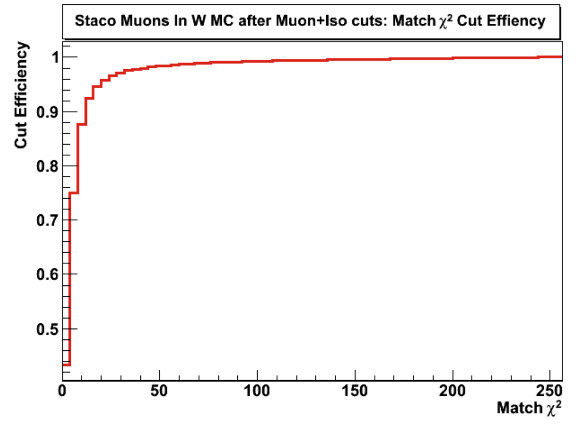

Figure 7.8: Efficiency of a match-χ^2 requirement as a function of the cut, for `STACO` combined muons in W Monte Carlo. A cut at 60 is 98.6% efficient.

high-p_{T} analysis. Of course, alternate solutions must be found for analyses interested in low-p_{T} muons. In Table 7.3, using a subset of runs from our total data sample, we compare the number of events before and after the muon MS track $p_{\mathrm{T}} > 10$ GeV cut, for loosely matched combined muons, and those with a full track refit. We observe much closer agreement between muons with loose matching (`STACO`) and with combined refit (`MuID`) after the application of this requirement.

We examine analogous requirements on the muon definition by examining distributions of muon track-related quantities in the 15 GeV preselection sample after imposition of the MS track-p_{T} requirement. In Figure 7.11(a), we show the muon Δp_{T} distribution for muons with at least 15 GeV p_{T}, and at least 10 GeV p_{T} in the spectrometer, superimposed upon the corresponding distribution for a muon Monte Carlo sample. In general there is excellent agreement, except for a few events in the tail unreproduced by the Monte Carlo. We also observe larger tails in the distribution of muon match-χ^2 in Figure 7.11(b).

Nevertheless, as already suggested, large Δp_{T} unreproduced in Monte Carlo can

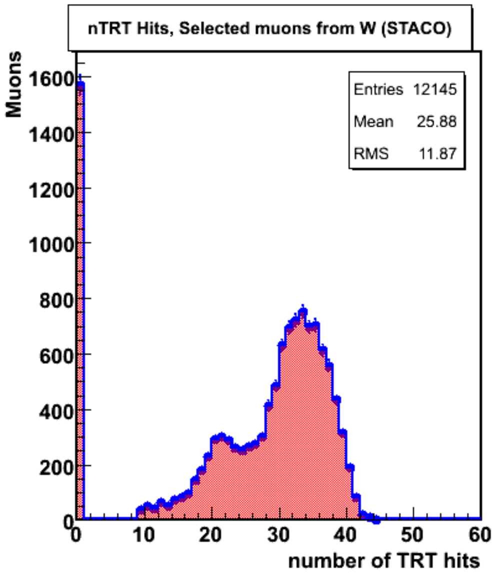

Figure 7.9: Number of TRT hits on a muon track for W Monte Carlo. A requirement that the muon possess TRT hits is 87.1% efficient for the signal, with an additional 6.7% being accounted for by virtue of their forward η

lead to contamination of the signal region via fake missing energy, so we attempt to reduce this contribution. We reiterate this point with Figure 7.12(a). To remove such muons, we select a requirement on the ID-MS Δp_{T} of < 15 GeV, as rejecting the tails while in Monte Carlo preserving almost 100% of the signal. We note that a full solution to the situation of imperfect tracking cannot generically rely solely on such kinematic requirements, and that requirements on tracking quantities like numbers of hits, outliers and holes in different detector technologies together with improvements in tracking are a superior medium-term solution. We show distributions of MDT holes (Figure 7.13(a)) and TRT hits (Figure 7.13(b)) on track as examples. Finally, we note that for our tracking outliers, there is a concentration in the bottom-half of the detector C-side ($z < 0$), compatible with the use of non-optimal alignment constants in this region for the Inner Detector in early data.

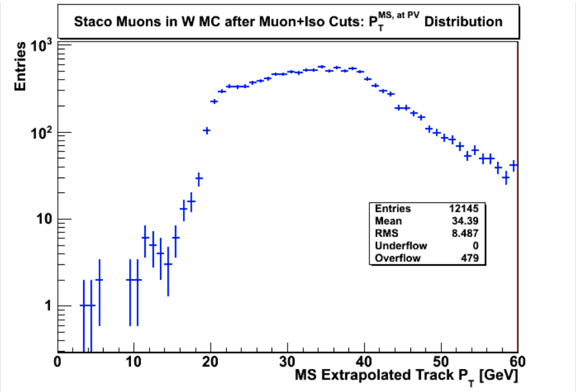

Figure 7.10: Muon spectrometer momentum (expressed at the primary vertex) for `STACO` combined muons, with combined track p_{T} above 20 GeV. Only 0.05% of W muons in Monte Carlo fail this requirement.

Cut #	Cut	Events (`STACO`)	Events (`MuID`)
1	Collision bunch crossing, GRL, ≥ 3 track vertex, muon $p_{\mathrm{T}} > 10$ GeV	391	304
2	Cut #1+ muon $p_{\mathrm{T}}^{MS} > 10$ GeV	228	227

Table 7.3: Fake removal: We compare the number of events with loose matching (`STACO`) and refitting (`MuID`) with basic muon collision event selection (Cut #1) and after an additional fake removal cut (Cut #2) .

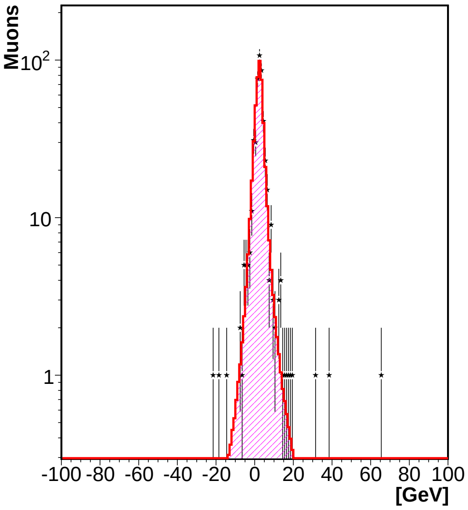

(a) Δp_{T} between ID and MS

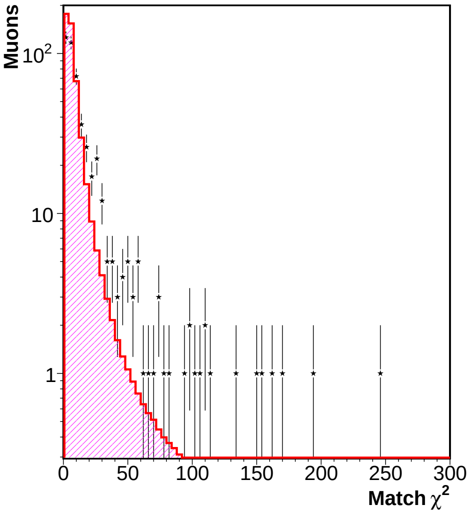

(b) Match χ^2 for preselected muons

Figure 7.11: Combined muons satisfying a 15 GeV p_{T} requirement with at least 10 GeV in the spectrometer, compared between data (black points) and a ($W \to \mu\nu$) muon Monte Carlo sample (red, shaded) normalized to the data. We observe excellent agreement in the bulk of the Δp_{T} distribution together with a handful of events in the tail. Observe also the larger tails in the match-χ^2 distribution in data.

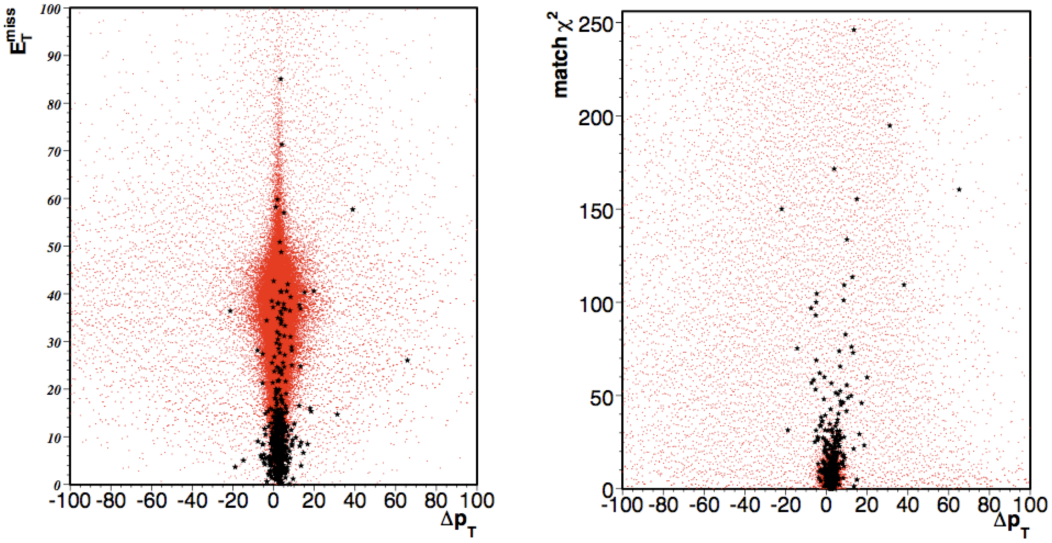

(a) $E_{\mathrm{T}}^{\mathrm{miss}}$ versus Δp_{T} between ID and MS

(b) Match χ^2 versus Δp_{T}

Figure 7.12: Combined muons satisfying a 15 GeV p_{T} requirement with at least 10 GeV in the spectrometer, compared between data (black stars) and a ($W \to \mu\nu$) muon Monte Carlo sample (red points). Observe that the tracking tails in Δp_{T} can lead to extra missing energy in the event, and also the imperfect correlation between high ID-MS momentum difference and high match-χ^2.

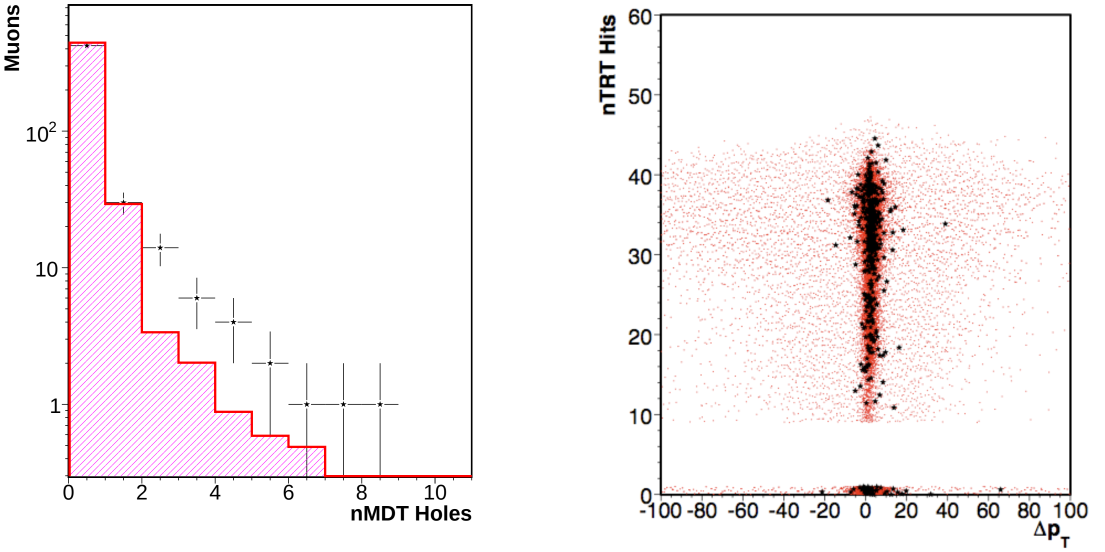

(a) Number of MDT holes on track

(b) Number of TRT hits-on-track versus Δp_{T}

Figure 7.13: Tracking quantities of interest in rejecting poor tracks, MDT holes on the left, and TRT hits on the right. The plots are for combined muons satisfying a 15 GeV p_{T} requirement and with at least 10 GeV in the spectrometer.

7.4 Event Selection

Collision event selection	
Primary vertex	$\mathrm{N}_{vtx} \geq 1$ with $N_{tracks} \geq 3$
	$\lvert z_{vtx} \rvert < 150$ mm
Jet cleaning	cleaning cuts
Trigger	$L1\_MU6$
High-p_T event selection	
Muon selection	combined tracks
	$p_{\mathrm{T}} > 15$ GeV, $\lvert \eta \rvert < 2.4$
Muon quality	$p_{\mathrm{T}}^{MS} > 10$ GeV
	$\lvert p_{\mathrm{T}}^{MS} - p_{\mathrm{T}}^{ID} \rvert < 15$ GeV
	$\lvert z_0 - z_{vtx} \rvert < 10$ mm
$W \to \mu\nu$ event selection	
Tight kinematics	$p_{\mathrm{T}} > 20$ GeV, $\lvert \eta \rvert < 2.4$
ID isolation	$\sum p_{\mathrm{T}}^{ID}/p_{\mathrm{T}} < 0.2$
Missing transverse energy	$E_{\mathrm{T}}^{\mathrm{miss}} > 25$ GeV
Transverse Mass	$m_{\mathrm{T}} > 40$ GeV

Table 7.4: Event selection applied searching for candidates [65].

Starting from the data described in Section 7.1, we select events with the features typical of $W \to \mu\nu$ events. Cuts applied are reported in Table 7.4. The first stage selects events which are the product of proton-proton collisions. Events are required to have at least one reconstructed vertex with at least three ID tracks. The vertex position along the beam axis must be within 15 cm of the nominal position, to account for beam-spot effects and reduce cosmic ray background. In order to reduce spurious missing transverse energy from jets generated by detector effects (coherent noise in the ECAL, spikes observed in the hadronic endcap calorimeter), cosmic ray showers and beam backgrounds, we check for jets in the event with the characteristics typical of these unphysical jets.[2] Events not passing this selection are discarded. The L1_MU6

---

[2] In this early analysis, these so-called jet cleaning requirements are of limited significance. This

trigger is then required leading to 5,132,898 selected events.

A preselection for high-p_{T} events is then applied. We require events to have at least one muon reconstructed as a combined track in the ID and MS, with transverse momentum greater than 15 GeV and $|\eta| < 2.4$, as discussed in Section 7.2.1. Then, the criteria detailed in Section 7.3 are applied: p_{T} measured in the muon spectrometer extrapolated to the primary vertex is required to be greater than 10 GeV, and we require $|p_{\mathrm{T}}^{MS} - p_{\mathrm{T}}^{ID}| < 15$ GeV, where p_{T}^{MS} is corrected for the mean energy loss in upstream material. The number of selected high-p_{T} events for the W analysis after applying this preselection is 20,712.

We show the properties of this preselection sample. The backgrounds are discussed in detail in Section 7.5, and include QCD, $t\bar{t}$, $W \to \tau\nu$, $Z \to \tau\tau$ and $Z \to \mu\mu$. Figure 7.14 shows the angular distributions of the muons in the detector. Figure 7.15 shows the p_{T} for these muons. The QCD background dominates the preselected sample. It is modeled using the muon-filtered `Pythia` jet samples, with the cross sections scaled down by multiplying by a factor of 0.611 (see Section 7.5.2). In these plots, and for the rest of the distributions in the section, signal and background shapes are normalized so that they integrate to the number of events in data.

The W candidate selection is applied on this sample. Figure 7.16 and 7.17 show the distributions of track isolation and $E_{\mathrm{T}}^{\mathrm{miss}}$ for events passing the preselection. The selections place a tighter kinematic requirement on the muon: $p_{\mathrm{T}} > 20$ GeV. Combined muon tracks are also required to be isolated in the ID to reject background from QCD events, as described in Section 7.2.1. Specifically, the track-based relative

---

does not remain the case in analysis with the full dataset, reported in Chapter 8. Additional details about jet cleaning are presented there.

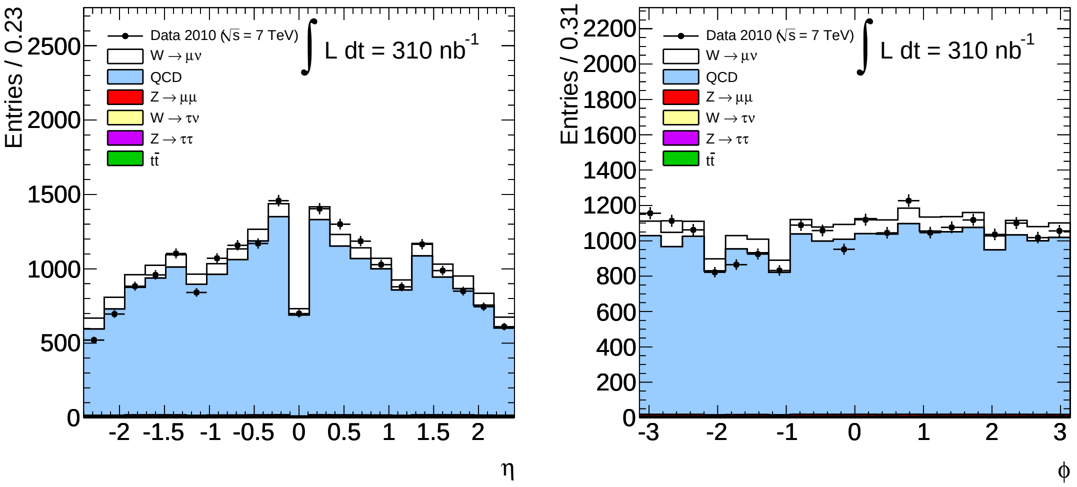

Figure 7.14: Pseudorapidity (left) and azimuth (right) of the highest-$p_{\rm T}$ muon in events passing the preselection [65].

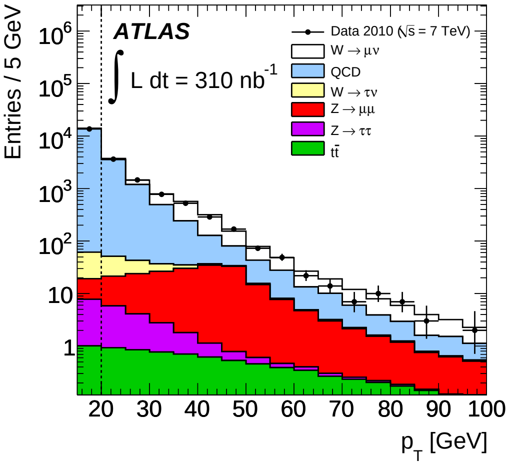

Figure 7.15: Transverse momentum of the hardest muon in events passing the preselection [65].

isolation of muons in a ΔR cone of size 0.4 is required to be less than 0.2. Then $E_{\mathrm{T}}^{\mathrm{miss}}$ is required to be greater than 25 GeV and final W candidates are counted in the region above transverse mass of 40 GeV. A total of 1,181 candidate events are found. Distributions for candidate events are presented in Section 7.10.1

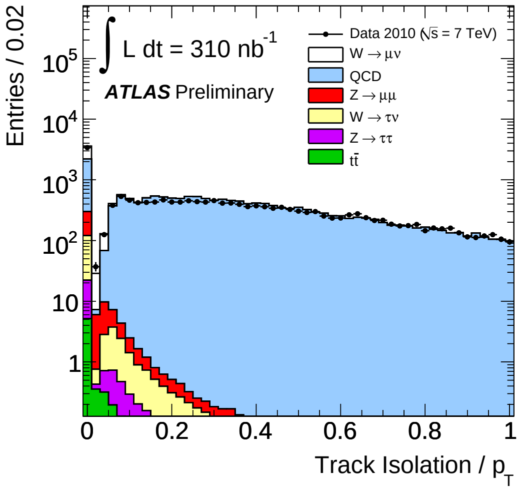

Figure 7.16: Track isolation in preselected events [65].

7.5 Background Estimation

Collision backgrounds to $W \to \mu\nu$ events can be broadly grouped into two categories[3]:

- QCD multijet events: these produce muons through the decay of a hadron containing a heavy quark (b or c), through the decay in flight of a π or K meson, or through the reconstruction of one or more hadrons as a muon.

---

[3] In addition, the 33 pb^{-1} analysis presented in Chapter 8 considers diboson backgrounds like WW, WZ and ZZ. These are processes with $\sigma \times \mathrm{BR}$ in the few tens of pb^{-1}, and are of limited interest with only 310 nb^{-1} of data.

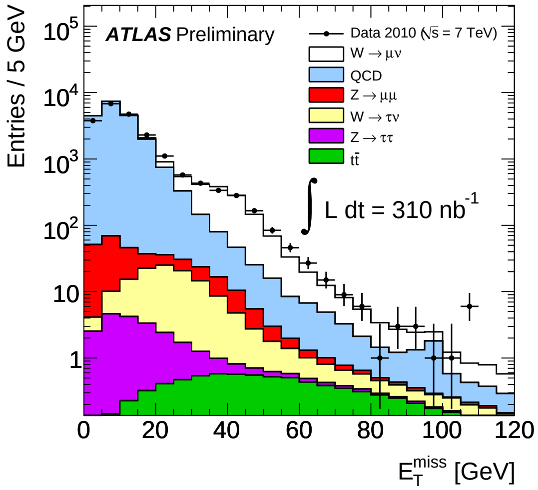

Figure 7.17: Missing transverse energy in events passing the preselection [65].

- W, Z and top: these process give real isolated muons in the final state. The Z in dimuon decays is a background when a muon is lost outside the muon acceptance. The category also includes cases where the muon is the product of the decay of a τ. We also include $t\bar{t}$ events, where the top quark is heavy enough to decay to a real W.

In addition, cosmic rays produce high-p_{T} muons which can pass the W event selection when they coincide in time with a filled bunch crossing and the muon track passes near the beam-spot. In the early dataset it is important to understand any potential cosmic-ray background. The dataset is acquired over a period of several months, with low luminosity and inclusive open-road triggers, increasing the chances of cosmic rays overlapping with a collision vertex. In addition, because of calibration issues, the inner detector during this early period frequently loses the second leg of cosmic rays in the bottom half of the detector, creating spurious missing energy.

Hence, this analysis includes a cosmic ray background estimate.

7.5.1 Electroweak Backgrounds

Some background events produce high-p_{T} muons because of the presence of a real W or Z boson. We consider as backgrounds $W \to \tau\nu$, $Z \to \mu\mu$, $Z \to \tau\tau$, and $t\bar{t}$. In the case of $W \to \tau\nu$ and $Z \to \tau\tau$, the muon is produced in the decay of a τ lepton. These backgrounds are estimated from Monte Carlo samples, based on the acceptance for each process, scaled by the cross section, and normalized to the integrated luminosity. The cross section estimates used have uncertainties of 5% for $Z \to \mu\mu$, $W \to \tau\nu$ and $Z \to \tau\tau$, and 6% for $t\bar{t}$, as discussed in Section 7.1. The predictions are also scaled using efficiency corrections as described in Section 7.6. The acceptances and predicted numbers of events for the various backgrounds are shown in Table 7.5. Systematic uncertainties on these background predictions are the same as those on the W acceptance, including the uncertainties on the muon and $E_{\mathrm{T}}^{\mathrm{miss}}$ scale and resolution, and on the trigger and reconstruction efficiencies for muons. In addition, we assign a 3% systematic uncertainty on the PDF dependence of the acceptance, based on the studies of the $W \to \mu\nu$ sample, and include the uncertainties on the theoretical cross sections used to normalize the background predictions. The systematic uncertainties total to 7.8% for $t\bar{t}$ and 6.4% for the W/Z backgrounds. We treat these uncertainties as 100% correlated among all the electroweak backgrounds, except for the $t\bar{t}$ cross section uncertainty, which is treated as uncorrelated with the other theoretical uncertainties. The total predicted background from electroweak-type events, including the systematic uncertainty, is 77.6 ± 0.3 (sta) ± 3.1 (sys) $\pm$

8.5 (lum) events.

Sample	Acceptance	Predicted Events
$Z \to \mu\mu$	12.52%	38.4 ± 0.19 (sta) $\pm$ 2.7 (sys) $\pm$ 4.2 (lum)
$W \to \tau\nu$	3.36%	33.6 ± 0.18 (sta) $\pm$ 2.4 (sys) $\pm$ 3.7 (lum)
$t\bar{t}$	15.84%	4.2 ± 0.02 (sta) $\pm$ 0.3 (sys) $\pm$ 0.5 (lum)
$Z \to \tau\tau$	0.45%	1.4 ± 0.01 (sta) $\pm$ 0.1 (sys) $\pm$ 0.2 (lum)
Total	-	77.6 ± 0.3 (sta) $\pm$ 5.4 (sys) $\pm$ 8.5 (lum)

Table 7.5: Acceptance and background prediction in 310 nb^{-1} analysis from electroweak processes [65].

7.5.2 QCD Background

The QCD background, in contrast to the electroweak background, is harder to estimate. One way of treating the kinematics of the continuum QCD background to muons is to use dijet Monte Carlo samples. We have access to `Pythia` samples generated for different p_{T} ranges for the outgoing partons, filtered to require a muon with $p_{\mathrm{T}} > 8$ GeV. Applying the $W \to \mu\nu$ selection to these samples, and applying scale corrections, we predict 15.9 ± 0.6 (sta) events from MC. A purely Monte Carlo-based expectation is problematic however, for a number of reasons. For example, the overall jet cross section has a large theoretical uncertainty, detector effects causing fake muons may not be well-modeled, the efficiencies for isolation or missing energy are not correctly modeled. Hence, input from data is valuable. A variety of techniques have been used to estimate the QCD contamination in the selected event sample, including a “matrix” method, an “ABCD” method, template fits in different variables, and extrapolation in muon momentum [65]. A description of some of these is given below. Some common principles in QCD background estimation are that QCD events tend to be less isolated than the signal since muons from heavy flavor quark decay lie in jets, and that they have lower $E_{\mathrm{T}}^{\mathrm{miss}}$ because a good fraction of it comes from mismeasurements.

Analytic Estimation, Using Matrix Method

The QCD background for this analysis is estimated using a "matrix" method. The method is also used for the analysis with the full 33 pb^{-1} dataset, presented in Chapter 8. The method there is more sophisticated, and is described in greater detail. Here, a summary is given; the interested reader is directed to [19, 65] for additional information. The basic idea is that QCD events tend to be less isolated than the signal and electroweak background. Hence, if we take a loose muon sample in data, and know the isolation efficiencies for QCD and prompt muons, we can solve a two-variable system of linear equations to estimate the QCD component.

Specifically, we define a loose muon sample with N_{loose} events, by removing the isolation requirement from the selection with N_{isol} events. The loose sample has 1272 events, while the isolated/tight sample has the 1181 candidate events. If we let $\epsilon_{\mathrm{nonQCD}}$ and ϵ_{QCD} denote the relative isolation efficiencies for non-QCD background (that is, from signal and from electroweak sources) and for the QCD background, then we have:

$$\begin{aligned} N_{\mathrm{loose}} &= N_{\mathrm{nonQCD}} + N_{\mathrm{QCD}} \\ N_{\mathrm{isol}} &= \epsilon_{\mathrm{nonQCD}} N_{\mathrm{nonQCD}} + \epsilon_{\mathrm{QCD}} N_{\mathrm{QCD}} \end{aligned} \tag{7.3}$$

From these two equations in terms of N_{nonQCD} and N_{QCD} we obtain:

$$N_{\text{QCD}} = \frac{N_{\text{loose}}\epsilon_{\text{nonQCD}} - N_{\text{isol}}}{\epsilon_{\text{nonQCD}} - \epsilon_{\text{QCD}}} \tag{7.4}$$

This is the number of QCD events before the isolation (tight) requirement. After that cut, the expected number of QCD events is $\epsilon_{\text{QCD}}N_{\text{QCD}}$, which is the final expected QCD background after the full selection. An advantage of the method is that it does not heavily rely on the agreement of distribution *shapes* between data and simulation samples.

The isolation efficiencies are obtained from data. For ϵ_{QCD}, the value is estimated from preselected muons between 15 and 20 GeV, which are expected to be predominantly from QCD processes. In Figure 7.18(b), we can see the flat QCD-dominated isolation efficiency in this momentum range. However, the muon isolation efficiency is different in the control and signal regions in muon momentum, as is seen in the Monte Carlo (Figure 7.18(a)). To correct for the drop in QCD isolation efficiency with p_{T}, we scale the isolation efficiency seen for $15-20$ GeV data using the ratio of isolation efficiencies in Monte Carlo above and below the 20 GeV cut, $(77.6 \pm 1.7)\%$. This scaled efficiency is $\epsilon_{\text{QCD}} = (22.64 \pm 00.57)\%$. We take the full range of this extrapolation as systematic uncertainty on the method.[4] The prompt muon efficiency is taken from $Z \to \mu\mu$ events, and is measured at $\epsilon_{\text{nonQCD}} = (98.4 \pm 1.0)\%$.

The result of the "matrix" based estimate is:

$$\epsilon_{\text{QCD}}N_{\text{QCD}} = 21.1 \pm 4.5 \text{ (sta) } \pm 8.7 \text{ (sys)}$$

---

[4] A more sophisticated treatment, incorporating also isolation variable dependences in $E_{\text{T}}^{\text{miss}}$ and m_{T}, is accomplished in Section 8.7.1.

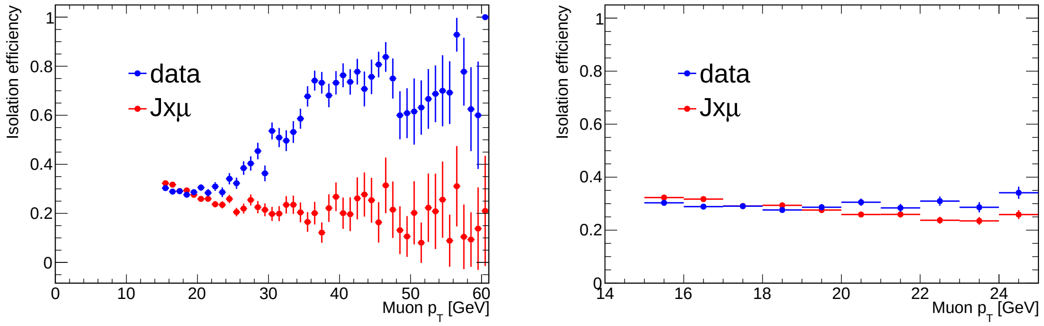

(a) Isolation efficiency

(b) Isolation efficiency 14 – 25 GeV

Figure 7.18: Efficiency of the isolation requirement in data and the QCD sample. On the right, efficiency in the low-p_T region, showing the flat of the spectrum in the 15 – 20 GeV regime. On the left, the fall of the efficiency with p_T in the jet sample. [65]

Estimation Using an Isolation Control Region

One useful check on the kinematics and normalization predicted by simulation is to compare non-isolated muons in simulation to non-isolated muons in data. After the muon selection but before the isolation requirement is applied, the single muon sample is mostly muons from QCD. By reversing the isolation requirement, we obtain a control sample which is orthogonal to our signal sample and dominated by the QCD background. To be explicit, this is the set of events with muons with $p_T > 20$ GeV and $|\eta| < 2.4$ but with relative track-based isolation (in a ΔR cone of size 0.4) greater than 0.2.

In this control sample, we examine distributions of E_T^{miss}, both in data and in the jet background Monte Carlo sample. We present Figure 7.19(a), where the simulated data have been normalized to the observed number of events, and observe that while the shapes agree fairly well, the Monte Carlo over-predicts the number of events in the control region. We also show the normalized cumulative distribution for the $E_{\mathrm{T}}^{\mathrm{miss}}$, (in Figure 7.19(b)), which indicates that the *fraction* of events passing various $E_{\mathrm{T}}^{\mathrm{miss}}$ requirements agrees between data and simulation. As such, we may expect the ratio of muon counts between data and Monte Carlo in the non-isolated window to probe the overall background normalization systematic uncertainty for our jet samples.

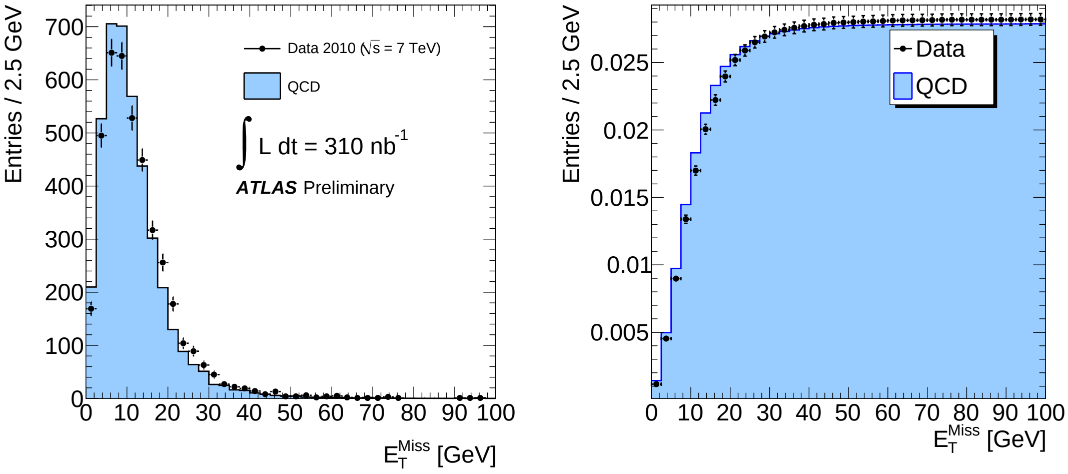

(a) Shape

(b) Normalization

Figure 7.19: $E_{\mathrm{T}}^{\mathrm{miss}}$ after reversing isolation cut, comparing data (black points) to the muon filtered jet samples (blue histogram). On the left, we compare the shapes of the $E_{\mathrm{T}}^{\mathrm{miss}}$ distributions for the two samples, while on the right the fractions of events passing different $E_{\mathrm{T}}^{\mathrm{miss}}$ requirements are shown.[65].

Comparing the number of muons in our control region in data and Monte Carlo, we obtain a scale factor of 0.611 ± 0.012 (sta). It must be noted that the scale factor thus obtained is dominated by the low $E_{\mathrm{T}}^{\mathrm{miss}}$ region and therefore is not strictly appropriate for the high $E_{\mathrm{T}}^{\mathrm{miss}}$ sample. Indeed, the dominant systematic uncertainty on the method is from comparing this overall scale factor for the isolation-reversed sample to its value only in the $E_{\mathrm{T}}^{\mathrm{miss}} > 25$ GeV sample. In addition, we have a systematic term from replacing the relative track-based isolation requirement with the same cut imposed on relative calorimeter-based isolation. Finally, we obtain a systematic uncertainty on the (low $E_{\mathrm{T}}^{\mathrm{miss}}$) shapes of the curves in data and Monte Carlo by taking the absolute difference of the scales to the left and right of the peaks. To be conservative, these systematic effects are treated as independent, and are shown in Table 7.6. The overall scale factor is 0.611 ± 0.012 (sta) ± 0.090 (sys). The QCD background dominates at low momentum, but is reduced significantly in the final selection. Hence, to understand the preselection and other plots with large QCD contamination, this scale factor is used to normalize the Monte Carlo shapes.

Sample	QCD Scale factor	Stat.	High $E_{\mathrm{T}}^{\mathrm{miss}}$ Syst.	Isol. Syst.	Shape Syst.	Total
$\mu\ p_{\mathrm{T}} > 15$ GeV	0.621	0.007	0.181	0.029	0.110	0.213
$\mu\ p_{\mathrm{T}} > 20$ GeV	0.611	0.012	0.213	0.036	0.083	0.231

Table 7.6: QCD scale factor for muons failing isolation requirements, separated by charge [65].

Estimate From Sidebands in $E_{\mathrm{T}}^{\mathrm{miss}}$ and Isolation

Another method for QCD background prediction is to estimate the jet contamination in the W signal region by extrapolating from control regions in $E_{\mathrm{T}}^{\mathrm{miss}}$ - muon isolation space. That is, we extrapolate the number of QCD events in the non-isolated, high $E_{\mathrm{T}}^{\mathrm{miss}}$ region to the signal region, using as scale the ratio of isolated to non-isolated events in the *low* $E_{\mathrm{T}}^{\mathrm{miss}}$ region. The method is of the “ABCD” type, so named for its division of the 2D space into four regions, labeled with the first four letters of the alphabet.

$$N^{\text{isolated}}_{\text{High}E_{\text{T}}^{\text{miss}}} = N^{\text{isolated}}_{\text{Low}E_{\text{T}}^{\text{miss}}} \times \frac{N^{\text{non-isolated}}_{\text{High}E_{\text{T}}^{\text{miss}}}}{N^{\text{non-isolated}}_{\text{Low}E_{\text{T}}^{\text{miss}}}} \tag{7.5}$$

To retain good statistics in the $E_{\text{T}}^{\text{miss}}$ vs isolation 2D plane, it is populated after lifting the requirement on the W transverse mass. The algebra in Equation 7.5 yields a jet background estimate of 159.5 ± 9.6 (sta). However, this estimate can be improved by correcting for electroweak backgrounds, since these also contribute to different regions of the plane. This is done by subtracting them out from each region before using Equation 7.5. For this purpose, Monte Carlo expectations from the $W \to \tau\nu$, $Z \to \mu\mu$, $Z \to \tau\tau$ and $t\bar{t}$ samples are used as described in the preceding section. After performing this subtraction, lower numbers are obtained, 113.9 ± 7.5. Note that these values are all for the QCD background before the imposition of the transverse mass requirement. The numbers are shown in Table 7.7.

Sample	Fail Isol. Fail $E_{\text{T}}^{\text{miss}}$	Fail Isol. Pass $E_{\text{T}}^{\text{miss}}$	Pass Isol. Fail $E_{\text{T}}^{\text{miss}}$	Pass Isol. Pass $E_{\text{T}}^{\text{miss}}$
EW Bkg Total	1.15	1.74	208.07	85.48
$W \to \tau\nu$	0.198	0.43	29.92	38.65
$Z \to \mu\mu$	0.67	0.33	166.33	39.84
$Z \to \tau\tau$	0.11	0.04	10.95	2.51
$t\bar{t}$	0.17	0.94	0.87	4.49
$W \to \mu\nu$	1.14	10.04	236.94	1198.79
Data	3827 ± 62	359 ± 19	1700 ± 41	1234 ± 35
Data After EW Subtraction	3826 ± 62	357 ± 19	1492 ± 41	1149 ± 35
Data After EW Bkg and $W \to \mu\nu$ Subtraction	3825 ± 62	347 ± 19	1255 ± 41	-50 ± 35

Table 7.7: Estimation of QCD background using "ABCD" method [65].

We also test the method in Monte Carlo, on the jet samples and find that the method over-predicts the background contribution, yielding an estimate of 139.6 ± 7.6 events as compared to an actual count of only 48.9 events. This is an overestimate by 65%, so we apply the same factor to the estimate from data as well, yielding a prediction of 39.9 ± 2.6. We also use half of this 65% discrepancy as a systematic uncertainty on the predicted number. As a further probe of the systematic uncertainty on this background, we perform a variation on the background estimate, by excluding some events in a buffer region around the signal region from the data-based estimate. The signal region is still defined by $E_{\mathrm{T}}^{\mathrm{miss}} > 25$ GeV and isolation < 0.2, but the control regions are now defined by $E_{\mathrm{T}}^{\mathrm{miss}} < 20$ GeV and/or isolation > 0.25. Events with 20 GeV $< E_{\mathrm{T}}^{\mathrm{miss}} <$ 25 GeV and $0.2 <$ isolation < 0.25 are excluded from the estimate. The predicted background for $p_{\mathrm{T}}^{\mu} > 20$ GeV after all corrections shifts from 113.9 events to 120.3, a 5.6% shift.

Since the transverse mass requirement is omitted in the calculation up to this point, we add in the efficiency now. The efficiency is the ratio of events in the muon-filtered jet samples passing all of the event selection to the number of events passing all of the event selection up to the transverse mass requirement. Numerically, it is 0.339. Combining the results of the extrapolation from control regions with the efficiency of the transverse mass cut and the systematic uncertainty on the method, we predict 13.5 ± 0.9 (sta) ± 12.7 (sys) background events from continuum QCD, compatible with the "matrix" result.[5]

---

[5] The ABCD method was used to estimate the QCD background for the first public ATLAS $W \to \mu\nu$ observation [21] and cross section [20] results.

7.5.3 Cosmic Ray Background

A cosmic ray muon may mimic a W when the cosmic ray overlaps in time with a collision event. An estimate of this background contamination can be derived in the form of a cross section as:

$$\sigma^{\mathrm{cosmic}} = \sigma_{\mathrm{mb}} \cdot p_{\mathrm{trig}}^{\mathrm{cosmic}} \cdot p_{\mathrm{reco}}^{\mathrm{cosmic}} \tag{7.6}$$

Here, σ_{mb} is the minimum-bias cross section, estimated at 50 mb. $p_{\mathrm{trig}}^{\mathrm{cosmic}}$ is the probability for a cosmic ray muon to pass the open-road `L1_MU0` trigger in time with a collision event. $p_{\mathrm{reco}}^{\mathrm{cosmic}}$ instead is the probability for a cosmic ray to pass the W selection.

The trigger probability can be derived, since the trigger rate of `L1_MU0` in colliding bunches is about 2.96 Hz. This is estimated as a time-weighted average of `L1_MU0` trigger rates (before prescale) over several runs in luminosity blocks without beam. The number of collision-bunches per second is about 90,000. Hence, the probability that a cosmic ray fires the trigger per collision-bunch is equal to $2.96/90,000 = 3.3 \cdot 10^{-5}$.

The probability to reconstruct a cosmic ray as a combined muon passing the W selection used in this analysis has also been derived, using events in unpaired bunches. When all selection criteria except vertex requirements are applied, only 14 events out of 137379 satisfy criteria. In addition, the $|z_0| < 10$ mm muon requirement relative to vertex should be satisfied by only 10/150 of cosmic ray muons, where the vertex location is assumed to be unbiased by the cosmic ray. As such, σ^{cosmic} is estimated to be: $50 \text{ mb} \times 3.3 \cdot 10^{-5} \times 0.34 \cdot 10^{-5} = (5.6 \pm 2.1 \text{ (sta) } \pm 1.4 \text{ (sys)}) \cdot 10^{-9}$ mb

The statistical error derives mainly from the uncertainty on the cosmic acceptance used in the cosmic reconstruction probability. The systematic uncertainty derives mainly from an uncertainty of 20% on minimum bias cross section and an uncertainty on the trigger rate (15% error derived from the RMS variation of the `L1_MU0` rate over several different runs). Using the effective cosmic cross section above, in the 310 nb^{-1} dataset, the cosmic ray background is:

$$N_{\text{cosmic}} = 1.7 \pm 0.7 \text{ (sta) } \pm 0.4 \text{ (sys) events.}$$

Using the measured cosmic ray muon charge ratio [40] $R_{\text{cosmic}} = N^+/N^- = 1.235 \pm 0.004$ (sta) ± 0.025 (sys), we can estimate the number cosmic events of positive charge (N^+_{cosmic}) and negative charge (N^-_{cosmic}). Thus we find:

$$N^+_{cosmic} = \frac{N_{cosmic} \times R_{cosmic}}{1 + R_{cosmic}} = 0.9 \pm 0.4 \text{ (sta) } \pm 0.2 \text{ (sys) events}$$

$$N^-_{cosmic} = \frac{N_{cosmic}}{1 + R_{cosmic}} = 0.8 \pm 0.3 \text{ (sta) } \pm 0.2 \text{ (sys) events.}$$

Timing Search for Cosmic Rays in Candidate Events

As a cross-check on the preceding cosmic ray background estimate, the in-situ timing calibration procedure described in Chapter 6 is used to search for events that satisfy cosmic ray timing criteria. For muons from collision, the fitted t_0 offsets for segments on the muon track are expected to be small. Indeed, they are typically centered at zero with an RMS width of about 6 ns. By contrast, for cosmic muons their average value can have a common offset since a cosmic muon can fall randomly in the 25 ns muon trigger window. Further, for the top half of the detector, the timing correlations between segments in the different layers of the spectrometer (Outer, Middle, Inner), is very different for cosmic muons. This is because of the reversed direction of their flight path (top-bottom direction) with respect to the bottom-top direction of collision muons coming from the collision impact point. Indeed, we expect the Δt_0 between layers to be consistent with twice the flight time of a muon traveling between the stations. In the bottom of the detector, the cosmic ray direction is the same as that for collisions, but we can still look at the absolute offset in each layer to determine if the muon was globally out of time with the collision expectations. To summarize, in the top half of the detector, we expect all three Δt_0 variables to be consistent with twice the time of flight (ToF) between the stations, while in the bottom we expect that all three segments should have roughly the same timing offset and be significantly out of time.

The correlation between Δt_0 offsets in different layers is shown (Figure 7.20) for events in the MS barrel, where the majority of cosmic rays passing the selection are expected to lie. The plot shows offset differences between outer-inner (BO-BI) and outer-middle ((BO-BM) layers. Here, the red points show timing distributions for cosmic rays, taken from standalone tracks in unpaired bunches. Similarly, the blue points show the expectation for muons from collision, taken from combined tracks in events passing good event criteria. The candidates (black) clearly line up very well with collision expectations.

To better understand events in the tails, and flag potential cosmics, we look for top-half muons that have at least two of their Δt_0 values significantly out of time (≥ 10 ns for the two smaller Δs, and ≥ 30 ns for Δt_0 (Outer - Inner)). For bottom-

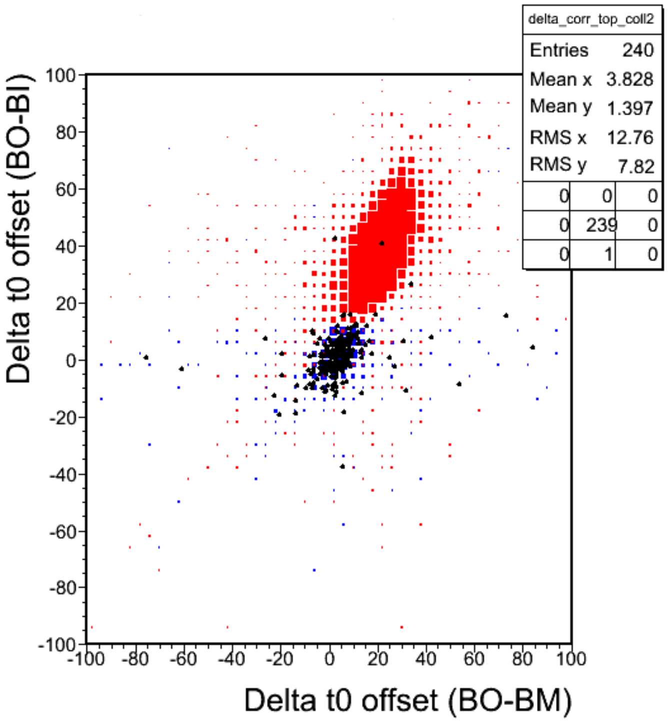

Figure 7.20: Relative timing distributions for $W \to \mu\nu$ candidates (black) compared to expectations for collision (blue) and cosmic-ray muons (red) [65].

half muons, we instead look for those which have at least two of their station t_0 offset values significantly out of time (≥ 30 ns). This is a loose test that allows us to examine muon timing. Of the $1,181$ $W \to \mu\nu$ candidates, only three are found with muons failing the out-of-time flags given above, compatible with the cosmic-ray background estimate given above. Of these, two are in the top half of the detector, and one is in the bottom. Moreover, the timing offsets, while unusual for collision events, also do not satisfy the flight-time criterion for cosmic rays. Thus, the cosmic ray contamination is consistent with the preceding prediction.

7.5.4 Summary of Backgrounds

The total estimated background to $W \to \mu\nu$ in 310 nb^{-1} of data is 100.4 ± 11.2 events (Table 7.8), where the uncertainty quoted includes the statistical and systematic uncertainties, but not the uncertainty on the luminosity for the electroweak background prediction. The systematic uncertainty on the QCD background is 41%. The uncertainty on the electroweak backgrounds is 7.1% for $Z \to \mu\mu$, $W \to \tau\nu$ and $Z \to \tau\tau$, and 7.8% for $t\bar{t}$. That includes the all of the same contributions as in the $W \to \mu\nu$ acceptance, in addition to uncertainties on the theoretical cross section calculations used to normalize the estimates and on the PDF dependence of the acceptance. The largest contributions to the background are from $Z \to \mu\mu$ which is 38% of the background and $W \to \tau\nu$ which is 33%. The QCD background is 21% of the total background, and the estimated cosmic background is 2% of the total.

sample	W	W$^+$	W$^-$
$Z \to \mu\mu$	38.4 ± 2.7	20.0 ± 1.4	18.4 ± 1.3
$W \to \tau\nu$	33.6 ± 2.4	19.7 ± 1.4	13.9 ± 1.0
$t\bar{t}$	4.2 ± 0.3	2.1 ± 0.2	2.1 ± 0.2
$Z \to \tau\tau$	1.4 ± 0.1	0.7 ± 0.1	0.7 ± 0.0
QCD	21.1 ± 9.8	11.1 ± 5.4	10.1 ± 4.8
Cosmic	1.7 ± 0.8	0.9 ± 0.4	0.8 ± 0.4
Total background	100.4 ± 11.2	54.4 ± 6.2	46.0 ± 5.4

Table 7.8: Summary of background expectations including non-luminosity systematic uncertainties, shown for W, W^+ and W^- separately [65].

7.6 Muon Efficiency

We correct trigger and muon reconstruction performance as seen in `GEANT4` based detector simulation to data, to ensure that the acceptance/efficiency used in the cross section calculation corresponds to the true detector performance. With sufficient statistics, an excellent method for this is to use the $Z \rightarrow \mu\mu$ sample, where the clean di-muon Z peak allows for precise, low-background measurements for prompt muons. Specifically, one leg of the Z can be reconstructed fully, with looser criteria imposed on the other. Then, since the Z peak tags the event, the other leg can probe various features of the prompt muon performance. However, with low luminosity, the Z muon sample is statistically limited. Hence, more complicated *single-muon* techniques relying on the much larger muon sample had to be used despite their relative complexity and larger systematic uncertainties. We discuss methods used to obtain trigger and muon reconstruction efficiencies in this section. We shall return to tag-and-probe methods in the context of the 33 pb^{-1} analysis, where the ×100 size of the data sample allows them to shine.[6]

7.6.1 Reconstruction efficiency

We here present measurements of the muon reconstruction efficiency from data, using the so-called "MS hit technique", which tags ID tracks using hits in the MS. This method was first used to measure muon efficiency in cosmic rays [40]. It starts with isolated ID tracks, and makes hit requirements on them to pick out high-quality tracks. It them extrapolates these tracks [91] into the MS, taking into account magnetic field, material distributions and energy loss. In the spectrometer, to pick tracks that are from muons, the method looks for the presence of hits in MDT tubes near the path of the extrapolated track. Multiple hits are sought in at least two layers,

---

[6] Tag-and-probe techniques have been tried for the early 310 nb^{-1} analysis itself, but the statistical limitations do not make them more powerful than the more complex single muon methods.

to reject combinatorial or noise effects. Given a high p_{T}, high-quality, isolated ID track with matching hits in the MS, we expect to be dealing with muons. The muon reconstruction efficiency is therefore the fraction of tagged ID tracks that are also matched to a combined muon track.

A number of systematic effects are considered, including the efficiency for ID tracking, MDT hardware efficiency and cut stability. However, the chief uncertainty comes from estimating the decay-in-flight background. The method as described imposes no rejection for decay-in-flight muons, which tends to lower the measured efficiency. For this, templates of the hit-residual distribution have been formed, using $W \to \mu\nu$ Monte Carlo and single-pion samples. By fitting the observed distribution of hit residuals in data to these templates, the prompt fraction is separately known for combined muons and for ID tags. The fits are shown in Figure 7.21. The measured reconstruction efficiency is

$$99.4\% \pm 0.6\% \text{ (sta) } \pm 2.4\% \text{ (sys)}$$

Because of the closeness of this value to unity (and the similar scale factor results from the Z sample), the quoted errors are used as systematic uncertainties on the muon reconstruction efficiencies, but no scale factor is applied.[7]

7.6.2 Trigger Efficiency

To measure the muon trigger efficiency, the technique adopted is to use an orthogonal trigger. A high-p_{T} jet trigger selects events, and those with a reconstructed muon

---

[7] The same holds for the muon isolation efficiency. Here too the efficiency comes from Monte Carlo, and we assign a 1% systematic uncertainty, based upon comparison to values seen in data.

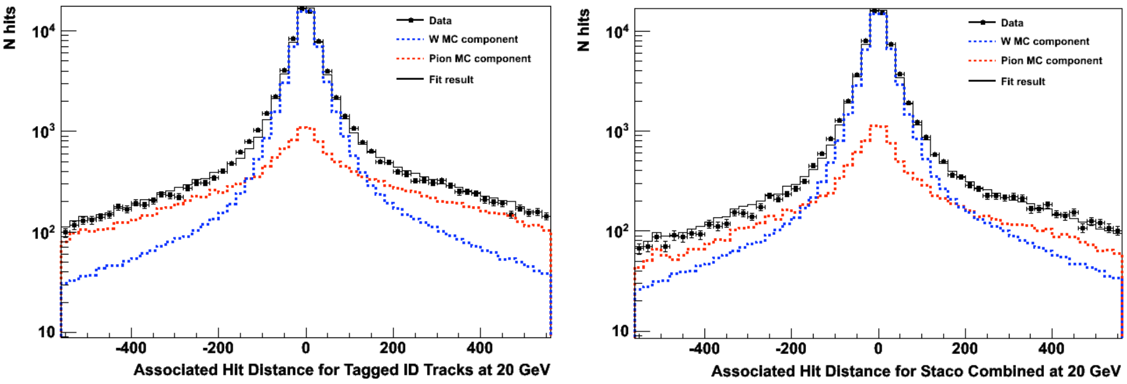

(a) ID tag

(b) Combined Muon

Figure 7.21: Fits of MS hit residuals in data to prompt muon and decay in flight samples [65].

passing analysis requirements are used to measure the trigger efficiency. Such events have no measurement bias relative to the muon trigger, and can therefore probe its performance.

These muons are extrapolated to the trigger chamber regions of interest, where trigger hits are sought. The efficiency is then defined as the fraction of selected muons matched with RoIs. The efficiency measurement is done separately in the barrel and in the endcap, since the barrel trigger uses RPCs while TGCs trigger in the endcap. The trigger efficiency curves as a function of reconstructed muon p_{T} are shown in Figure 7.22. The systematic uncertainty on this method is determined by comparing `MuID` and `STACO`, by changing trigger hit association criteria in the extrapolation, by varying the selection of reconstructed muons used, and from the difference in the pseudorapidity of the selected muons from the W sample. The ratio of data and Monte Carlo efficiencies gives a scale factor to correct the Monte Carlo trigger efficiencies. We show these scale factors, separately for the barrel (RPC) and the endcap (TGC), in Table 7.9.

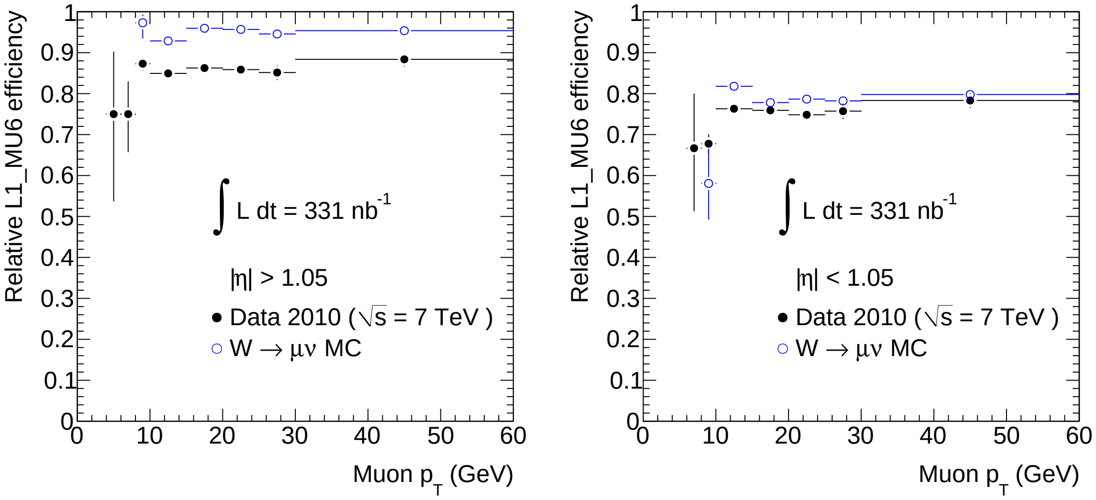

(a) Endcap (b) Barrel

Figure 7.22: p_{T} distribution, and muon trigger efficiency as a function of muon p_{T} [65].

parameter	result
barrel single muon SF	0.9594 ± 0.0116 (sta) ± 0.0157 (sys)
endcap single muon SF	0.9070 ± 0.0089 (sta) ± 0.0145 (sys)

Table 7.9: Muon trigger scale factors. [65]

7.7 Muon Momentum Scale and Resolution

The muon momentum scale and resolution in data are not well-reproduced in the MC simulation, since effects like MS and ID alignment, magnetic field map and the material description are not perfectly simulated. For muons with p_{T} around 45 GeV, the muon resolution is determined largely by the hit position, and by detector misalignment. These factors degrade the muon performance to make it worse than that in the Monte Carlo, so those samples need additional muon scaling and smearing. This additional smearing is found using fits of the measured and simulated Z mass peak, with a Breit-Wigner distribution convoluted with a Gaussian distribution. The fitted mean of the Breit-Wigner distribution indicates the Z peak position while the fitted width of the Gaussian distribution indicates the detector resolution. The results are reported in Table 7.10 for `STACO` muons. The momentum scale and resolution for different detector regions are found to be consistent with each other within statistical uncertainties. Figure 7.23 shows the measured muon momentum scale and additional smearing needed for the MC simulation using muons in both barrel and endcap regions. For the W cross section measurements, the central value of the acceptance is calculated using MC simulation without scaling and smearing. We take for the systematic uncertainty the difference between the acceptance without scaling and smearing and the acceptance using 0.01 scaling and 5% smearing for the barrel and 9% for the endcap regions.

	Scale	Extra Smear
all	0.991 ± 0.005	0.055 ± 0.012
barrel	0.992 ± 0.010	0.031 ± 0.020
endcap	0.980 ± 0.012	0.063 ± 0.031

Table 7.10: Scale and extra resolution parameters from fitting the Z boson mass peak [65].

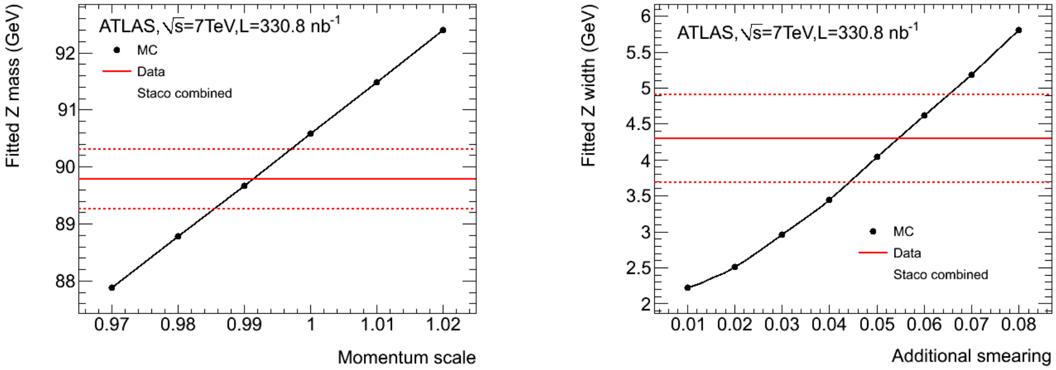

Figure 7.23: Muon momentum scale (left) and additional smearing (right) needed for the MC simulation. The red lines are the fitted peak position (width) and statistical uncertainty from data and the black points are the fitted peak position (width) from MC [65].

7.8 Summary of Systematic Uncertainties

The missing energy systematic uncertainty has a calorimeter and a muon component. The muon-component of the missing energy is perfectly correlated with the muon measurement itself. When the muon is smeared/scaled, in order to account for the correlations between the $E_{\mathrm{T}}^{\mathrm{miss}}$ and the muon variables, $E_{\mathrm{T}}^{\mathrm{miss}}$, the relative track isolation, and the transverse mass are recalculated after shifting the muon momentum. Hence, the same systematic term covers both. The overall effect due to the muon momentum scale and resolution is 1.2%. The calorimeter missing energy component is considered independent of the muon contribution. The calorimeter cluster energy scale is known to about 7% and the energy resolution is known to 5%. The net effect of these yields a 2% uncertainty on the acceptance. We summarize the experimental systematic uncertainties in Table 7.11.

parameter	$\delta C_W(\%)$
Trigger efficiency	1.9
Reconstruction efficiency	2.5
Muon momentum scale	1.2
Muon momentum resolution	0.2
$E_{\mathrm{T}}^{\mathrm{miss}}$ scale and resolution	2
Isolation efficiency	1.0
Total experimental uncertainty	4.0

Table 7.11: Experimental systematic uncertainties on $W \to \mu\nu$ acceptance from different sources.

7.9 Cross Section Methodology

The W cross section is given by[8]:

$$\sigma_{tot} = \sigma_W \times BR(W \to \mu\nu) = \frac{N - B}{A_W C_W L_{int}}, \tag{7.7}$$

where

- N is the number of candidate events measured in data,
- B is the number of background events,
- L_{int} is the integrated luminosity for the dimuon decay channel corresponding to the L1_MU6 trigger,
- A_W and C_W are the factorized acceptances, defined below, corrected for any discrepancy in reconstruction and trigger efficiencies between data and Monte Carlo.

---

[8] We carry the analysis out inclusively in light of the low statistics. Instead, for the 33 pb^{-1} analysis in Chapter 8, we use 44 bins in charge and pseudorapidity. There we provide the appropriate extensions to the single-bin formalism here.

We measure the cross section within a kinematical fiducial region and as an inclusive value, factorizing the total selection acceptance in the two terms A_W and C_W defined as:

- A_W: Fraction of the generated $W \rightarrow \mu\nu$ events passing the kinematic and geometric selection of the analysis at generator level. It is the fraction of generated events satisfying $p_{\mathrm{T}}^{\mu} > 20$ GeV, $|\eta^{\mu}| < 2.4$, $p_{\mathrm{T}}^{\nu} > 25$ GeV, and $m_{\mathrm{T}}(\mu, \nu) > 40$ GeV, where all of these quantities refer to the truth-level muon and neutrino, before any final state radiation. It extrapolates to the total cross section, and is estimated using `Pythia` to be 0.480 ± 0.014.

- C_W: Correction for the detector efficiency, resolution and QED radiation effects. It is calculated from `Pythia` using the generated events as reconstructed after full detector simulation. The denominator is the number of events passing the generator-level requirements that form the numerator of A_W, and the numerator is the fraction of events passing the full analysis selection. The uncorrected value of C_W^{MC} is estimated to be 0.816 ± 0.002 (stat). Data-driven corrections, namely, efficiency scale factors defined as $\epsilon_{data}/\epsilon_{MC}$, are made for muon reconstruction efficiency and for trigger efficiency.

We briefly summarize the theoretical uncertainties on the acceptance here. More details are given in [93]. The geometrical acceptance factor A_W suffers from relatively large uncertainties. Three types of uncertainties are: uncertainties within one PDF set chosen as CTEQ 6.6 NLO and evaluated with `MC@NLO`, differences between different PDFs sets chosen as CTEQ 6.6 NLO, MRST LO* and HERAPDF 1.0 NLO evaluated using `Pythia`, and differences in parton shower and other theoretical modeling evaluated by comparing `MC@NLO` and `Pythia` with the same PDF chosen as CTEQ 6.6 NLO. The result of these extensive studies is a total systematic uncertainty of ±3% on A_W (both W^+ and W^-). The experimental correction factor C_{W} is also subject to theoretical uncertainties, for example due to the not fully known rapidity distribution within the fiducial region and efficiencies with rapidity dependence. The uncertainties were estimated in [93] by reweighting the fully simulated `Pythia` sample from MRST LO* to CTEQ 6.6 NLO and HERAPDF 1.0 NLO, yielding a moderate uncertainty of about ±0.3% on C_{W}.

The cross section measured in the fiducial region, corresponding to the geometrical acceptance of the detector and of the kinematical selection of the analysis, is obtained setting $A_W = 1$ in 7.7. For $W \to \mu\nu$, we measure the acceptance times efficiency in a sample of simulated $W \to \mu\nu$ events generated by `Pythia`, obtaining a value of 39.22% with negligible statistical error. This pure Monte Carlo acceptance has been corrected for discrepancies between data and simulation observed in the trigger and reconstruction efficiencies (see Sections 7.6.1 and 7.6.2), as well as the effects of pileup events (see Section 7.2.3).

The total systematic uncertainty on the acceptance and efficiency (C_W) is 4.0% as shown in Table 7.11. The signal acceptances measured from Monte Carlo for all W events and for W^+ and W^- events separately are summarized in Table 7.12. Total acceptance and the factorized values A_W and C_W are reported here corrected by the scale factors for trigger and reconstruction efficiencies calculated above to take into account differences between data and Monte Carlo. The scale factors are also summarized in the table.

	W (all)	W^+	W^-
A_W	0.480 ± 0.014	0.484 ± 0.015	0.474 ± 0.014
C_W	0.758 ± 0.031	0.765 ± 0.031	0.748 ± 0.030
Total Acceptance	0.364 ± 0.018	0.370 ± 0.019	0.355 ± 0.018
Trigger Efficiency SF	0.929 ± 0.010 (stat) ± 0.015 (syst)		
Reconstruction Efficiency SF	1.000 ± 0.006 (stat) ± 0.024 (syst)		

Table 7.12: Total and factorized acceptances, and scale factors, for all W events and for positive and negative Ws separately.

7.10 Result

We show the successive impact of the selection requirements, described in Section 7.4, in Table 7.13. There are 1,181 W candidates found, of which 710 have a μ^+ while 471 have a negatively charged muon. This compares to an expectation of $1,180 \pm 84$ signal events and 100 ± 11 background events, where the uncertainty includes all components except for the 11% luminosity component. The details of the background expectations and observed candidates are itemized in Table 7.14. Uncertainties in Table 7.14 include all contributions.

7.10.1 Kinematics of Candidate Events

The W event selection is designed to be efficient for the $W \to \mu\nu$ signal while rejecting background. This can be illustrated by the distributions of muon isolation, $E_{\mathrm{T}}^{\mathrm{miss}}$, and m_{T} in events where all but those selections have been applied. The signal and background distributions are normalized to the expected number of events in 310 nb^{-1}. Figure 7.24 shows the $E_{\mathrm{T}}^{\mathrm{miss}}$ (left) and the track isolation (right), and Figure 7.25 shows the transverse mass.

We re-examine the muon kinematics, but now in a sample dominated by the

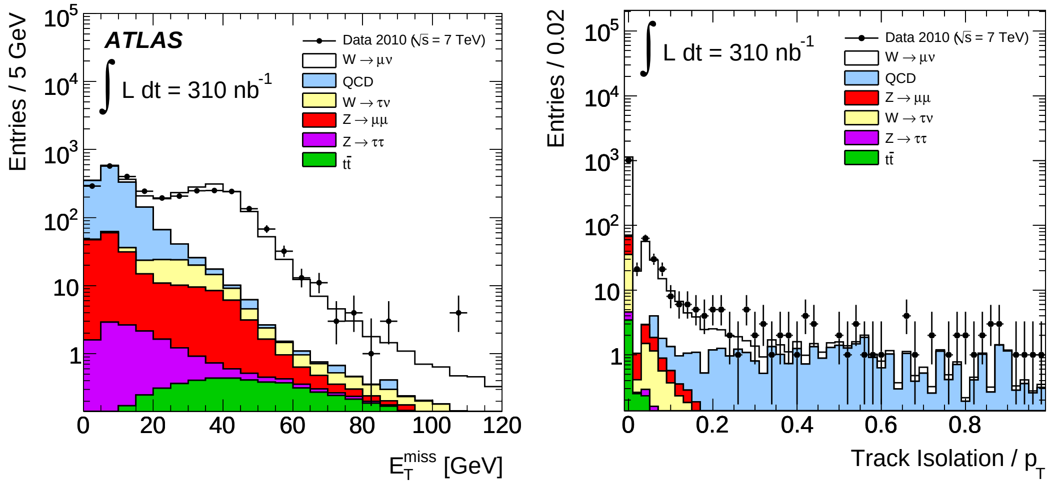

Figure 7.24: $E_{\mathrm{T}}^{\mathrm{miss}}$ (left) in events passing all requirements except for the $E_{\mathrm{T}}^{\mathrm{miss}} >$ 25 GeV requirement. Track isolation of muon candidates (right) in events passing all other requirements [65].

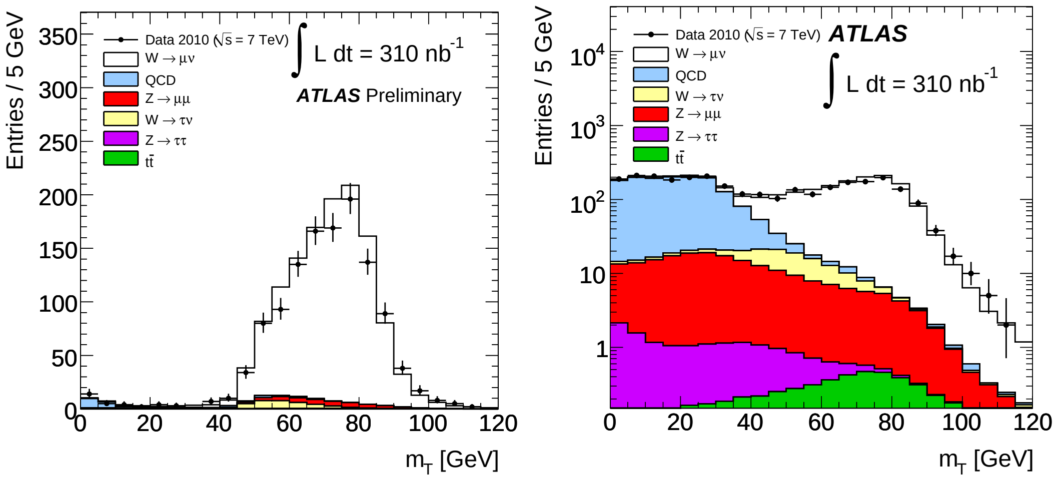

Figure 7.25: m_{T} of muon and $E_{\mathrm{T}}^{\mathrm{miss}}$ system for events passing all requirements except for that on m_{T} in events passing all W selection except for the $m_{\mathrm{T}} >$ 40 GeV requirement (left). On the right, the $E_{\mathrm{T}}^{\mathrm{miss}} >$ 25 GeV is relaxed as well [65].

Cut	N_{evt}	Efficiency [%]	Relative Efficiency [%]
All	49611864	100.00 ± 0.00	—
Good Run List	33598320	67.72 ± 0.01	67.72 ± 0.01
Jet cleaning	33595324	67.72 ± 0.01	99.99 ± 0.00
Trigger	5132898	10.35 ± 0.00	15.28 ± 0.01
Vertex	4788689	9.65 ± 0.00	93.29 ± 0.01
Combined μ	1732022	3.49 ± 0.00	36.17 ± 0.02
μ $\lvert\eta\rvert < 2.4$	1710926	3.45 ± 0.00	98.78 ± 0.01
μ $p_T > 15$ GeV	24332	$(4.90 \pm 0.03) \cdot 10^{-2}$	1.42 ± 0.01
μ $p_T^{MS} > 10$ GeV	21071	$(4.25 \pm 0.03) \cdot 10^{-2}$	86.60 ± 0.22
$\lvert p_{\mathrm{T}}^{MS} - p_{\mathrm{T}}^{ID}\rvert < 15$ GeV	20881	$(4.21 \pm 0.03) \cdot 10^{-2}$	99.10 ± 0.07
$\lvert z_0 - z_{vtx}\rvert < 10$ mm	20712	$(4.17 \pm 0.03) \cdot 10^{-2}$	99.19 ± 0.06
μ $p_{\mathrm{T}} > 20$ GeV	7052	$(1.42 \pm 0.02) \cdot 10^{-2}$	34.05 ± 0.33
Isolation	2920	$(0.59 \pm 0.01) \cdot 10^{-2}$	41.41 ± 0.59
$E_{\mathrm{T}}^{\mathrm{miss}} > 25$ GeV	1220	$(0.25 \pm 0.01) \cdot 10^{-2}$	41.78 ± 0.91
$m_{\mathrm{T}} > 40$ GeV	1181	$(0.24 \pm 0.01) \cdot 10^{-2}$	96.80 ± 0.50

Table 7.13: Number of events in data passing successive selection requirements [65].

$W \to \mu\nu$ signal. Figures 7.27 (left) and 7.26 show the leading muon p_{T}, η, and ϕ, respectively. Finally, we show the reconstructed p_{T} of the W candidates, compared to the signal and background expectations, in Figure 7.27 (right).

7.10.2 Cross Section Measurement

From the analysis described above, using 310 nb^{-1} of data, we expect 1,280 ± 165 events and observe 1,181. The acceptance factors and backgrounds needed to calculate the results are summarized in Table 7.15. The resulting $W \to \mu\nu$ cross sections are reported in Table 7.16. The systematic uncertainties include contributions from both the systematic uncertainties on the acceptance and on the backgrounds, although it is dominated by the uncertainties on the signal acceptance. The luminosity and systematic uncertainties are correlated between the signal acceptance and

sample	W	W^+	W^-
$Z \to \mu\mu$	38.4 ± 5.0	20.0 ± 2.6	18.4 ± 2.4
$W \to \tau\nu$	33.6 ± 4.4	19.7 ± 2.6	13.9 ± 1.8
$t\bar{t}$	4.2 ± 0.6	2.1 ± 0.3	2.1 ± 0.3
$Z \to \tau\tau$	1.4 ± 0.2	0.7 ± 0.1	0.7 ± 0.1
QCD	21.1 ± 9.8	11.1 ± 5.4	10.1 ± 4.8
Cosmic ray	1.7 ± 0.8	0.9 ± 0.4	0.8 ± 0.4
Total background	100.4 ± 14.1	54.4 ± 7.8	46.0 ± 6.6
$W \to \mu\nu$ signal	1179.9 ± 154.4	706.7 ± 92.5	473.3 ± 62.0
Total predicted	1280.3 ± 164.8	761.1 ± 98.2	519.3 ± 66.7
Number observed	1181	710	471

Table 7.14: Summary of expected number of events, including systematic and luminosity uncertainties, compared to the observed number [65].

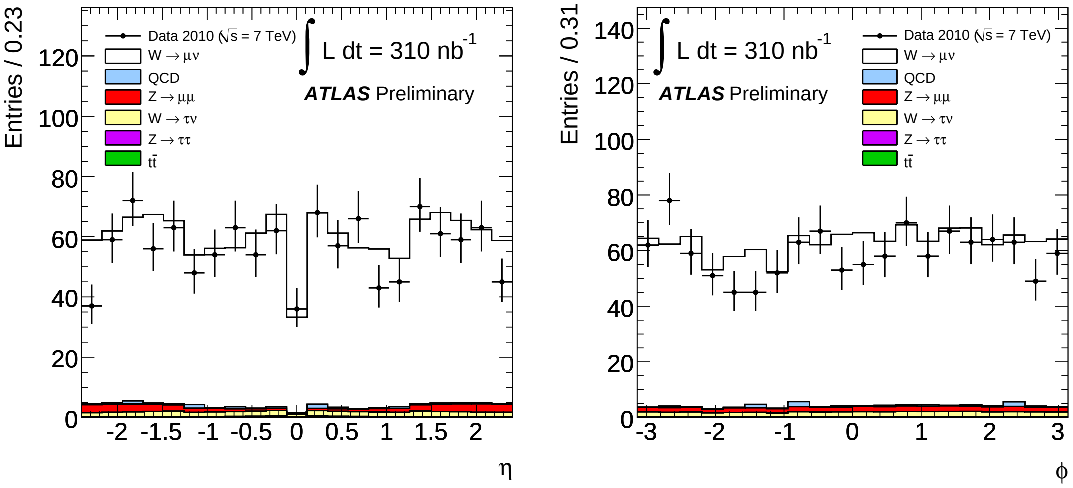

Figure 7.26: η of highest-p_{T} muon in selected events (left). ϕ of highest-p_{T} muon in selected events (right) [65].

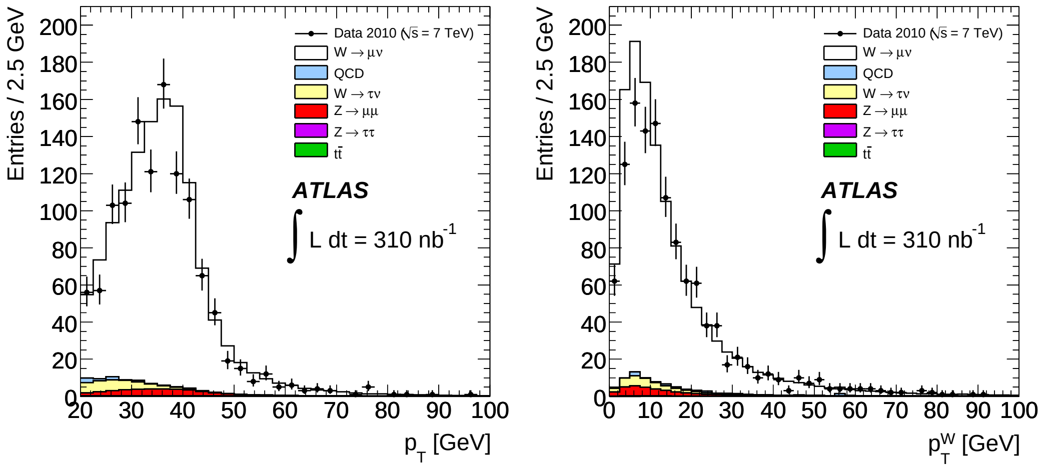

Figure 7.27: p_{T} of the highest-p_{T} muon in selected events passing all $W \to \mu\nu$ selection (left). p_{T} of W candidate, reconstructed from the p_{T} of the leading muon and the $E_{\mathrm{T}}^{\mathrm{miss}}$ (right) [65].

the electroweak and $t\bar{t}$ backgrounds. However, the impact of the correlation is less than 0.3% relative to the size of the total systematic or luminosity uncertainties, and is considered negligible. We also divide the $W \to \mu\nu$ sample into the positive and negative samples. The total number of events predicted to pass the selection with positive (negative) muons is 761 ± 98 (519 ± 67) and the number observed is 710 (471). The corresponding cross sections are reported in Table 7.17.

	W (all)	W^+	W^-
A_W	0.4800 ± 0.0144	0.4840 ± 0.0145	0.4743 ± 0.0143
C_W	0.7578 ± 0.0306	0.7646 ± 0.0309	0.7479 ± 0.0302
Total background	100.4 ± 14.1	54.4 ± 7.8	46.0 ± 6.6
Number observed	1181	710	471

Table 7.15: The ingredients for the cross section calculation for W, W^+ and W^- are summarized.

A comparison of the measured cross section values for W production to theoretical predictions including next-to-next-to-leading order QCD corrections are shown in

$\sigma_W \times \mathrm{BR}(W \to \mu\nu)$	9.58 ± 0.30 (stat) ± 0.50 (sys) ± 1.05 (lum)	nb.
$\sigma_W^{fid} \times \mathrm{BR}(W \to \mu\nu)$	4.60 ± 0.15 (stat) ± 0.20 (sys) ± 0.51 (lum)	nb.

Table 7.16: $W \to \mu\nu$ total and fiducial cross section measurements [65].

$\sigma_{W^+} \times \mathrm{BR}(W^+ \to \mu^+\nu)$	5.71 ± 0.23 (stat) ± 0.30 (sys) ± 0.63 (lum)	nb.
$\sigma_{W^-} \times \mathrm{BR}(W^- \to \mu^-\bar{\nu})$	3.86 ± 0.20 (stat) ± 0.20 (sys) ± 0.42 (lum)	nb.
$\sigma_{W^+}^{fid} \times \mathrm{BR}(W^+ \to \mu^+\nu)$	2.77 ± 0.11 (stat) ± 0.12 (sys) ± 0.30 (lum)	nb.
$\sigma_{W^-}^{fid} \times \mathrm{BR}(W^- \to \mu^-\bar{\nu})$	1.83 ± 0.09 (stat) ± 0.08 (sys) ± 0.20 (lum)	nb.

Table 7.17: $W^+ \to \mu^+\nu$ and $W^- \to \mu^-\bar{\nu}$ total and fiducial cross section measurements [65].

Figure 7.28. The calculations were performed using the programs FEWZ [18] and ZWPROD [68], as discussed earlier in Section 2.6. Within an overall theoretical uncertainty of 5%, the calculations for W production agree well with the measured cross sections. In addition, the expected asymmetry between the W^+ and W^- cross sections is confirmed.

In Figure 7.29, the results are combined with the corresponding electron-channel analysis, and compared to theoretical predictions and to previous measurements of the total production cross sections by other collaborations. The theoretical predictions are in good agreement with all measurements, and energy dependence of the total production cross sections is well described.

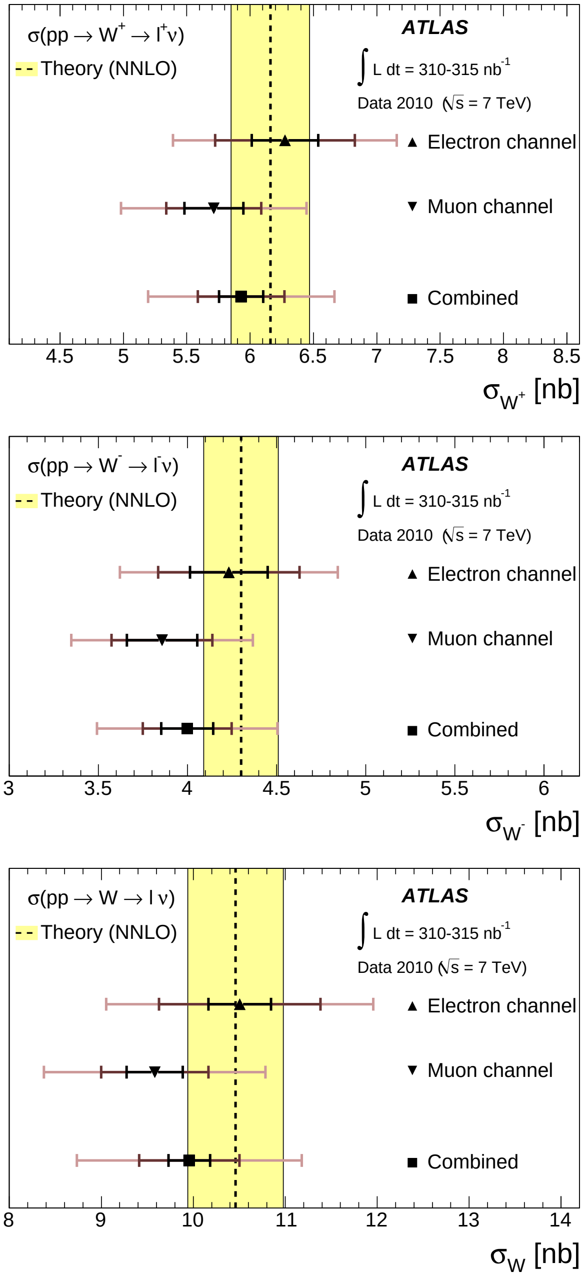

Figure 7.28: The measured values of $\sigma_W \cdot \mathrm{BR}\ (W \to \ell\nu)$ for W^+, W^- and for their sum compared to the theoretical predictions based on NNLO QCD calculations. Results are shown for the electron and muon final states as well as for their combination.

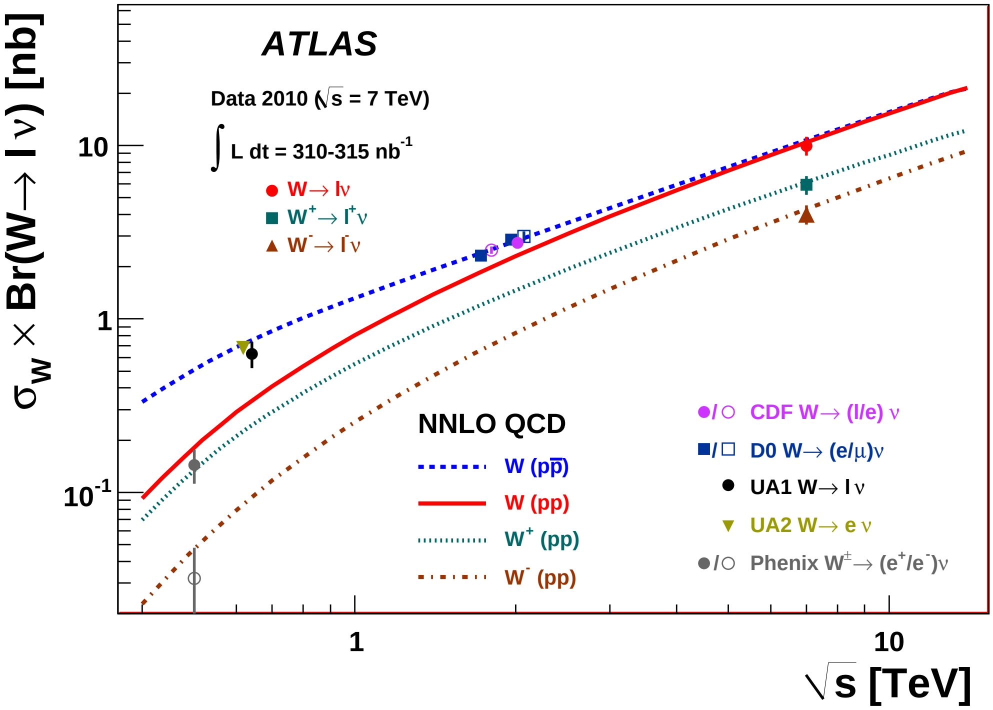

Figure 7.29: The measured values of $\sigma_W \cdot \mathrm{BR}\,(W \to \ell\nu)$ for W^+, W^- and for their sum compared to the theoretical predictions based on NNLO QCD calculations. Results are shown for the combined electron-muon results. The predictions are shown for both proton-proton and proton-antiproton colliders as a function of $\sqrt{s}$. In addition, previous measurements at proton-antiproton and proton-proton colliders are shown. The data points at the various energies are staggered to improve readability. The CDF and D∅ measurements are shown for both Tevatron collider energies, $\sqrt{s} = 1.8$ TeV and $\sqrt{s} = 1.96$ TeV. All data points are displayed with their total uncertainty. The theoretical uncertainties are not shown.

Chapter 8

$W \to \mu\nu$ Cross Section with $33\ \mathrm{pb}^{-1}$

This chapter presents the ATLAS $W \to \mu\nu$ production cross section result achieved with the full dataset accumulated in 2010, corresponding to 33 pb^{-1} of analyzed data. This is the main result of this thesis; it is a significant improvement over the results documented in Chapter 7, for several reasons. The integrated luminosity increased by a multiplicative factor of one hundred. Hence, the statistical uncertainty on the $W \to \mu\nu$ inclusive measurement comes down to the few per-mille level. The increased statistics, corresponding to almost $12,000$ $Z \to \mu\mu$ candidate events, permit detailed probes of the detector with a well-understood clean, isolated, high-momentum prompt muon sample. The resulting tag-and-probe studies, described in Section 8.3, help reduce the large systematic uncertainties from muon trigger, reconstruction and isolation efficiency seen in Table 7.11. This is certainly needed, since the luminosity uncertainty has decreased from 11% to 3.4% with more precise measurement of beam currents and profiles.

In addition, because of the hundredfold increase in statistics, the analysis is strongly limited by systematic, not statistical effects. It is possible to get a better understanding of systematic uncertainties by separating the dataset into different bins, each bin containing events with greater uniformity in terms of detector effects. This analysis computes efficiency and scale corrections separately for the two charges, and in addition divides the acceptance into 22 bins in muon pseudorapidity, the bins reflecting Muon Spectrometer segmentation to collect events with similar detector characteristics. We update the cross section calculation itself to sum partial cross sections in these 22 bins, instead of computing one number.

The background estimation also differs significantly from that shown in Section 7.5; cosmic-rays are not a significant background source, the QCD calculation with the "matrix" method (seen before in Section 7.5.2) has a more sophisticated treatment of the extrapolation uncertainties, and we consider additional electroweak backgrounds.

The software and calibration configuration of the detector showed significant improvement, with ID and MS alignment constants being updated, improved magnetic field and material descriptions in the simulation, and with updates to the muon reconstruction software. In particular, the extensive difficulties with loosely matched fake muons (Section 7.3) are solved with the adoption of tightened reconstruction requirements in `STACO` together with ID quality criteria. As such, we can avoid kinematic criteria on muon's constituent track momenta.

Some new issues come into play however: the rapidly increasing luminosity meant that thresholds for unprescaled triggers increased, and the high-level trigger had to be used. In fact, our analysis dataset uses two different muon triggers, both requiring study for efficiency. The treatment of pileup events is more important with increasing instantaneous luminosity; the increased number of bunches in the beam means we have to consider effects not just from other collisions in the same bunch, but also from detector response to pileup events in preceding bunch crossings (out-of-time pileup). The treatment of jet cleaning (removal of spurious jets from calorimetric noise, beam background and cosmic ray showers) gains extra importance, with naive vetoing of poorly timed jets leading to a significant, poorly-modeled decrease in the sample acceptance.

We now proceed to discuss the measurement, including the data and Monte Carlo samples, event selection, backgrounds, systematic uncertainties, acceptances and the final results.

8.1 Dataset and Simulated Samples

We utilize the full 2010 7 TeV dataset, with the exception of the first few pb^{-1} acquired in early running.[1] The events in the 310 nb^{-1} dataset used for Chapter 7 are not in this dataset, for example. These data are processed with a new reconstruction software release[2] compared to the previous result. Machine, detector and data-quality flags are employed to produce a common good run list for muon-based W/Z analysis. The net sample corresponds to an integrated luminosity of 33 pb^{-1}.

Simulated Monte Carlo samples are as described in Section 7.1 and summarized in

---

[1] In this initial period, the RPC trigger timing as well as TGC road configuration were changing rapidly, and there were alignment configuration issues in the muon trigger software during some data-taking periods.

[2] For reference, we use ATLAS software release `16.0.2.3 - 16.0.2.6`.

Process	Generator	$\sigma\cdot$ BR [nb]	N_{evt} [10^6]
WW	`Herwig`	$44.9 \cdot 0.389$	0.25
WZ	`Herwig`	$18.5 \cdot 0.310$	0.25
ZZ	`Herwig`	$6.02 \cdot 0.212$	0.25

Table 8.1: Extra Monte Carlo samples used, in addition to those listed in Table 7.1.

Table 7.1. There are a few MC sample differences between this and the early analysis:

- the $t\bar{t}$ background sample is generated with `MC@NLO` [54] and not `PowHeg`. Note that we do use the same production cross section value as before.
- diboson WW, WZ and ZZ samples generated with `Herwig` permit estimation of their background contribution. We provide the corresponding sample details in Table 8.1.
- the modeling of pileup now includes the effects of out-of-time pileup, as discussed in Section 8.2.2.
- The Monte Carlo production benefits from knowledge gained with ATLAS data collected in 2010, regarding alignment, material effects and tunes for the underlying event.

8.2 Event Selection

We use the same missing energy definition for this measurement as that in Section 7.2.2. Primary vertexing is slightly modified, with a 20 cm requirement on the primary vertex position in $|z|$. The muon selection uses new trigger and muon quality requirements. In addition to these, we describe the modified pileup reweighting and jet cleaning.

8.2.1 Muon Selection

Several analysis requirements for muons are unchanged from Section 7.2.1: the muon transverse momentum requirement is the same (20 GeV), as is the isolation requirement, and the requirement that the muon be within 10 mm of a primary vertex. Muon trigger and quality criteria are modified however, so we discuss them in some detail.

Muon Trigger

The muon trigger for this analysis uses all three stages of the muon trigger (Section 5.5) instead of relying on only a 6 GeV hardware trigger threshold, as was done for the earlier study (Section 7.2.1). In particular, at the Event Filter (EF) stage, the triggering algorithm uses the `MuGirl` algorithm, described in Section 5.6.2 and 5.6.3. We make this choice for several reasons: `MuGirl` has less dependence on MS tracking in the trigger, in particular on calibration and alignment settings which can be out-of-date or incorrect in the online trigger. In addition, because its inside-out algorithm logic is very different from that in `MuID` and `STACO`, the trigger efficiency is more conceptually independent from the offline reconstruction. Also, the trigger has somewhat higher efficiency measured relative to offline-reconstructed muons, because looser reconstruction settings are used.

It is worthwhile to minimize the number of triggers used in the analysis, since the performance of each requires understanding. For this `MuGirl` trigger, we use a 13 GeV p_{T} threshold; this is the lowest unprescaled trigger threshold available for use over the full data period. The threshold is still sufficiently lower than the 20 GeV muon selection that the analysis is not conceptually affected, though the preselection p_{T} requirement at 15 GeV may be affected by the trigger.

This threshold corresponds to two different triggers however: for the first part of the dataset, the trigger used is the `EF_mu13_MG`. Instead, for the latter period, we use the `EF_mu13_MG_tight` trigger instead. Both of these are event filter 13 GeV `MuGirl` triggers, the difference being that `EF_mu13_MG_tight` is seeded by a 10 GeV L1 muon trigger, while `EF_mu13_MG` starts from a level-1 trigger with fully open trigger roads (and hence is not "tight"). The datasets acquired by the two triggers are comparable in size. Because the two level-1 triggers for these chains are different, the muon trigger performance must be studied separately for the two trigger samples. We describe studies of the trigger efficiency in data, in Section 8.3.2. These provide bin-by-bin efficiency differences between data and Monte Carlo, which we apply as scale factors to Monte Carlo predictions (Section 8.5.1).

Muon Definition

As in the previous analysis (Section 7.2.1), we employ combined muons (Section 5.6.2) using the `STACO` algorithm for this analysis. We note that in contrast to that result, the algorithm settings are *not* loose; the muon reconstruction has tightened matching to remove the fakes discussed in Section 7.3. In addition, we make requirements upon the inner detector track to ensure good quality ID reconstruction.

These include a requirement of silicon hits, and a criterion to eliminate tracks with missing TRT hits (as were seen in Figures 7.6(c) or 7.13(b)):

- Require at least one b-layer hit on the muon track, if such hits are geometrically expected;
- $N_{PIX}+N_{DEAD-PIX} > 1$, where N_{PIX} is the number of pixel hits and $N_{DEAD-PIX}$ is the number of crossed dead pixel sensors;
- $N_{SCT}+N_{DEAD-SCT} \geq 6$, where N_{SCT} is the number of SCT hits and $N_{DEAD-SCT}$ is the number of crossed dead SCT sensors;
- $N_{DEAD-PIX} + N_{DEAD-SCT} < 2$;
- Require a successful TRT extension (see Section 4.3.4) in the η acceptance of the TRT. If $N_{TRT-HITS}$ denotes the number of TRT hits on the muon track, $N_{TRT-OUTLIERS}$ the number of TRT outliers on the muon track, and $N_{TRT} = N_{TRT-HITS} + N_{TRT-OUTLIERS}$, then
  - in the interval $|\eta| < 1.9$: require $N_{TRT} > 5$ and $N_{TRT-OUTLIERS}/N_{TRT} < 0.9$;
  - in the interval $|\eta| > 1.9$: if $N_{TRT} > 5$ then require $N_{TRT-OUTLIERS}/N_{TRT} < 0.9$, otherwise accept the muon.

With this muon definition, in Figure 8.1 we present the standalone MS track momentum and relative MS-ID p_{T} difference for muons passing the 15 GeV preselection. The momentum compatibility problems of the previous analysis are much more manageable, though for the background enriched preselection sample there are still tails not reproduced by the Monte Carlo samples used. Instead, in Figure 8.2, for muons in events passing the full event selection, the agreement is better still.

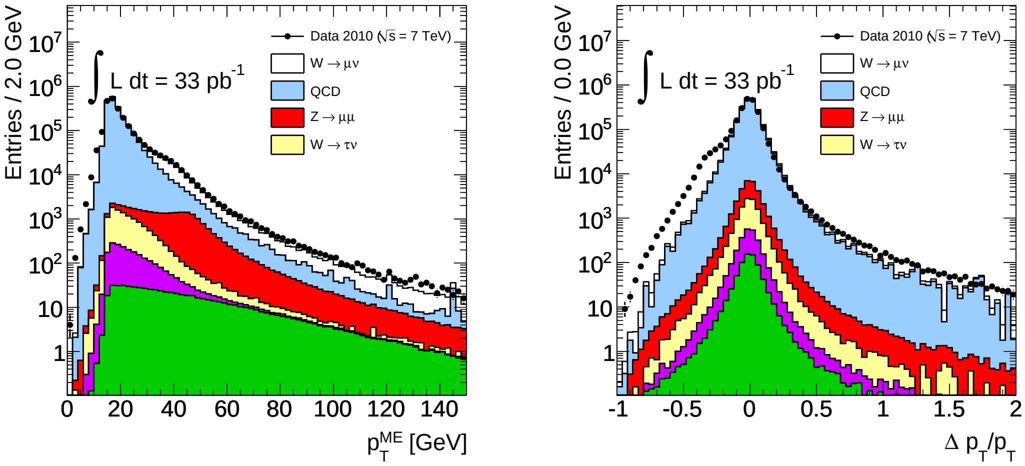

(a) (b)

Figure 8.1: Standalone MS muon p_{T} (left) and relative difference (MS-ID)/ID) for preselected muons.

8.2.2 Pileup Simulation and Reweighting

As compared to pileup as discussed in Section 7.2.3, with the number of bunches in the beam increasing, there is increased particle activity from proton-proton interactions occurring in previous bunch crossings from the main interaction. To model pileup effects, we deploy simulated MC samples in the so-called *bunch-train* setup. Here, the hard-scattering event has simulated minimum bias interactions overlaid on top. The timing structure is as follows. Individual bunches are separated by 150 ns, in trains of eight bunches length. A second bunch train follows with a time separation equal to 225 ns, followed by a longer pause before the next bunch train [42]. As before,

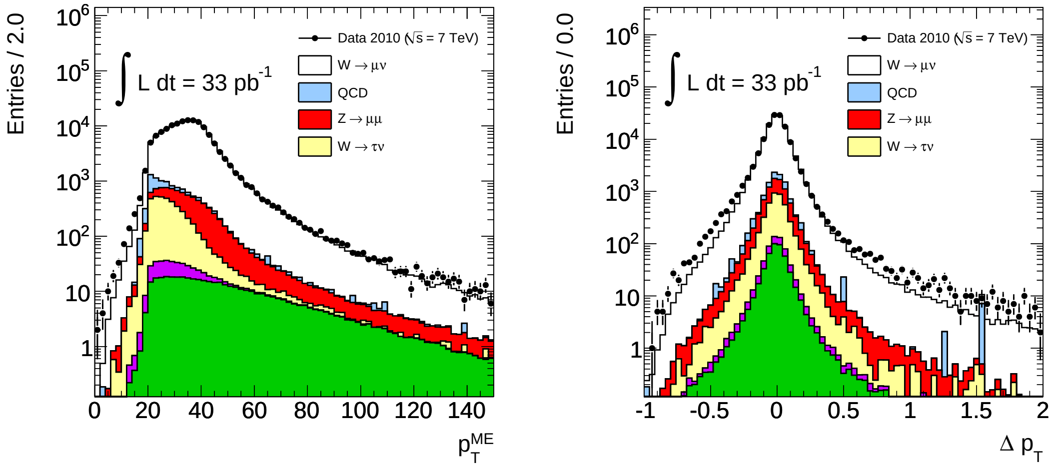

(a) (b)

Figure 8.2: Standalone MS muon p_{T} (left) and relative difference (MS-ID)/ID) for $W \to \mu\nu$ candidate events.

we reweight the vertex multiplicity in Monte Carlo events to match the distribution in data. The vertex distributions are shown for MC and data for a $Z \to \mu\mu$ sample in Figure 8.2.2.[3] The corresponding event vertex weights are shown in Table 8.2. Note that events with higher vertex counts have larger weights than in Table 7.2, which is expected given the increasing number of vertices in events with the rising luminosity.

8.2.3 Jet Cleaning Criteria

We impose jet cleaning criteria to veto events that have fake jets produced by detector effects (coherent noise in the Liquid Argon Calorimeter, "spikes" seen in the Hadronic Endcap Calorimeter) and cosmic and beam backgrounds. These re-

---

[3] The difference between weights for $Z \to \mu\mu$ and $W \to \mu\nu$ is at the sub-per-mille level, so common weights are utilized.

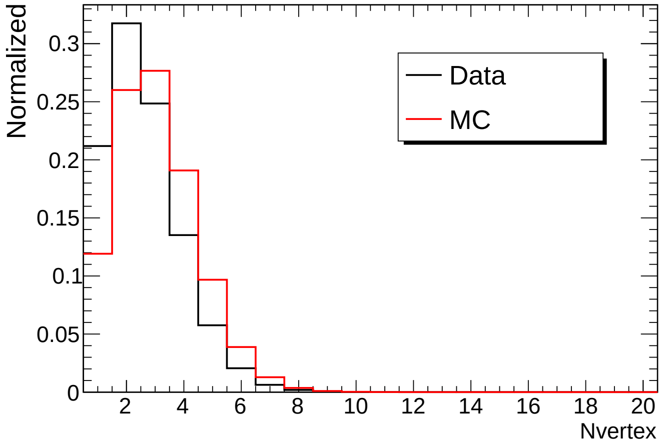

Figure 8.3: Comparison of number of reconstructed vertices in data and MC simulation [42].

N_{vertex}	Event Weight
0	-
1	1.777
2	1.220
3	0.898
4	0.709
5	0.596
6	0.532
7	0.489
8	0.518
9	0.495
10	0.465
11	0.674
12	0.981

Table 8.2: Number of reconstructed primary vertices and corresponding pileup weights [42].

quirements, being under rapid testing and improvement for the new software release, impose in their standard form an almost 1% inefficiency for the data. We have examined events that *fail* these jet cleaning requirements, as shown in Table 8.3. This jet cleaning implementation rejects 0.85% of events, giving an "effective luminosity" of 286 nb^{-1} for the associated data-sample. In this sample, we find 1,894 $W \to \mu\nu$ candidates satisfying the rest of our analysis requirements. Representative distributions are shown in Figure 8.4, Figure 8.5 and Figure 8.6. In these plots we have normalized Monte Carlo samples to the effective luminosity just mentioned.

Selection	Number of Events	Absolute Efficiency (%)	Relative Efficiency (%)
All	62071847	100.00 ± 0.00	—
Good Run List	51799873	83.45 ± 0.00	83.45 ± 0.00
Fail Jet cleaning	437942	0.71 ± 0.00	0.85 ± 0.00
Trigger	62789	0.10 ± 0.00	14.34 ± 0.05
Vertex	62787	0.10 ± 0.00	100.00 ± 0.00
Combined μ	51667	0.08 ± 0.00	82.29 ± 0.15
μ $\lvert\eta\rvert < 2.4$	51146	0.08 ± 0.00	98.99 ± 0.04
μ $p_{\mathrm{T}} > 15$ GeV	26562	$(4.28 \pm 0.03) \cdot 10^{-2}$	51.93 ± 0.22
$\lvert z_0 - z_{vtx}\rvert < 20$ mm	26555	$(4.28 \pm 0.03) \cdot 10^{-2}$	99.97 ± 0.01
μ $p_{\mathrm{T}} > 20$ GeV	9599	$(1.55 \pm 0.02) \cdot 10^{-2}$	36.15 ± 0.29
Isolation	4369	$(0.70 \pm 0.01) \cdot 10^{-2}$	45.52 ± 0.51
$E_{\mathrm{T}}^{\mathrm{miss}} > 25$ GeV	2011	$(0.32 \pm 0.01) \cdot 10^{-2}$	46.03 ± 0.75
$m_{\mathrm{T}} > 40$ GeV	1894	$(0.31 \pm 0.01) \cdot 10^{-2}$	94.18 ± 0.52

Table 8.3: Impact of successive selection requirements in data on events failing the jet cleaning criteria [42].

Examining these distributions, which compare well to standard $W \to \mu\nu$ distributions as presented in Section 8.8.1, we notice that events failing standard jet cleaning contain signal-like events. Indeed, such events are in fact *more* likely to pass other $W \to \mu\nu$ selection criteria than the rest of the data set. The excess, compared to

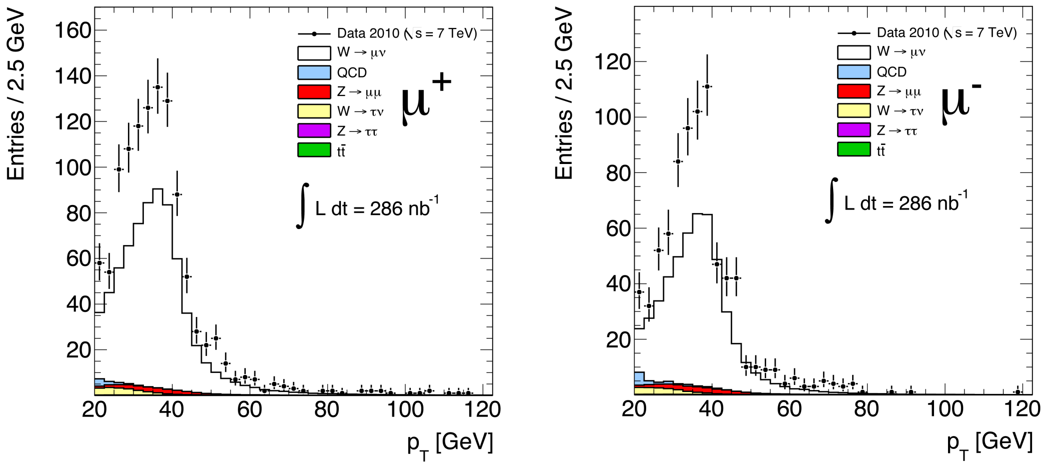

(a) Positive

(b) Negative

Figure 8.4: Muon p_{T} for events satisfying all requirements except jet cleaning, which fails. We normalize signal and background MC to an effective luminosity of 286 nb^{-1}.

events in data passing the jet cleaning requirement, is seen in the fact that 0.43% of events with bad jets pass the $W \to \mu\nu$ selection, while the corresponding figure for events passing this requirement is 0.27%. Hence, we adopt a looser version of these cuts, relax the requirement on the jet timing variable from 10 ns to 25 ns. We present the variable in question in Figure 8.7, for jets with at least 20 GeV of transverse momentum. We note that the $W \to \mu\nu$ signature involves an isolated, hard muon emerging from the primary vertex, while cosmic and beam-background events of the type this requirement is meant to veto should not display these characteristics. The modified requirement has an efficiency of 99.92%.

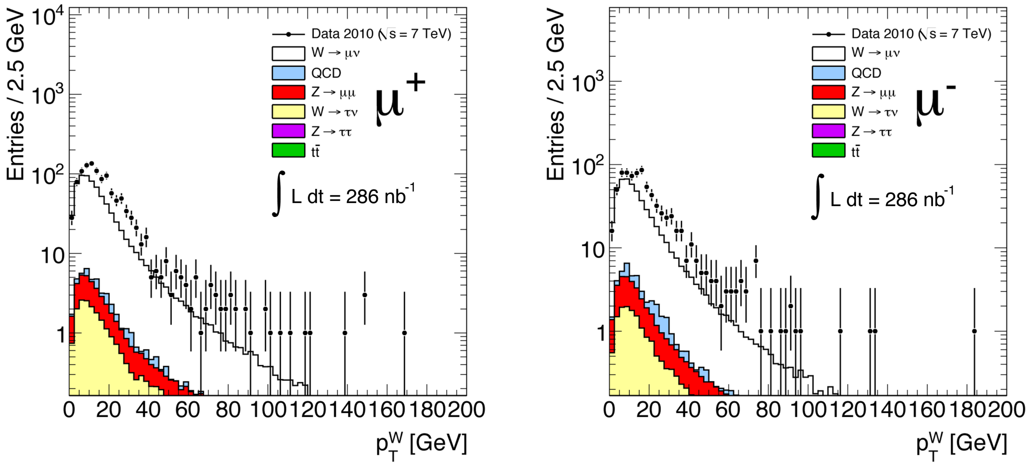

(a) Positive (b) Negative

Figure 8.5: W candidate p_{T} for events satisfying all requirements except jet cleaning, which fails. We normalize signal and background MC to an effective luminosity of 286 nb^{-1} [42].

8.2.4 W Selection

The collection of requirements applied to the $W \to \mu\nu$ selection is summarized in Table 8.4. We present corrected distributions for candidate events satisfying these requirements in Section 8.8.1, following an investigation of the requisite scale factors and background estimates.

8.3 Muon Efficiency

As mentioned in Section 7.6, we compare muon efficiencies between data and Monte Carlo to extract scale factors that correct the MC for any differences observed. This ensures that the acceptance/efficiency used in the cross section calculation corresponds to the true detector performance. We extract these efficiencies and scale factor

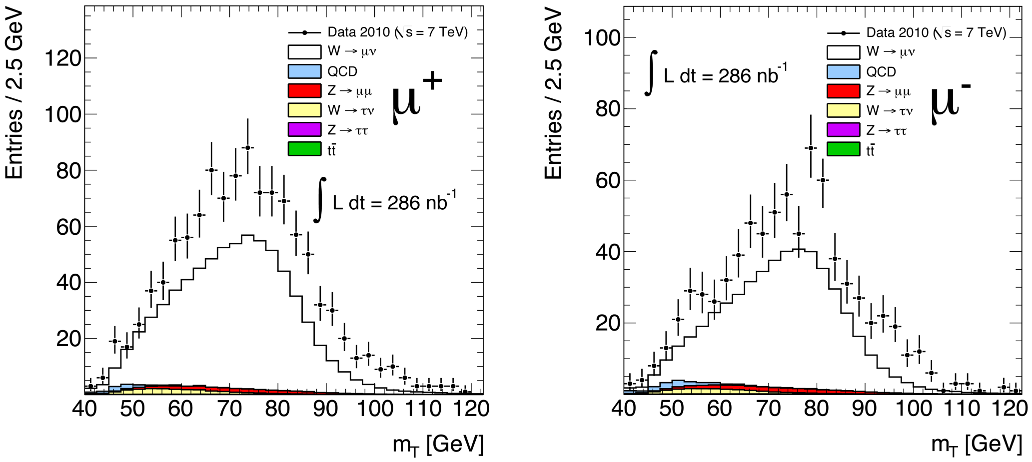

(a) Positive (b) Negative

Figure 8.6: W candidate m_{T} for events satisfying all requirements except jet cleaning, which fails. We normalize signal and background MC to an effective luminosity of 286 nb^{-1} [42].

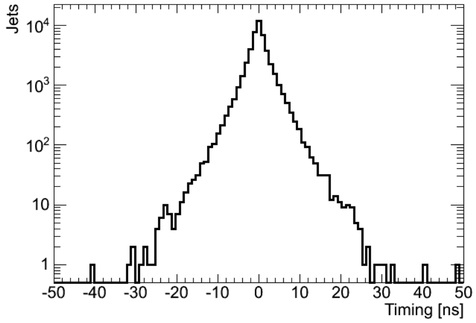

Figure 8.7: Timing cut on jets with at least 20 GeV of transverse momentum [42].

for muon reconstruction, and for the two triggers `EF_mu13_MG` and `EF_mu13_MG_tight`. In addition, the muon isolation efficiency, which presented a 1% systematic uncertainty in the old analysis, is brought under control by measuring it in data. With the relatively large luminosity sample available for this analysis, we use the Z to

GRL	
Primary Vertex	$N_{vtx} \geq 1$ with $N_{tracks} \geq 3$ and $\lvert z_{PV} \rvert < 200$ mm
Trigger	`EF_mu13_MG` or `EF_mu13_MG_tight`
jet cleaning	cleaning cuts
Muon types	≥ 1 combined muon
p_{T} and $\lvert\eta\rvert$	$p_{\mathrm{T}} > 20$ GeV; $\lvert\eta\rvert < 2.4$
Muon quality	
z-extrapolation	$\lvert z_{extr} - z_{PV} \rvert < 10$ mm
Isolation	$\sum_{tracks} p_{\mathrm{T}}/p_{\mathrm{T}}^{\mu} < 0.2$
$E_{\mathrm{T}}^{\mathrm{miss}}$	$E_{\mathrm{T}}^{\mathrm{miss}} > 25$ GeV
m_{T}	$m_{\mathrm{T}} > 40$ GeV

Table 8.4: List of cuts applied for the $W \to \mu\nu$ selection [42].

extract efficiencies, in lieu of the more systematically limited single-muon techniques discussed earlier. The method is based on the kinematic correlations between the muons coming from the Z boson decay. The idea is to "tag" one of the two muons with tight criteria, then take advantage of the mass peak to select the second muon leg with loose criteria. This second leg is a high purity probe that tests efficiencies without using the system probed. The method relies on the low background under the Z peak. With about 34 pb^{-1} of data analyzed, the measured efficiencies have overall systematic plus statistical error of $\sim 0.5\%$. We find good agreement between measured and expected performance.

8.3.1 Reconstruction Efficiency

We present measurements of the muon reconstruction efficiency from data here. Tag-and-probe on Z is used, as described above, to check that the probe is a combined muon satisfying the analysis muon reconstruction requirements. An isolation requirement pre-imposed upon the probe further reduces the background contamination in the efficiency measurement. Note that the tag-and-probe for muon reconstruction includes the muon quality requirements delineated in Section 8.2.1. Hence, the procedure accounts for any differences between data and Monte Carlo for these requirements.

There is residual background contamination in the Z sample, from electroweak and QCD events. We estimate the electroweak backgrounds from $W \rightarrow \mu\nu$, $W \rightarrow \tau\nu$, $Z \rightarrow \tau\tau$, and $t\bar{t}$ in Monte Carlo, while QCD background from $b\bar{b}$ and $c\bar{c}$ is found in data using template fits. In each case, we subtract background out from the efficiency numerator and denominators. The overall background contamination is $\sim 0.9\%$.

We show the resulting efficiencies in data and Monte Carlo, in Figure 8.8. The leading uncertainties in the method are from background contamination. Systematic uncertainties emerge from varying selection requirements on “tag” muons or the Z, or from varying the background contribution within theoretical (electroweak) and fit (QCD) uncertainties. The overall systematic uncertainty on the efficiency ratio between data and Monte Carlo is estimated at 0.4%. We use the data and Monte Carlo efficiencies in Figure 8.8 to correct Monte Carlo samples. The correction is bin-by-bin in η, as discussed in Section 8.5.2. See, for example Table 8.8 for averages of these efficiencies over the W muon distribution.

8.3.2 Trigger Efficiency

To measure the muon trigger efficiency, the technique adopted is similar to that used for the reconstruction efficiency. In each of the two data periods corresponding

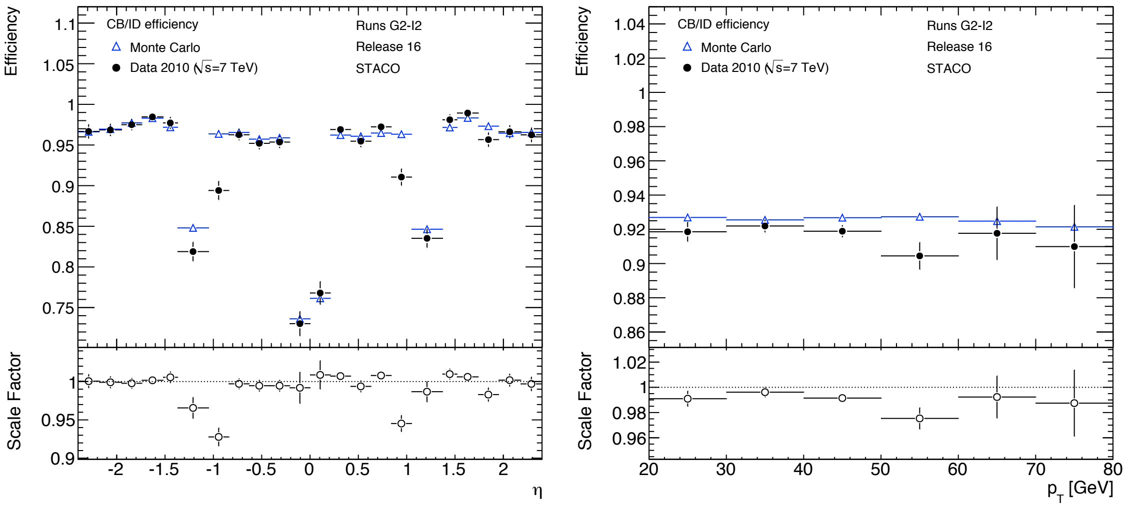

(a) vs. η.

(b) vs. p_{T}.

Figure 8.8: Muon Reconstruction efficiency for data, compared to the Monte Carlo expectation. Data efficiencies are background subtracted [42].

to the `EF_mu13_MG` and `EF_mu13_MG_tight` triggers, we select tag muons, requiring that they pass the appropriate trigger. We then use isolated muon probes to look for trigger objects matching to them. We show efficiencies in data and Monte Carlo for the two triggers, in Figures 8.9 and 8.10.

The systematic uncertainty estimates come from background contamination, and from varying the selection criteria. In addition, there are small discrepancies between results obtained using simple ntuple-based matching (in "D^{3}PD") relative to measurements made using the full trigger decision tree (on "AOD"). The data and Monte Carlo efficiencies are shown in Figures 8.9 and 8.10. We use these bin-by-bin in η to correct Monte Carlo samples, as discussed in Section 8.5.1. See, for example Table 8.6 for averages of these efficiencies over the W muon distribution. The systematic uncertainty on bin-by-bin ratios is estimated at 0.3% and 0.5% for the loose and tight

`MuGirl` triggers respectively.

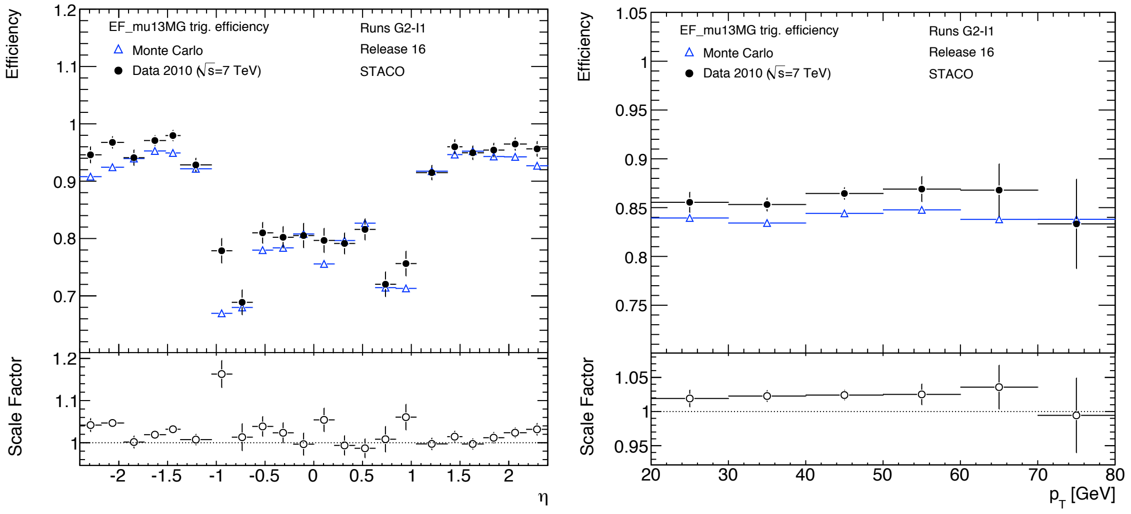

(a) vs. η. (b) vs. p_{T}.

Figure 8.9: `EF_mu13_MG` trigger efficiency with respect to combined reconstruction from data, compared to the Monte Carlo expectation. Data efficiency is background subtracted [42].

8.3.3 Isolation Efficiency

The isolation efficiency measurement uses a similar tag-and-probe procedure, except that the probe naturally is not required to be isolated. Note too that, in the isolation efficiency measurement, the QCD background has some importance despite its relatively small contribution: QCD events differ significantly from Z muons in isolation characteristics, as also discussed in the background estimation in Section 8.7.1. Figure 8.11 shows the behavior of the isolation cut efficiency, comparing data (black) to `Pythia` (red) and `MC@NLO` (blue) $Z \to \mu\mu$ samples, with respect to the cut value. The isolation requirement has very good data/Monte Carlo agreement with `Pythia`

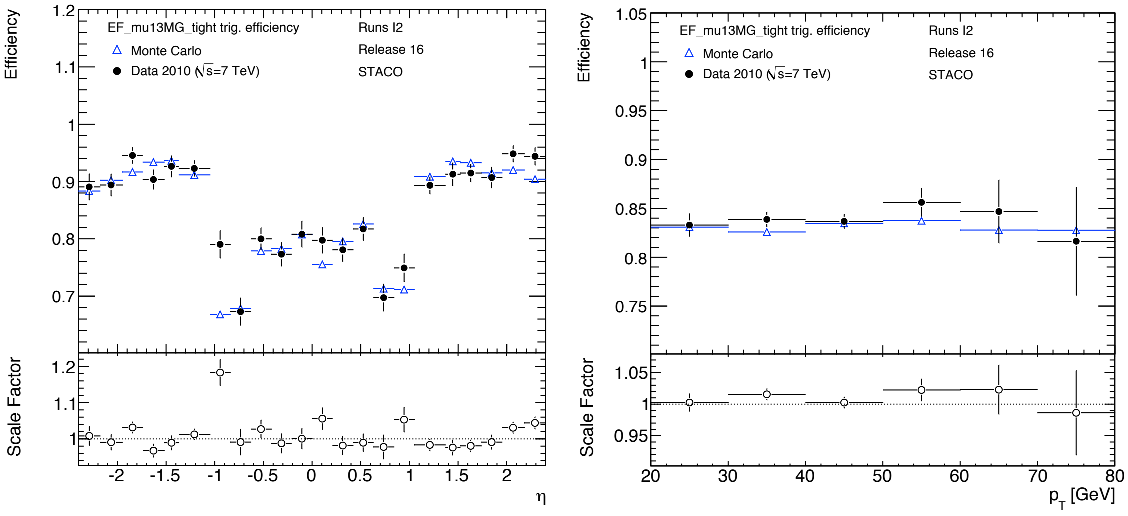

(a) vs. η.

(b) vs. p_{T}.

Figure 8.10: `EF_mu13_MG_tight` trigger efficiency with respect combined reconstruction from data, compared to the Monte Carlo expectation. Data efficiency is background subtracted [42].

at the analysis cut value of 0.2, and the estimated systematic uncertainty on isolation efficiency measurement is 0.3%. Table 8.10 produces averages of these efficiencies over the W muon distribution. The resultant scale factors as a function of η, shown in Section 8.5.3, are close to unity.

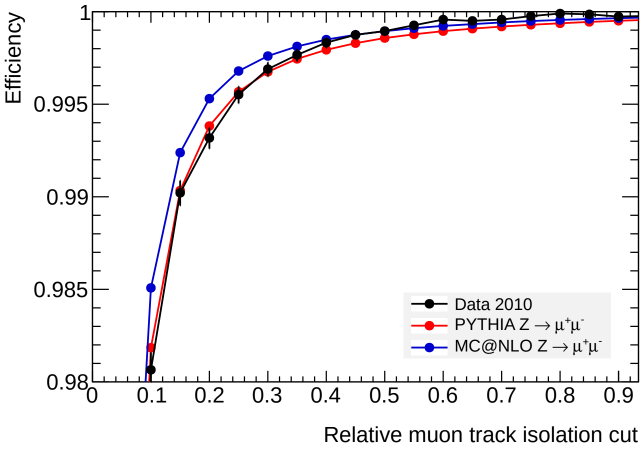

Figure 8.11: Efficiency of the relative muon track isolation cut, for background–subtracted data (black dots), `Pythia` (red curve) and `MC@NLO` (blue curve) $Z \to \mu\mu$. Errors are statistical [42].

8.4 Cross Section Methodology

The cross section calculation is similar to that described in Section 7.9, and C_{W} and A_W are as defined there. The theoretical uncertainties on the acceptance are also as described there. In contrast to that calculation however, we obtain the result by summing over bins in muon pseudorapidity.

$$\sigma_{tot} \times BR(W \to \mu\nu) = \sum_i \left(\sigma_i^{fid}\right) / A_W \tag{8.1}$$

$$= \sum_i \left(\frac{N_i - B_i}{C_{\mathrm{W}i} L_{int}}\right) \times \frac{1}{A_W} \tag{8.2}$$

The method used is to sum over binned fiducial cross sections to obtain a total fiducial cross section. We then extrapolate the result outside the fiducial region using the charge-dependent geometric acceptance A_W. Effectively, we produce a fully differential result for the fiducial cross section, then sum over the η bins taking any bin-by-bin uncertainty correlations into account where appropriate. The benefit of this approach is to facilitate rapid production of an upcoming binned, differential cross section result. Bin-by-bin uncertainties are either correlated or uncorrelated (or partly correlated), depending on the source of uncertainty and its relation between different pseudorapidity bins. The details of uncertainty treatment for such an approach are discussed in Section 8.6.

The basic principle is to apply any variations to *both* the numerator (background estimate B_i) and the denominator ($C_{\mathrm{W}i}$) simultaneously where appropriate. For example, when we vary the trigger efficiency by the scale factor uncertainty to estimate the impact, this is done in both the $C_{\mathrm{W}i}$ term, and in the electroweak part of the background term B_i. We provide a detailed description of the handing of scale factor systematic uncertainties in Section 8.6.1. As a sanity-check, and to facilitate integration with parallel fully inclusive single-bin results (for $Z \rightarrow \mu\mu$ or $W \rightarrow e\nu$, for example), we also provide effective single-bin C_{W} and background estimates.

8.5 Acceptance of $W \rightarrow \mu\nu$ Selection

The combined acceptance × efficiency is defined as in Section 7.9, as the number of events passing all of our selection, divided by the number generated. We measure this in a sample of simulated $W \rightarrow \mu\nu$ events generated using `Pythia`, obtaining a value of 37.81% with negligible statistical error. We give the number of signal events passing each step of the selection, and the efficiencies of each step relative to the previous one, in Table 8.5.

We correct this pure Monte Carlo acceptance for discrepancies between data and simulation observed in the trigger, reconstruction and isolation efficiencies, (see Section 7.6), as well as for the effects of pileup events (see Section 8.2.2). In Figure 8.12, we show the fraction of the W acceptance contributed by muons in the different detector η regions. Observe that the acceptance is reduced in the barrel because of the lower trigger coverage, and also that the bin widths are not all equal.

8.5.1 Trigger Efficiency Scale Factors

The trigger efficiency determination in data, shown in Section 8.3.2, is used to correct Monte Carlo samples. The scale factor computation is as follows: we always require simulated events to pass the `EF_mu13_MG` trigger as part of the event selection.

Selection	Number of Events	Absolute Efficiency (%)	Relative Efficiency (%)
All	6955568	100.00 ± 0.00	—
Trigger	3946209	56.73 ± 0.02	56.73 ± 0.02
Vertex	3945157	56.72 ± 0.02	99.97 ± 0.00
Combined μ	3784744	54.41 ± 0.02	95.93 ± 0.01
μ $\|\eta\| < 2.4$	3718524	53.46 ± 0.02	98.25 ± 0.01
μ $\mathrm{p}_T > 15$ GeV	3601631	51.78 ± 0.02	96.86 ± 0.01
$\|z_0 - z_{vtx}\| < 20$ mm	3593933	51.67 ± 0.02	99.79 ± 0.00
μ $p_{\mathrm{T}} > 20$ GeV	3269051	47.00 ± 0.02	90.96 ± 0.02
Isolation	3245338	46.66 ± 0.02	99.27 ± 0.00
$E_{\mathrm{T}}^{\mathrm{miss}} > 25$ GeV	2656329	38.19 ± 0.02	81.85 ± 0.02
$m_{\mathrm{T}} > 40$ GeV	2630028	37.81 ± 0.02	99.01 ± 0.01

Table 8.5: Effect of the selection criteria on simulated $W \to \mu\nu$ events. The absolute efficiency is versus the number of events in the sample, while relative efficiencies are relative to the previous step of the selection. Event counts are raw numbers from the simulation, and are not corrected for reconstruction or trigger efficiencies, or reweighted to match the pileup vertex distribution in the data. Quoted uncertainties are statistical [42].

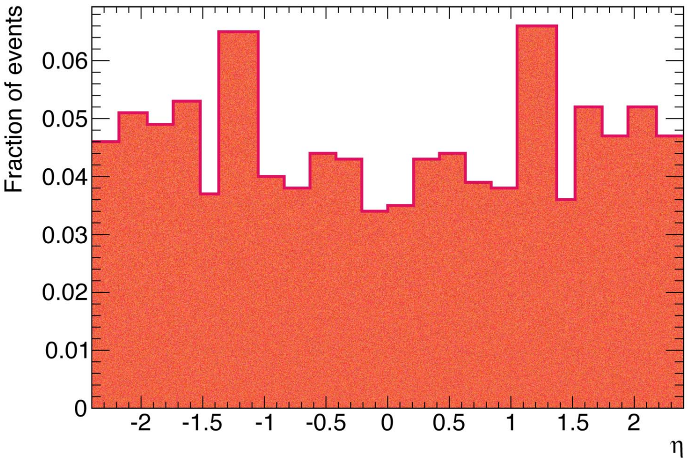

Figure 8.12: Fraction of events in the $W \to \mu\nu$ `Pythia` sample passing the event selection, as a function of muon η. Corrections for pileup, and trigger, reconstruction and isolation efficiencies have been applied [42].

In data instead we use a combination of triggers, `EF_mu13_MG` for the first part of the data (through run `167576` in period `I1`), switching to `EF_mu13_MG_tight` for the rest. These two spans are comparable in luminosity gathered, representing about 16 pb^{-1} and 18 pb^{-1} respectively. For each period, we correct the Monte Carlo by the ratio of triggering probability seen in data to that in simulation. Because of the use of different triggers in data, we apply the luminosity-weighted average of these two scale factors to Monte Carlo events. This luminosity-averaged scale factor f_{trig}, obtained separately in each of the 22 η bins, is shown in Figure 8.13. We show trigger scale factors for positive and negative muons separately, together with a scale factor averaged over them, where the charge average is on the tag-and-probe $Z \to \mu\mu$ sample. We use charge-separated scales for the trigger, and apply them bin-by-bin to Monte Carlo events in all the electroweak samples. In addition to the statistical errors shown in Figure 8.13, the trigger scale factor has fractional systematic uncertainties of 0.3% for `EF_mu13_MG` and 0.5% for `EF_mu13_MG_tight`, as discussed in Section 8.3.2. Again, we use the luminosity-weighted average (0.41%) of these two numbers in the analysis.

We also calculate the weighted average of trigger efficiencies in data and in simulation using the η distribution of $W \to \mu\nu$ muons passing all selection criteria. We report the values in Table 8.6, and the resulting average scale factor in Table 8.7.

8.5.2 Muon Reconstruction Efficiency Scale Factors

To obtain the scale factor for muon reconstruction efficiency, f_{reco}, we compare data and Monte Carlo muon reconstruction efficiencies (as seen in Section 8.3.1), bin-

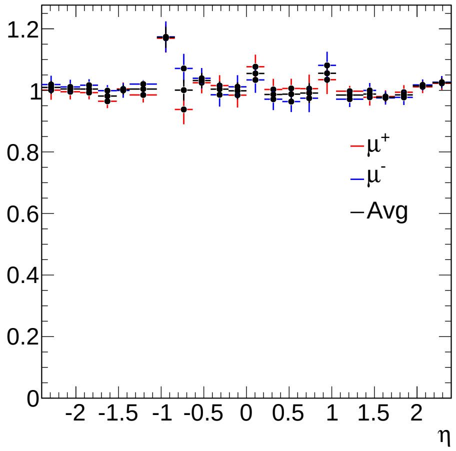

Figure 8.13: Scale factor applied in the $W \to \mu\nu$ analysis to correct for differences in trigger efficiency between data and simulation, shown separately versus η bin for positive (red), negative (blue) and all muons (black). The scales have been averaged over the two triggers used. Errors are statistical [42].

Charge	Efficiency in Data	Efficiency in MC
μ^+	0.870 ± 0.004	0.866
μ^-	0.867 ± 0.004	0.858

Table 8.6: Event trigger efficiencies in data and Monte Carlo, weighted over the $W \to \mu\nu$ muon η distribution. The errors reflect the statistics of the efficiency, not that of the weighting distribution [42].

by-bin, separately for the two charges. This scale factor also accounts for the muon quality criteria detailed in Section 8.2.1, and its systematic uncertainties include any differences in their relative impact upon data and Monte Carlo. The scale factor with its statistical uncertainties is shown in Figure 8.14. In addition, f_{reco} has a fractional systematic uncertainty of 0.4% (Section 8.3.1). The weighted averages of the reconstruction efficiencies (over the corresponding muon η distributions in W Monte Carlo) are shown in Table 8.8 and the associated scale factors appear in Table 8.9.

Charge	Scale Factor	Statistical Error	Systematic Error
μ^+	1.004	0.004	0.004
μ^-	1.011	0.004	0.004

Table 8.7: Trigger efficiency scale factor for $W \to \mu\nu$ with associated errors (the systematic term is fractional).

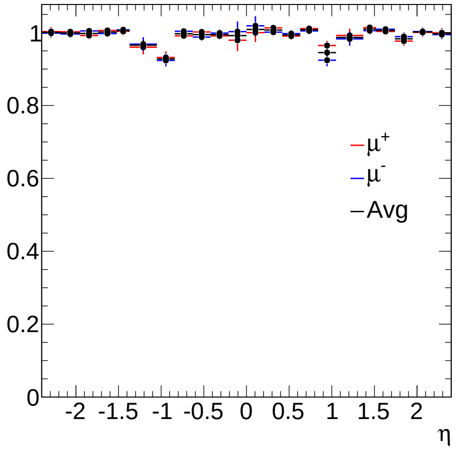

Figure 8.14: Scale factor applied in the $W \to \mu\nu$ analysis to correct for differences in muon reconstruction efficiency between data and simulation, shown separately versus η bin for positive (red), negative (blue) and all muons (black). Errors are statistical [42].

8.5.3 Muon Isolation Efficiency Scale Factors

With increased statistics, it is possible to account for differences in isolation efficiency between data and simulation, and we apply a correction f_{isol} to the Monte Carlo isolation efficiency. We show the scale factor in Figure 8.15, where it is clear that the statistical error is small and that the scale factor is close to unity. The statistical error is dominated by the systematic term, which is estimated at 0.3%. (Section 8.3.3). Our results are tabulated in Tables 8.10 and 8.11.

Charge	Efficiency in Data	Efficiency in MC
μ^+	0.931 ± 0.003	0.938
μ^-	0.928 ± 0.003	0.936

Table 8.8: Muon reconstruction efficiencies in data and Monte Carlo, weighted over the $W \to \mu\nu$ muon η distribution. The errors reflect the statistics of the efficiency, and not that of the weighting distribution [42].

Charge	Scale Factor	Statistical Error	Systematic Error
μ^+	0.993	0.003	0.004
μ^-	0.991	0.003	0.004

Table 8.9: Reconstruction efficiency scale factor for $W \to \mu\nu$ events with associated errors (the systematic term is fractional) [42].

8.5.4 Overall Muon Scale Factors

We independently apply all the scale factors f_{trig}, f_{reco} and f_{isol} to Monte Carlo events, treating the associated uncertainties as independent, as discussed in Section 8.6.1. This amounts to a combined scale factor that is the product of the individual scale factors discussed above, where the relative errors for the scale factors combine quadratically. This combined scale factor is shown in Table 8.12.

Charge	Efficiency in Data	Efficiency in MC
μ^+	0.993 ± 0.001	0.994
μ^-	0.994 ± 0.001	0.994

Table 8.10: Muon isolation efficiencies in data and Monte Carlo, weighted over the $W \to \mu\nu$ muon η distribution. The errors reflect the statistics of the efficiency, and not that of the weighting distribution [42].

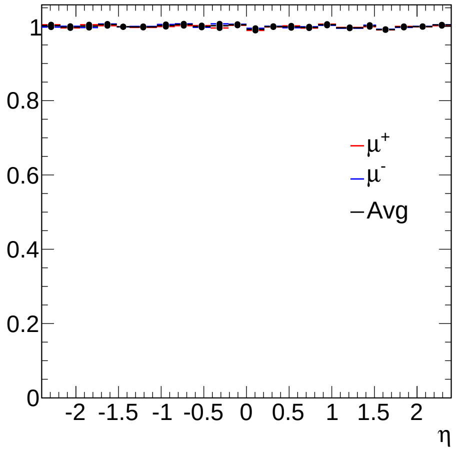

Figure 8.15: Scale factor applied in the $W \to \mu\nu$ analysis to correct for differences in muon isolation efficiency between data and simulation, shown separately versus η bin for positive (red), negative (blue) and all muons (black). Errors are statistical [42].

Charge	Scale Factor	Statistical Error	Systematic Error
μ^+	0.999	0.001	0.003
μ^-	1.000	0.001	0.003

Table 8.11: Isolation efficiency scale factor for $W \to \mu\nu$ events with associated errors (the systematic term is fractional) [42].

Charge	Scale Factor	Statistical Error	Systematic Error
μ^+	0.996	0.005	0.006
μ^-	1.002	0.005	0.006

Table 8.12: Overall muon scale factor for $W \to \mu\nu$ with associated errors (the systematic term is fractional) [42].

8.5.5 Fiducial Acceptance C_W for $W \to \mu\nu$

The fiducial acceptance is defined as in Section 7.9. The overall analysis C_W comes from the $W \to \mu\nu$ Monte Carlo, with corrections for pileup weights, as well as for trigger, reconstruction and isolation efficiencies. We show C_W for both positive and negative muons in Figure 8.16, and apply these weights in a binned manner, separately for the two charges, as described in Section 8.6.

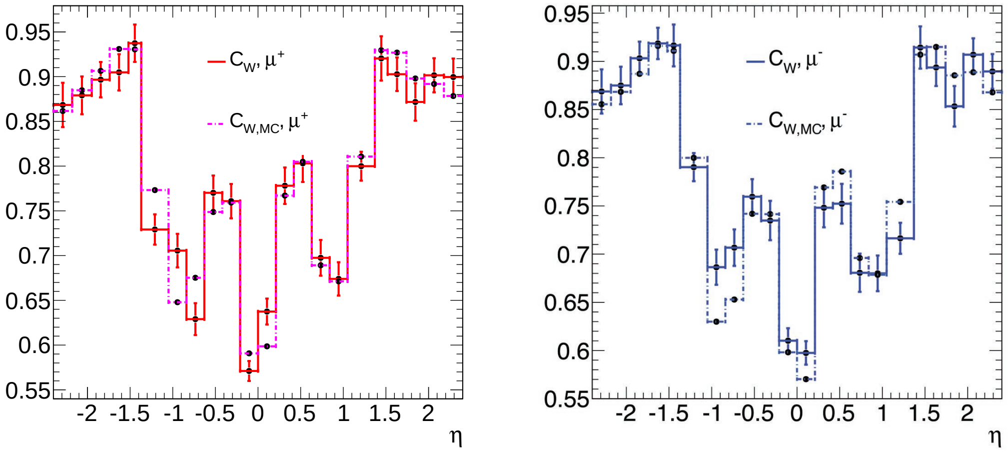

(a) μ^+

(b) μ^-

Figure 8.16: Fiducial acceptance C_W, shown separately for positive (left) and negative (right) muons. The solid (dashed) plots are (un)corrected for trigger, reconstruction and isolation scale factors. Errors are statistical, and include Monte Carlo statistics, as well as those on the scale factors (for the solid plots) [42].

Our analysis sums the binned fiducial cross sections, but we also provide an integrated C_{W}. The central values are the weighted averages of the binned C_{W}, where the weights are the respective cross sections. For the average over positive and negative charges, we also include differences in A_W between the charges. The associated error combines those in Tables 8.15 - 8.17 for the muon trigger, reconstruction and isolation efficiencies, muon p_{T} resolution and scale, missing energy resolution and scale and jet cleaning. Background uncertainties instead are not included in the C_{W} and are shown in Section 8.7.2. These C_{W} values are presented in Table 8.13.

W	W^+	W^-
0.7896 ± 0.0176	0.7944 ± 0.0201	0.7800 ± 0.0189

Table 8.13: Muon fiducial acceptance C_{W}. The central values are the weighted averages of the binned C_{W} in Section 8.5.5, where the binned cross sections are used as weights. The errors include all non-background systematic uncertainties [42].

8.5.6 Geometrical Acceptance A_W for $W \to \mu\nu$

Geometrical acceptances for the muon analysis are as for the previous iteration of this analysis, and are reported in Table 8.14. The central values for A_W are obtained using `Pythia` with MRST LO*.

W	W^+	W^-
$0.4800 \pm 3\%$	$0.4840 \pm 3\%$	$0.4743 \pm 3\%$

Table 8.14: Muon geometrical acceptance A_W [42].

8.6 Systematic Uncertainties

The determination of the correction factors C_{W} for the fiducial cross section measurements includes all detector effects. We consider experimental systematic uncertainties on the $W \to \mu\nu$ measurement arising from scale factors (on trigger, muon reconstruction and identification, and isolation efficiencies), muon momentum resolution and scale, $E_{\mathrm{T}}^{\mathrm{miss}}$ scale and resolution, and event preselection, specifically the jet cleaning requirement. We describe briefly our procedure for extracting and combining these uncertainties now.

8.6.1 Scale Factors

The trigger, muon reconstruction, and isolation efficiency scale factors f_{trig}, f_{reco} and f_{isol} with their statistical and systematic uncertainties are topics already considered in Section 8.5. We apply these scale factors to both signal and the electroweak Monte Carlo samples, and corrections are made bin-by-bin, separately for the two charges. We now describe the propagation of scale factor uncertainties to the cross section.

For the statistical part of the scale factor uncertainty, we deploy a toy Monte Carlo procedure. For each η bin i in the two charges q separately, we vary the scale factor $f^{i,q}$ by a Gaussian die-roll governed by its statistical error. This modified scale factor we apply to C_{W} and to the electroweak backgrounds, recomputing the fiducial cross section σ_{FID} in the bin. Repeating the procedure $1,000$ times, we get distributions of binned fiducial cross section distributions, which may be fitted to Gaussians. The distributions of binned fiducial cross sections obtained from these toy variations are shown in Figures 8.17, 8.18 and 8.19. The fit widths then give the error on the fiducial cross section in i, q from the scale factor. The same procedure also yields the uncertainty upon the integrated cross section, where we fit instead for the width of the sum of fiducial cross sections in the bins, iterated $1,000$ times, relying on the toy Monte Carlo to handle the statistical errors in the sum over bins. Fits to these integrated distributions are shown in Figures 8.20, 8.21 and 8.22. The error for the sum over positive and negatively-charged muon events is simply the quadratic sum of the respective toy Monte Carlo errors.

Instead, for the systematic component, we vary the scale factor in all bins up or down together by 1σ using the fractional scale factor errors given in Section 8.3. The error on the cross section for the up (down) variation in the scale factor systematic uncertainty is the difference between the modified and nominal fiducial cross sections. The up and down variations give very similar results, so we take their average. The overall error on the cross section from the scale factor is from the combination of the statistical and systematic components just described. In each bin, the combination of systematic and statistical errors is quadratic. Across bins, the statistical part is combined quadratically while the systematic portion sums linearly. The systematic term for positive muons is deemed fully correlated with that for negative ones. We summarize scale factor systematic uncertainties on the cross section in Tables 8.15, 8.16 and 8.17. The statistical uncertainties from f_{trig}, f_{reco} and f_{isol} are currently treated as independent.

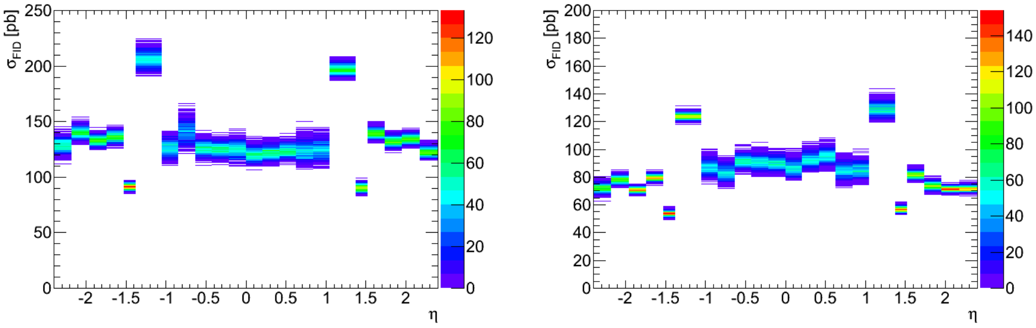

(a) μ^+ (b) μ^-

Figure 8.17: Toy Monte Carlo variations of the trigger scale factor, showing the impact upon fiducial cross sections for positive (left) and negative (right) muons. We fit the distributions in the bins to Gaussians, with the widths giving errors on the cross section from the statistics of f_{trig} [42].

8.6.2 Muon Resolution

The detector alignment and material descriptions in Monte Carlo are somewhat improved from those in Section 7.7. Nevertheless, we need additional smearing of the muon p_{T} to reproduce the data. The procedure is to introduce correction terms for the p_{T} measurements in both the ID and the MS. For this, we use a template technique, varying Monte Carlo distributions till they best match data [37]. The distributions used are the dimuon invariant mass distribution, and the q/p difference for MS and ID measurements of the muon. We use four Muon Spectrometer regions in η for these additional smearing: barrel, transition region, endcap and forward (CSC).

Unlike in Section 7.7, the central value of the cross section is obtained by using the smeared Monte Carlo samples. The smearing is performed for both signal and electroweak background samples. For consistency, we recompute the isolation, missing energy and transverse mass using the smeared momentum. We conservatively

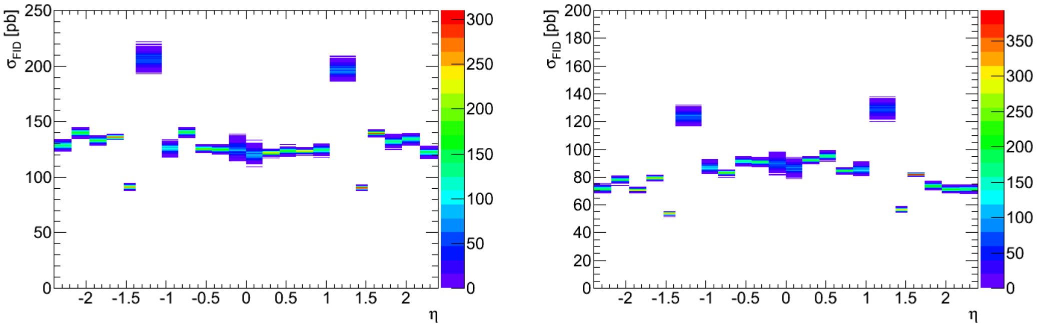

(a) μ^+

(b) μ^-

Figure 8.18: Toy Monte Carlo variations of the muon reconstruction scale factor, showing the impact upon fiducial cross sections for positive (left) and negative (right) muons. We fit the distributions in the bins to Gaussians, with the widths yielding errors on the cross section from the statistics of f_{reco} [42].

estimate the effect of this smearing upon our result by extracting the cross section without use of resolution smearing, and taking the full difference as systematic. This systematic term is correlated between η bins and charges. Tables 8.15, 8.16 and 8.17 provide the net impact upon the cross sections.

8.6.3 Muon Momentum Scale

We do not impose an additional scale upon muons in Monte Carlo for the central value. However, we examine the impact of momentum-scale mis-measurements upon the cross section by extracting the cross section after applying momentum-scale corrections (determined from momentum-scale measurements performed in an earlier software release), and treating the full range as systematic. This systematic uncertainty is subject to improvement with more detailed scale studies on Z and W bosons. We treat the number as correlated between charges and η bins, results being given in

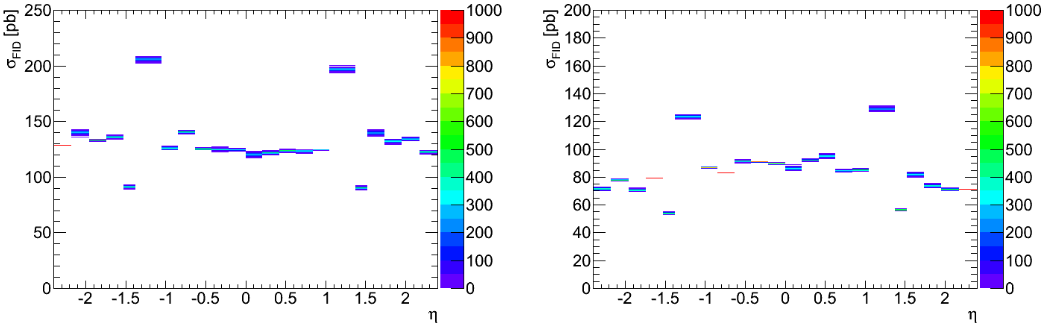

(a) μ^+

(b) μ^-

Figure 8.19: Toy Monte Carlo variations of the muon isolation scale factor, showing the impact upon fiducial cross sections for positive (left) and negative (right) muons. We fit the distributions in the bins to Gaussians, with the widths giving errors on the cross section from the statistics of f_{isol} [42].

Tables 8.15, 8.16 and 8.17.

8.6.4 Missing Energy Resolution and Scale

The treatment of muon resolution and scale above covers the systematic uncertainty on the muon part of $E_{\text{T}}^{\text{miss}}$ (`MET_MuonBoy` and `MET_RefMuonTrack`), since the muon part of the missing energy is fully correlated with the muon measurement. As such, recalculating the $E_{\text{T}}^{\text{miss}}$, isolation and m_{T} after the muon resolution/scale accounts for the full impact of muon resolution on the measurement, including the impact via missing energy.

Instead the calorimeter component, `MET_LocHadTopo`, has been studied separately and the cluster energy scale and resolution are known to 7% and 5% respectively. We have assessed the net impact upon $W \to \mu\nu$ as a constant (charge and η independent) 2% uncertainty on the acceptance.

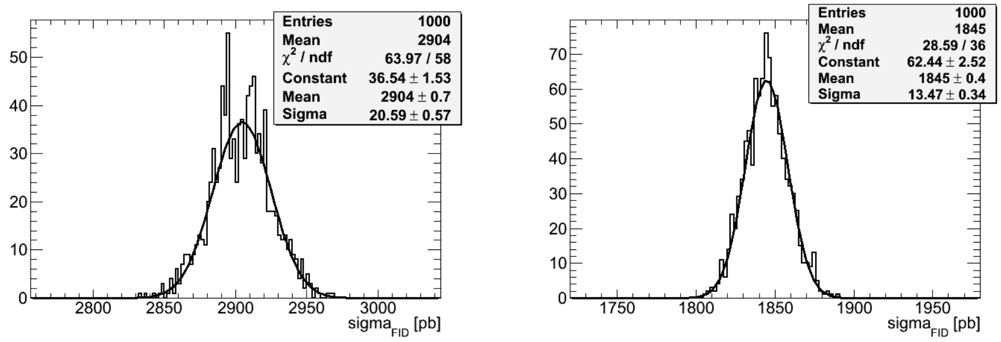

(a) μ^+

(b) μ^-

Figure 8.20: Fit to the distribution of integrated fiducial cross sections upon toy Monte Carlo variations of f_{trig}. The width gives the error on the cross section from the statistics of the scale factor [42].

8.6.5 Jet Cleaning Criteria

The modified jet cleaning requirement discussed in Section 8.2.3 has 99.92% efficiency in our dataset, comparable to the value in Table 7.13. However, as shown in figures 8.4, 8.5 and 8.6, events failing this requirement look signal-like. Hence we take the inefficiency of this requirement as a fractional systematic, 0.07% on the cross section.

8.6.6 Summary of Systematic Uncertainties

We present the systematic uncertainties for W^+, W^- and W in Tables 8.15 - 8.17.

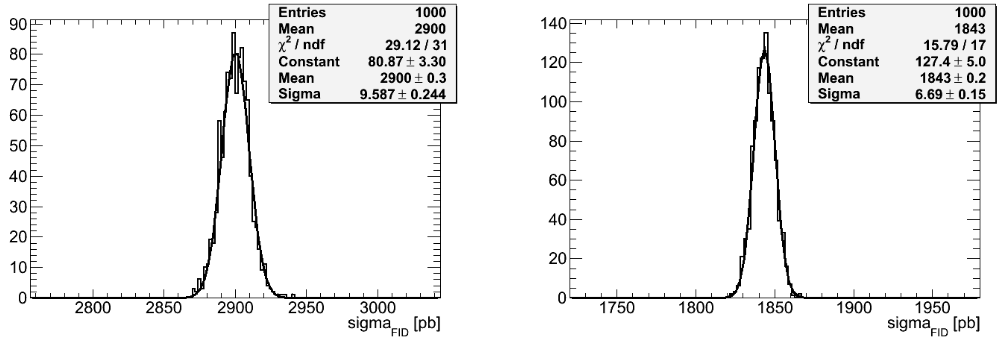

(a) μ^+ (b) μ^-

Figure 8.21: Fit to the distribution of integrated fiducial cross section upon toy Monte Carlo variation of $f_{\rm reco}$. The width gives the error on the cross section from the statistics of the scale factor [42].

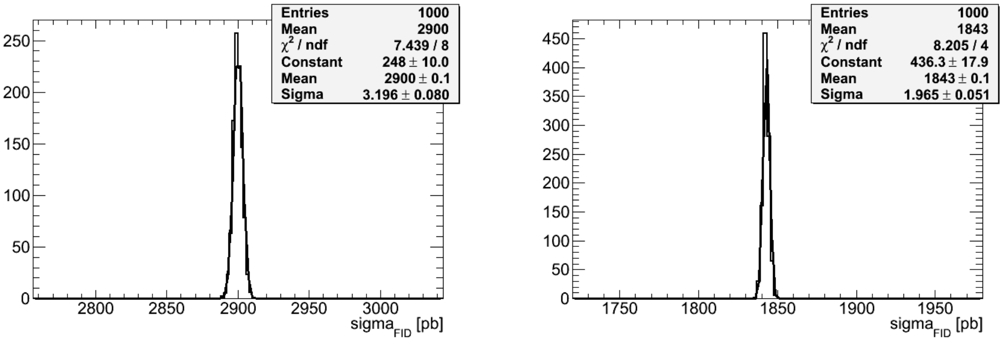

(a) μ^+ (b) μ^-

Figure 8.22: Fit to the distribution of integrated fiducial cross section upon toy Monte Carlo variation of $f_{\rm isol}$. The width gives the error on the cross section from the statistics of the scale factor [42].

Type	Systematic (%)	Systematic (Value) [pb]
Electroweak Background	0.38	22.85
Trigger Efficiency	0.83	50.00
Reconstruction Efficiency	0.55	32.67
Isolation Efficiency	0.34	20.30
QCD Estimation	0.67	40.40
Muon p_{T} Resolution	0.03	1.63
Muon p_{T} Scale	1.13	67.84
Jet Cleaning	0.07	4.01
$E_{\mathrm{T}}^{\mathrm{miss}}$ Resolution and Scale	2.00	119.82
Experimental	2.65	158.47
Theoretical	3.00	179.73
Non-luminosity	4.00	239.62
Luminosity	3.40	217.13

Table 8.15: Systematic uncertainties for W^+ signal [42].

Type	Systematic (%)	Systematic (Value) [pb]
Electroweak Background	0.50	19.84
Trigger Efficiency	0.86	34.12
Reconstruction Efficiency	0.57	22.53
Isolation Efficiency	0.34	13.62
QCD Estimation	1.12	44.53
Muon p_{T} Resolution	0.02	0.64
Muon p_{T} Scale	0.82	32.30
Jet Cleaning	0.07	2.65
$E_{\mathrm{T}}^{\mathrm{miss}}$ Resolution and Scale	2.00	79.17
Experimental	2.72	107.48
Theoretical	3.00	118.76
Non-luminosity	4.05	160.18
Luminosity	3.40	146.32

Table 8.16: Systematic uncertainties for W^- signal [42].

Type	Systematic (%)	Systematic (Value) [pb]
Electroweak Background	0.43	42.64
Trigger Efficiency	0.68	67.65
Reconstruction Efficiency	0.50	49.53
Isolation Efficiency	0.33	33.07
QCD Estimation	0.83	82.81
Muon p_{T} Resolution	0.02	2.28
Muon p_{T} Scale	0.37	36.41
Jet Cleaning	0.07	6.67
$E_{\mathrm{T}}^{\mathrm{miss}}$ Resolution and Scale	2.00	199.00
Experimental	2.42	240.37
Theoretical	3.00	298.49
Non-luminosity	3.85	383.24
Luminosity	3.40	363.39

Table 8.17: Systematic uncertainties for W signal [42].

8.7 Backgrounds

8.7.1 QCD Background

We estimate the QCD background to $W \to \mu\nu$ using an improved version of the "matrix" method, described for the early analysis in Section 7.5.2. We again use loose and tight muon samples defined using relative isolation to solve a two-variable linear system for the number of QCD events in data. However, for the 33 pb^{-1} analysis, we compute this expectation separately for each charge, and for each bin in η. Suppose in η bin i we have $N^{+(-)}_{\mathrm{loose,i}}$ positive (negative) charge muon events in data without the isolation requirement, and instead $N^{+(-)}_{\mathrm{isol,i}}$ positive (negative) muon events after imposing the relative track-isolation requirement. If we let $\epsilon^{+(-)}_{\mathrm{non-QCD,i}}$ and $\epsilon^{+(-)}_{\mathrm{QCD,}}$ denote the relative isolation efficiencies (in bin i, for the appropriate muon charge) for non-QCD events (that is, from signal and from electroweak sources) and for the QCD background, then we have:

$$\begin{aligned} N^{+(-)}_{\mathrm{loose,i}} &= N^{+(-)}_{\mathrm{non-QCD,i}} + N^{+(-)}_{\mathrm{QCD,i}} \\ N^{+(-)}_{\mathrm{isol,i}} &= \epsilon^{+(-)}_{\mathrm{non-QCD,i}} N^{+(-)}_{\mathrm{non-QCD,i}} + \epsilon^{+(-)}_{\mathrm{QCD,i}} N^{+(-)}_{\mathrm{QCD,i}} \end{aligned} \tag{8.3}$$

From these two equations in $N^{+(-)}_{\mathrm{non-QCD,i}}$ and $N^{+(-)}_{\mathrm{QCD,i}}$ we obtain:

$$N^{+(-)}_{\mathrm{QCD,i}} = \frac{N^{+(-)}_{\mathrm{loose,i}} \epsilon^{+(-)}_{\mathrm{non-QCD,i}} - N^{+(-)}_{\mathrm{isol,i}}}{\epsilon^{+(-)}_{\mathrm{non-QCD,i}} - \epsilon^{+(-)}_{\mathrm{QCD,i}}} \tag{8.4}$$

The statistical uncertainty on $N^{+(-)}_{\mathrm{QCD,i}}$ is as follows, where $\alpha^{+(-)}_i = N^{+(-)}_{\mathrm{isol,i}} / N^{+(-)}_{\mathrm{loose,i}}$

is the efficiency of the isolation requirement on all data:

$$\begin{aligned}\frac{\delta N^{+(-)}_{\mathrm{QCD,i}}}{N^{+(-)}_{\mathrm{QCD,i}}} = & \quad \frac{1}{\sqrt{N^{+(-)}_{\mathrm{loose,i}}}} \oplus \left(\frac{\delta\epsilon^{+(-)}_{\mathrm{non-QCD,i}}}{\epsilon^{+(-)}_{\mathrm{non-QCD,i}} - \alpha_i^{+(-)}} - \frac{\delta\epsilon^{+(-)}_{\mathrm{non-QCD,i}}}{\epsilon^{+(-)}_{\mathrm{non-QCD,i}} - \epsilon^{+(-)}_{\mathrm{QCD,i}}} \right) \\ & \oplus \frac{\delta\alpha_i^{+(-)}}{\epsilon^{+(-)}_{\mathrm{non-QCD,i}} - \alpha_i^{+(-)}} \oplus \frac{\delta\epsilon^{+(-)}_{\mathrm{QCD,i}}}{\epsilon^{+(-)}_{\mathrm{non-QCD,i}} - \epsilon^{+(-)}_{\mathrm{QCD,i}}} \end{aligned} \tag{8.5}$$

The expected number of QCD events after the isolation (tight) requirement is then $\epsilon^{+(-)}_{\mathrm{QCD,i}} N^{+(-)}_{\mathrm{QCD,i}}$. The relative uncertainty on this final number is:

$$\begin{aligned} & \frac{1}{\sqrt{N^{+(-)}_{\mathrm{loose,i}}}} \oplus \frac{\delta\epsilon^{+(-)}_{\mathrm{non-QCD,i}} \left(\alpha_i^{+(-)} - \epsilon^{+(-)}_{\mathrm{QCD,i}}\right)}{\left(\epsilon^{+(-)}_{\mathrm{non-QCD,i}} - \alpha_i^{+(-)}\right)\left(\epsilon^{+(-)}_{\mathrm{non-QCD,i}} - \epsilon^{+(-)}_{\mathrm{QCD,i}}\right)} \oplus \\ & \frac{\delta\alpha_i^{+(-)}}{\left(\epsilon^{+(-)}_{\mathrm{non-QCD,i}} - \alpha_i^{+(-)}\right)} \oplus \frac{\delta\epsilon^{+(-)}_{\mathrm{QCD,i}} \epsilon^{+(-)}_{\mathrm{non-QCD,i}}}{\epsilon^{+(-)}_{\mathrm{QCD,i}} \left(\epsilon^{+(-)}_{\mathrm{non-QCD,i}} - \epsilon^{+(-)}_{\mathrm{QCD,i}}\right)} \end{aligned} \tag{8.6}$$

We find the isolation efficiency for QCD events from a control sample of muons between 15 and 20 GeV, in events with $E_{\mathrm{T}}^{\mathrm{miss}} < 25$ GeV and $m_{\mathrm{T}} < 40$ GeV. We expect these muons to be predominantly QCD (inspect, for example the preselection plots in Section 7.4). Nevertheless, we perform electroweak subtraction using the $W \to \mu\nu$, $W \to \tau\nu$, $Z \to \mu\mu$, $Z \to \tau\tau$ and $t\bar{t}$ samples, utilizing an iterative procedure to normalize these samples. The iterations converge rapidly, as can be seen in Figure 8.23, and the variation in the central value of the QCD estimate is negligible. These isolation efficiencies in control-region data are shown for the two charges in Figure 8.24(a). We apply the difference between data and Monte Carlo efficiencies in this control sample bin-by-bin as a systematic uncertainty upon the QCD efficiency in the control region.

We correct the control region data efficiency using the ratio of isolation efficiencies in jet Monte Carlo above and below the p_{T}, $E_{\mathrm{T}}^{\mathrm{miss}}$ and m_{T} cuts, to transport the isolation efficiencies to the signal regime in muon p_{T}. The scale is shown in Figure 8.24(b). To estimate the systematic uncertainty on this correction, we compare efficiencies between QCD Monte Carlo and electroweak subtracted data, in two different partial-extrapolation scenarios. First, in $p_{\mathrm{T}}(\mu)$ versus m_{T}, we proceed from control to signal region by examining the efficiency difference versus $p_{\mathrm{T}}(\mu)$ at low m_{T} followed by examining the efficiency difference versus m_{T} at high $p_{\mathrm{T}}(\mu)$. The corresponding plots are shown for the two charges in Figures 8.25 and 8.26. The total efficiency difference between data and Monte Carlo from this pathway gives us a systematic uncertainty on the QCD isolation efficiency. We repeat the procedure in the $p_{\mathrm{T}}(\mu)$ versus $E_{\mathrm{T}}^{\mathrm{miss}}$ plane, where we examine efficiency difference in $p_{\mathrm{T}}(\mu)$ at low $E_{\mathrm{T}}^{\mathrm{miss}}$ followed by looking in $E_{\mathrm{T}}^{\mathrm{miss}}$ at high $p_{\mathrm{T}}(\mu)$, as seen in Figures 8.27 and 8.28. We linearly add the systematic uncertainties from the different extrapolations, and apply the larger value to both charges. This is a conservative estimate of the systematic uncertainty that affects the correction of the QCD efficiency from the 15 GeV $< p_{\mathrm{T}}(\mu) <$ 20 GeV, $E_{\mathrm{T}}^{\mathrm{miss}} <$ 25 GeV, $m_{\mathrm{T}} <$ 40 GeV to the $p_{\mathrm{T}}(\mu) >$ 20 GeV, $E_{\mathrm{T}}^{\mathrm{miss}} >$ 25 GeV, $m_{\mathrm{T}} >$ 40 GeV samples.

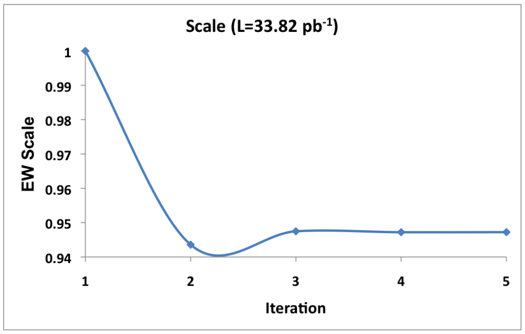

Figure 8.23: Iterative variation in electroweak scale in QCD prediction [42].

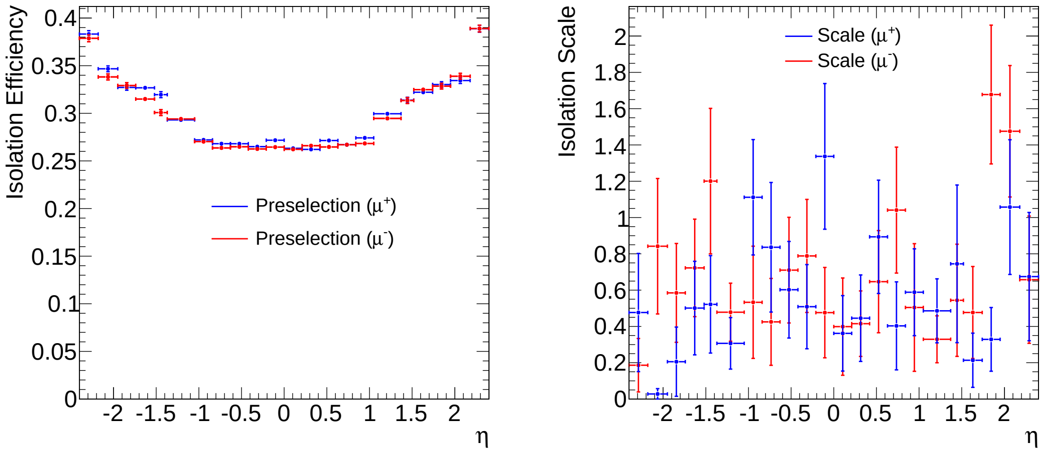

(a) Isolation efficiency, Control region data

(b) Isolation scale, QCD MC

Figure 8.24: Efficiency of the isolation requirement for QCD events is estimated using 15 − 20 GeV muons in data, for which the isolation efficiency is shown on the left. This is extrapolated into the signal region using as scale the ratio between the respective isolation efficiencies in the muon-filtered jet sample (right) [42].

The isolation efficiency for prompt muons $\epsilon_{\text{non-QCD}}$ comes from $Z \to \mu\mu$ events using tag-and-probe methods. The overall isolation efficiencies $\epsilon_{\text{QCD,i}}$ and $\epsilon_{\text{non-QCD,i}}$ are depicted in Figure 8.29. Given these isolation efficiencies, we can apply them to a suitable "loose" sample in data, specifically the set of events passing all requirements except the isolation itself; equivalently, our isolated/tight sample is in fact the W selection itself. The ratio $N^{+(-)}_{\text{isol,i}}/N^{+(-)}_{\text{loose,i}}$ is the fraction of events (which includes QCD and non-QCD events) passing the isolation requirement, as shown in Figure 8.30. The final prediction is 1079 ± 147 (sta) ± 484 (sys) for positive muon events, while for negative muons it is 1248 ± 168 (sta) ± 557 (sys), the systematic uncertainties being correlated between the two charges. To propagate these errors to the cross section, we use the techniques already described for the scale factors in Section 8.6.1, with

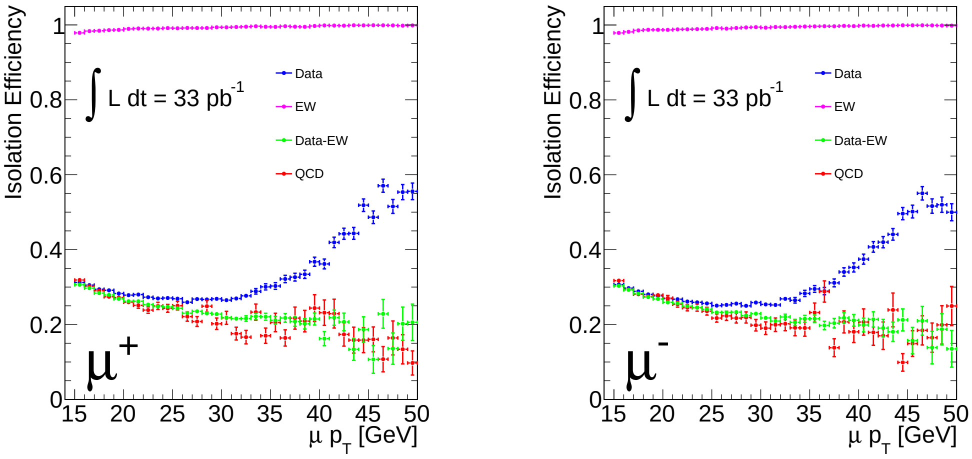

(a) Positive

(b) Negative

Figure 8.25: Efficiency of the isolation requirement versus muon p_{T}, compared between electroweak subtracted data and jet Monte Carlo, for events in the control region in m_{T} [42].

a toy MC procedure performed upon the statistical part, and combined in a correlated manner with the systematic component. The corresponding plots are shown in Figures 8.32 and 8.33.

8.7.2 Electroweak Backgrounds

Electroweak backgrounds produce high-p_{T} muons from a real W or Z bosons, as described in Section 7.5.1. As backgrounds to $W \to \mu\nu$, we consider the W/Z backgrounds $W \to \tau\nu$, $Z \to \mu\mu$, and $Z \to \tau\tau$, $t\bar{t}$, and the diboson backgrounds WW, WZ and ZZ. For these backgrounds, we estimate the number of events in our candidate sample based upon the acceptance for each process, scaled by the cross section for the process, and normalised to the integrated luminosity of the data set.

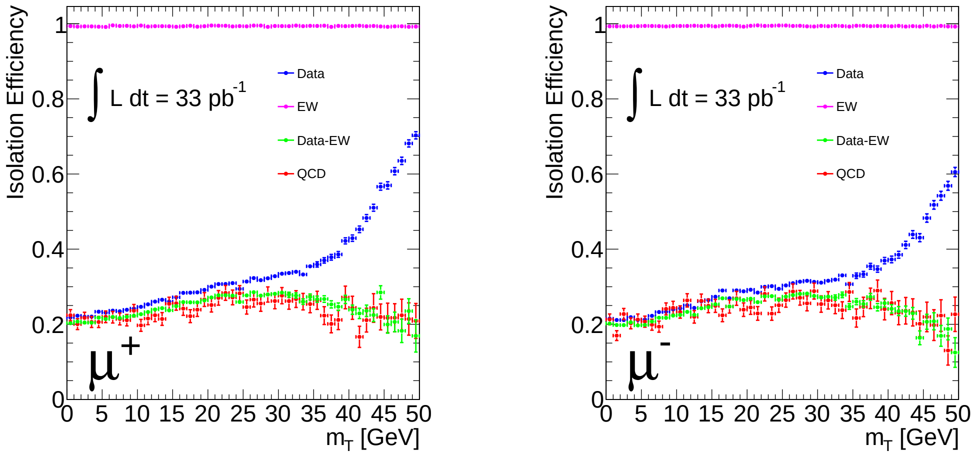

(a) Positive (b) Negative

Figure 8.26: Efficiency of the isolation requirement versus m_{T}, compared between electroweak subtracted data and jet Monte Carlo, for events in the signal region in muon p_{T} [42].

Predictions are also scaled by the efficiency scale factor corrections trigger efficiency corrections f_{trig}, f_{reco} and f_{isol}. We show the predicted fractions of events for these various background samples, in Tables 8.18 and 8.19.

We assign a 3% background systematic uncertainty from PDF dependence, and also consider uncertainties on the theoretical cross sections used to normalize the predictions. These cross section uncertainties are 5% for $W \to \tau\nu$, $Z \to \mu\mu$, $Z \to \tau\tau$, WW and ZZ, 6% for $t\bar{t}$ and 7% for WZ. We treat these cross section uncertainties as fully correlated among the electroweak backgrounds. The PDF and cross section uncertainties are treated as uncorrelated among themselves. The predicted background from electroweak-type events with these uncertainties is 4320 ± 27 (sta) ± 254 (sys) for negative W while for W^+ it is 5136 ± 32 (sta) ± 302 (sys).

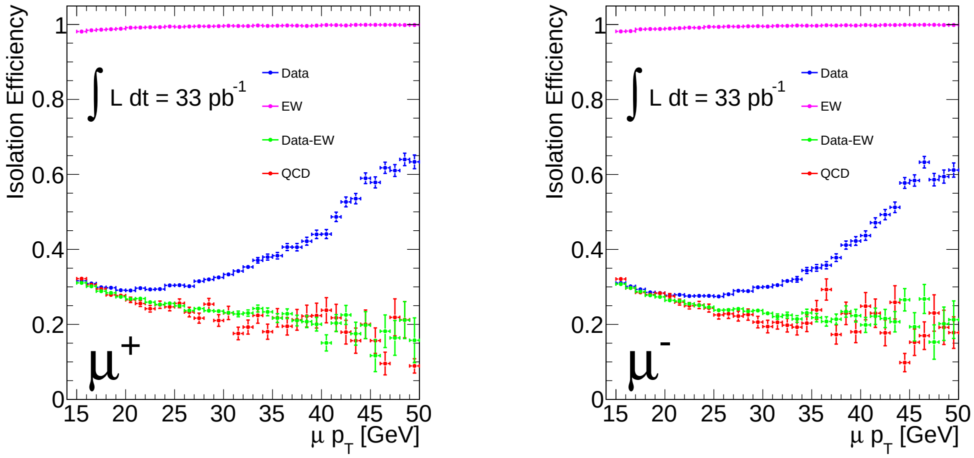

(a) Positive

(b) Negative

Figure 8.27: Efficiency of the isolation requirement versus muon p_{T}, compared between electroweak subtracted data and jet Monte Carlo, for events in the control region in $E_{\mathrm{T}}^{\mathrm{miss}}$ [42].

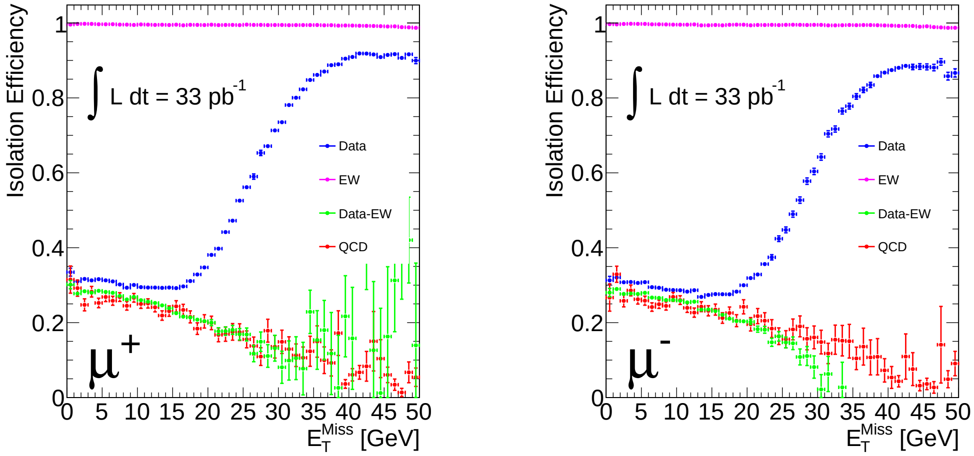

(a) Positive

(b) Negative

Figure 8.28: Efficiency of the isolation requirement versus $E_{\mathrm{T}}^{\mathrm{miss}}$, compared between electroweak subtracted data and jet Monte Carlo, for events in the signal region in muon p_{T} [42].

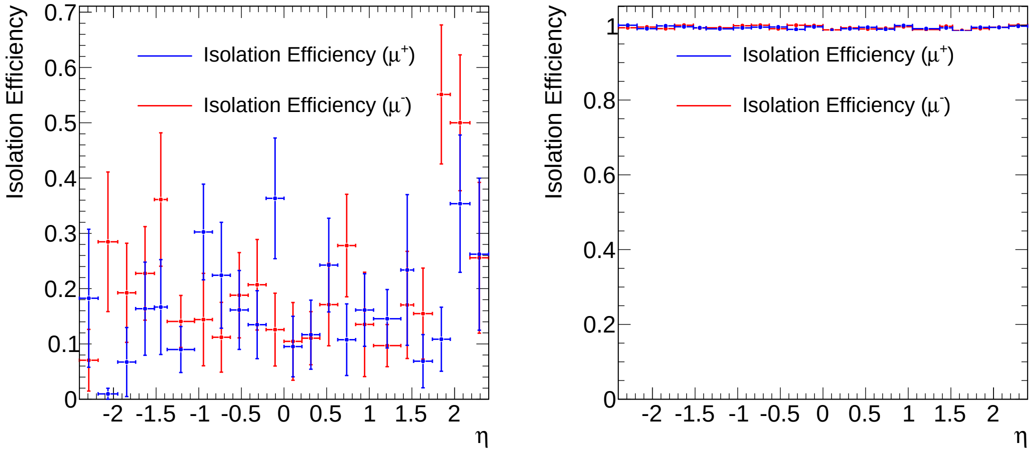

(a) Isolation efficiency, QCD muons (b) Isolation efficiency, prompt muons

Figure 8.29: Efficiency of the isolation requirement for QCD muons on the left, after extrapolation to the signal region. On the right, the isolation efficiency for prompt muons, with Z tag-and-probe [42].

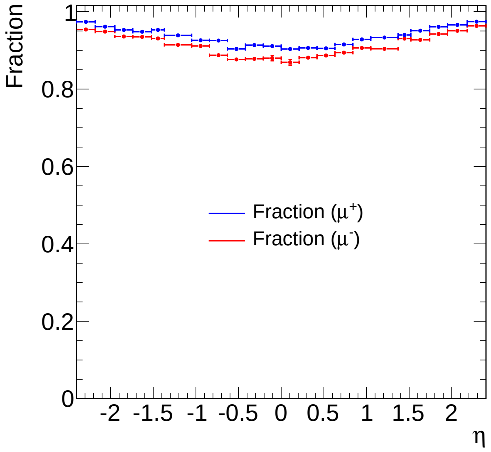

Figure 8.30: Fraction of events passing the isolation requirement in data after all other cuts have been applied [42].

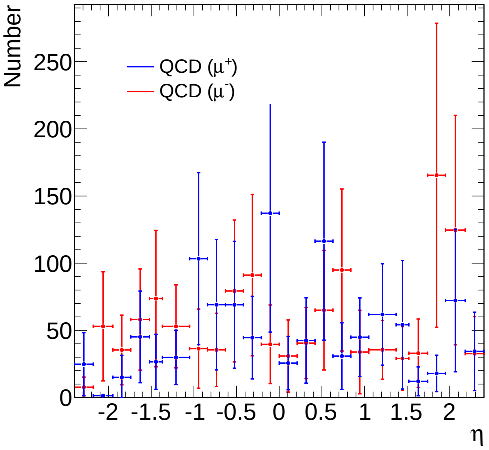

Figure 8.31: The QCD prediction for positive and negatively charged muons is shown, with the combined uncertainty [42].

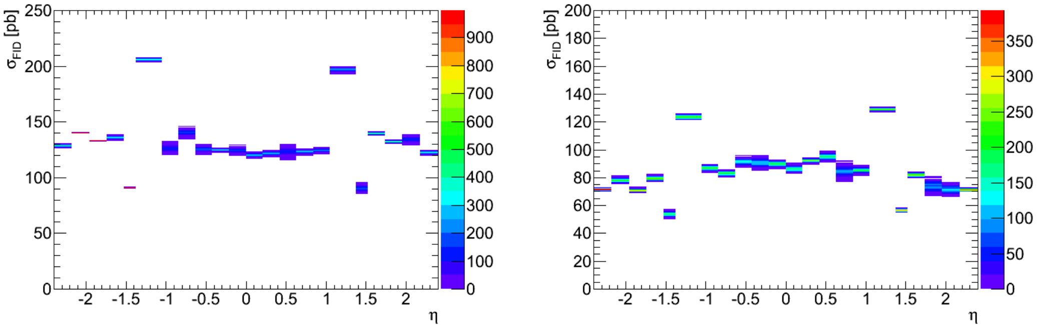

(a) μ^+ (b) μ^-

Figure 8.32: Toy Monte Carlo variation of QCD statistical error, showing the impact upon the fiducial cross section for positive (left) and negative (right) muons. The distributions in the bins are fitted to Gaussians, the widths giving errors on the cross section from the statistics of the scale factor [42].

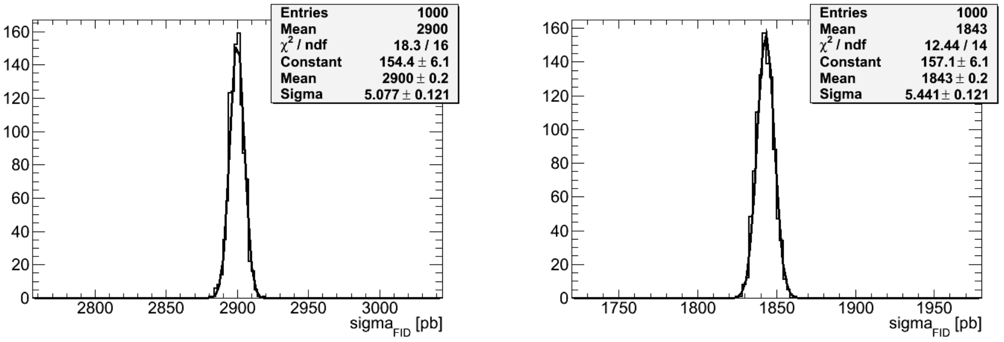

(a) μ^+

(b) μ^-

Figure 8.33: Fit to distribution of integrated fiducial cross section upon Toy Monte Carlo variation of the QCD statistical error. The width gives the error on the cross section from QCD statistics [42].

Sample	Predicted Events (%)	Statistical error (%)	Systematic error (%)
$Z \rightarrow \mu\mu$	2.981	0.021	0.174
$W \rightarrow \tau\nu$	2.689	0.032	0.157
$Z \rightarrow \tau\tau$	0.114	0.002	0.007
$t\bar{t}$	0.293	0.003	0.020
WW	0.080	0.001	0.005
WZ	0.025	0.000	0.001
ZZ	0.002	0.000	0.000
QCD	1.299	0.176	0.564
Total	7.484	0.181	0.927

Table 8.18: Predicted background for positive charge, as a percentage of the number of positive candidates seen in data. For the electroweak backgrounds we show the PDF and cross section uncertainties only [42].

Sample	Predicted Events (%)	Statistical error (%)	Systematic error (%)
$Z \to \mu\mu$	4.202	0.029	0.245
$W \to \tau\nu$	2.973	0.039	0.173
$Z \to \tau\tau$	0.162	0.003	0.009
$t\bar{t}$	0.449	0.004	0.030
WW	0.123	0.001	0.007
WZ	0.026	0.000	0.001
ZZ	0.004	0.000	0.000
QCD	2.293	0.308	0.992
Total	10.231	0.312	1.459

Table 8.19: Predicted background for negative charge, as a percentage of the number of negative candidates seen in data. For the electroweak backgrounds we show the PDF and cross section uncertainties only [42].

8.8 Results

The result of applying the selection requirements discussed in Section 8.2.4 on the muon data set is shown in Table 8.20. After all requirements have been imposed, we find 139, 266 $W \to \mu\nu$ candidates, where 84, 103 of these are positively charged, while 55, 163 are negatively charged.

Selection	Number of Events	Absolute Efficiency (%)	Relative Efficiency (%)
All	62071847	100.00 ± 0.00	—
Good Run List	51799873	83.45 ± 0.00	83.45 ± 0.00
Jet cleaning	51756656	83.38 ± 0.00	99.92 ± 0.00
Trigger	5191708	8.36 ± 0.00	10.03 ± 0.00
Vertex	5191451	8.36 ± 0.00	100.00 ± 0.00
Combined μ	4335118	6.98 ± 0.00	83.50 ± 0.02
μ $\|\eta\| < 2.4$	4291760	6.91 ± 0.00	99.00 ± 0.00
μ $\mathrm{p}_T > 15$ GeV	2192711	$(353.25 \pm 0.23) \cdot 10^{-2}$	51.09 ± 0.02
$\|z_0 - z_{vtx}\| < 20$ mm	2191982	$(353.14 \pm 0.23) \cdot 10^{-2}$	99.97 ± 0.00
μ $p_{\mathrm{T}} > 20$ GeV	769998	$(124.05 \pm 0.14) \cdot 10^{-2}$	35.13 ± 0.03
Isolation	329440	$(53.07 \pm 0.09) \cdot 10^{-2}$	42.78 ± 0.06
$E_{\mathrm{T}}^{\mathrm{miss}} > 25$ GeV	144958	$(23.35 \pm 0.06) \cdot 10^{-2}$	44.00 ± 0.09
$m_{\mathrm{T}} > 40$ GeV	139266	$(22.44 \pm 0.06) \cdot 10^{-2}$	96.07 ± 0.05

Table 8.20: Number of events in data passing successive selection requirements [42].

8.8.1 Kinematics of Candidate Events

The muon kinematics for our candidate events are compared to Monte Carlo expectations. In these plots, the QCD background is normalized to the matrix prediction. Signal and background Monte Carlo samples are smeared, and have scale factors applied to them for the trigger, reconstruction and isolation efficiencies, but do not have any additional momentum scale imposed. In Figure 8.34 we show the p_{T} for the hardest muon in candidate events, while the pseudorapidity distribution for these muons is shown in Figure 8.35. The missing transverse energy is plotted in Figure 8.36.

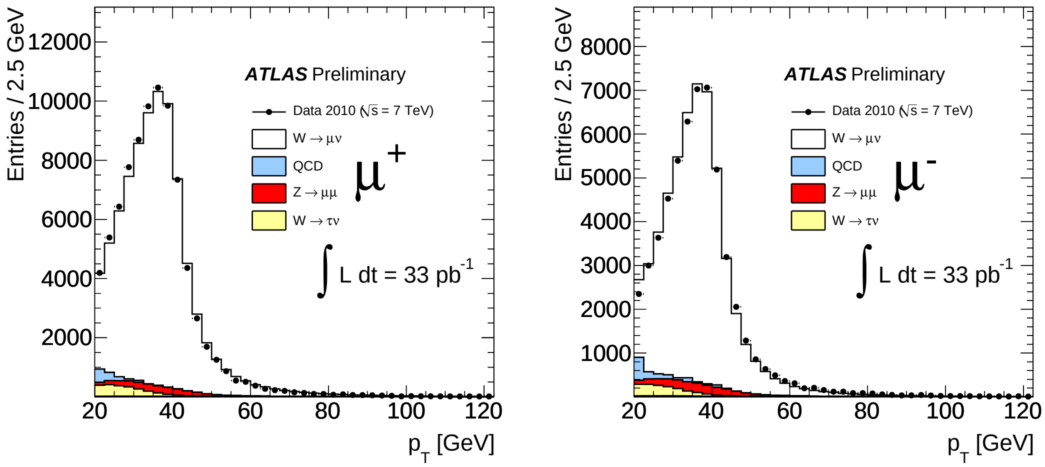

(a) μ^+ (b) μ^-

Figure 8.34: Transverse momentum of the highest-p_{T} muon in events passing the full $W \to \mu\nu$ selection, shown for positive (left) and negative (right) muon candidates. Signal and background are normalized to data for 32.6 pb^{-1} [42].

Using the combination of the muon and the missing transverse energy, we obtain the kinematics of the candidate W bosons, specifically their transverse momenta and masses. We show the transverse mass distribution of the candidates in Figure 8.37, and their p_{T} in Figure 8.38.

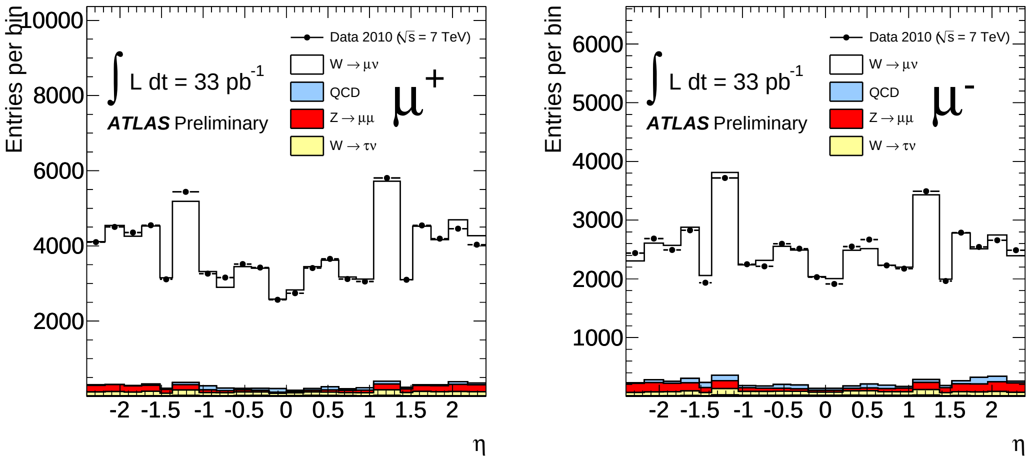

(a) μ^+ (b) μ^-

Figure 8.35: Pseudorapidity of the highest-p_{T} muon in events passing the full $W \to \mu\nu$ selection, shown for positive (left) and negative (right) muon candidates. Signal and background are normalized to data for 32.6 pb^{-1} [42].

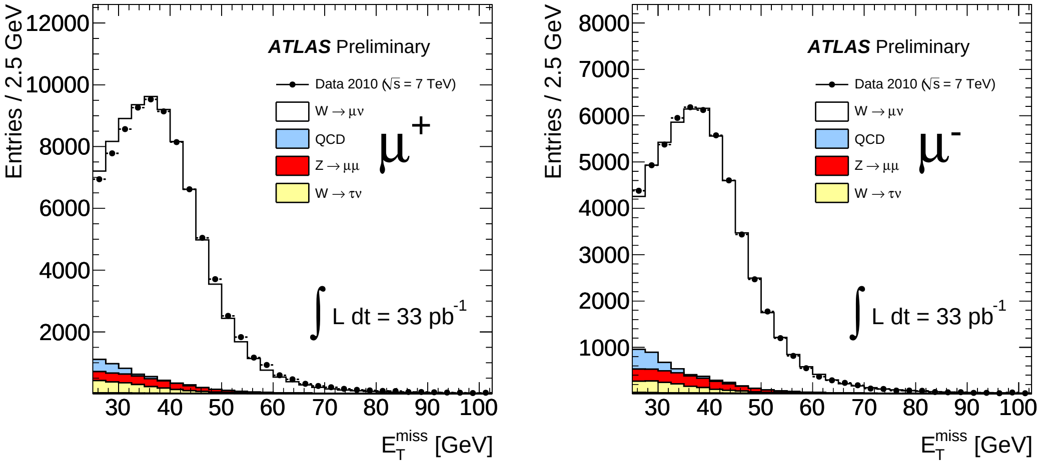

(a) μ^+ (b) μ^-

Figure 8.36: Missing transverse energy in events passing the full $W \to \mu\nu$ selection, shown for positive (left) and negative (right) muon candidates. Signal and background are normalized to data for 32.6 pb^{-1} [42].

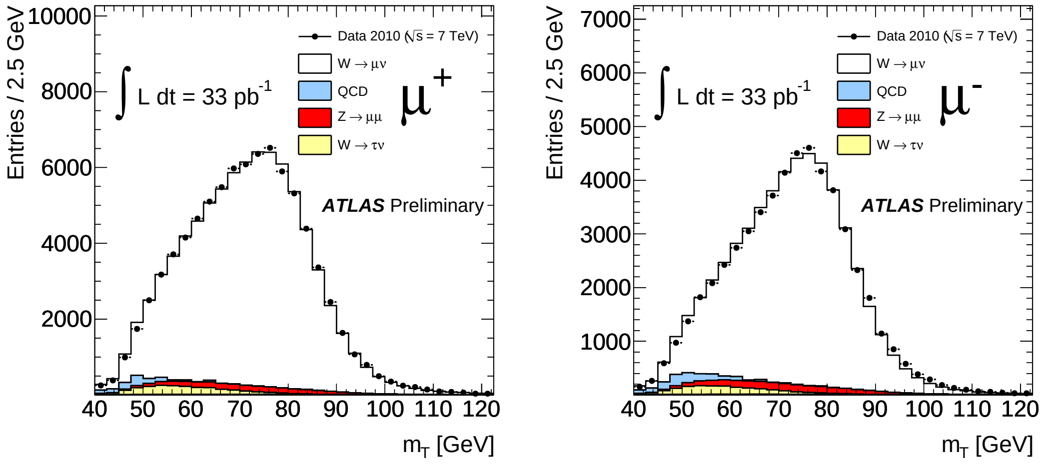

(a) W^+ (b) W^-

Figure 8.37: Transverse mass of candidate W^+ (left) and W^- (right) after the full selection. Signal and background are normalized to data for 32.6 pb^{-1} [42].

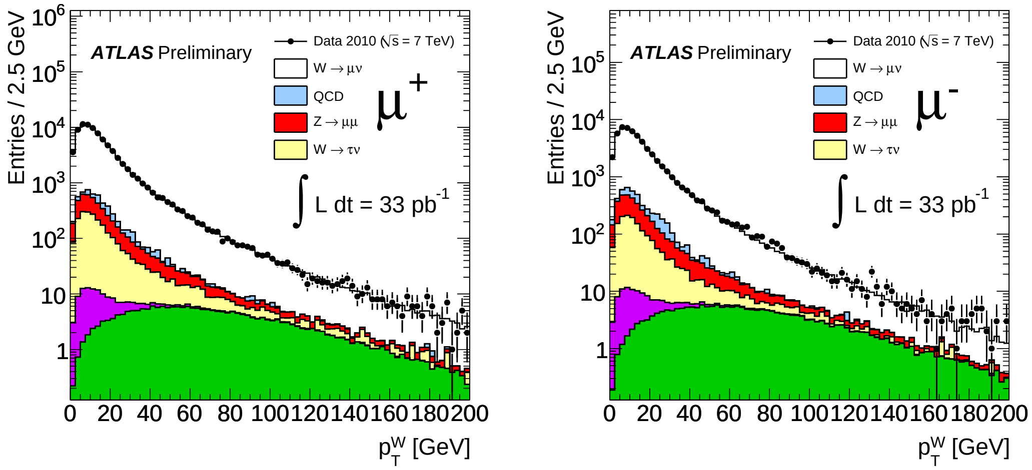

(a) W^+ (b) W^-

Figure 8.38: p_{T} of candidate W^+ (left) and W^- (right) after the full selection. Signal and background are normalized to data for 32.6 pb^{-1} [42].

	W^+	W^-	$W^\pm$
N	84103 ± 290	55163 ± 235	139266 ± 373
B	$6214 \pm 150 \pm 770$	$5569 \pm 170 \pm 794$	$11783 \pm 227 \pm 1564$
C_{W}	$0.7944 \pm 0.0003 \pm 0.0201$	$0.7800 \pm 0.0004 \pm 0.0189$	$0.7896 \pm 0.0002 \pm 0.0176$
A_W	$0.4840 \pm 0.0003 \pm 0.0145$	$0.4743 \pm 0.0003 \pm 0.0143$	$0.4800 \pm 0.0003 \pm 0.0144$
L		$[32.6 \pm 1.1]\mathrm{pb}^{-1}$	

Table 8.21: Components of the cross section in the $W \to \mu\nu$ channel. The errors listed are first statistical followed by systematic [42].

8.8.2 Cross Section Measurement

The analysis in preceding sections culminates in estimates for signal and background event counts and corrected acceptance, shown in Table 8.21. The resulting fiducial cross sections are shown in Table 8.22. The overall result for the cross section is summarized in Table 8.23.

$\sigma_{W^+}\times$ BR $(W \to \mu^+\nu)$	$[3.008 \pm 0.011(\text{sta}) \pm 0.080(\text{sys}) \pm 0.109(\text{lum})]$ [nb]
$\sigma_{W^-}\times$ BR $(W \to \mu^-\nu)$	$[1.950 \pm 0.009(\text{sta}) \pm 0.053(\text{sys}) \pm 0.072(\text{lum})]$ [nb]
$\sigma_{W}\times$ BR $(W \to \mu\nu)$	$[4.959 \pm 0.015(\text{sta}) \pm 0.120(\text{sys}) \pm 0.181(\text{lum})]$ [nb]

Table 8.22: Fiducial cross sections for W^+, W^- and W in the $\mu\nu$ decay [42].

$\sigma_{W^+}\times$ BR $(W \to \mu^+\nu)$	$[6.215 \pm 0.023(\text{sta}) \pm 0.165(\text{sys}) \pm 0.225(\text{lum}) \pm 0.187(\text{acc})]$ [nb]
$\sigma_{W^-}\times$ BR $(W \to \mu^-\nu)$	$[4.107 \pm 0.020(\text{sta}) \pm 0.112(\text{sys}) \pm 0.152(\text{lum}) \pm 0.123(\text{acc})]$ [nb]
$\sigma_{W}\times$ BR $(W \to \mu\nu)$	$[10.322 \pm 0.030(\text{sta}) \pm 0.249(\text{sys}) \pm 0.377(\text{lum}) \pm 0.310(\text{acc})]$ [nb]

Table 8.23: Measured cross sections for W^+, W^- and W in the $\mu\nu$ decay [42].

Chapter 9

Discussion and Outlook

9.1 Discussion

We have presented two measurements of the W boson inclusive cross section in the $\mu\nu$ channel, both using pp data at the LHC gathered with the ATLAS detector. The first analysis is the earliest measurement of the W cross section at a new energy frontier of 7 TeV. The obtained cross section (detailed in Chapter 7) is:

$$\sigma_W \times \mathrm{BR}(W \to \mu\nu) = [9.58 \pm 0.30(\mathrm{sta}) \pm 0.50(\mathrm{sys}) \pm 1.05(\mathrm{lum})]\ \mathrm{nb} \tag{9.1}$$

The measured cross section is found to agree well with theoretical predictions within (relatively large) uncertainties, a testament to the rapid understanding of the ATLAS detector and analytic techniques achieved upon start of 7 TeV data taking. This result was published [19] within just a few months after the startup of the LHC.

This first result uses only 310 nb^{-1} of data, less than one percent of the full 2010 dataset. This 33 pb^{-1} sample reduces statistical uncertainties by a factor of ten to the per mille level, and in addition facilitates the use of more powerful analytic techniques, reducing the experimental systematic uncertainty from 4% to 2.4%. Together with a better understanding of the luminosity, these better analysis methods have enabled more detailed investigation of QCD predictions, in a new low-x, large Q^2 regime. Our updated results have been summarized in Table 8.22 for the fiducial cross section, and in Table 8.23 for the total cross section.

Compared to the first ATLAS cross section measurement, there is dramatic improvement in the precision of the result; the measured fiducial cross section is:

$$\sigma_W \times \mathrm{BR}(W \to \mu\nu) = [4.959 \pm 0.015(\mathrm{sta}) \pm 0.120(\mathrm{sys}) \pm 0.181(\mathrm{lum})]\mathrm{nb} \tag{9.2}$$

This is the most precise result in our analysis for direct comparison with theory, avoiding uncertainties from extrapolation to the full phase space. Our dominant experimental systematic uncertainty is a 2% effect from the calorimetric component of the transverse missing energy. The understanding of muon performance is impressive, with the higher statistical power of the $Z \to \mu\mu$ based tag-and-probe methods reducing muon reconstruction, trigger and isolation uncertainties from 3.3 % to under a percent.

The total cross section obtained is:

$$\sigma_W \times \mathrm{BR}(W \to \mu\nu) = [10.322 \pm 0.030(\mathrm{sta}) \pm 0.249(\mathrm{sys}) \pm 0.377(\mathrm{lum}) \pm 0.310(\mathrm{acc})]\ \mathrm{nb} \tag{9.3}$$

There is a three percent uncertainty in the total cross section from extrapolating the result out from the fiducial region to the full phase space. This is the largest non-luminosity uncertainty in the measurement, and is traced to the use of leading order MC generators for this extrapolation. The measured value is consistent with parallel results obtained in the $W \to e\nu$ decay channel, where the cross section observed is:

$$\sigma_W \times \mathrm{BR}(W \to e\nu) = [10.551 \pm 0.032(\mathrm{sta}) \pm 0.300(\mathrm{sys}) \pm 0.359(\mathrm{lum}) \pm 0.316(\mathrm{acc})]\ \mathrm{nb} \tag{9.4}$$

In addition to serving as a check on both results, this enables combination of electron and muon channel results. We show the combined electron and muon channel cross sections observed in Table 9.1. We compare these results with theoretical predictions obtained using ZWPROD [68] and FEWZ [18, 56]. For the comparisons, we use four different sets of NNLO parton distributions, shown in Table 2.1. Figure 9.1 shows the cross section times leptonic branching ratios for W^+ vs. W^-. The missing transverse energy uncertainty is treated as fully correlated. In Figure 9.1 the total W cross section summed over the two charges is compared to Z cross section measurement performed over the same dataset. The luminosity uncertainty is fully correlated between these two analyses. Within the total accuracy of the present cross section measurement of about 5 %, all NNLO predictions are consistent with the data.

	$\sigma \cdot$ BR$(W \to \ell\nu)$ [nb]
W^+	6.257 ± 0.017(sta) ± 0.152(sys) ± 0.213(lum) ± 0.188(acc)
W^-	4.149 ± 0.014(sta) ± 0.102(sys) ± 0.141(lum) ± 0.124(acc)
W	10.391 ± 0.022(sta) ± 0.238(sys) ± 0.353(lum) ± 0.312(acc)

Table 9.1: Total cross section times leptonic branching ratios for W^+, W^- and W in the combined electron and muon final states [41].

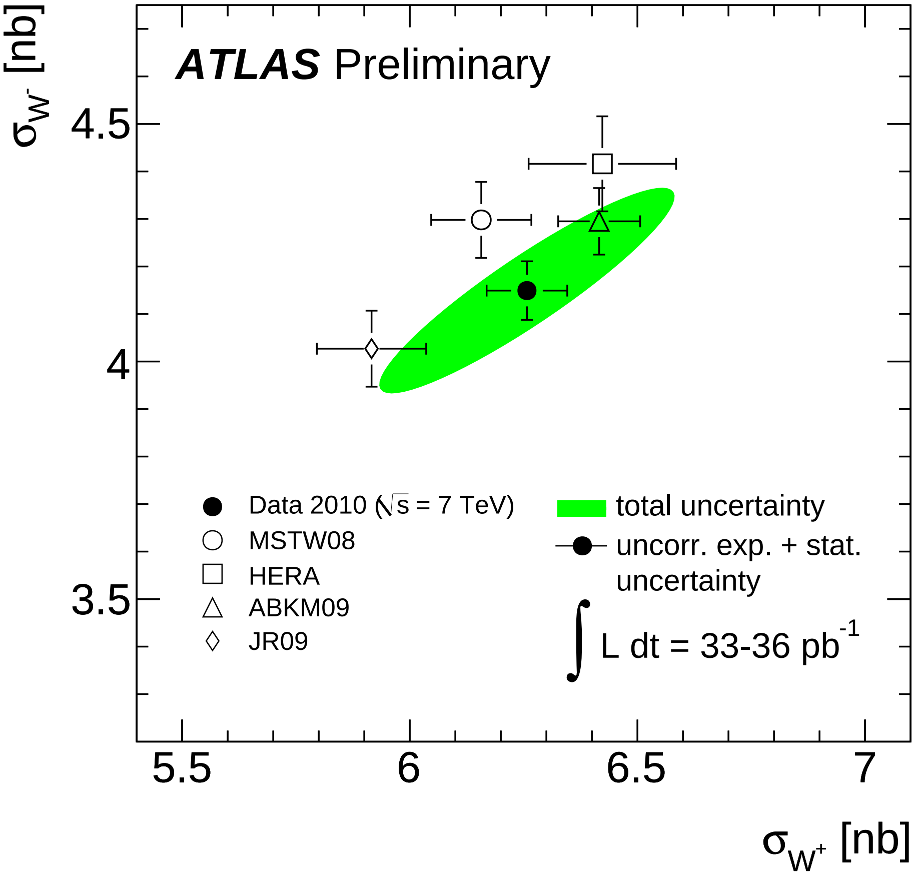

Figure 9.1: Measured and predicted cross sections times leptonic branching ratios for σ_{W^-} vs. σ_{W^+}. The projections of the ellipse to the axes correspond to one standard deviation uncertainty of the cross sections. The uncertainties of the predictions are the PDF uncertainties only [41].

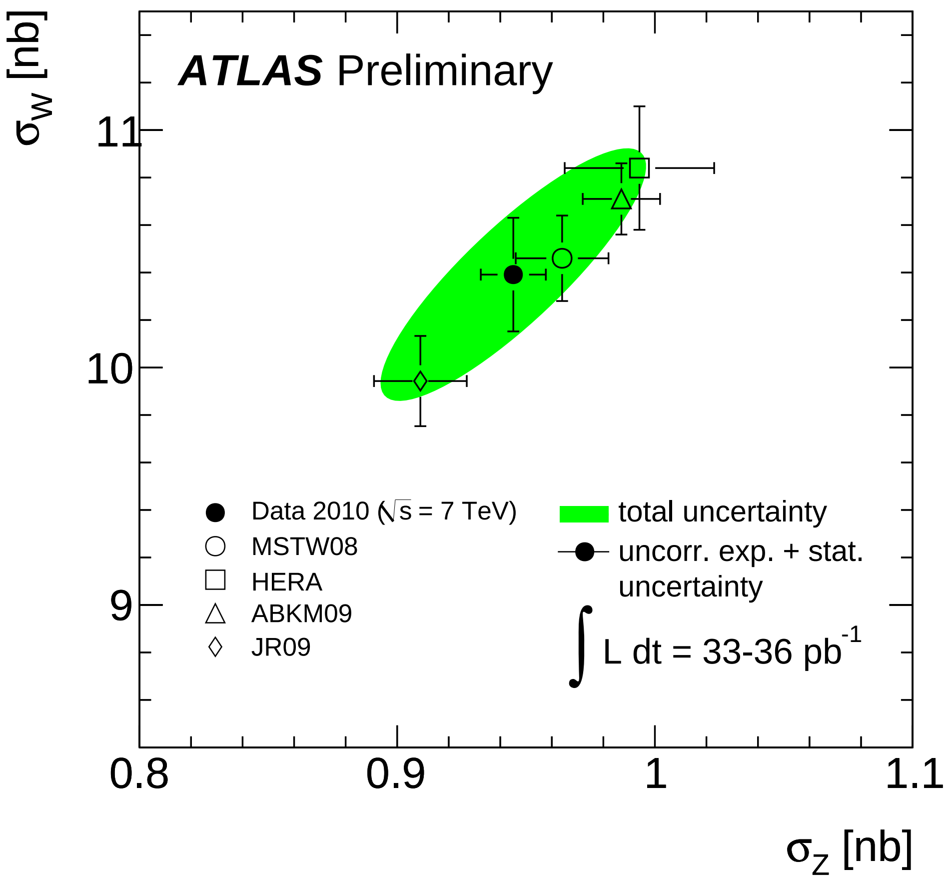

Figure 9.2: Measured and predicted cross sections times leptonic branching ratios for $(\sigma_{W^+} + \sigma_{W^-})$ vs. σ_{Z/γ^*}. The systematic uncertainties on the luminosity and on the acceptance extrapolation are treated as fully correlated between W and Z channels. The projections of the ellipse to the axes correspond to one standard deviation uncertainty of the cross sections. The uncertainties of the predictions are the PDF uncertainties only [41].

9.2 Update and Outlook

As discussed in Section 8.4, our analytical methodology for this dissertation was directly geared toward the measurement of a differential result in the muon pseudorapidity. During the period immediately succeeding this analysis, we have produced such a differential cross section result, which is currently undergoing publication [25] as this dissertation goes to the printer. The update also addresses chief limitations of the results here discussed. A detailed discussion is beyond the purview of this document, but a full discussion of the update is to be found in [11]. Briefly, we have used NLO (`MC@NLO`) Monte Carlo programs for the acceptance instead of `Pythia`, reducing the theoretical uncertainty on the cross section to 1.5%. Also, we have reduced the $E_{\mathrm{T}}^{\mathrm{miss}}$ uncertainty by using an updated definition which permits studies of the effects of jet energy scale/resolution and soft terms on the missing energy. This brings the impact of the calorimetric missing energy down from 2% to 0.5%. The overall experimental systematic uncertainty decreases to 1.6%, as shown in Figure 9.3.

The differential fiducial cross sections for W^+ and W^- are depicted in Figure 9.4, while the updated inclusive muon channel cross section is:

$$\sigma_W \times \mathrm{BR}(W \to \mu\nu) = [10.210 \pm 0.030(\mathrm{sta}) \pm 0.166(\mathrm{sys}) \pm 0.347(\mathrm{lum}) \pm 0.153(\mathrm{acc})]\ \mathrm{nb} \tag{9.5}$$

From the updated comparisons of W^+ versus W^- and W versus Z fiducial cross sections (Figure 9.5), we see that the results show sensitivity to the different theoretical predictions. We expect that these results will reduce the uncertainties of PDF determinations.

Looking to the future, the 2011 LHC dataset in the several fb^{-1} range vastly sur-

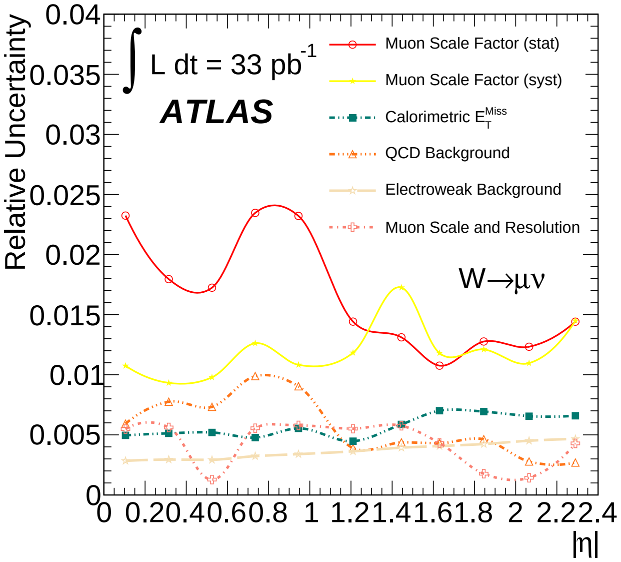

Figure 9.3: Summary of bin-by-bin experimental systematic uncertainties for the updated η_μ differential $W \to \mu\nu$ analysis. Numbers given are relative to the fiducial cross section in each bin. The dominant uncertainty comes from the statistical component of the muon scale factors [25].

passes the statistical power of the analyzed data for this measurement. The dominant experimental uncertainty in the updated analysis is a 1% contribution from the muon trigger, reconstruction and isolation efficiency. As suggested in Section 8.3, this uncertainty is, in significant measure, a statement about the limited statistical power of the 2010 Z sample. With the 2011 data, these efficiencies will be measured with a few hundred times more $Z \to \mu\mu$ events, significantly reducing the muon uncertainties. This will be especially useful for the differential result where, as seen in Figure 9.3, the bin-by-bin uncertainties are dominated by muon scale factor effects. However, the 2011 dataset is acquired at higher instantaneous luminosity with reduced bunch spacing. The resulting degradation in $E_{\mathrm{T}}^{\mathrm{miss}}$ resolution from pileup effects poses a significant challenge for the calorimetric $E_{\mathrm{T}}^{\mathrm{miss}}$ uncertainty. Similarly, the worsened

$E_{\mathrm{T}}^{\mathrm{miss}}$ resolution is expected to lead to a higher QCD background contribution, and a more precise result will need to estimate it with more powerful techniques. More precise measurements of the $W \to \mu\nu$ inclusive and η differential cross sections will likely hinge upon the deployment of improved methods for understanding such issues.

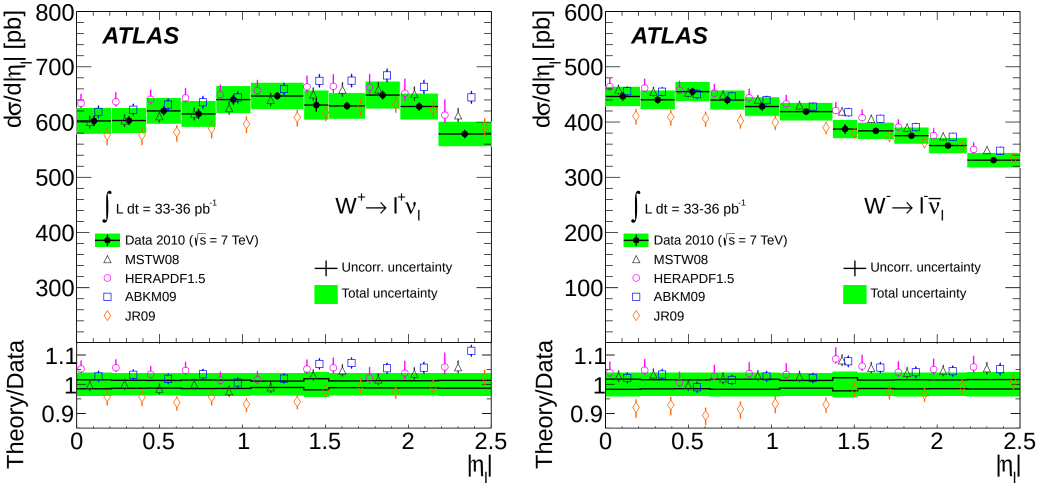

Figure 9.4: . Updated differential $\mathrm{d}\sigma/\mathrm{d}|\eta_{\ell^+}|$ (left) and $\mathrm{d}\sigma/\mathrm{d}|\eta_{\ell^-}|$ (right) cross section measurements for $W \to \ell\nu$ compared to the NNLO theory predictions using various PDF sets. The kinematic requirements are $p_{T,\ell} > 20\,\mathrm{GeV}$, $p_{T,\nu} > 25\,\mathrm{GeV}$ and $m_T > 40\,\mathrm{GeV}$. The ratio of theoretical predictions to data is also shown. Theoretical points are displaced for clarity within each bin [25].

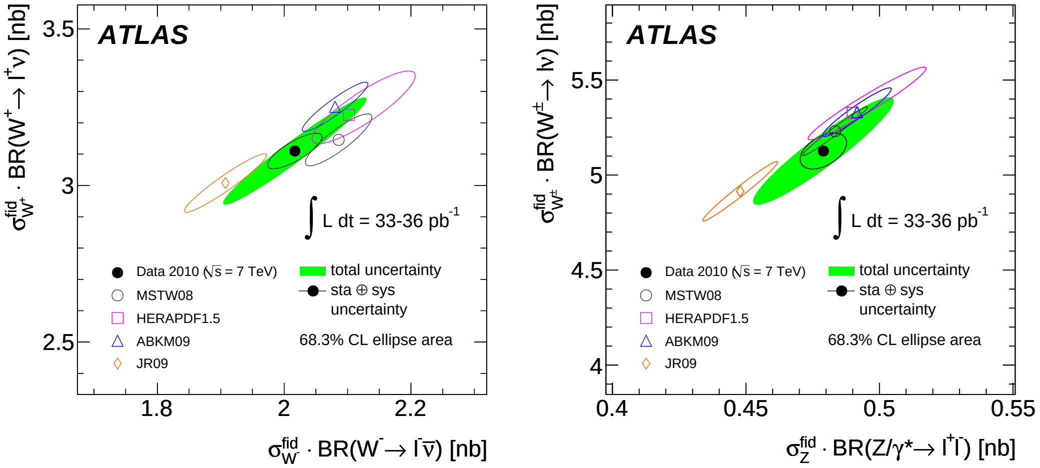

Figure 9.5: Measured and predicted fiducial cross sections times leptonic branching ratios, σ_{W^+} vs. σ_{W^-}. The ellipses illustrate the 68 % CL coverage for total uncertainties (full green) and excluding the luminosity uncertainty (open black). The uncertainties of the theoretical predictions are the PDF uncertainties only [25].

Bibliography

[1] G Aad et al. ATLAS Pixel Detector Electronics and Sensors. *J. Instrum.*, 3(07):P07007, 2008.

[2] G. Aad et al. Commissioning of the ATLAS Muon Spectrometer with Cosmic Rays. *Eur. Phys. J.*, C70:875–916, 2010.

[3] F.D. Aaron et al. H1prelim-10-044/ZEUS-prel-10-008 (2010)
see also V. Radescu, Proceedings of the ICHEP10 Conference, Paris, http://pos.sissa.it/archive/conferences/120/168/ICHEP.

[4] F.D. Aaron et al. Combined Measurement and QCD Analysis of the Inclusive ep Scattering Cross Sections at HERA. *JHEP*, 01:109, 2010.

[5] B. Abbott et al. Extraction of the width of the W boson from measurements of $\sigma(p\bar{p} \to W + X) \times B(W \to e\nu)$ and $\sigma(p\bar{p} \to Z + X) \times B(Z \to ee)$ and their ratio. *Phys. Rev.*, D61:072001, 2000.

[6] F. Abe et al. Measurement of $\sigma B(W \to e\nu)$ and $\sigma B(Z \to e^+e^-)$ in $p\bar{p}$ collisions at $\sqrt{s} = 1.8$ TeV. *Phys. Rev. Lett.*, 76:3070–3075, 1996.

[7] A. Abulencia et al. Measurements of Inclusive W and Z Cross Sections in $p\bar{p}$ Collisions at $\sqrt{s} = 1.96$ TeV. *J. Phys.*, G34:2457–2544, 2007.

[8] D. Adams et al. Track reconstruction in the ATLAS Muon Spectrometer with MOORE 007. Technical Report ATL-SOFT-2003-007, CERN, Geneva, May 2003.

[9] A. Adare et al. Cross Section and Parity Violating Spin Asymmetries of $W^{\pm}$ Boson Production in Polarized $p + p$ Collisions at $\sqrt{s} = 500$ GeV. *Phys. Rev. Lett.*, 106:062001, 2011.

[10] S. Agostinelli et al. GEANT4: A simulation toolkit. *Nucl. Instrum. Meth.*, A506:250–303, 2003.

[11] M. Aharrouche et al. Total and differential $W \to \ell\nu$ and $Z \to \ell\ell$ Cross Section Measurements in proton-proton Collisions at $\sqrt{s} = 7$ TeV with the ATLAS

Detector. Technical Report ATL-COM-PHYS-2011-751, CERN, Geneva, Jun 2011.

[12] C. Albajar et al. Intermediate Vector Boson Cross-Sections at the CERN Super Proton Synchrotron Collider and the Number of Neutrino Types. *Phys. Lett.*, B198:271, 1987.

[13] S. Alekhin, J. Blumlein, P. Jimenez-Delgado, S. Moch, and E. Reya. NNLO Benchmarks for Gauge and Higgs Boson Production at TeV Hadron Colliders. *Phys. Lett.*, B697:127–135, 2011.

[14] S. Alekhin, J. Blumlein, S. Klein, and S. Moch. The 3-, 4-, and 5-flavor NNLO Parton from Deep Inelastic Scattering Data and at Hadron Colliders. *Phys. Rev.*, D81:014032, 2010.

[15] J. Alitti et al. A Measurement of the W and Z production cross sections and a determination of $\Gamma(W)$ at the CERN $\bar{p}p$ collider. *Phys. Lett.*, B276:365–374, 1992.

[16] S. Allwood-Spiers et al. Vertex Reconstruction for Analysis of Charged Particle Multiplicities in pp Interactions at $\sqrt{s} = 900$ GeV. Technical Report ATL-INDET-INT-2010-016, CERN, Geneva, Sep 2010.

[17] Guido Altarelli and G. Parisi. Asymptotic Freedom in Parton Language. *Nucl. Phys.*, B126:298, 1977.

[18] C. Anastasiou, L.J. Dixon, K. Melnikov, and F. Petriello. High precision QCD at hadron colliders: Electroweak gauge boson rapidity distributions at NNLO. *Phys. Rev.*, D69:094008, 2004.

[19] ATLAS Collaboration. Measurement of the $W \to \ell\nu$ and $Z/\gamma^* \to \ell\ell$ production cross sections in pp collisions at $\sqrt{s} = 7$ TeV with the ATLAS detector. *JHEP*, 12:060, 2010.

[20] ATLAS Collaboration. Measurement of the $W \to \ell\nu$ production cross-section and observation of $Z \to \ell\ell$ production in pp collisions at $\sqrt{s} = 7$ TeV with the ATLAS detector. Technical Report ATLAS-CONF-2010-051, CERN, Geneva, Jul 2010.

[21] ATLAS Collaboration. Observation of $W \to \ell\nu$ and $Z \to \ell\ell$ production in pp collisions at $\sqrt{s} = 7$ TeV with the ATLAS detector. Technical Report ATLAS-CONF-2010-044, CERN, Geneva, Jul 2010.

[22] P. Bagnaia et al. Calibration model for the MDT chambers of the ATLAS Muon Spectrometer. Technical Report ATL-MUON-PUB-2008-004, CERN, Geneva, Feb 2008.

[23] C. Balazs and C.P. Yuan. Soft Gluon Effects on Lepton Pairs at Hadron Colliders. *Phys. Rev.*, D56:5558–5583, 1997.

[24] M. Bellomo et al. Observation of $W \to \mu\nu$ and $Z \to \mu\mu$ in pp collisions at $\sqrt{s} = 7$ TeV with the ATLAS detector. Technical Report ATL-PHYS-INT-2010-087, CERN, Geneva, Sep 2010.

[25] M Bellomo et al. A Measurement of the Inclusive $W^{\pm}$ and Z/γ^{*} Cross Sections in the e and μ Decay Channels in pp collisions at $\sqrt{s} = 7$ TeV with the ATLAS Detector. Technical Report ATL-COM-PHYS-2011-845, CERN, Geneva, Jul 2011.

[26] A. Belloni et al. In-situ t_0 calibration for MDT segments. Technical Report ATL-COM-MUON-2009-006, CERN, Geneva, Apr 2009.

[27] A. Belloni et al. Beam splash studies with MDT chambers: Timing and flux. Technical Report ATL-COM-MUON-2010-006, CERN, Geneva, Feb 2010.

[28] A. Belloni et al. Muon definition for high-p_{T} physics: Algorithmic fakes. Technical Report ATL-COM-MUON-2010-009, CERN, Geneva, May 2010.

[29] M. Beneke, M. Czakon, P. Falgari, A. Mitov, and C. Schwinn. Threshold expansion of the gg(qq) $\to$ QQ+X cross section at O(α_{S}^{4}). *Phys. Lett.*, B690:483–490, 2010.

[30] S. F. Biagi. Monte carlo simulation of electron drift and diffusion in counting gases under the influence of electric and magnetic fields. *Nuclear Instruments and Methods in Physics Research Section A: Accelerators, Spectrometers, Detectors and Associated Equipment*, 421(1-2):234 – 240, 1999.

[31] R.K. Bock and A. Vasilescu. *The Particle Detector BriefBook, Transition Radiation.* Springer, 1999.

[32] R. Bonciani, S. Catani, M. Ll. Mangano, and P. Nason. NLL resummation of the heavy-quark hadroproduction cross-section. *Nucl. Phys.*, B529:424, 1998.

[33] R. Brun and F. Rademakers. ROOT: An Object Oriented Data Analysis Framework. *Nucl. Instrum. Meth.*, A389:81–86, 1997.

[34] Rene Bruns. ROOT Class Documentation. Online Class Index for ROOT, July 2006.

[35] N. Cabibbo. Unitary symmetry and leptonic decays. *Phys. Rev. Lett.*, 10(12):531–533, Jun 1963.

[36] J.M. Campbell, J.W. Huston, and W. J. Stirling. Hard Interactions of Quarks and Gluons: A Primer for LHC Physics. *Rept. Prog. Phys.*, 70:89, 2007.

[37] F. Cerutti et al. Muon Momentum Resolution in First Pass Reconstruction of *pp* Collision Data Recorded by ATLAS in 2010. Technical Report ATLAS-COM-CONF-2011-003, CERN, Geneva, Jan 2011.

[38] The ATLAS Collaboration. The ATLAS Experiment at the CERN Large Hadron Collider. *J. Instrum.*, 3:S08003. 437 p, 2008. Also published by CERN Geneva in 2010.

[39] The ATLAS Collaboration. Charged particle multiplicities in *pp* interactions at $\sqrt{s} = 7$ TeV measured with the ATLAS detector at the LHC. Technical Report ATLAS-CONF-2010-024, CERN, Geneva, Jul 2010.

[40] The ATLAS Collaboration. Measurement of the Cosmic Ray Muon Charge Ratio using the ATLAS Muon Spectrometer. Technical Report ATL-COM-PHYS-2010-265, CERN, Geneva, 2010.

[41] The ATLAS Collaboration. A measurement of the total W and Z/γ^*cross sections in the e and μ decay channels and of their ratios in *pp* collisions at $\sqrt{s} = 7$ TeV with the ATLAS detector. Technical Report ATLAS-CONF-2011-041, CERN, Geneva, Mar 2011.

[42] The ATLAS Collaboration. $W \to \ell\nu$ and $Z \to \ell\ell$ cross-sections measurements in *pp* collisions at $\sqrt{s} = 7$ TeV with the ATLAS detector. Technical Report ATL-COM-PHYS-2011-178, CERN, Geneva, Feb 2011.

[43] T Cornelissen et al. Concepts, Design and Implementation of the ATLAS New Tracking (NEWT). Technical Report ATL-SOFT-PUB-2007-007. ATL-COM-SOFT-2007-002, CERN, Geneva, Mar 2007.

[44] E. Diehl and D. Levin. University of Michigan Gas Monitoring web page. `http://mdtgasmon.grid.umich.edu/rt/`.

[45] Yuri L. Dokshitzer. Calculation of the Structure Functions for Deep Inelastic Scattering and e^+e^- Annihilation by Perturbation Theory in Quantum Chromodynamics. *Sov. Phys. JETP*, 46:641–653, 1977.

[46] S. D. Drell and Tung-Mow Yan. Partons and their applications at high energies. *Ann. Phys.*, 66:578, 1971.

[47] R.O. Duda and P.E. Hart. Use of the Hough Transformation to Detect Lines and Curves in Pictures. *Commun. ACM*, 15:11–15, January 1972.

[48] F. J. Dyson. The s matrix in quantum electrodynamics. *Phys. Rev.*, 75(11):1736–1755, Jun 1949.

[49] F. Englert and R. Brout. Broken symmetry and the mass of gauge vector mesons. *Phys. Rev. Lett.*, 13(9):321–323, Aug 1964.

[50] L. Evans and P. Bryant. LHC machine. *J. Inst.*, 3(08):S08001, 2008.

[51] Fermilab. Elementary particles. `http://www.fnal.gov/pub/inquiring/matter/madeof/standardmodel.jpg`.

[52] R.P. Feynman. Space-time approach to quantum electrodynamics. *Phys. Rev.*, 76(6):769–789, Sep 1949.

[53] R.P. Feynman. Mathematical formulation of the quantum theory of electromagnetic interaction. *Phys. Rev.*, 80(3):440–457, Nov 1950.

[54] S. Frixione and B.R. Webber. Matching NLO QCD computations and parton shower simulations. *JHEP*, 06:029, 2002.

[55] Stefano Frixione, Paolo Nason, and Carlo Oleari. Matching NLO QCD computations with Parton Shower simulations: the POWHEG method. *JHEP*, 11:070, 2007.

[56] R. Gavin, Y. Li, F. Petriello, and S. Quackenbush. FEWZ 2.0: A code for hadronic Z production at next-to- next-to-leading order. *arXiv*, 2010.

[57] M. Gell-Mann. A schematic model of baryons and mesons. *Physics Letters*, 8(3):214 – 215, 1964.

[58] S. L. Glashow, J. Iliopoulos, and L. Maiani. Weak interactions with lepton-hadron symmetry. *Phys. Rev. D*, 2(7):1285–1292, Oct 1970.

[59] Sheldon L. Glashow. Partial-symmetries of weak interactions. *Nuclear Physics*, 22(4):579 – 588, 1961.

[60] Piotr Golonka and Zbigniew Was. PHOTOS Monte Carlo: A Precision tool for QED corrections in Z and W decays. *Eur. Phys. J.*, C45:97–107, 2006.

[61] V. N. Gribov and L. N. Lipatov. e+ e- pair annihilation and deep inelastic e p scattering in perturbation theory. *Sov. J. Nucl. Phys.*, 15:675–684, 1972.

[62] D.J. Griffiths. *Introduction to Elementary Particles.* Wiley-VCH, 2008.

[63] João Pedro Barreiro Guimarães da Costa. *Search for a fourth generation quark more massive than the Z0 boson in proton anti-proton collisions at* $\sqrt{s} = 1.8$ TeV. PhD thesis, Univ. Michigan, 2000. FERMILAB-THESIS-2000-31.

[64] J.B. Guimaraes da Costa, M. Bellomo, et al. $W \to \mu\nu$ and $Z \to \mu\mu$ cross-sections measurements in pp collisions at $\sqrt{s} = 7$ TeV with the ATLAS detector. Technical Report ATL-COM-PHYS-2010-685, CERN, Geneva, Aug 2010.

[65] J.B. Guimaraes da Costa, M. Bellomo, et al. $W \to \mu\nu$ and $Z \to \mu\mu$ cross sections measurements in pp collisions at $\sqrt{s} = 7$ TeV with the ATLAS detector. Technical Report ATL-PHYS-INT-2011-019, CERN, Geneva, Mar 2011.

[66] G.S. Guralnik, C.R. Hagen, and T.W.B. Kibble. Global conservation laws and massless particles. *Phys. Rev. Lett.*, 13(20):585–587, Nov 1964.

[67] F. Halzen and A.D. Martin. *Quarks and Leptons: An Introductory Course in Modern Particle Physics.* Wiley, 1984.

[68] R. Hamberg, W.L. van Neerven, and T. Matsuura. A Complete calculation of the order α_s^2 correction to the Drell-Yan K factor. *Nucl. Phys.*, B359:343–405, 1991.

[69] T.J. Hanks et al. Splash. http://www.imdb.com/title/tt0088161/, Mar 1984.

[70] P.W. Higgs. Broken symmetries and the masses of gauge bosons. *Phys. Rev. Lett.*, 13(16):508–509, Oct 1964.

[71] F James and M Roos. Minuit - a system for function minimization and analysis of the parameter errors and correlations. *Methods*, 10(6):343–367, 1975.

[72] P. Jimenez-Delgado and E. Reya. Dynamical NNLO parton distributions. *Phys. Rev.*, D79:074023, 2009.

[73] M. Kobayashi and T. Maskawa. CP-violation in the renormalizable theory of weak interaction. *Progress of Theoretical Physics*, 49(2):652–657, 1973.

[74] F. Landry, R. Brock, P.M. Nadolsky, and C.P. Yuan. Tevatron Run-1 Z boson data and Collins-Soper-Sterman resummation formalism. *Phys. Rev.*, D67:073016, 2003.

[75] U. Langenfeld, S. Moch, and P. Uwer. Measuring the running top-quark mass. *Phys. Rev.*, D80:054009, 2009.

[76] J.F. Laporte. Muonboy documentation. `https://twiki.cern.ch/twiki/bin/view/AtlasProtected/MuonboyDocumentation`.

[77] J.F. Laporte. Staco documentation. `https://twiki.cern.ch/twiki/bin/view/AtlasProtected/STACODocumentation`.

[78] C Lefevre. LHC: the guide (english version). Guide du LHC (version anglaise), Feb 2009.

[79] D. Levin. Muonrecopedia. `https://twiki.cern.ch/twiki/bin/view/AtlasProtected/MuonRecoPedia`.

[80] D Lopez Mateos et al. A Bayesian Method for Estimating the Energy Loss of Muons in Calorimeters. Technical Report ATL-MUON-INT-2009-001. ATL-COM-MUON-2008-007, CERN, Geneva, Mar 2008.

[81] A. D. Martin, W. J. Stirling, R. S. Thorne, and G. Watt. Parton distributions for the LHC. *Eur. Phys. J.*, C63:189–285, 2009.

[82] A.D. Martin, R.G. Roberts, W.J. Stirling, and R.S. Thorne. Parton distributions and the LHC: W and Z production. *Eur. Phys. J.*, C14:133–145, 2000.

[83] B. Martin and G. Shaw. *Particle Physics (Manchester Physics Series)*. Wiley, 2008.

[84] S. Moch and P. Uwer. Theoretical status and prospects for top-quark pair production at hadron colliders. *Phys. Rev. D*, 78(3):034003, Aug 2008.

[85] E. Moyse. Tracking software overview. `https://twiki.cern.ch/twiki/bin/view/Atlas/TrackingSoftwareOverview`.

[86] Pavel M. Nadolsky et al. Implications of CTEQ global analysis for collider observables. *Phys. Rev.*, D78:013004, 2008.

[87] K Nakamura and Particle Data Group. Review of particle physics. *Journal of Physics G: Nuclear and Particle Physics*, 37(7A):075021, 2010.

[88] R Nicolaidou, L Chevalier, S Hassani, J F Laporte, E Le Menedeu, and A Ouraou. Muon identification procedure for the ATLAS detector at the LHC using Muonboy reconstruction package and tests of its performance using cosmic rays and single beam data. *Journal of Physics: Conference Series*, 219(3):032052, 2010.

[89] D.H. Perkins. *Introduction to High Energy Physics.* Cambridge University Press, 2000.

[90] A. Salam. Elementary particle theory: Relativistic groups and analyticity (nobel symposium no. 8), 1968.

[91] A Salzburger. The atlas track extrapolation package. Technical Report ATL-SOFT-PUB-2007-005. ATL-COM-SOFT-2007-010, CERN, Geneva, Jun 2007.

[92] A Salzburger, S Todorova, and M Wolter. The ATLAS Tracking Geometry Description. Technical Report ATL-SOFT-PUB-2007-004. ATL-COM-SOFT-2007-009, CERN, Geneva, Jun 2007.

[93] M. Schott, D. Froidevaux, and M. Boonekamp. *Total inclusive W and Z boson cross-section measurements, cross-section ratios and combinations in the electron and muon decay channels at* 7 TeV *based on 300 nb*$^{-1}$. ATL-COM-PHYS-2010-703, 2010.

[94] J. Schwinger. On quantum-electrodynamics and the magnetic moment of the electron. *Phys. Rev.*, 73(4):416–417, Feb 1948.

[95] A. Sherstnev and R. S. Thorne. Parton Distributions for LO Generators. *Eur. Phys. J.*, C55:553–575, 2008.

[96] Torbjorn Sjostrand, Stephen Mrenna, and Peter Z. Skands. PYTHIA 6.4 Physics and Manual. *JHEP*, 05:026, 2006.

[97] Jochem Snuverink. *The ATLAS Muon Spectrometer: Commissioning and Tracking*. PhD thesis, Twente, Twente U., Enschede, Twente, 2009. Presented on 16 Oct 2009.

[98] D.E. Soper. The physics of parton showers, Jun 2009.

[99] Adobe Systems. Photoshop. http://en.wikipedia.org/wiki/Adobe_Photoshop.

[100] S. Tomonaga. On a relativistically invariant formulation of the quantum theory of wave fields. *Progress of Theoretical Physics*, 1(2):27–42, 1946.

[101] N Van Eldik. *The ATLAS Muon Spectrometer: Calibration and Pattern Recognition*. PhD thesis, Univ. Amsterdam, Amsterdam, 2007. Presented on 22 Feb 2007.

[102] Rob Veenhof. Garfield, recent developments. *Nuclear Instruments and Methods in Physics Research Section A: Accelerators, Spectrometers, Detectors and Associated Equipment*, 419(2-3):726 – 730, 1998.

[103] T.S. Virdee. The LHC project: The accelerator and the experiments. *Nuclear Instruments and Methods in Physics Research Section A: Accelerators, Spectrometers, Detectors and Associated Equipment*, 623(1):1 – 10, 2010. 1st International Conference on Technology and Instrumentation in Particle Physics.

[104] Steven Weinberg. A model of leptons. *Phys. Rev. Lett.*, 19(21):1264–1266, Nov 1967.

[105] G Zweig. An SU_3 model for strong interaction symmetry and its breaking; part i. *Developments in the Quark Theory of Hadrons*, 1(CERN-TH-401):24 p, Jan 1964.

[106] G Zweig. An SU_3 model for strong interaction symmetry and its breaking; part ii. *Developments in the Quark Theory of Hadrons*, 1(CERN-TH-412):80 p, Feb 1964.